OPTIMISATION OF ACCELERATOR OPTICS AND THE APPLICATION OF NUCLEAR MICROSCOPY TO THE BIOMEDICAL FIELD

by

Mohamed Eltayeb M. Eisa

Dissertation submitted to the
UNIVERSITY OF CAPE TOWN
in fulfillment of the requirements for the degree of
DOCTOR OF PHILOSOPHY

Department of Physics
University of Cape Town

March 2005

To my Parents and my wife Huda.....

Declaration

Hereby I, Mohamed Eltayeb Mohamed Eisa, declare that this study project is my own original work and that all sources have been accurately reported and acknowledged, and that this document has not previously in its entirety or in part been submitted at any university in order to obtain an academic qualification.

Signed by candidate

Mohamed E. M. Eisa 15 March 2005

ACKNOWLEGMENTS

I would like to express my most sincere appreciation to all those who assisted me in bringing this thesis to completion and in particular to:

- First of all my supervisor at iThemba LABS, Dr Carlos A. Pineda-Vargas, Senior Specialist Scientist at Groote Schuur Hospital, for his guidance, active participation, continuous support and enthusiasm during the execution of this project,
- My co-supervisor at iThemba LABS, Dr Lowry Conradie, Accelerator Group Head, for his patience, constant support and guidance on the accelerator optics optimisation study,
- My university supervisor, Prof. Craig Comrie of the Department of Physics at the University of Cape Town, for his support and encouragement through the years of association with his department,
- Dr Chris Theron, Materials Research Group Head at iThemba LABS, for his kind help, support and encouragement during the time of this work,
- The National Research Foundation through iThemba LABS for the financial support without which this project could have not been completed,
- Prof. Usuf Chikte, Associated Dean, Faculty of Health Sciences, University of Stellenbosch, for his encouragement to use the research on teeth erosion as an application for nuclear microscopy,
- Prof. Sue Naidoo, Specialist at the Department of Community Dentistry, Faculty of Health Sciences, University of Stellenbosch, for her enthusiasm and for kindly supplying the set of teeth from Gugulethu,
- Prof. Allen Rodgers, Head of the Department of Chemistry, University of Cape Town, for the research discussions and suggestions on the study of kidney stone concretions,
- Dr. Adriaan Botha for his kind help and assistance in the writing of the section on optics optimization,

- Dr. Piet Celliers, Deputy Head, Accelerator Group, iThemba LABS, for his assistance on the measurements of the ion source emittance,
- Mr Tshepo Ntsoane, Materials Research Group, iThema LABS, for his help with the experiments on X-ray diffraction,
- Messrs. Garret De Villiers and Dirk Fourie , Accelerator Group, iThemba LABS, for their help in assistance with software,
- Hans Deslink , for his help with the ion source operation,
- Dr Wojtek Przybylowicz, for his kind help, assistance and constructive discussions in nuclear microscopy,
- Prof. Reyno Scheepers from the Geology Department, University of Stellenbosch for making his facilities for samples preparation available to me,
- Lawrence Ashworth, from the MRG workshop, for his help on technical matters,
- Messrs. Karl Springhon, Colin Doyle and Solomon Marsh, for their efficient assistance of the Van De Graaff accelerator and other technical information concerned to the Nuclear Microprobe,
- Mrs Mandy Raman Accelerator Group Secretary for her help and assistance with the writing,
- Ms Lisa Godana, MRG Secretary, for her kind help and assistance in all administrative matters related to my thesis,
- My parents and my wife for their prayers and patience from very far away,
- All MRG staff (iThemba LABS) for their very kind treatment during my stay between them.

OPTIMISATION OF ACCELERATOR OPTICS AND APPLICATION OF NUCLEAR MICROSCOPY TO THE BIOMEDICAL FIELD

Mohamed Eltayeb M. Eisa

iThemba LABS, P.O. Box 722, Somerset West 7129, South Africa

March 2005

Abstract

With the aim of improving the reliability and stability of the beams delivered to the nuclear microprobe at iThemba LABS, as well as optimization of the beam characteristics along the Van de Graaff accelerator beamlines in general, relevant modifications were implemented. The design and layout of the beamlines were revised. The beam-optical characteristics through the accelerator, from the ion source up to the analysing magnet directly after the accelerator, were calculated and the design optimised, using the computer codes TRANSPORT, IGUN and TOSCA. The ion source characteristics and optimal operating conditions were determined on an ion source test bench. The measured optimal emittance for 90% of the beam intensity was about 50π mm mrad for an extraction voltage of 6 kV. These changes allow operation of the Nuclear Microprobe at proton energies in the range 1 MeV to 4 MeV with beam intensities of tens of a pA at the target surface. The capabilities of the nuclear microprobe facility were evaluated in the improved beamline, with particular emphasis to the characterisation of hard human calcium-rich tissue materials.

The process of demineralization in teeth erosion due to exposure to acidic media was investigated in a group of test and control healthy human molar teeth. Samples were cut in cubes of ~2 mm side prior to exposure for 20 h in a 3.6 pH solution. Analysis by micro-PIXE and proton-Backscattering (BS) showed that the levels of trace elements (TE) were enriched and/or depleted according to experimental treatment. The atomic ratios of major constituents in the matrix were characteristic of test or controls with typical ratios: $O_5P_1Ca_3F_1$ for tests and $O_6P_{0.5}Ca_3F_{0.5}$ for controls. The correlation between maps of Ca and Zn in and around the interface between dentine and enamel in control samples showed two kinds of correlation strengths (for enamel and dentine). The strongest correlation was related to the enamel area.

Two groups of human kidney concretions from South Africa and Sudan were compared in terms of their matrix-phases as determined by XRD and proton-BS. Trace elements analysed by micro-PIXE, Fe, Ni, Cu, Zn, Se, Sr and Br showed a possible linear relationship of the mean profile for trace elements for each group of stones. Statistical analysis of micro-PIXE evaluated by correspondence analysis showed that the plot could explain the formation of two clusters corresponding to each the South African and the Sudanese stone groups.

With the aim to compare element content and spatial distribution within scalp hair-shaft cross sections of two distinct human population groups, and to assess possible similarities and/or differences, hair samples from Sudan and South Africa were collected. Proton backscattering and Micro-PIXE were used to determine the matrix composition and content of light and middle transition elements. Mapping analysis showed a relatively similar content distribution for S, Cl, K and Ca within each group. However significant differences, particularly for heavier metals, such as Fe and Zn were also found. Correspondence Analysis of the data showed a clear separation between the two groups when the total content over the hair cross section was considered.

SUMMARY

The ion beam probe characteristics such as, lateral resolution, chromatic aberration and beam current stability are basic requirements for good nuclear microscopy. To be able to deliver ion beams on target with the right conditions for micro analytical work in addition to an optimal object, quadrupole lens and scanning coil set-up, the optimisation of accelerator optics parameters is required to be able to obtain adequate operational properties for the ion beam. Recently a new generation of ion accelerating machines, designed for nuclear microscopy are provide with a better microprocessor control over the optics of the accelerator. This on the other hand helps to maintain an optimal beam probe for high resolution at target surface.

However there are still worldwide a substantial number of "old" accelerators which have been used for more than 40 years for research development, particularly in the field of nuclear microscopy. One of these machines is the iThemba LABS single-ended Van de Graff electrostatic accelerator (manufactured by High Voltage in the sixties) at the Materials Research Group. Due to increase in age, continuous break-downs and high operating costs, management was faced with the difficult task and decision to close down this "old" VDG. However, iThemba management decided in 2001 to re-engineer it and convert this "old machine" into a modern version of a High Voltage 6 MV vertical accelerator, more capable of serving a nuclear microprobe facility. Coupled with physical modifications to the different parts of the accelerating line it was required at first to do an optimisation study on the beam profile optics to be able to determine the main constraints for routine delivery of quality beams for nuclear microscopy operation.

Following previous studies of the VDG accelerator the present research work focused on the optimisation of beam optics and the reliability and stability of the beams delivered to the nuclear microprobe. Relevant modifications were implemented concerning the ion source and the optical characteristics of the accelerator.

Bench study and optimization of the ion source

The optimum operating conditions of a hot cathode duoplasmatron such as the filament current, cathode and anode voltages and the gas flow under which stable beams can be delivered reliably were determined:

- *Optimization of the arc current*

  The beam current for different hydrogen ion species as a function of the arc current was measured. Both the H_1^+ and H_2^+ current increased with increasing arc current while the H_3^+ current decreased with increasing arc current, arc voltage and source temperature. At the higher ion and electron energy as well as at higher discharge temperatures less recombination takes place. For high proton beam intensity the source should be operated at a high arc current and arc voltage to minimize recombination of protons with electrons and hydrogen gas molecules.

- *Optimization of the beam current with the gas flow*

  The gas flow to the ion source was varied to determine the optimum condition for the maximum proton beam current. Because there are no flanges available for pressure gauges on the ion source and the gas flow was too low to be measured, the pressure in the beam pipe of the test bench was measured and used as an indication of the gas flow to the source. The beam current for different hydrogen ion species was measured at an arc current of 1 A, a filament current of 25 A and an extraction voltage of 5 kV. When the gas flow was increased the arc voltage decreases form 97 V to 81 V in order to maintain a constant arc current of 1 A since the arc power supply is current stabilized. Below a pressure of 6×10^{-5} mbar the ion source becomes unstable.

- *Optimization of the beam current with extracting voltage*

  The beam current for different hydrogen ion species as a function of the extraction voltage showed that the source behavior is to a large extent in agreement with the Child-Langmuir law. Furthermore, it indicates that the beam losses in the beam line due to space-charge effects are small and only of importance for operation at low extraction voltages For high beam intensity the source should be operated at the highest possible extraction voltage without jeopardizing reliability of beam delivery due to sparking.

- *Emittance measurement*

  The emittance of the ion source measured at a voltage of 83 V, current of 1 A, a filament voltage of 24 V and extracting voltage of 5 kV was (at 90% of the proton beam intensity, 26 μA), 50.9 π mm mrad. This value was used to calculate the beam transmission through the Van de Graaff accelerator.

Calculation of the optical characteristics of the VDG accelerator

For the calculation of the beam optics at the terminal section the program IGUN was used because it incorporates space-charge effects. For the calculation of the beam optics through the accelerator over its full length the programs TOSCA and TRANSPORT were used:

- *The beam profile in the high-voltage terminal*

  The operational voltages on the electrodes which are obtained by optimizing the beam through the Van de Graaff accelerator were used to calculate the beam profile. In the calculated beam profile the focal points of the beam coincide with the positions of the two collimators, which is essential for good transmission through the machine. The TOSCA results for the terminal section agreed well with the IGUN results.

- *Accelerating tube up to analyzing magnet beam profile*

  Results from TOSCA were compared to the beam width which was measured at the exit of the accelerator. The beam characteristics at the end of the terminal section, were used as the starting condition for the accelerator. The results of the terminal section and the accelerator were then combined to give an overall calculated beam envelope from the ion source to the exit of the accelerator. These results were used to adapt the accelerator electrode inputs for the program TRANSPORT in order to match its results with those of TOSCA. In TRANSPORT the dimensions of the gaps between the first few electrodes of the accelerator tube were modified to obtain similar focusing conditions at the exit of the accelerator compared to the results of TOSCA. In future TRANSPORT can be used for further calculations with these modified lenses since with TRANSPORT the calculations are less time-consuming.

Subsequent to the optimisation of beam optics, relevant applications to demonstrate the capabilities of the nuclear microprobe at iThemba LABS were undertaken with emphasis in the characterisation and spatial distribution of trace metals in hard human tissues such as kidney concretions, teeth enamel and hair cross sections:

- *In vitro teeth enamel-dentine interface exposed to acidic conditions*

  Information on the major components showed marked differences between controls and tests particularly for O, P and F. Analysis by micro-PIXE showed that the levels of trace elements were enriched or depleted according to the type of erosion treatment. Mapping comparison showed that the structure of dentine and enamel is not uniform with respect to the spatial distribution of trace elements and this may determine the cause of teeth demineralization processes exposed to acidic media. A complementary study of teeth enamel from a disadvantaged community in Gugulethu, Cape Town, showed that in spite of high variability of the trace elements concentration the mean value appear to be similar for all sub-groups (male, females, adult or children).

- *Comparison of kidney concretions from two population groups*

  Two groups of human kidney concretions from South Africa and Sudan were compared in terms of their matrix-phases as determined by XRD and proton-BS. The concentration values of the trace elements analysed by μPIXE (Fe, Cu, Zn, Se, Br and Sr) showed a linear trend when their mean was plotted for both groups of stones. Statistical analysis of micro-PIXE data evaluated by correspondence analysis showed the formation of two clusters, corresponding to each the South African and the Sudanese stone groups.

- *Analysis of hair cross sections*

  The main objective was to compare element content and spatial distribution within scalp hair-shaft cross sections of this two distinct human population groups, and to assess possible similarities and/or differences. Mapping analysis showed a relatively similar content distribution for K and Ca within each group. However significant differences, particularly for heavier metals, such as Ti and Zn were also found. Correspondence Analysis of the data showed a clear separation between the two groups when the total content over the hair cross section was considered.

TABLE OF CONTENTS

Biomedical Applications using Nuclear Microprobe

LIST OF FIGURES

LIST OF TABLES

CHAPTER 1

MOTIVATION AND OUTLINE

1.1 HISTORICAL OVERVIEW AND INTRODUCTION

In the early nineteen sixties the main accelerator in South Africa was the locally built fixed-frequency cyclotron [Bur58, Bur60] at the Council for Scientific and Industrial Research (CSIR) in Pretoria. The cyclotron was originally designed and built to accelerate alpha particles to 32 MeV, deuterons to 16 MeV and protons, as singly charged hydrogen molecules, to 8 MeV and was mainly used for nuclear physics research and the production of radioisotopes for medicine and industry. Subsequently it was upgraded to a variable-energy machine capable of accelerating protons, deuterons, alpha particles and Helium-3 in the energy ranges 5.8 to 15.2 MeV, 11.5 to 17.3 MeV, 23 to 34.6 MeV and 18 to 37 MeV, respectively [Bot70].

At about the same time the late Prof. P.B. Zeeman, at that stage head of the department of Physics of the University of Stellenbosch, took the initiative to acquire an accelerator for the Western Cape. As a result the Southern Universities Nuclear Institute (SUNI) was established near Faure to provide facilities for nuclear physics and solid-state physics research for the Universities of Stellenbosch and Cape Town. The newly created institute bought a 6 MV Van de Graaff accelerator from the company High Voltage Corporation in the United States of America.

In the early nineteen seventies it became clear that the then existing accelerator facilities in South Africa no longer met the requirements for nuclear physics research and the production of radioisotopes. Mainly as a result of the initiative of Prof. W.L. Rautenbach, then head of the Nuclear Physics Division at the CSIR, the design of a new cyclotron was started. At the same time radiotherapists in South Africa were considering the acquisition of a cyclotron for particle radiotherapy. To make optimum use of available funds physicists and radiotherapists decided to establish the National Accelerator Centre (NAC) on a site adjacent to SUNI and to build a 200 MeV separated-sector cyclotron as the main accelerator [Abi75, Tec76]. In due time SUNI was incorporated in the NAC, which has been renamed as iThemba Laboratories for Accelerator

Based Sciences. iThemba LABS provide beams of accelerated charged particles and facilities for particle radiotherapy, basic and applied nuclear physics research, ion beam analysis, solid-state and materials research and the production of radioisotopes for nuclear medicine and industry [Sto01]. A wide variety of beams are delivered to users by three cyclotrons: a 200 MeV separated-sector cyclotron with two solid-pole injector cyclotrons for acceleration of high-intensity beams of light ions and acceleration of heavy and polarized hydrogen ions, as well as 6 MV Van de Graaff accelerator.

A valuable addition to the research facilities at the Van de Graaff accelerator was the nuclear microprobe, which was installed during 1991. The microprobe was obtained from the company Oxford Microbeams [Oxf90] Although the facility has proved to be extremely useful for the analysis of micro samples from a wide variety of fields its full potential could not be exploited due to limitations in the quality of available beams.

In order to improve the quality and intensity of the beams delivered to the microprobe facility and other users equipment the design of the beamlines, which dates back to about 1995, has recently been analyzed, using the latest computer programs for beamline and magnet design, and several modifications are at present in progress. Therefore, it was decided on January of 2001 to develop a plan to upgrade and optimize the different components and parameters from ion source to switching magnet at the VDG accelerator with the purpose of improving the delivery of higher current and stable focused beams for the purpose of Nuclear Microprobe analysis of a wide variety of sample materials with different experimental requirements, translated in real terms on current ranges at target surface of the order of 10s of pA for a 1-3 μm proton beam size.

1.2 MOTIVATION FOR THIS STUDY

Although the recent study of [Mai02] the Van de Graaff beamlines lead to significant improvements, the Van de Graaff accelerator itself and its ion source have not been included in the study. Past experience with operation of the accelerator suggests that design of the electrostatic lenses, immediately below the ion source, has not been optimized and that it may be worthwhile to improve the design. The beam intensity available at the microprobe facility is in spite of recent improvements limited to only 0.1 nA for a beamspot size between 1-3

microns.

The main objectives of this study are therefore to determine the characteristics and optimum stable operating conditions of the ion source and to calculate the beam behavior in the Van de Graaff accelerator to determine the limitations on the quality and intensity of the beams delivered to the users, and especially to the nuclear microprobe facility. Since the early nineteen sixties computers and computer programs for orbit calculations in accelerators and beamlines have developed dramatically and it may now be possible to improve on the existing designs with the latest available calculation techniques. The beam characteristics at the entrance to the microprobe facility will be determined and compared with those before modifications were made to the accelerator and its ion source

1.3 OUNTLINE OF THE THESIS

The accelerator facilities at iThemba LABS are briefly described in chapter 2. Chapter 3 is an outline of the mathematical formalism for transport calculations and beamline elements. In chapter 4 the results of measurements on the Van de Graaff ion source and the beam emittance measured in an ion source test bench are presented. The computer programs TRANSPORT, TOSCA and IGUN and their application to the calculation of particle paths through the Van de Graaff accelerator as well as modifications for improvement of the beam quality and intensity are treated in chapter 5.

The last three chapters deal with biomedical applications of protons microscopy Chapter 6 gives a general review of the theoretical background on Nuclear Microprobes, description of techniques used in proton microscopy such as PIXE, pBS and PIGE as well as the software used for deconvolution .of spectra, particularly PIXE data. Chapter 7 presents an overview of the experimental conditions and currently accessible techniques at the nuclear microprobe facility this includes the optics set up from object to target and the algorithm by dynamic analysis up to the dynamic mapping on hard human tissues. Chapter 8 deals with applications of proton microprobe in the characterization of human hard tissues such as kidney concretions, teeth dentine and enamel and scalp hair cross sections. Appendix A and B show an example of the IGUN and TRANSPORT programs input information used for the beam optics optimization of the VDG accelerator this includes the mathematical equation solution to the Poisson's equation which is shown in appendix C

CHAPTER 2

THE ACCELERATOR FACILITY AT ITHEMBA LABS

2.1 CYCLOTRON FACILITIES

The wide range of applications of accelerated charged particle beams for which the cyclotron facilities were originally planned necessitated the unique design of the accelerators and the layout of the facilities shown in figure 2.1. For nuclear physics research beams of light and heavy ions, as well as polarized hydrogen ions, with variable energy up to a maximum of 200 MeV for protons were required. The 200 MeV beam would also be suitable for proton therapy. For the production of radioisotopes and neutron therapy 100 μA and 30 μA beams of 66 MeV protons were, respectively, planned.

The main accelerator, the 200 MeV separated-sector cyclotron (SSC) [Rau75, Jun75, Bot75], was chosen for the good extraction efficiency of such machines due the high dee voltages, more than 200 kV, which can be obtained with the dees in the open spaces between the magnet sectors. Because there are no high voltage electrodes between the magnet poles the pole gaps can be made small thereby increasing the azimuthal modulation of the field which results in excellent vertical beam focusing in spite of the radial increase in the average field. The small pole gaps also allow an isochronous magnetic field up to the extraction radius, which results in sharp beams with low energy spread over the whole radial extent of the cyclotron, and a sharp drop off in the magnetic field beyond the extraction radius. This alleviates extraction of the beam, which is done with septum magnets for which ample space is available between the sector magnets. The SSC has four sector magnets with a sector angle of 34 degrees and two half-wave resonators, which can be tuned over the frequency range 7 MHz to 27 MHz. The maximum dee voltage of 230 kV results in an energy gain of almost an MeV per turn. By measuring the beam phase with a capacitive probe and tuning the 28 trim coil power supplies the magnetic field can be made isochronous to such an extent that particles remain to within a few degrees in phase with the dee voltage.

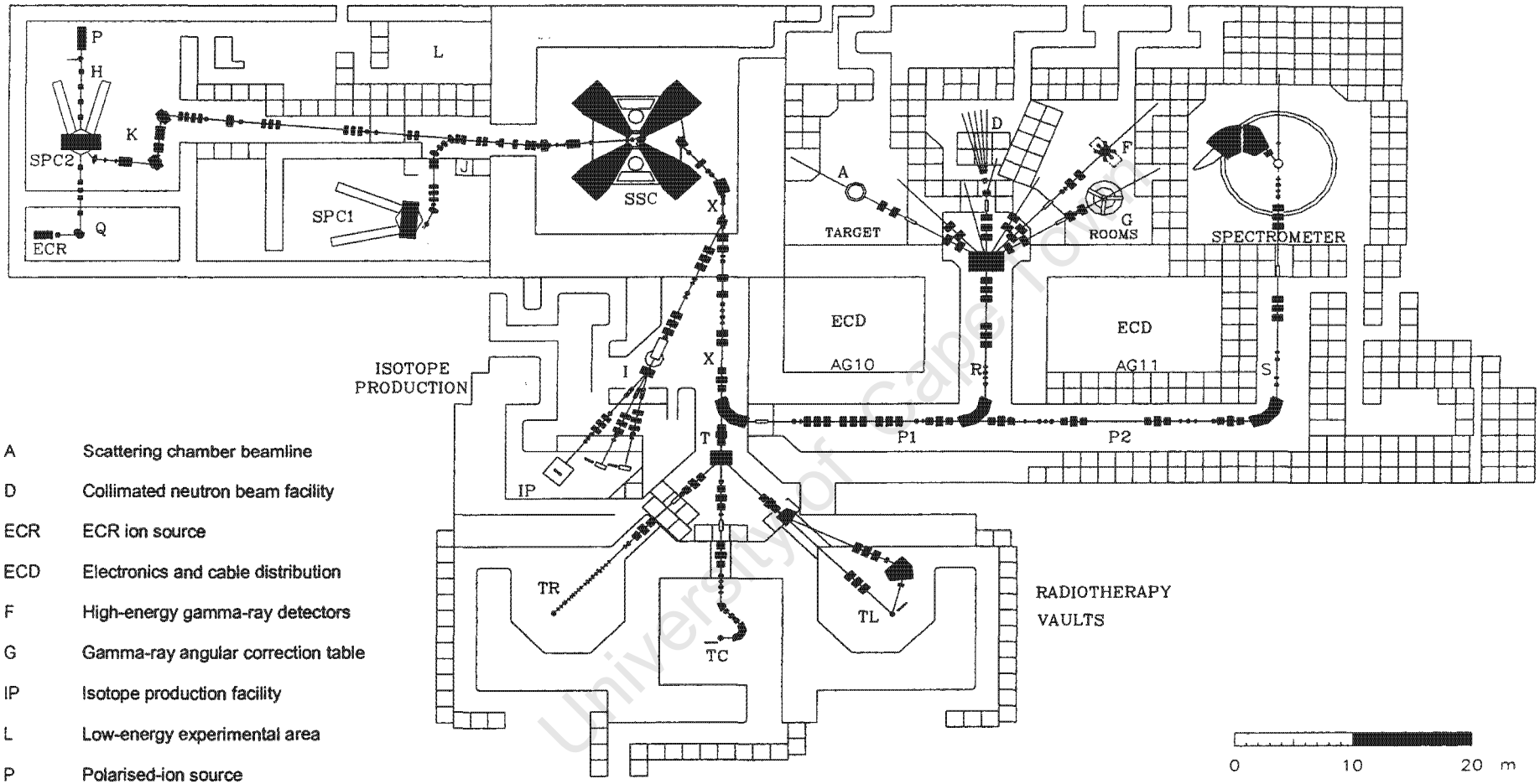

A	Scattering chamber beamline
D	Collimated neutron beam facility
ECR	ECR ion source
ECD	Electronics and cable distribution
F	High-energy gamma-ray detectors
G	Gamma-ray angular correction table
IP	Isotope production facility
L	Low-energy experimental area
P	Polarised-ion source
SPC1	Solid-pole injector cyclotron for light ions
SPC2	Solid-pole injector cyclotron for heavy i

Figure 2.1: Layout of the cyclotron facilities at iThemba LABS

The beam is injected with two bending magnets, a magnetic inflection channel and an electrostatic channel and is extracted with two septum magnets. Because the sector magnets and resonators of a separated-sector cyclotron cannot, due to space limitations, extend to a too small radius, one or more pre-accelerators are required. In the case of the SSC two K=8 solid-pole injector cyclotrons (SPC1 and SPC2) [Dut87, bot87a, Bot87b, Dut95] are used for pre-acceleration. SPC1 operates with an internal Penning Ion Gauge (PIG) ion source and delivers high-intensity beams of light ions [Con92] for injection into the SSC. For the pre-acceleration of heavy and polarized hydrogen ions SPC2 is used. The Electron Cyclotron Resonance Ion Source (ECRIS) for heavy ions and the ion source for polarized hydrogen ions are external to SPC2. Apart from the ion sources and the axial injection system in SPC2, the two-injector cyclotrons are in many respects similar, if not identical. For instance both have four sector magnets and two ninety-degree dees connected to quarter wave resonators and in both cases beam is extracted with an electrostatic channel and two septum magnets.

As shown in figure 2.1 the beam is guided from the injector cyclotrons to the SSC and from the SSC to vaults for the production of radioisotopes, particle radiotherapy and nuclear physics experiments along beamlines that consist mainly of quadrupole and dipole magnets.

2.2 THE VAN DE GRAAFF FACILITIES

2.2.1 THE VAN DE GRAAFF ACCELERATOR FACILITIES

The 6 MV Van de Graaff accelerator, shown schematically in figure 2.2, is a high precision variable-energy machine, capable of accelerating light and heavy ions to energies between 0.5 and 20 MeV with an energy spread of less than one part in 10000. The accelerator, which is in operation since 1962, is used mainly for materials and solid-state physics research in collaboration with the universities and technikons, as well as local and international laboratories. The facilities at the Van de Graaff accelerator are for atomic and solid-state physics and the application of nuclear analytical techniques in ion beam analysis and materials sciences. Research projects use accelerated particles for identification and quantification of elements in microelectronics, archaeology, geology, super-conducting materials, optical and new materials. The layout of the beamlines to the different users areas is shown in fig. 2.3 and 2.4.

Facilities for target manufacture, surface preparation and radioactivity counting are available. Radioactive tracers and nuclear techniques are utilized in basic and applied investigations. Data acquisition and analysis are fully computerized.

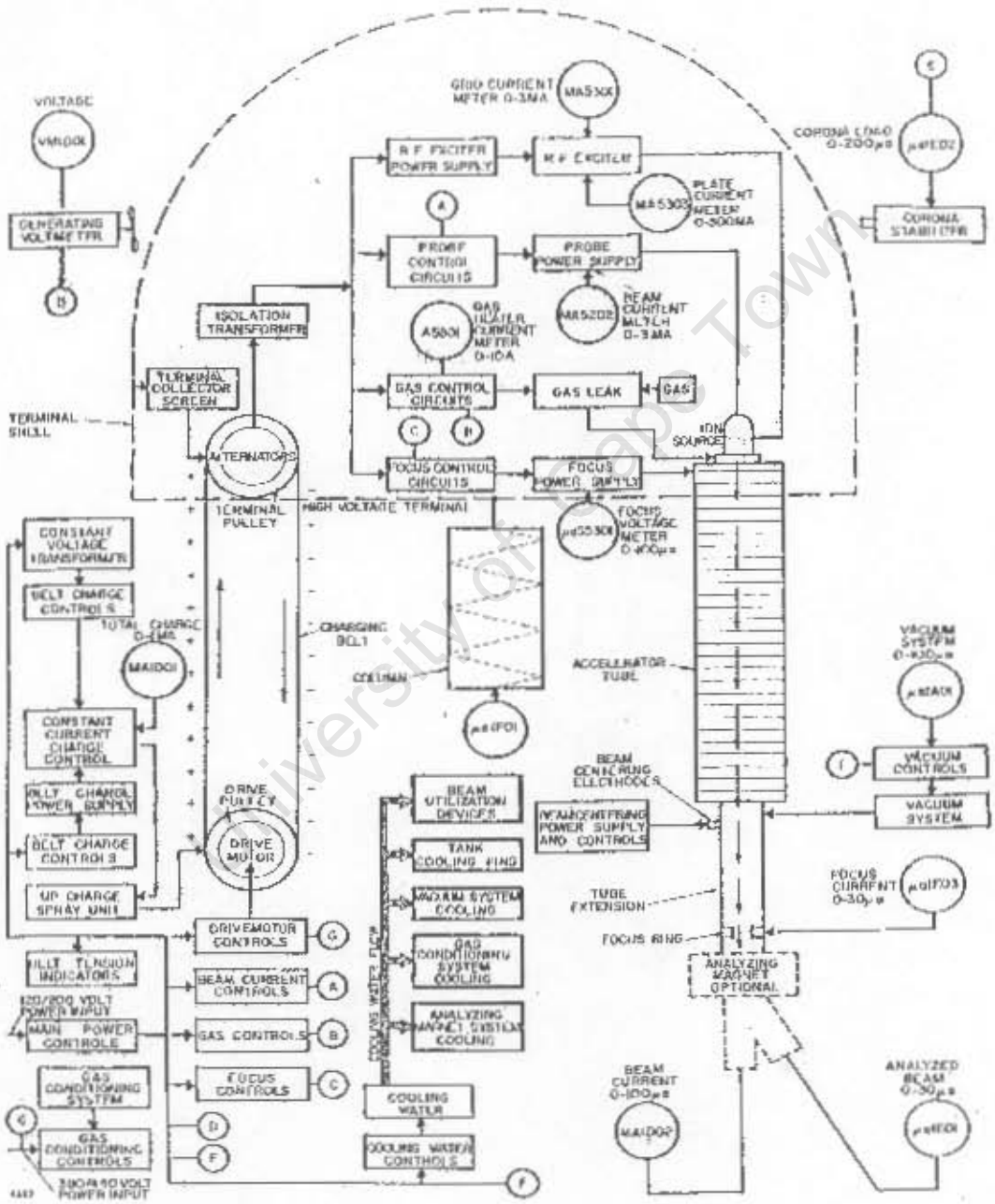

Fig.2.2: Schematic drawing of the Van de Graaff accelerator

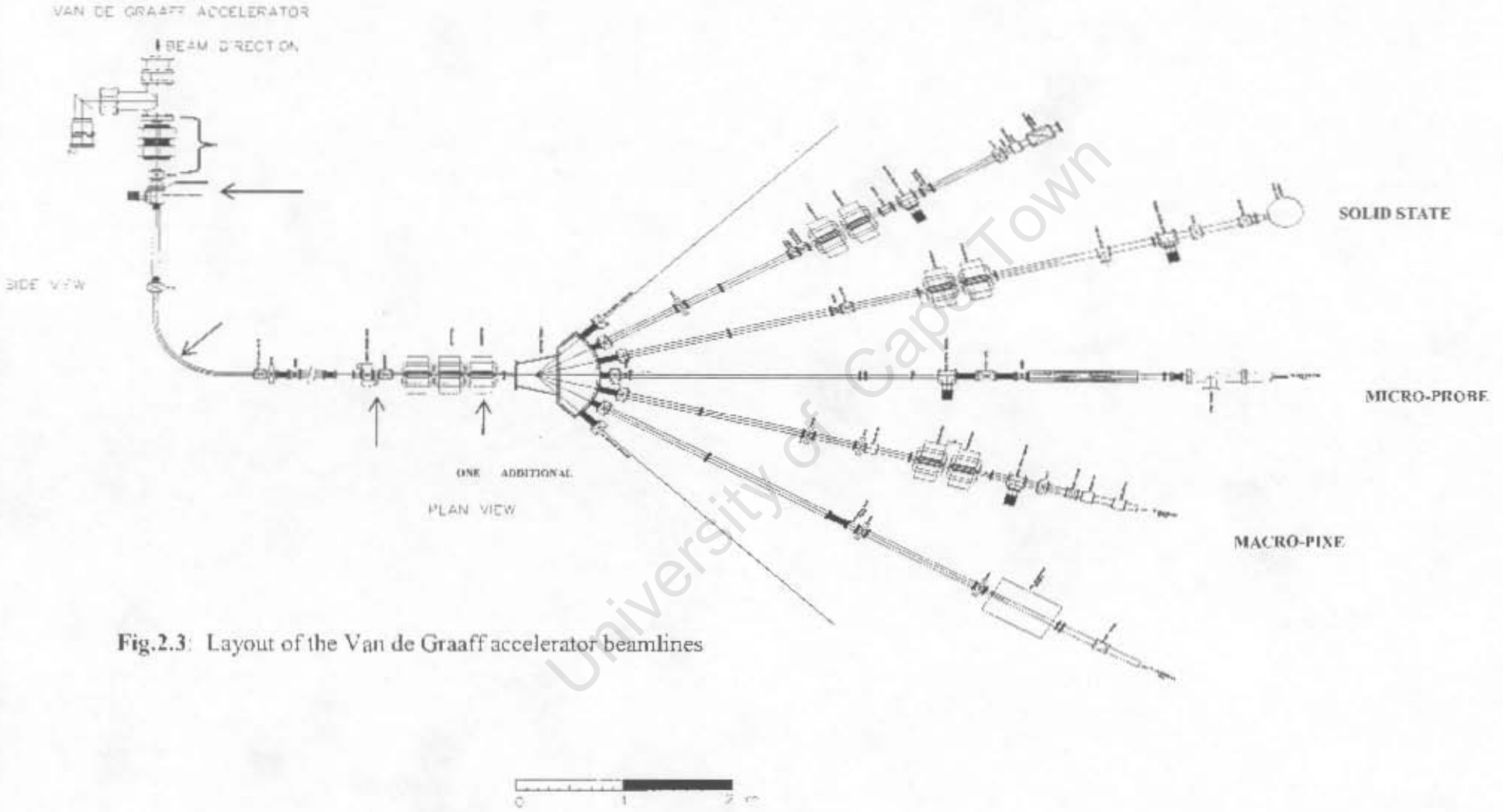

Fig.2.3: Layout of the Van de Graaff accelerator beamlines

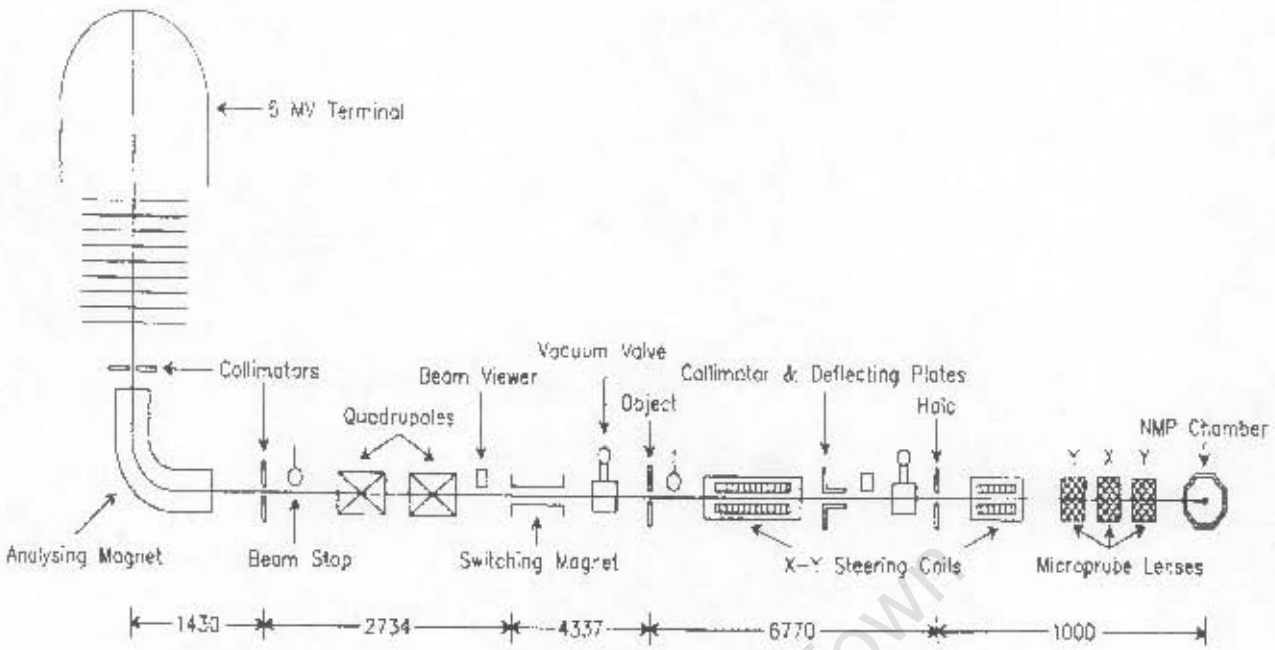

Figure 2.4: Layout of the beamline to the microprobe facility.

2.2.2 THE MICRO-BEAM FACILITY

The high-brightness scanning nuclear microprobe, of which the layout is shown in figure 7.7, has a resolution of less than 1 micron and enables researchers to observe, identify and measure precise quantities of trace elements, as well as more abundant elements, in the samples from many different fields. The facility has been operational since 1991 and is utilized especially in geology and materials sciences.

Nuclear microprobes have been used in biological studies since the early 1970s. In most cases 1-4 MeV proton beams are used and often these facilities are described as proton microprobes. One of their strengths is the possibility of the simultaneous use of a number of ion-based techniques using various incident particles (proton, alpha particles) in the MeV energy range. Typically particle induced X-ray emission (PIXE) is used together with Rutherford backscattering spectrometry (RBS) and scanning transmission microscopy (STIM) or secondary electron microscopy (SE) at iThemba LABS [Prz99].

CHAPTER 3

MATHEMATICAL FORMALISM FOR BEAM TRANSPORT AND BEAMLINE ELEMENTS

3.1 INTRODUCTION

Beams of charged particles emerge from ion sources and accelerators with positional and momentum spreads in both the longitudinal and transverse directions and have therefore to be focused, in addition to being directed to the intended destination, with electromagnetic fields. In beamlines between accelerators and between accelerators and external targets quadrupole magnets are the most often used for beam focusing and dipole magnets for changing the beam direction, although dipole magnets can also be designed to contribute to focusing.

Instead of calculating and studying the paths of a large number of individual particles, representative of the beam, through the complicated fields of beamline elements it is for many purposes sufficient to calculate only the path of the central particle with the desired energy and zero transverse momentum and positional deviations and to calculate and present the behavior of particles with deviations in energy, position and transverse momentum, with respect to the central particle, through the beamline, in phase space. This has the advantage that only bounded regions in phase space have to be considered, rather than following a large number of trajectories [Lic69]. Phase-space trajectories do not cross each other and phase-space points that are initially bounded remain so, because of Liouville's theorem [Gol80], throughout the beamline. It is therefore only necessary to know the behavior of the boundary of the beam in phase space.

Beam behavior in accelerators and beamlines is generally described in the six-dimensional phase space. The six dimensions are the transverse (horizontal and vertical) position deviations and divergence, the longitudinal position and energy deviations with respect to the central particle. In the remaining part of this chapter the description of a beam of particles in six-dimensional phase space and the influence of beamline elements such as quadrupole and dipole magnets are discussed. The mathematical formulation of beam transport elements and systems has been described in several reports. The formulation by Carey [Car87] is followed below to derive first the linear equations of motion and their application to drift spaces and quadrupole

and dipole magnets, and then to derive the second order terms in the equations of motion.

3.2 THE LINEAR EQUATIONS OF MOTION

In the following vector differential equation of motion, for a charged particle with velocity v and charge q in a static magnetic field B, the time rate of change of momentum is given by the Lorentz force:

$$\dot{\mathbf{p}} = q(\mathbf{v} \times \mathbf{B}) \tag{3.1}$$

The Lorentz force is always perpendicular to the direction of motion and the magnitude of the momentum remains constant. A new moving coordinate system, defined in figure 3.1, whose origin is always on the trajectory of the central particle, is now introduced to eliminate time from equation 3.1. The new coordinates x, y, and t specify the position of an arbitrary particle with respect to the central particle in the horizontal, vertical and longitudinal directions, respectively. In the new coordinate system the equation of motion becomes:

$$\frac{dT}{dt} = \frac{q}{p}\frac{dT}{dt} \times \mathbf{B} \tag{3.2}$$

Where the vector **T** and the scalar t indicate the position and path length of an arbitrary particle, respectively. The unit vector tangent to the particle trajectory is $\frac{dT}{dt}$. The three mutually perpendicular unit vectors $\hat{\mathbf{x}}$, $\hat{\mathbf{y}}$, $\hat{\mathbf{t}}$ along the three coordinate axes satisfy the following relations:

$$\begin{aligned} \hat{x} &= \hat{y} \times t \\ \hat{y} &= \hat{t} \times \hat{x} \\ t &= \hat{x} \times \hat{y} \end{aligned} \tag{3.3}$$

The derivatives of the unit vectors with respect to t are given by:

$$\begin{aligned} \hat{\mathrm{x}}' &= h\hat{\mathrm{t}} \\ \hat{\mathrm{y}}' &= 0 \\ \hat{\mathrm{t}}' &= -h\hat{\mathrm{x}} \end{aligned} \tag{3.4}$$

where h, the curvature of a trajectory, is defined as the rate of change of direction with respect to path length. The curvature h(t) is also the reciprocal of the local radius of curvature ρ_0 of the central trajectory. The term $\rho d\theta$ for the azimuthal distance in cylindrical coordinates takes the form (1+hx), where (1+hx) indicates the relative sizes of ρ and ρ_0. The differential line element along an arbitrary trajectory is given by:

$$d\mathbf{T} = \hat{\mathbf{x}}\,dx + \hat{\mathbf{y}}\,dy + (1+hx)\,\hat{\mathbf{t}}\,dt \tag{3.5}$$

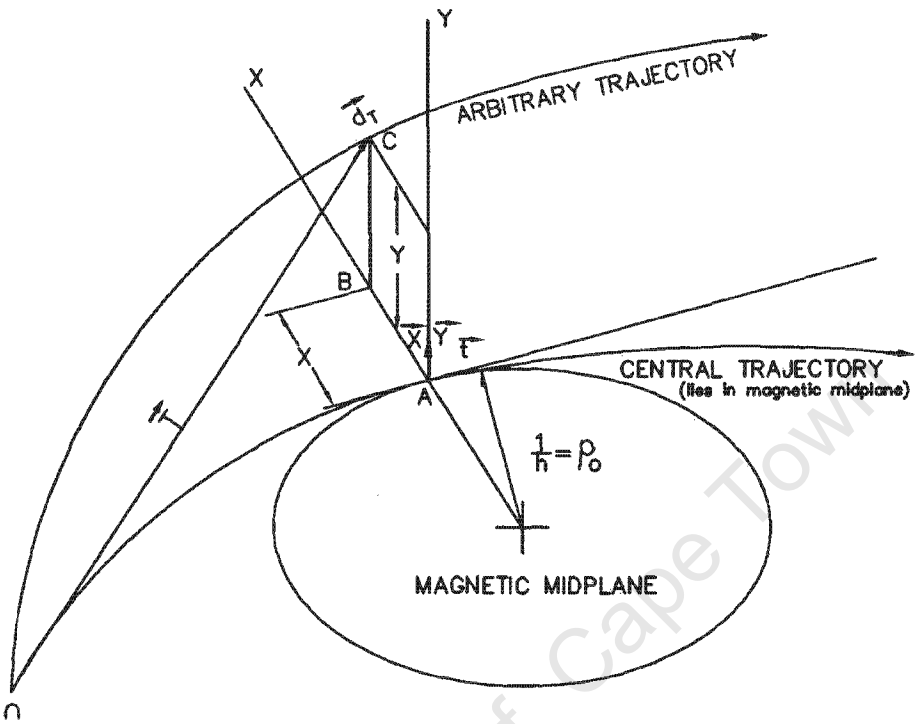

Figure 3.1: Moving coordinate system for the equations of motion with respect to the central particle

The two transverse components of the equation of motion now become:

$$\begin{aligned} x'' - h(1+hx) &= \frac{q}{p}(1+hx)[y'B_t - (1+hx)B_y] \\ y'' &= \frac{q}{p}(1+hx)[(1+hx)B_x - x'B_t] \end{aligned} \tag{3.6}$$

For the central particle x and y as well as their derivatives are equal to zero and the following equation is obtained:

$$h = \frac{q}{p_0}B_y(0,0,t) \quad or \quad B\rho_0 = \frac{p_0}{q} \tag{3.7}$$

In any region of space containing no electric currents, the field of a static electromagnet can be expressed in terms of a scalar potential Φ so that:

$$\mathbf{B} = \nabla\Phi \tag{3.8}$$

The usual minus sign is here considered as included in the potential Φ. Because of the mid-plane symmetry the field component is the y-direction, which is obtained by differentiating the

potential with respect to y, can only contain constant and even powers in y. An expansion of the scalar potential Φ in a power series should therefore only contain uneven powers is y. Furthermore, the only terms that contribute to the first-order equations of motion are at most linear in x and y. Therefore only up to quadratic terms in Φ are considered:

$$\Phi(x,y,t) = A_{10}y + A_{11}xy \tag{3.9}$$

where the coefficients A_{10} and A_{11} are functions of t. The two coefficients can be chosen independently because only in second and higher orders does Laplace's equation impose relationships among the coefficients. The components of the magnetic field are then given by:

$$\begin{aligned} B_x(x,y,t) &= \frac{\partial \Phi}{\partial x} = A_{11}y \\ B_y(x,y,t) &= \frac{\partial \Phi}{\partial y} = A_{10} + A_{11}x \\ B_t(x,y,t) &= \frac{1}{(1+hx)}\frac{\partial \Phi}{\partial t} = A'_{10}y + (A'_{11} - hA'_{10})xy \end{aligned} \tag{3.10}$$

The coefficient A_{11} can be expressed in terms of a dimensionless parameter n so that:

$$\begin{aligned} A_{10} &= \frac{hp_o}{q} \\ A_{11} &= -hA_{10}n \end{aligned} \tag{3.11}$$

The field index n is given in terms of the vertical magnetic field component by:

$$n = \left[\frac{1}{hB_y}\left(\frac{\partial B_y}{\partial x}\right)\right]_{\substack{x=0 \\ y=0}} \tag{3.12}$$

The expressions for the components of the magnetic field from equations 3.10 and 3.11 can now be substituted into the equations of motion. A new quantity $\delta = \frac{\Delta p}{p_0}$, the fractional deviation of the momentum from that of the central trajectory, is defined by:

$$p = p_0(1+\delta) \tag{3.13}$$

By making use of the equation of motion for the central trajectory and by retaining only terms of first order the following equations are obtained from equations 3.6:

$$\begin{aligned} x'' + (1-n)h^2 x &= h\delta \\ y'' + nh^2 y &= 0 \end{aligned} \tag{3.14}$$

The general solution of the differential equations 3.14 for x and y as functions of t can be

written in terms of sine-like functions, $s_x(t)$ and $s_y(t)$, cosine-like functions, $c_x(t)$ and $c_y(t)$ and their derivatives as well as a dispersion function $d_x(t)$:

$$\begin{aligned} x(t) &= x_0 c_x(t) + x_0' s_x(t) + \delta d_x(t) \\ y(t) &= y_0 c_y(t) + y_0' s_y(t) \end{aligned} \tag{3.15}$$

where x_0, x_0', y_0, y_0' are the respective initial values. The sine- and cosine-like functions are solutions of the homogeneous equations. The function $d_x(t)$ is a particular integral of the first of equations 3.14 and can be obtained by means of Green's function G [Bar89, Mat65]:

$$G(t,\tau) = s(t)c(\tau) - c(t)s(\tau) \tag{3.16}$$

$$d_x(t) = s_x(t)\int_0^t c_x(\tau)h(\tau)d\tau - c_x(t)\int_0^t s_x(\tau)h(\tau)dt \tag{3.17}$$

Using equations 3.14 the solutions for $x, x', y,$ and y' can be expressed in terms of the following matrix equations:

$$\begin{pmatrix} x(t) \\ x'(t) \\ \delta \end{pmatrix} = \begin{pmatrix} cx(t) & s_x(t) & d_x(t) \\ c_x'(t) & s_x'(t) & d_x'(t) \\ 0 & 0 & 1 \end{pmatrix} \begin{pmatrix} x_0 \\ x_0' \\ \delta \end{pmatrix}$$
$$\begin{pmatrix} y(t) \\ y'(t) \end{pmatrix} = \begin{pmatrix} c_y(t) & sy(t) \\ c_y'(t) & s_y'(t) \end{pmatrix} \begin{pmatrix} y_0 \\ y_0' \end{pmatrix} \tag{3.18}$$

The total transfer matrix R_t for a beamline is obtained by multiplication of the matrices $R_1, R_2, \ldots R_n$ for the individual segments of the beamline:

$$R(T) = R_n \ldots R_2 R_1 \tag{3.19}$$

The full six by six transfer matrix for linearized motion in a static magnetic system with mid-plane symmetry now becomes:

$$\begin{pmatrix} x(t) \\ x'(t) \\ y(t) \\ y'(t) \\ \ell(t) \\ \delta(t) \end{pmatrix} = \begin{pmatrix} R_{11} & R_{12} & 0 & 0 & 0 & R_{16} \\ R_{21} & R_{22} & 0 & 0 & 0 & R_{26} \\ 0 & 0 & R_{33} & R_{34} & 0 & 0 \\ 0 & 0 & R_{43} & R_{44} & 0 & 0 \\ R_{51} & R_{52} & 0 & 0 & 1 & R_{56} \\ 0 & 0 & 0 & 0 & 0 & 1 \end{pmatrix} \begin{pmatrix} x_0 \\ x_0' \\ y_0 \\ y_0' \\ \ell_0 \\ \delta_0 \end{pmatrix} \tag{3.20}$$

Since particles in the median plane experience no force in the vertical direction the matrix elements R_{31}, R_{32}, R_{35}, R_{36}, R_{41}, R_{42}, R_{45}, R_{46} are zero. Because only static magnetic fields and no electric fields are considered the particle energy remains constant. R_{61}, R_{62}, R_{63}, R_{64}, R_{65} are therefore zero and R_{66} is equal to one. R_{15}, R_{25}, R_{35}, R_{45} and R_{65} are zero because the forces on particles do not depend on their longitudinal position, except for the case of bunchers,

which are not considered here. In the linear approximation of the equations of motion the contribution of the displacement of the beam in the vertical direction to the longitudinal position is neglected. R_{53} and R_{54} are therefore zero. In the same approximation the momentum spread does not contribute to the vertical motion, and the vertical motion not to the horizontal motion, with the result that R_{36}, R_{46}, R_{13}, R_{14}, R_{23} and R_{24} are zero.

The path length difference expressed in terms of the initial coordinates is given by:

$$\ell = x_0 \int_0^t c_x(\tau)h(\tau)d\tau + x_0' \int_0^t s_x(\tau)h(\tau)d\tau + \delta_0 \int_0^t d_x(\tau)h(\tau)d\tau \qquad (3.21)$$

The matrix elements related to path length in the six by six matrices can be evaluated from:

$$\begin{aligned} R_{51} &= (\ell|x_0) = \int_0^t c_x(\tau)h(\tau)d\tau \\ R_{52} &= (\ell|x_0') = \int_0^t s_x(\tau)h(\tau)d\tau \\ R_{56} &= (\ell|\delta) = \int_0^t d_x(\tau)h(\tau)d\tau \end{aligned} \qquad (3.22)$$

For a length L_0 of the reference trajectory and the velocity v_0 of the central particle the longitudinal separation, i.e. the distance is which the central particle is behind a particle with momentum p traversing a path length L, at the end of the beamline, is given by:

$$\ell = L - L_0 - L_0 \frac{1}{\gamma^2}\delta \qquad (3.23)$$

Where $\gamma^2 = 1 - \frac{v^2}{c^2}$ and c the velocity of light in vacuum.

3.3 THE TRANSFER MATRICES OF SOME BEAMLINE ELEMENTS

3.3.1 TRANSFER MATRICE OF A DRIFT SPACE

The simplest beamline element is a drift space, a field-free region in the beamline, which is specified by a single parameter L, the length. In such a space the longitudinal and transverse momenta are conserved and both n and h are zero. From this and equations 3.14 it follows that:

$$x'' = 0,\ y'' = 0,\ x'(t) = x_0',\ y' = y_0',\ c_x(t) = 1,\ c_y(t) = 1,\ s_x(t) = t,\ s_y(t) = t,\ d_x(t) = 0 \qquad (3.24)$$

and at the end of the drift space:

$$\begin{aligned} &x(L) = x_0 + x_0'L,\ y(L) = y_0 + y_0'L \\ &x'(L) = x_0',\ y'(L) = y_0' \end{aligned} \qquad (3.25)$$

Since h is equal to zero the only contribution to the change in path length due to the momentum

spread is:

$$\ell = -L\,\frac{1}{\gamma^2}\delta$$

To follow the convention commonly used in the literature on beam transport theory the minus sign is left out in the following matrix R for a drift space, to indicate the distance that the particle with momentum p is ahead of the central particle at the end of the drift space:

$$R = \begin{pmatrix} x(t) \\ x'(t) \\ y(t) \\ y'(t) \\ \ell(t) \\ \delta(t) \end{pmatrix} = \begin{pmatrix} 1 & L & 0 & 0 & 0 & 0 \\ 0 & 1 & 0 & 0 & 0 & 0 \\ 0 & 0 & 1 & L & 0 & 0 \\ 0 & 0 & 0 & 1 & 0 & 0 \\ 0 & 0 & 0 & 0 & 1 & L/\gamma^2 \\ 0 & 0 & 0 & 0 & 0 & 1 \end{pmatrix} \begin{pmatrix} x_0 \\ x_0' \\ y_0 \\ y_0' \\ \ell_0 \\ \delta_0 \end{pmatrix} \tag{3.26}$$

3.3.2 TRANSFER MATRICES FOR A QUADRUPOLE MAGNET

In quadrupole and dipole magnets the magnetic field is in most cases constant along the path of the central trajectory. In such cases the homogeneous form of equations 3.14 can be written as:

$$q'' \pm k^2 q = 0 \tag{3.27}$$

For the positive sign the functions *c(t)* and *s(t)* are now:

$$\begin{aligned} c(t) &= \cos kt \\ s(t) &= \frac{1}{k}\sin kt \end{aligned} \tag{3.28}$$

For the negative sign in equation 3.27 the trajectory is divergent and the general solution can be expressed as:

$$\begin{aligned} c(t) &= \cosh kt \\ s(t) &= \frac{1}{k}\sinh kt \end{aligned} \tag{3.29}$$

The dispersion function is given by:

$$d_x(t) = \frac{h}{k_x^2}(1 - c_x(t)) \tag{3.30}$$

Figure 3.2 shows a cross section through the hyperbolic pole tips of a quadrupole magnet looking in the direction of the reference trajectory. The scalar potential of the field of a quadrupole magnet can be obtained by conformal mapping and is in rectangular coordinates given by:

$$\Phi = \frac{B_0 xy}{a} \tag{3.31}$$

where B_0 is the magnetic field on a pole tip at a point closest to the optical axis x = 0, y = 0 and a is the distance from the origin to this point. The magnetic field components can be expressed as the gradient of the scalar potential:

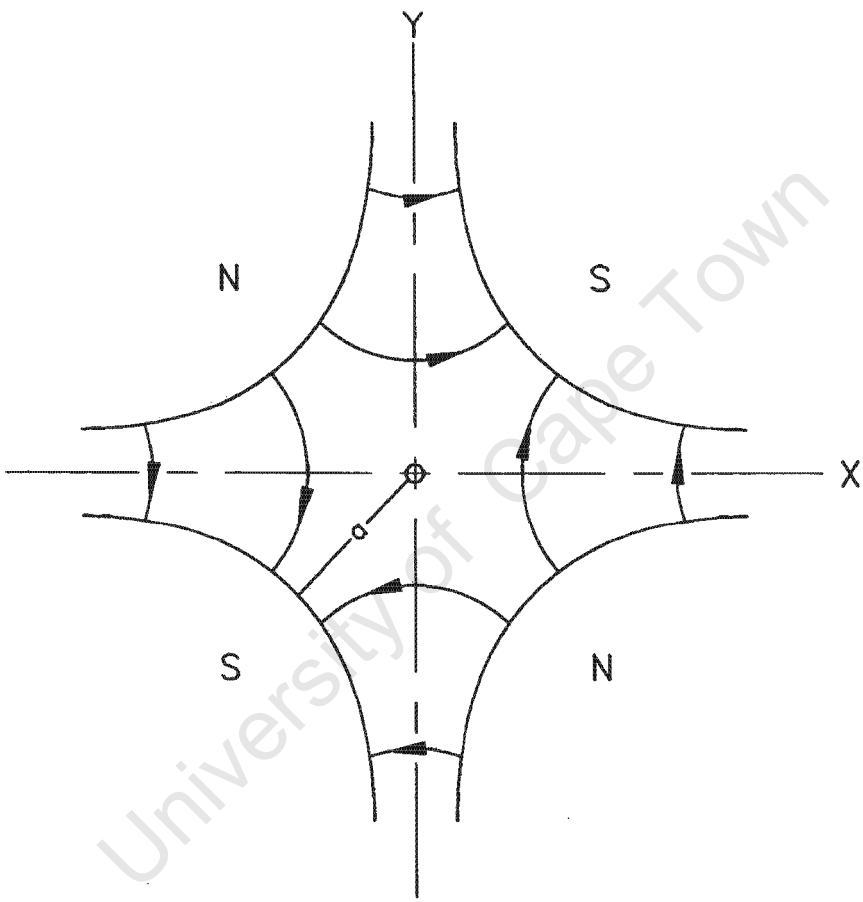

Figure 3.2: A cross section through the hyperbolic pole tips of a quadrupole magnet.

$$B_x = \frac{B_o y}{a} = gy$$
$$B_y = \frac{B_0 x}{a} = gx \qquad (3.32)$$

The magnitude of the field B as a function of the radius r is given by:

$$B = gr \qquad (3.33)$$

The field has the following symmetry about both horizontal and vertical planes:

$$\begin{aligned} B_x(x,y,t) &= -B_x(x,-y,t) = \quad B_x(-x,y,t) \\ B_y(x,y,t) &= \quad B_y(x,-y,t) = -B_y(-x,y,t) \end{aligned} \tag{3.34}$$

In a quadrupole magnet the curvature h of the central trajectory is zero and equations 3.6 become:

$$\begin{aligned} x'' &= -\frac{q}{p}B_y \\ y'' &= \frac{q}{p}B_x \end{aligned} \tag{3.35}$$

With the field components substituted from equations 3.35 the following equations of motion for a quadrupole magnet are obtained:

$$\begin{aligned} x'' + k_q^2 x &= 0 \\ y'' - k_q^2 y &= 0 \end{aligned} \tag{3.36}$$

with:

$$k_q^2 = \frac{qg}{p_0} \tag{3.37}$$

Equations 3.32, 3.36 and 3.37 show that for positive field strength the beam is focused horizontally and defocused vertically. The solutions to these equations 3.36 are given by 3.28 and 3.29 for the x- and y-directions, respectively. Since the central trajectory has no curvature the change in path lengths due to the momentum spread is again given by the same expression $L\,\frac{1}{\gamma^2}\delta$ as for a drift space, with L the length of the magnet. For the same reason the dispersion function d_x is also zero. The transfer matrix R for a quadrupole magnet for horizontal focusing and vertical defocusing is therefore given by:

3.3.3 TRANSFER MATRICES FOR A BENDING MAGNET

In beamlines bending magnets are not only used for changes in the beam direction but also for focusing and energy selection. The equations of motions, the dispersion function and the expression for changes in the longitudinal positions of particles, due to the momentum spread, have already been given above for a dipole magnet with median plane symmetry. The relevant

equations 3.14, 3.15, 3.17, 3.21, 3.22 and 3.23 yield the transfer matrix R, given on the next

$$R=\begin{bmatrix} \cos k_q L & \frac{1}{k_q}\sin k_q L & 0 & 0 & 0 & 0 \\ -k_q \sin k_q L & \cos k_q L & 0 & 0 & 0 & 0 \\ 0 & 0 & \cosh k_q L & \frac{1}{k_q}\sinh k_q L & 0 & 0 \\ 0 & 0 & k_q \sinh k_q L & \cosh k_q L & 0 & 0 \\ 0 & 0 & 0 & 0 & 1 & \frac{L}{\gamma^2} \\ 0 & 0 & 0 & 0 & 0 & 1 \end{bmatrix} \qquad (3.38)$$

page, for a bending magnet with edges perpendicular to the reference trajectory.

A further contribution to beam focusing can be made by shaping of the entrance and exit pole edges of a bending magnet as shown in figure 3.3. The pole face rotation angle β is defined as positive if a particle with a positive x displacement remains for a shorter distance in the magnet gap, than would have been the case if the pole face would have been perpendicular to the reference trajectory. A particle with a negative displacement, with respect to the reference trajectory, in the x-direction, remains in the magnetic field for a distance $|x|\tan\beta$ longer at the magnet edge than would have been the case if the magnet edge were perpendicular to the reference trajectory. With a radius of curvature ρ_0 the additional angle through which the particle is deflected in the negative x-direction, is to a first order given by $(|x|\tan\beta)/\rho_0$. This explains element R_{21} in the following transfer matrix for an edge angle, apart from a correction ψ to the angle β, which is necessary in cases of extended stray fields. For positive values of β the beam is defocused horizontally. The x-component in the stray field at vertical displacements with respect to the median plane, for values of β different from zero, and the longitudinal velocity of the particles cause a focusing force in the vertical direction for positive values of β, as is indicated in the transfer matrix 3.37 for an edge angle.

$$R = \begin{vmatrix} \cos k_x L & \frac{1}{k_x}\sin k_x L & 0 & 0 & 0 & \frac{1}{\rho k_x^2}(1-\cos k_x L) \\ -k_x \sin k_x L & \cos k_x L & 0 & 0 & 0 & \frac{1}{\rho}\sin k_x L \\ 0 & 0 & \cos k_y L & \frac{1}{k_y}\sin k_y L & 0 & 0 \\ 0 & 0 & -k_y \sin k_y L & \cos k_y L & 0 & 0 \\ -\frac{1}{\rho}\sin k_x L & -\frac{1}{\rho k_x^2}(1-\cos k_x L) & 0 & 0 & 1 & -\frac{1}{\rho^2 k_x^3}(k_x L - \sin k_x L) + \frac{L}{\gamma^2} \\ 0 & 0 & 0 & 0 & 0 & 1 \end{vmatrix}$$

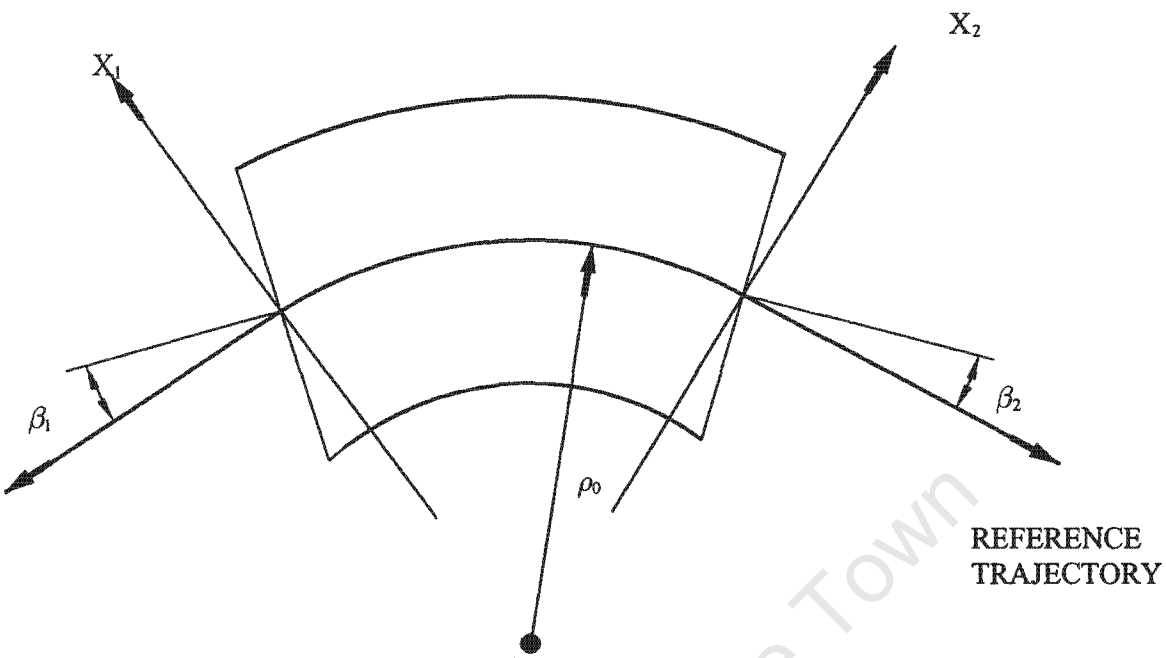

Figure 3.3: Bending magnet with shaped entrance and exit pole edges for beam focusing

$$R = \begin{bmatrix} 1 & 0 & 0 & 0 & 0 & 0 \\ \frac{\tan(\beta-\psi)}{\rho_o} & 1 & 0 & 0 & 0 & 0 \\ 0 & 0 & 1 & 0 & 0 & 0 \\ 0 & 0 & -\frac{\tan(\beta-\psi)}{\rho_o} & 1 & 0 & 0 \\ 0 & 0 & 0 & 0 & 1 & 0 \\ 0 & 0 & 0 & 0 & 0 & 1 \end{bmatrix} \quad (3.37)$$

3.4 THE BEAM ELLIPSE AND EMITTANCE

With the transfer matrices the motion of particles can be individually traced through a beamline. Of more importance, however, is to use these matrices to calculate the behavior of a beam consisting of many particles, without considering the behavior of individual particles. For this purpose the area occupied by the beam in phase space is approximated by an ellipse, which includes all the particles that have to be transported through the beamline. Unwanted particles can be stopped on the jaws of slits. The choice of an ellipse is customary because in circular accelerators such as cyclotrons, particles execute sine-like trajectories around the reference orbit and at any fixed azimuthal position particles execute sinusoidal oscillations in both the vertical and horizontal directions. The derivative of the transverse displacement with respect to longitudinal position, i.e. the divergence, is therefore a cosine function and by combining the displacement and the divergence through elimination of the longitudinal position an ellipse is obtained in phase space.

A symmetric ellipse is defined by the matrix:

$$\sigma = \begin{pmatrix} \sigma_{11} & \sigma_{12} \\ \sigma_{12} & \sigma_{22} \end{pmatrix} \tag{3.38}$$

The equation of the ellipse is given by:

$$\mathrm{X}^T \sigma^{-1} \mathrm{X} = 1 \tag{3.39}$$

where the two-component vector X is given by:

$$\mathrm{X} = \begin{pmatrix} x \\ x' \end{pmatrix} \tag{3.40}$$

The maximum extents of the ellipse, shown in figure 3.4, in the x and x′ directions are given by the square roots of the diagonal elements:

$$\begin{aligned} x_{\max} &= \sqrt{\sigma_{11}} \\ x'_{\max} &= \sqrt{\sigma_{22}} \end{aligned} \tag{3.41}$$

The area of the ellipse is given in terms of the determinant of the ellipse matrix by:

$$A = \pi \left| \sigma \right|^{1/2} = \pi x_{\max} x'_{\text{int}} = \pi x_{\text{int}} x'_{\max} \tag{3.42}$$

The correlation between x and x′, which specifies the orientation of the ellipse, is given by:

$$r_{12} = \frac{\sigma_{12}}{\sqrt{\sigma_{11}\sigma_{22}}} \tag{3.43}$$

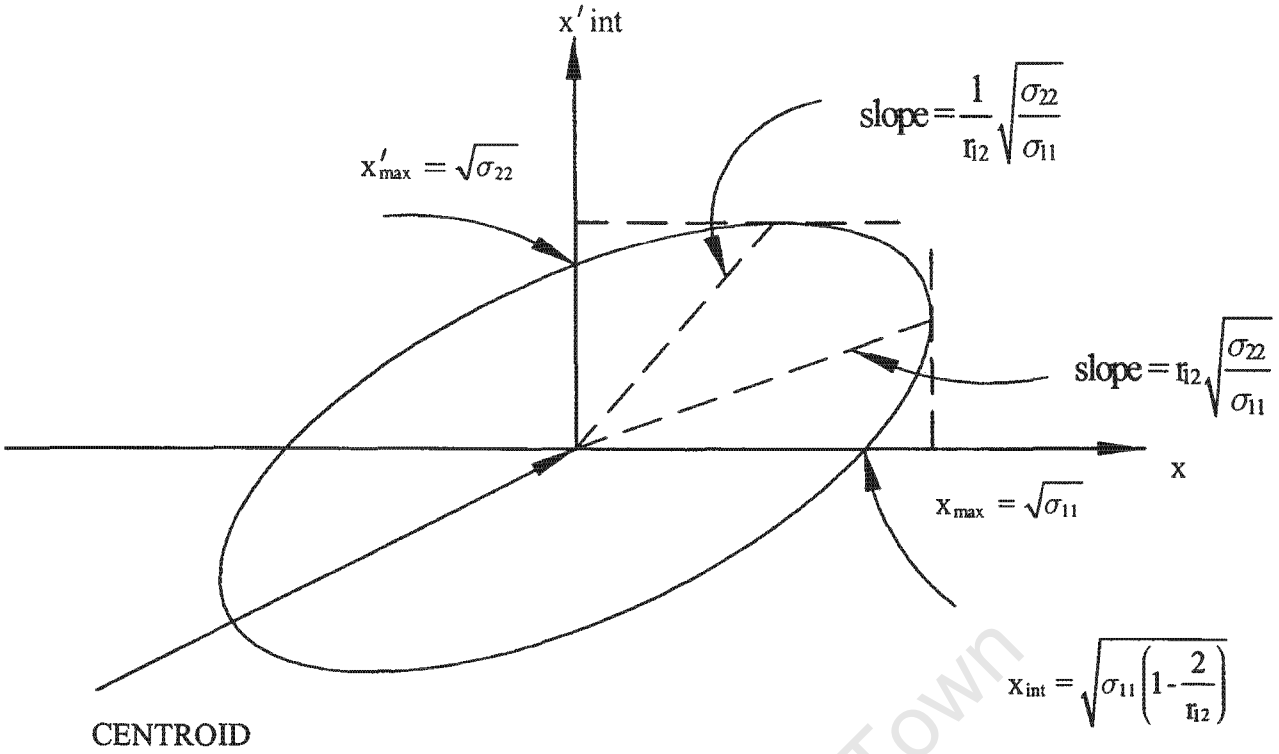

Figure 3.4: A two-dimensional ellipse in phase space showing the parameters which are used to describe the ellipse

The beam ellipse in phase space has now been defined at a specific location. The transformation to another location has now to be determined. For this purpose equation 3.39 is rewritten with the argument 0 to indicate the initial point in the beamline:

$$X^T(0)\sigma(0)^{-1}X(0)=1 \qquad (3.44)$$

At a point downstream the coordinates in phase space of an individual particle are given in terms of the initial coordinates by:

$$X(1)=R\,X(0) \qquad (3.45)$$

By substituting X(0) from equation 3.45 in 3.44 the following is obtained:

$$X^T(1)R^{T-1}\sigma(0)^{-1}R^{-1}X(1)=1 \qquad (3.46)$$

The beam ellipse at the new location is therefore given by:

$$\sigma(1)=R\sigma(0)R^T \qquad (3.47)$$

With the σ-matrix formalism, which can be extended to include the vertical and longitudinal motion, the behavior of a beam of particles in a beamline can be calculated and presented in phase space by using the transfer matrices for the linearized motion of individual particles. The linearized or first order equations described above are used in the computer program TRANSPORT for the basic design of a beamline.

3.5 THE SECOND-ORDER EQUATIONS OF MOTION

To evaluate second and higher order effects in a beamline the trajectories of individual particles can be calculated by solving the complete equations of motion numerically using interpolated field values from calculated or measured magnetic field maps. This is the method used by the computer program TOSCA, which will be discussed below. By selecting a number of particles, representative of the beam as a whole, the data can also be presented in phase space. Another method is to extend the matrix method used above by including second order matrix elements. With second-order terms included the two transverse components of the equation of motion now become [Car87]:

$$\begin{aligned} x'' - h(1+hx) - x'(hx' + h'x) &= \frac{q}{p}T'\left[y'B_t - (1+hx)B_y\right] \\ y'' - y'(hx' + h'x) &= \frac{q}{p}T'\left[(1+hx)B_x - x'B_t\right] \end{aligned} \tag{3.48}$$

To obtain second-order terms in the equations for the field components the Taylor expansion for the potential should include cubic terms:

$$\Phi(x,y,t) = A_{10}y + A_{11}xy + \frac{1}{2}A_{12}x^2y + \frac{1}{6}A_{30}y^3 \tag{3.49}$$

Because of the requirement of mid-plane symmetry terms with even powers in y cannot be included. Terms in x, x^2 and x^3 only would yield an x component for the field in the median plane and have therefore also to be excluded. The coefficients A_{10}, A_{11}, A_{12} and A_{30} are functions of the longitudinal coordinate only. The components of the differential line segment, equation 3.5, can be used to write Laplace's equation in the x, y, t coordinate system [Gre84]:

$$\nabla^2\Phi = \frac{1}{1+hx}\frac{\partial}{\partial x}\left[(1+hx)\frac{\partial\Phi}{\partial x}\right] + \frac{\partial^2\Phi}{\partial y^2} + \frac{1}{1+hx}\frac{\partial}{\partial t}\left[\frac{1}{1+hx}\frac{\partial\Phi}{\partial t}\right] = 0 \tag{3.50}$$

By substituting the expression for the potential into the Laplace equation and equating the coefficient of y to zero the following relationship among the coefficients is obtained:

$$A_{30} = -A_{10}'' - A_{12} - hA_{11} \tag{3.51}$$

Without the third order terms equation 3.49 reduces to equation 3.9 for which A_{10} and A_{11} have already been determined and are given by equation 3.11. Because of the relationship between the potential coefficients in equation 3.51 and the previously determined expressions for A_{10} and A_{11} only one additional coefficient can be specified independently. The coefficient A_{12} is customarily defined in terms of a dimensionless field parameter β, which is unrelated to the previously used symbol β for the pole face rotation angle:

$$A_{12} = 2\beta h^2 A_{10} \tag{3.52}$$

By substitution in equation 3.51 the following expression for A_{30} is obtained:

$$A_{30} = -\left[\frac{h''}{h} - nh^2 + 2\beta h^2\right] A_{10} \tag{3.53}$$

The parameter β can also be written in terms of the second derivative of the vertical field component with respect to x on the midplane:

$$\beta = \left[\frac{1}{2h^2 B_y}\left(\frac{\partial^2 B_y}{\partial x^2}\right)\right]_{\substack{x=0\\y=0}} \tag{3.54}$$

The field components are given by the gradient of the potential function:

$$\begin{aligned} B_x(x,y,t) &= \frac{p_0}{q}\left[-nh^2 y + 2\beta h^3 xy\right] \\ B_y(x,y,t) &= \frac{p_0}{q}\left[h - nh^2 x + \beta h^3 x^2 - \frac{1}{2}(h'' - nh^3 + 2\beta h^3)y^2\right] \\ B_t(x,y,t) &= \frac{p_0}{q}\left[h'y - (n'h^2 + 2nhh' + hh')xy\right] \end{aligned} \tag{3.55}$$

On the midplane the vertical component of the field has the following form:

$$B_y(x,0,t) = B_y(0,0,t)\left[1 - nhx + \beta h^2 x^2\right] \tag{3.56}$$

Substitution of the field components from equations 3.55 in equations 3.48 yield the following equations in which only terms up to the second order have been retained:

$$\begin{aligned} &x'' + (1-n)h^2 x = h\delta + (2n-1-\beta)h^3 x^2 + h'xx' + \frac{1}{2}hx'^2 \\ &+(2-n)h^2 x\delta + \frac{1}{2}(h'' - nh^3 + 2\beta h^3)y^2 + h'yy' - \frac{1}{2}hy'^2 - h\delta^2 \\ &y'' + nh^2 y = 2(\beta - n)h^3 xy + h'xy' - h'x'y + hx'y' + nh^2 y\delta \end{aligned} \tag{3.57}$$

These equations can be solved by first solving the linearized equations 3.14 and substituting the functions $s_x(t)$, $c_x(t)$ and $d_x(t)$ thus obtained in equations 3.57. Particular integrals for the equations 3.57 can be obtained by using the Green's function method mentioned before. The influence of the second order terms can be presented in a triangular second order matrix, T, which together with the first order matrix, R, can be used to calculate the beam characteristics along a beamline [Bro82]:

$$x_i(1) = \sum_j R_{ij} x_j(0) + \sum_{j,k} T_{ijk} x_j(0) x_k(0)$$

The second order matrix for beam transport between two points indicated by 0 and 2 in a beamline can be calculated from the transfer matrices between point 0 and an intermediate point

1 and the matrices for beam transfer between positions 1 and 2 according to the following rule [Car87]:

$$T_{ijk}(0 \to 2) = \sum_{\ell} R_{i\ell}(1 \to 2) T_{\ell jk}(0 \to 1) + \sum_{\ell m} T_{i\ell m}(1 \to 2) R_{\ell j}(0 \to 1) R_{mk}(0 \to 1)$$

The computer program TURTLE and TRANSPORT have been developed to study these second order effects.

3.6 INCLUSION OF ELECTROSTATIC LENSES IN THE COMPUTER PROGRAM TRANSPORT

The equations of motion in cylindrical coordinates (z, r, θ) for the calculation of the trajectories of meridional charged particles in acceleration tubes with axial symmetry have been described by Rose and Galejs [Ros64, Ros67]. The momentum components p_z and p_r are:

$$p_z = m_o \gamma \dot{z} \quad p_r = m_o \gamma \dot{r} \tag{3.58}$$

where:

$$\gamma = \sqrt{(1 - v^2 / c^2)} \tag{3.59}$$

Under the square root c is the velocity of light and:

$$v^2 = \dot{z}^2 + \dot{r}^2$$

The equations of motion with, m_0 the rest mass, q the charge of the particle, V is the electrostatic potential and t the time, are now:

$$\begin{aligned} m_o \frac{d}{dt}\left(\gamma \frac{dz}{dt}\right) &= -q \frac{\partial V}{\partial z} \\ m_o \frac{d}{dt}\left(\gamma \frac{dr}{dt}\right) &= q \frac{\partial V}{\partial r} \end{aligned} \tag{3.60}$$

The differential equation for the trajectory is obtained by eliminating the time from equations 3.60:

$$r'' = \frac{1}{\dot{z}} \frac{d}{dt} \frac{\gamma \dot{r}}{\gamma \dot{z}} = \frac{-q\gamma}{moc^2} \frac{1 + r'^2}{(\gamma^2 - 1)} \left[\frac{\partial V}{\partial r} - r' \frac{\partial V}{\partial z} \right] \tag{3.61}$$

with:

$$r' = dr / dz = \dot{r} / \dot{z} \tag{3.62}$$

By writing: $$Q = m_0^2 c^2 \left[-\frac{2qV}{m_0 c^2} + \left(\frac{qV}{m_0 c^2} \right)^2 \right] \tag{3.63}$$

And: $$\gamma = 1 - qV/m_0c^2, \tag{3.64}$$

the relativistic electrostatic ray equation is obtained :

$$r'' = \frac{1+r'^2}{2Q}\left[\frac{\partial Q}{\partial r} - r'\frac{\partial Q}{\partial z}\right] \tag{3.65}$$

For paraxial non-relativistic particles equation 3.61 reduces for electrostatic fields with cylindrical symmetry to:

$$r'' + \frac{V_0'}{2V_0}r' + \frac{V_0''}{4V_0} = 0 \tag{3.66}$$

where V_0 is the axial potential. Equations 3.65 and 3.66 can be written as two first order differential equations, which can be solved by a numerical method such as the Runge-Kutta method. Numerical integration, although capable of yielding accurate results, is not very suitable for presenting beam characteristics in phase space, unless the trajectories of a large number of representative particles are calculated.

A recent version [Roh01] of the computer program TRANSPORT includes the facility to calculate the transport of beams through electrostatic lenses in phase space. Instead of solving the equations derived above with measured and / or calculated field values transfer matrices are calculated by using an approximate method [Gal67]. The axial potential is replaced by a number of sections with homogeneous but different field strengths through which equation 3.66 is integrated. For each section and its accompanying breakpoints, as is shown in figure (3.5), the following total transfer matrix can be written for the radius r and the radial momentum p_r = mvr [Stu55, Ga67]:

$$\begin{bmatrix} r_1 \\ p_{r1} \end{bmatrix} = \begin{bmatrix} \frac{3p_i - p_f}{2p_i} & \frac{2d}{p_i + p_f} \\ -\frac{3}{4d}\frac{p_f - p_i}{p_i p_f}(V_f - V_i) & \frac{3p_f - p_i}{2p_f} \end{bmatrix} \begin{bmatrix} r_0 \\ p_{r0} \end{bmatrix} \tag{3.67}$$

where p_i and p_f are the initial and final longitudinal momentum values. The remaining symbols are defined in figure 3.5. The matrix for the section and breakpoints is obtained by multiplication of the matrices for a breakpoint:

$$\left[M_{\text{breakpoint}}\right] = \begin{bmatrix} 1 & 0 \\ -\frac{E_f - E_i}{2p} & 1 \end{bmatrix} \tag{3.68}$$

with the matrix for the uniform field section:

$$\left[M_{uniform\ field}\right]=\begin{bmatrix}1 & \dfrac{2d}{p_i+pf}\\ 0 & 1\end{bmatrix} \tag{3.69}$$

and then again with the matrix for a breakpoint. By successive multiplication of the transfer matrices M_{total} the matrix for all the sections together can be obtained.

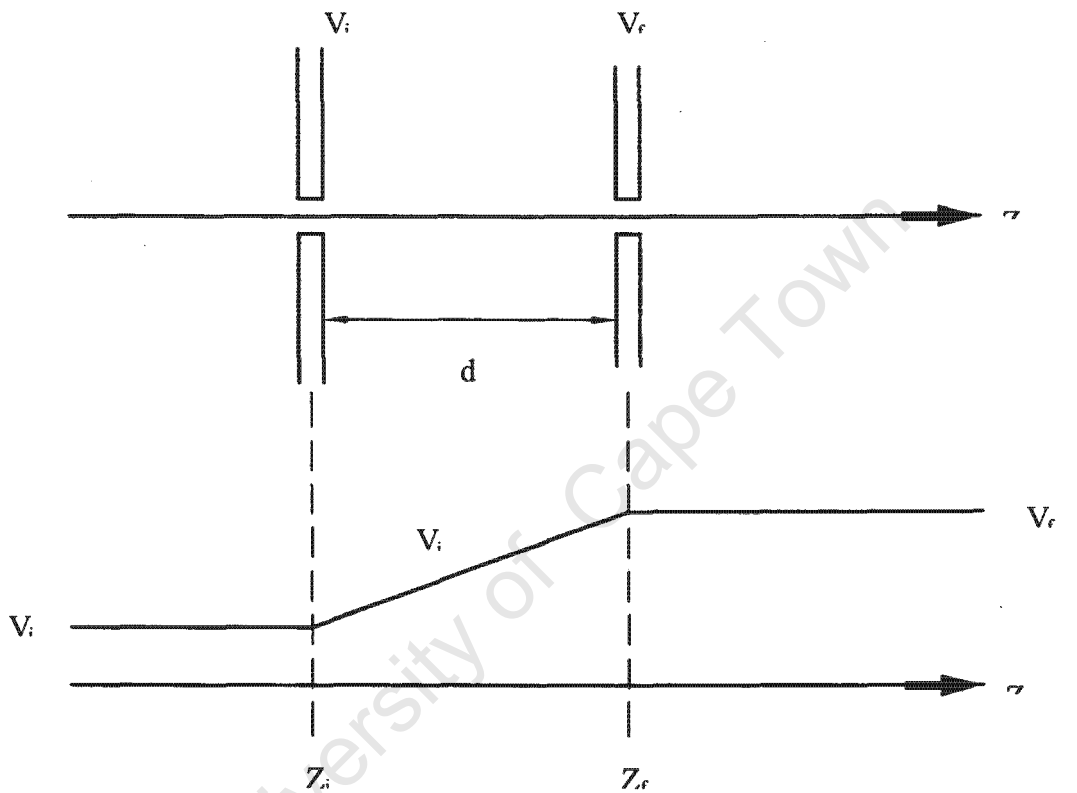

Figure 3.5: Section of homogeneous field with break points at the beginning and end of the section.

CHAPTER 4

CHARACTERIZATION AND OPTIMIZATION OF THE OPERATING CONDITIONS OF THE VAN DE GRAAFF ION SOURCES

4.1 INTRODUCTION

At the *i*Themba LABS NMP facility two duoplasmatron ion sources, with hot and cold cathodes respectively, as well as a cold-cathode Penning Ionization Gauge (PIG) source are available for the Van de Graaff accelerator. The quality and intensity of the beams delivered by the accelerator are to a large extent determined by those of the ion sources. It is therefore important to improve the beam quality and intensity of the sources and to know their characteristics as well as the factors that limit their performance. The calculation of particle trajectories through the Van de Graaff accelerator and its beamlines parameters such as the energy spread and the horizontal and vertical emittances of the beams extracted from these sources should be known. The optimum operating conditions, such as the filament current, cathode and anode voltages and gas flow under which stable beams can be delivered reliably to the users, with a reasonably long source lifetime, should be determined, since no experimental data are available. The source lifetime is of great importance because maintenance work on the source implies removal of the Van de Graaff tank and ventilation of the accelerating tube, which has afterwards to be evacuated again – a process which normally takes three days during which beam will not be available. The aim of this study is therefore to characterize and optimize the ion sources on an ion source test bench, equipped with the necessary diagnostic apparatus for this purpose. With the characteristics and limitations of the sources known it may become clear which further development work would be advantageous.

4.2 THE ION SOURCE TEST BENCH

Since it is not possible to calculate the performance of ion sources with accuracy from the dimensions of the electrodes, the gas flow and the applied voltages and currents, it is standard practice to determine the source characteristics on a test bench [Mal76]. Figure 4.1 shows a layout of the ion source test bench at *i*Themba LABS [Mok02]. The ion source under test and

all its power supplies are at a positive potential, the extraction voltage, with respect to the beam pipe of the test bench. The diagnostic equipment consists of two Faraday cups for the measurement of the beam intensity and adjustable horizontal and vertical slits for selection of portions of the beam, after it has passed through the pole gap of a bending magnet [Mai02] and a drift space. The vertical slit has two independently adjustable jaws to select ions with a specific charge-to-mass ratio within a limited momentum range. For a 1 mm object slit width, i.e. the aperture in the extraction electrode directly in front of the ion source, the charge state, the mass and momentum resolving power at the vertical slit jaws is 0.9%. For the same slit size the energy resolving power is 1.8%. Downstream from the vertical slit two horizontal slits with fixed apertures of 1 mm, but with adjustable positions, are installed at a distance of 90 mm apart for emittance measurement.

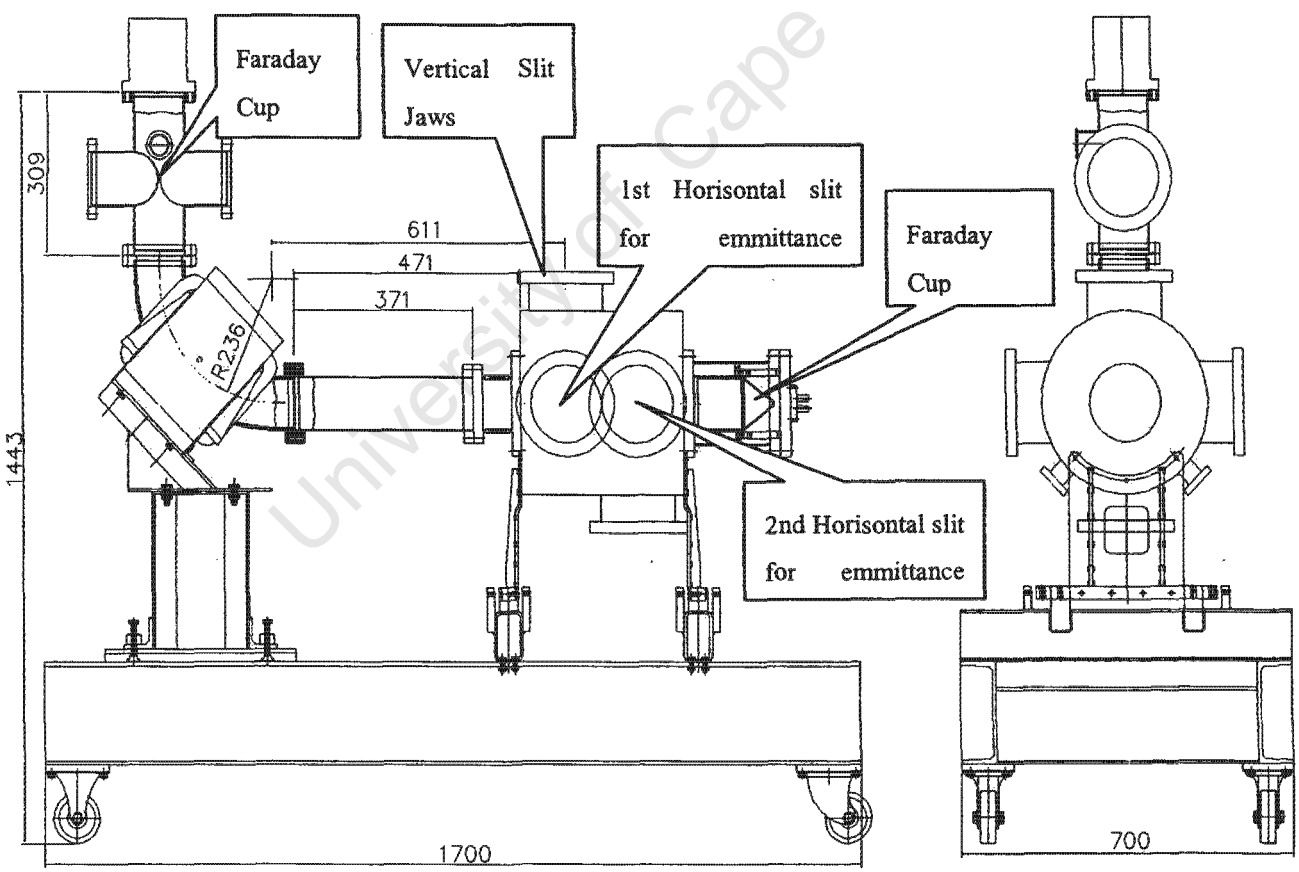

Figure 4.1: Layout of the ion source test bench at iThemba LABS showing side (left) and front (right) views. The dimensions in the figure are in millimeters.

Figure 4.2 shows the main components of the test bench with an ion source and some electrostatic lenses between the source and the beam pipe. Since the ion source is at a potential of a few kilovolt with respect to the beam pipe, which is at ground potential, the ion source power supplies and measuring equipment are all connected through a high-voltage isolation transformer to the mains supply

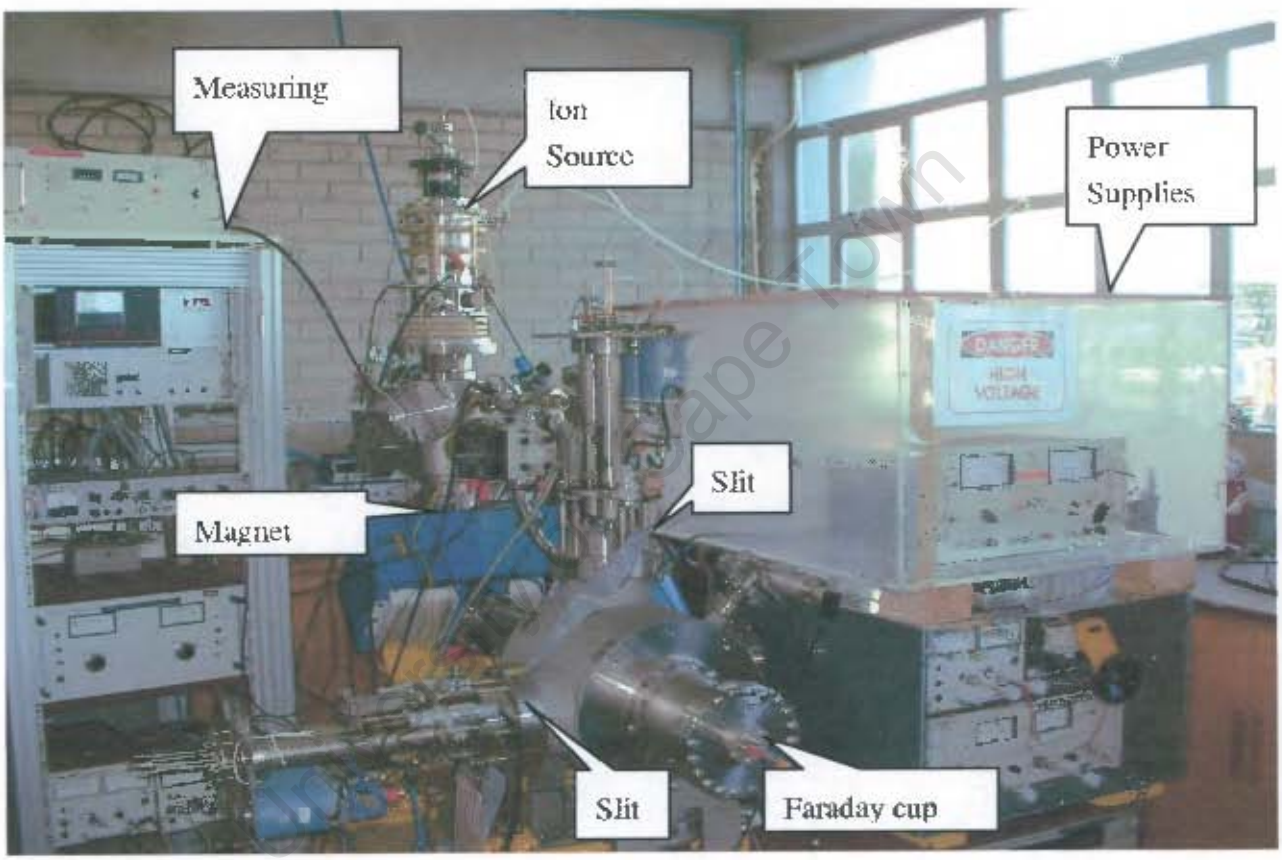

Figure 4.2: The ion source test bench at iThemba LABS.

With the 90° bending magnet the beam from the ion source is focused in both the horizontal and vertical directions to a width of a few mm at a point halfway between the two horizontal slits. To obtain this double-focusing characteristic the magnet has been manufactured with edge angles of 34.7 degrees.

4.3 THE HOT-CATHODE DUOPLASMATRON ION SOURCE

4.3.1 THE CONSTRUCTION OF THE SOURCE AND ITS OPERATING PRINCIPLES

The layout of a hot-cathode duoplasmatron ion source is shown in figure 4.3. A filament, which acts as a cathode, is heated by sending an ac current of typically 100 A through it. Electrons emitted from the hot cathode are accelerated in the electric field, created by the cathode power supply of about 100 V, and gain energy as they move towards the intermediate electrode. Once they have sufficient energy the electrons start to ionize the gas that enters the ion source on the cathode side. The positive ions move towards the cathode under the influence of the electric field. Electrons pass through the narrow channel in the intermediate electrode and enter the region between this electrode and the anode. In this region a strong magnetic field is created by the coil and magnet steel core configuration shown in figure 4.3. Between the intermediate electrode and the anode the motion of both electrons and ions are to a large extent confined to the axial direction by the applied axial magnetic field. In the space between the cathode and the intermediate electrode the magnetic field is practically zero. The gas flows through the narrow channel in the intermediate electrode and through the 0.5 mm diameter orifice in the anode. By directing the gas and the fast moving electrons together through the channel in the intermediate electrode a high degree of ionization, typically more than 90%, is obtained [Val77]. The ionization processes in the plasma are the following [Hed91]:

$$H_2 + e \Rightarrow H_2^+ + 2e$$
$$H_2^+ + e \Rightarrow H^+ + H + e$$
$$H + e \Rightarrow H^+ + 2e$$
$$H_2^+ + H_2 \Rightarrow H_3^+ + H$$
$$H_3^+ + e \Rightarrow H^+ + H_2 + e$$

The duoplasmatron ion source was invented by von Ardenne in 1956 [Ard56] and has since then become a popular ion source for accelerators and especially for Van de Graaff accelerators because of its low gas consumption. To prevent sparking due to the high voltage in the accelerator tube of a Van de Graaff, a good vacuum is required, and because of the high pressure of 1.8 MPa as well as the limited space and power available in the terminal, the vacuum pumps are connected at ground potential, six meters away from the ion source. A low gas load from the ion source is therefore advantageous.

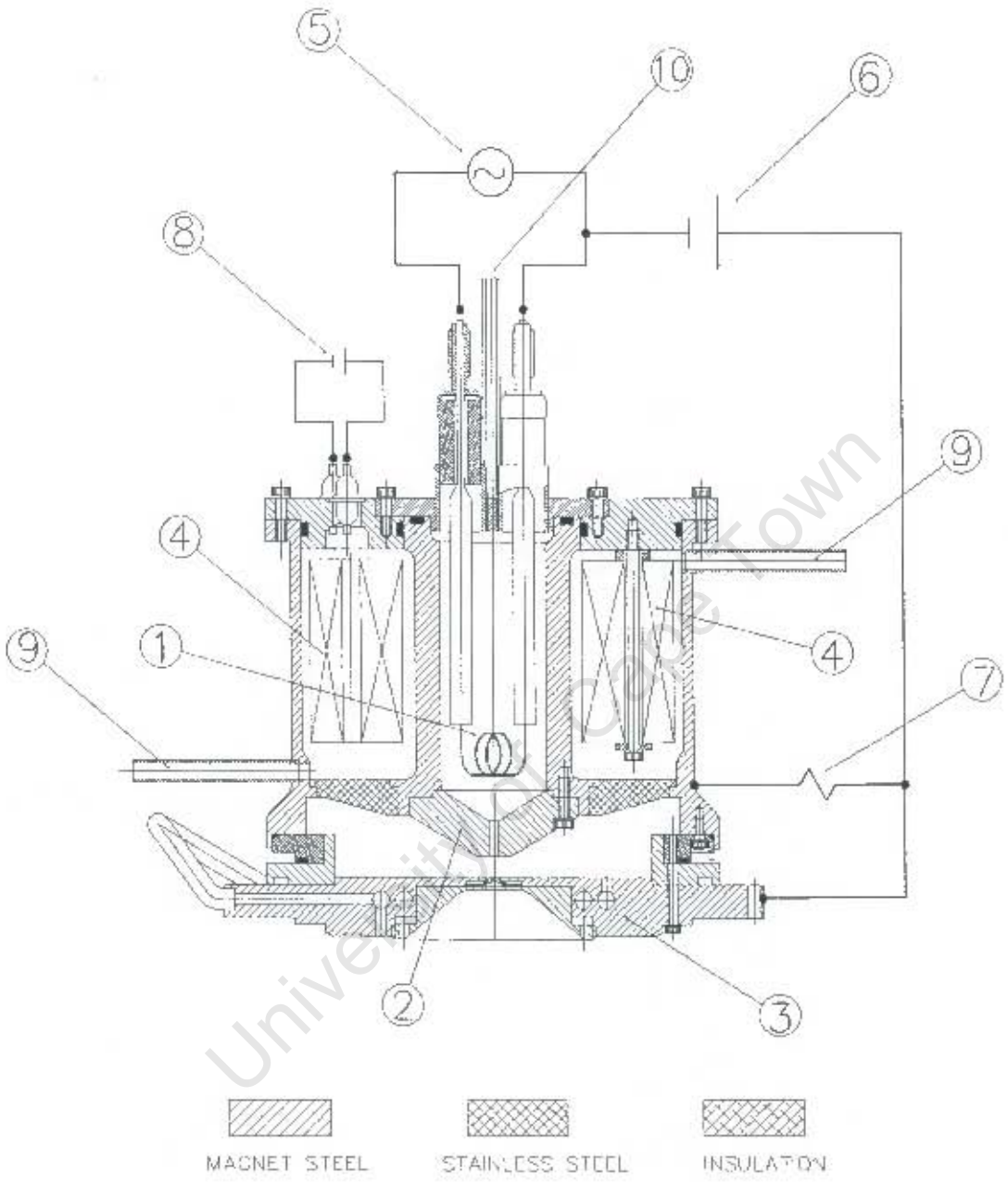

Figure 4.3: Cross-section of the hot-cathode duoplasmatron ion source showing: (1) the cathode, (2) the intermediate electrode, (3) the anode, (4) the magnet windings, (5) the filament power supply, (6) the cathode power supply, (7) the 2.4 kΩ intermediate-electrode resistor, (8) the magnet power supply, (9) the coolant connections for the magnet windings and (10) the gas inlet. The source has a diameter of 130 mm and a length of 120 mm.

Because of its compact construction the inner parts of a duoplasmatron are not accessible for diagnostic purposes development work is done by trial and error. To gain a better understanding of a duoplasmatron source Lejeune [Lej74a, Lej74b] constructed a special large-scale source to measure the characteristics of the discharge inside the source. Figure 4.4 shows typical [Ang94] electric potential and magnetic field distributions inside a duoplasmatron ion source.

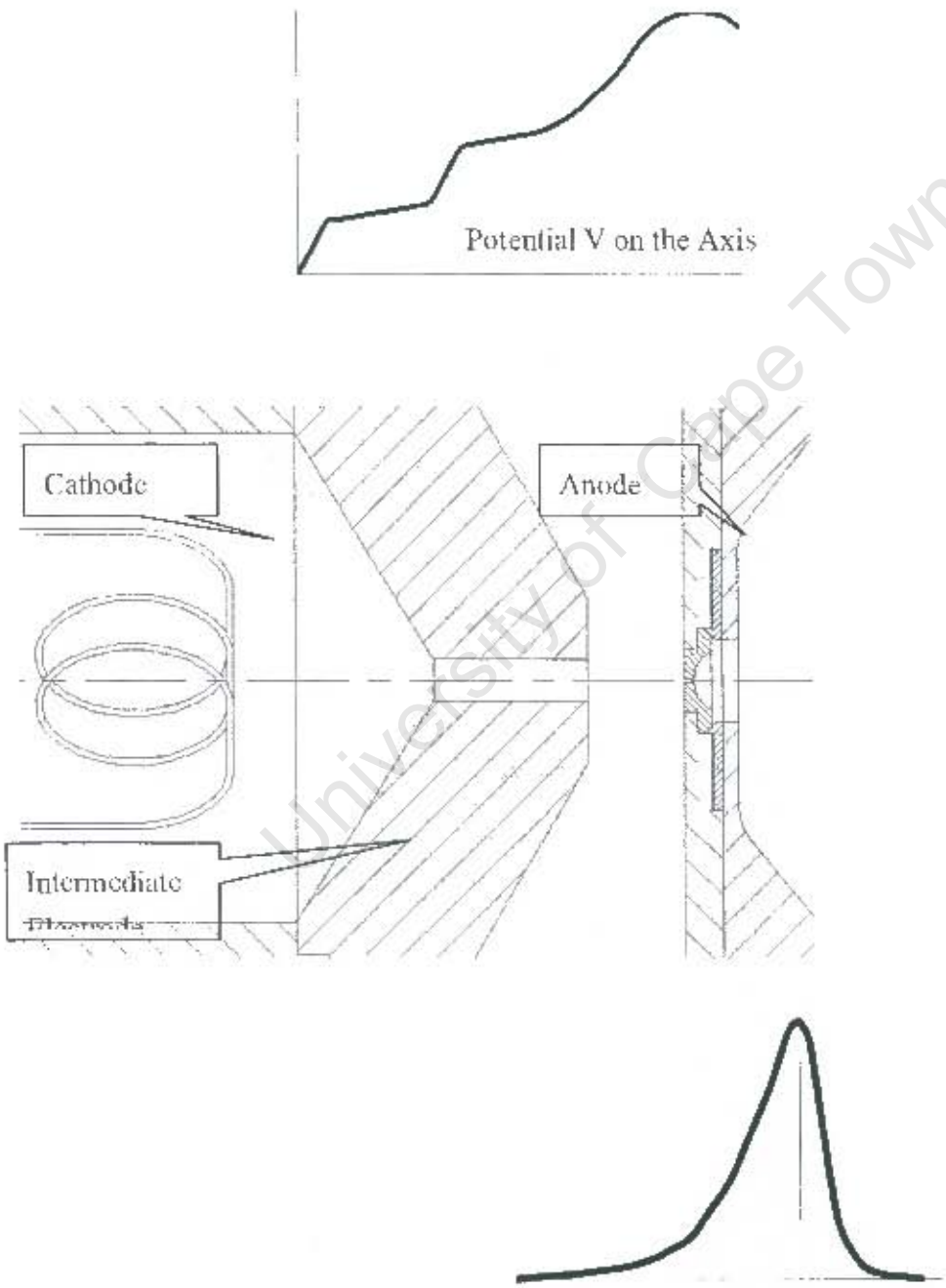

Figure 4.4: Typical electrostatic potential, V, and magnetic field, B, distributions along the axis of a hot-cathode duoplasmatron ion source.

The regions in which the potential increases linearly correspond to neutral plasma, since the second derivative of the potential with respect to the axial co-ordinate is zero, which implies according to Poisson's equation, that the charge density due to electrons and positive ions have the same absolute values in these regions. The regions of sharp increases in potential along the axis are explained [Ang56] in terms of the existence of an excessive concentration of positive ions near the cathode and in terms of a double layer of positive ions and electrons near the intermediate electrode. That the existence of such layers of charge can be responsible for the observed potential distributions can be seen by solving Poisson's equation for two parallel plates with thin layers of charge interspaced between the plates or just by applying Gauss' law to such a configuration. The charge layers in figure 4.4 correspond to regions where the potential graph deviates from a straight line, i.e. where the second derivative of the potential is different from zero. Electrons leave the cathode with very low velocities, which means that the ion current close to the cathode is much greater than the electron current, although the charge density in this region is negative. This negative layer together with a positive layer, still close to cathode but slightly away from it, forms the cathode double layer [Ill72]. The next region of slow-rising voltage consists of almost neutral plasma and is followed by layers of negative and positive charge, respectively [Kis65].

In the region between the intermediate electrode and the anode the magnetic field increases sharply which means that the field lines converge strongly. In such a field there is, due to the magnetic field, a resultant horizontal force component, directed away from the anode and back to the intermediate electrode, on a charged particle with a transverse speed component. The mirror [Che74] formed by the magnetic field therefore reflects electrons leaving the channel in the intermediate electrode with a sufficiently large transverse speed component. In the magnetic field B the magnetic moment $mv_p^2/(2B)$ of a charged particle with mass m and perpendicular speed component v_p is an adiabatic invariant [Che74, Sim72]. The helical paths of electrons in the magnetic field increase their ionization efficiency. The increased concentration of positive ions due to the reflection of electrons from the anode explains the drop in voltage in front of the anode [Lej74a]. The drop in potential towards the anode corresponds to an electric field directed towards the anode, which is favorable for acceleration of positive ions to the orifice in the anode. The positive ion beam is extracted at a point where the plasma density is high and from which the plasma expands in the decreasing magnetic field, by application of a negative potential of a few kilovolt to the extraction electrode in front of the anode.

4.3.2.1 EXPERIMENTAL RESULTS

4.3.2.1 OPTIMIZATION OF THE BEAM CURRENT BY VARYING THE GAS FLOW TO THE ION SOURCE

The gas flow to the ion source was varied to determine the optimum condition in terms of intensity for protons. The gas consumption of the duoplasmatron ion source is, however, so low that that the gas flow could not be measured with the available equipment. Because of the limitations of size the pressure could also not be measured in the ion source on the test bench. The pressure in the beam pipe of the test bench was therefore measured and used as a measure of the gas flow to the source. Figure 4.5 shows the measured beam current for different hydrogen ion species at an arc current of 1 A, a filament current of 25 A and an extraction voltage of 5 kV. As the gas flow is increased the arc voltage decreases form 97V to 81V in order to maintain a constant arc current of 1 A since the arc power supply is current stabilized. Below a pressure of 6×10^{-6} mbar the ion source becomes unstable. In this pressure range the arc current can no longer be maintained and the arc extinguishes. The maximum current for protons is obtained at a pressure slightly above the gas flow at which instability sets in. This fact can be used to adjust the gas flow when the source is used in the Van de Graaff accelerator.

Although the currents for the individual ion species vary strongly, the total current does not change by more than 11% over the pressure range in which the measurements were carried out. The increase in H_3^+-ion current and the drop in the H^+- and H_2^+-ion currents with pressure are probably due to recombination of H^+- and H_2^+-ions with unionized Hydrogen molecules in the ion source according to the following reactions:

$$H^+ + H_2 \Rightarrow H_3^+$$

$$H_2^+ + H_2 \Rightarrow H_3^+ + H$$

For the optimum proton beam current the source should be operated at a gas flow slightly higher than at which it becomes unstable.

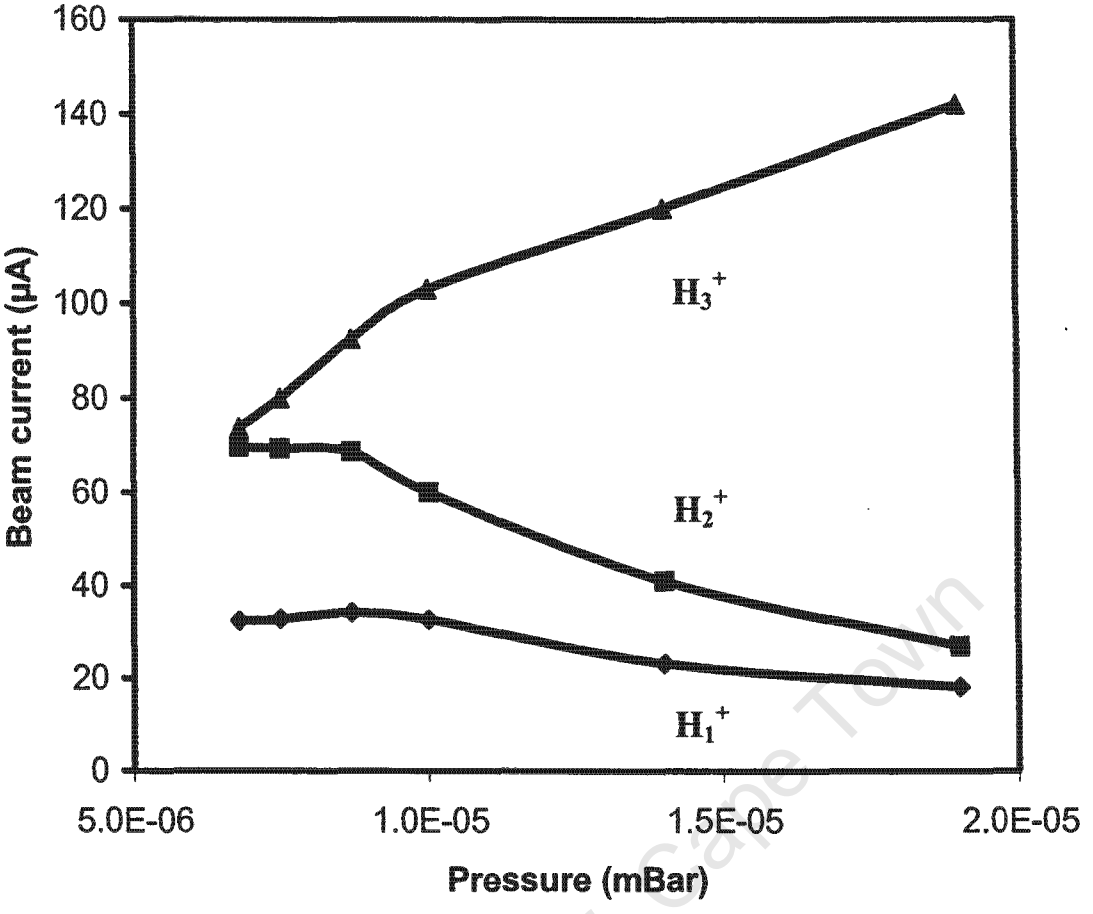

Figure 4.5: Measured beam current for different Hydrogen ion species as a function of the pressure in the beam line of the ion source test bench, for the hot-cathode duoplasmatron ion source, operated under the following conditions: arc current = 1 A, filament current = 25 A, extraction voltage = 5 kV. The arc voltage decreased from 97 V to 81 V as the gas flow to the source was increased.

4.3.2.2 OPTIMIZATION OF THE BEAM CURRENT BY VARYING THE EXTRACTION VOLTAGE

The solid lines in figure 4.6 show the measured beam current for different Hydrogen ion species as a function of the extraction voltage. The remaining ion source parameters were kept at the following constant values: arc current = 1 A, arc voltage = 83 V, filament current = 25 A, pressure = 10^{-5} mbar. According to the Child-Langmuir law [Ian89] the extracted ion beam current I should be proportional to the extraction voltage V to the power 3/2. The dotted lines in the figure are least-square fits of the equation I = constant × $V^{3/2}$ to the measured data for the different ion species and show that the source behavior is to a large extent in agreement with the

Child-Langmuir law which means that the beam current extracted from the source is limited by the space charge in the region between the anode and extraction electrode. It also indicates that the beam losses in the beamline due to space-charge effects are small and only of importance for operation at low extraction voltages, as shown in figure 4.6. For high beam intensity the source should be operated at as high as possible an extraction voltage without jeopardizing reliability of beam delivery due to sparking.

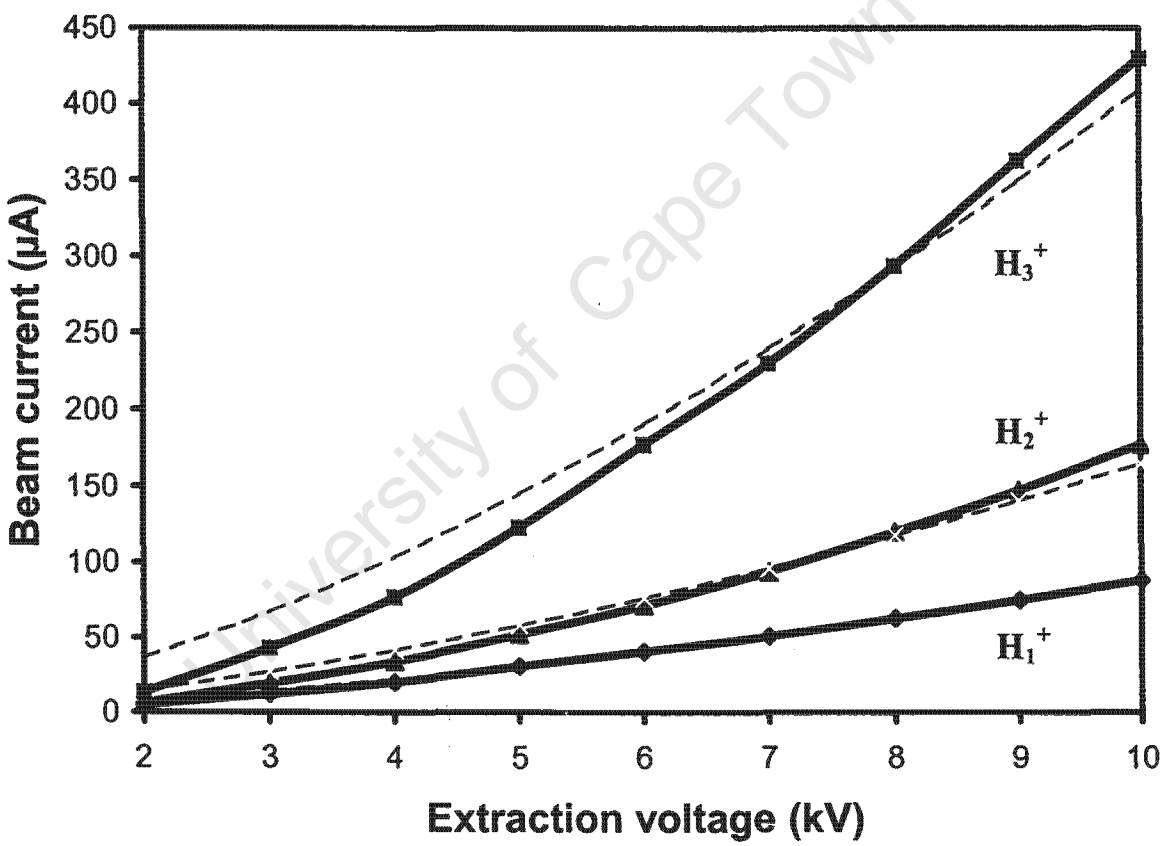

Figure 4.6: Measured beam current (solid lines) for different Hydrogen ion species as a function of the extraction voltage, for the hot-cathode duoplasmatron ion source and least-square fits (dotted lines) of the Child-Langmuir law. The measurements were made under the following conditions: arc current = 1 A, arc voltage = 83 V, filament current = 25 A, pressure = 10^{-5} mBar.

4.3.2.3 OPTIMIZATION OF THE BEAM CURRENT BY VARYING THE ARC CURRENT OF THE ION SOURCE

Figure 4.7 shows the measured beam current for different Hydrogen ion species as a function of the arc current. The proton and H_2^+-ion current increase with increasing arc current while the H_3^+-ion current decreases with increasing arc current, arc voltage and source temperature. At the higher ion and electron energy as well as higher discharge temperature fewer recombinations take place. For high proton beam intensity the source should be operated at a high arc current and arc voltage to minimize recombination of proton with electrons and hydrogen gas molecules.

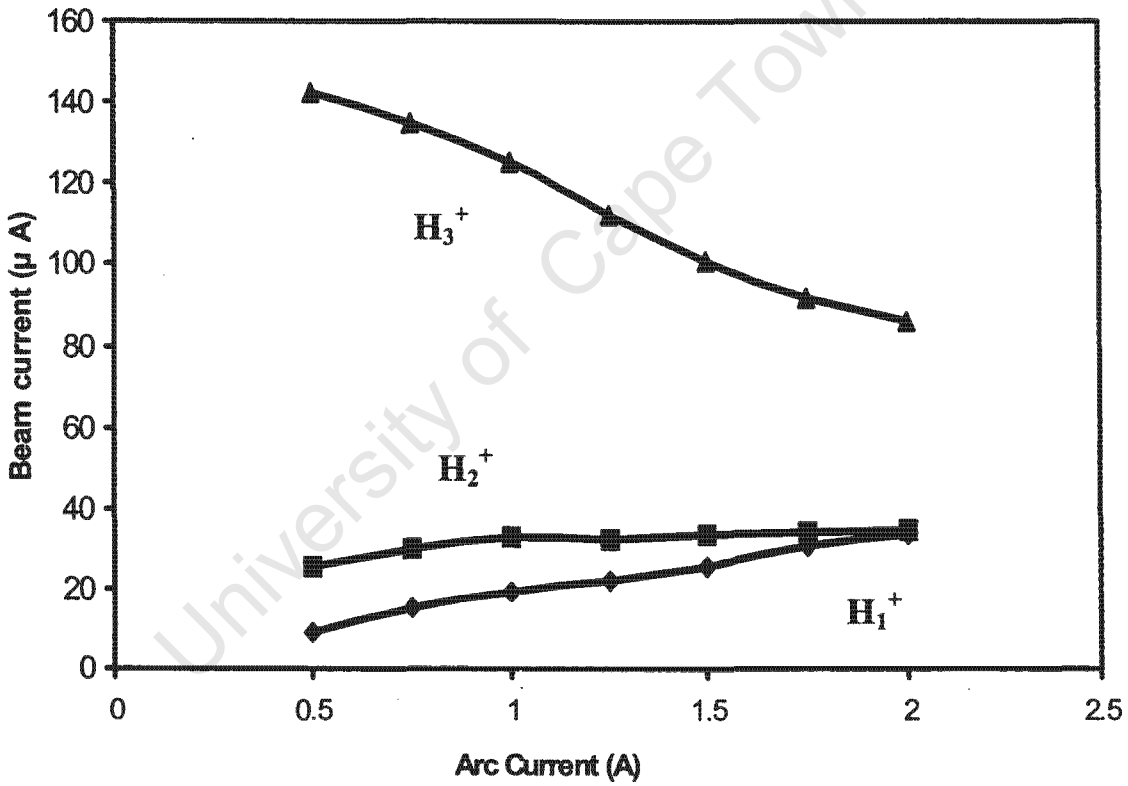

Figure 4.7: Measured beam current for different Hydrogen ion species as a function of the arc current, for the hot-cathode duoplasmatron ion source, operated under the following conditions: pressure in the beamline of the ion source test bench $=10^{-5}$ mBar, filament current = 25 A, extraction voltage = 5 kV

4.4 EMITTANCE MEASUREMENTS

An ion beam can be represented by a group of points in six-dimensional phase space. According to Liouville's theorem the motion of a group of particles under the action of

conservative force fields is such that the local density in the six-dimensional phase-space x, p_x, y, p_y, z, p_z remains everywhere constant. If the transverse components of motion of a group of particles are mutually independent and space-charge effects are neglected the motion of the particles in the orthogonal planes (x, p_x), (y, p_y) and (z, p_z) can be treated separately. The areas in the x, p_x and y, p_y planes are conserved independently and are called the horizontal and vertical emittances ε_x and ε_y, respectively. For the case where p_z is constant and both p_x and p_y are small in comparison with p_z, the transverse momenta p_x, p_y are replaced respectively by the horizontal and vertical angular divergences x′ and y′:

$$\frac{p_y}{p_z} = \frac{dy}{dz} = y' \tag{4.1}$$

$$\frac{p_x}{p_z} = \frac{dx}{dz} = x' \tag{4.2}$$

To account for changes in the axial momentum p_z of an ion beam, the concept of normalized emittance is used and is at beam energies low with respect to the rest energy of the particles defined as:

$$\varepsilon_{nx} = \pi x x' \sqrt{E} \tag{4.3}$$

$$\varepsilon_{ny} = \pi y y' \sqrt{E} \tag{4.4}$$

where E is the energy of the ion beam in MeV. The units of emittance are given in terms of π mm mrad $(MeV)^{1/2}$ [Alt87]

4.4.1 EXPERIMENTAL RESULTS OF EMITTANCE MEASUREMENTS

The emittance of the ion source was measured with two slits, 90 mm apart, and a Faraday cup in the ion source test bench at an arc voltage of 83 V, an arc current of 1 Amp, a filament voltage of 24 V and an extraction voltage of 5 kV. The beam intensity as a function of the positions of the two slits is shown in Figure 4.8. The phase ellipse of the beam is shown in figure 4.9. The measured emittance for 90 % of the beam intensity is 48 π mm mrad. This figure will be used to calculate the beam transmission through the Van de Graaf accelerator. The intensity profile of the beam at the second slit (Fig 4.1) is shown in figure 4.10.

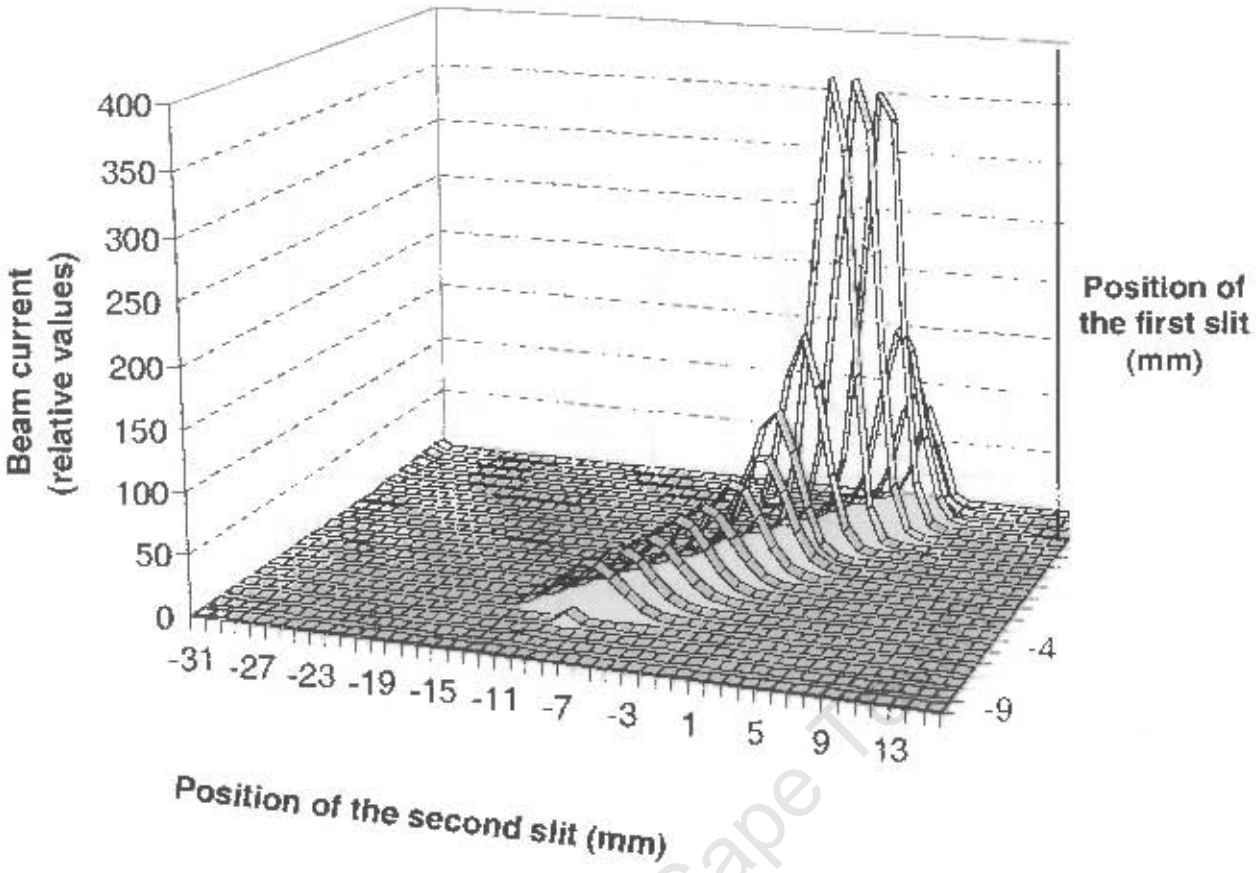

Figure 4.8:The beam intensity distribution for the hot-cathode duoplasmatron ion source at different positions of the two slits in the ion source test bench with which the emittance

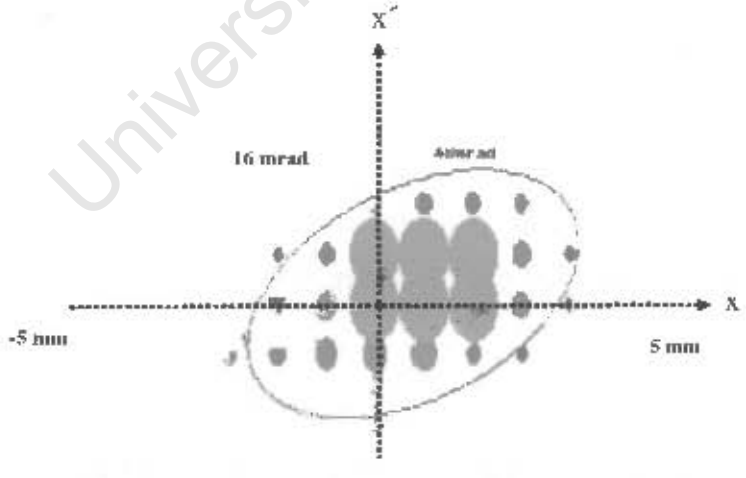

Figure 4.9:The phase ellipse of the beam from the hot-cathode duoplasmatron ion source with 90 % of the beam included in the ellipse. The emittance was 48π mm mrad The area covered by the smaller dots outside the ellipse represents the remaining part of the beam.

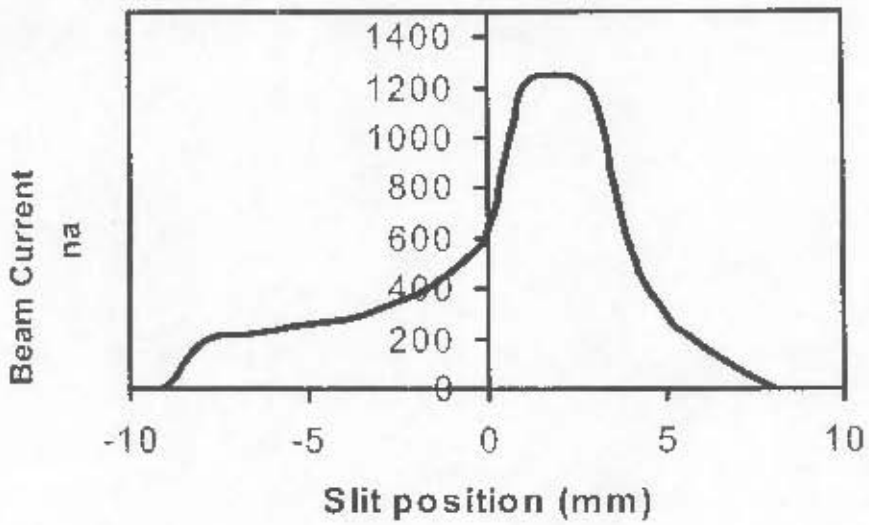

Figure 4.10: The horizontal intensity profile of the proton beam from the hot-cathode duoplasmatron ion source at the first slit of the ion source test bench.

The relatively sharp cut-off of the beam profile on the left in figure 4.10 is due to the fact the beam at this point extends beyond the entrance opening of the Faraday cup. The asymmetry in the beam profile as a whole can only be explained by a deviation from the desired circular shape of the 0.2 mm diameter aperture in the electrode through which the beam is extracted from the ion source. This electrode operates at a high temperature due to ion bombardment and the aperture sometimes becomes partly or completely blocked due to melting.

In general the source has a life-time of four to six weeks during which the coating of Barium- , Strontium- and Calcium carbonate on the filament, that is used to increase the electron emissivity, slowly erodes away due to sputtering by positive ions, with the result that a discharge can no longer be ignited.

4.5 THE COLD-CATHODE DUOPLASMATRON ION SOURCE

A cross-section of the cold-cathode duoplasmatron ion source, constructed with permanent magnets, [Mok02] is shown in figure 4.11 with an extraction electrode and extraction power supply. The source length and diameter are 100 mm and 80 mm, respectively. The design is based on that of an existing ion source [Qay94] and has the advantage for a Van de Graaff accelerator that it operates without a filament, which would have to be replaced regularly. It

further does not require a power supply in the Van de Graaff terminal, where the space and the power available are limited, for the excitation of the magnetic field, since permanent ring magnets are used for this purpose. Contrary to the previous duoplasmatron ion source, the discharge in the region of the hollow cathode is also magnetically confined.

The source has been tested and the beam current measured at an extraction voltage of 11 kV [Mok92]. The total beam current as a function of the arc current at an extraction voltage of 11 kV is shown in figure 4.12. At the Van de Graaff the maximum extraction voltage is, however, limited to 8 kV to prevent excessive sparking. At this voltage a beam current of only 6 μA is obtained for protons. The source can be operated stably up to arc currents of 50 to 60 mA. Above that the source becomes unstable due to excessive heating of the electrodes. This source is therefore on account of its low beam current of little use for the Van de Graaff accelerator.

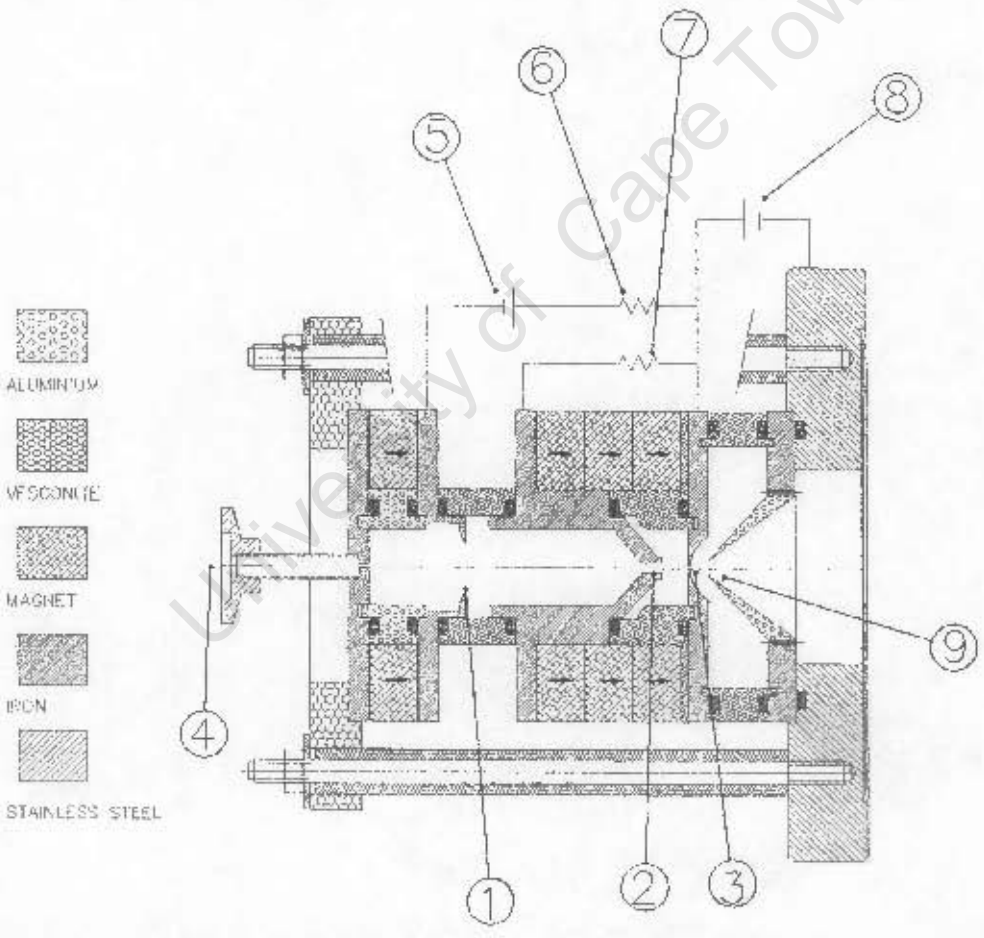

Figure 4.11: Cross-section of the cold-cathode duoplasmatron ion source with permanent magnets for the Van de Graaff accelerator showing: (1) the cathode, (2) the intermediate electrode, (3) the anode, (4) the gas inlet (5) the anode power supply (6) the cathode resistor (7) the anode resistor (8) the extraction power supply and (9) the extraction electrode

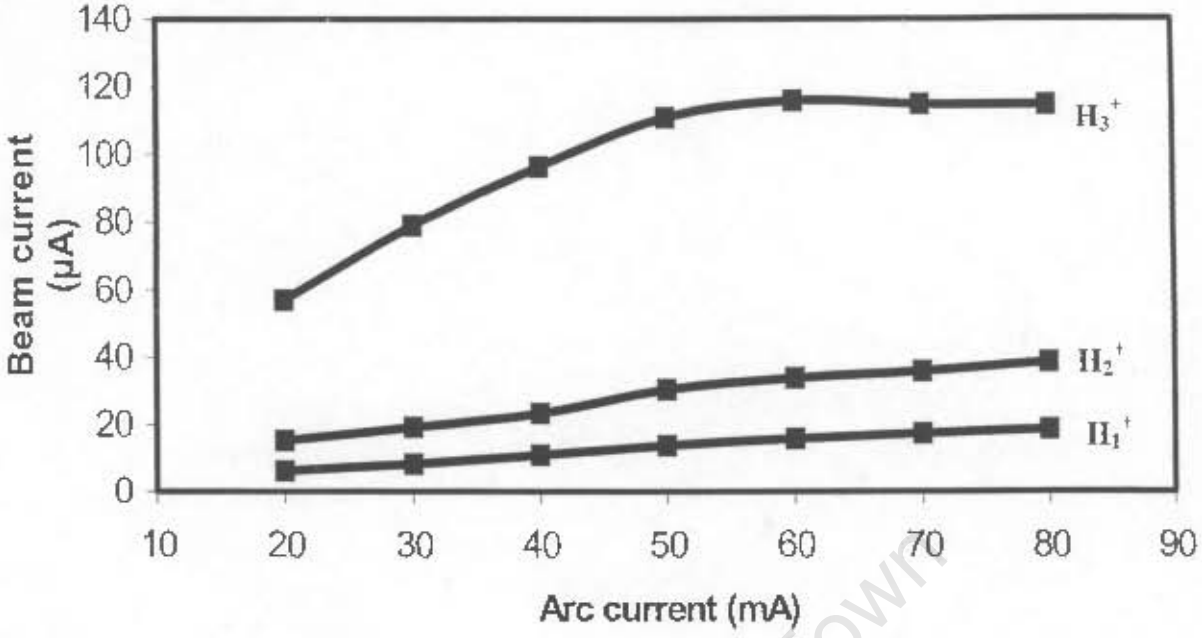

Figure 4.12: Total beam current as a function of arc current, for the cold-cathode dupolasmatron ion source constructed with permanent magnets, at an extraction voltage of 11kV for Hydrogen ions.

4.6 THE PENNING GAUGE (PIG) ION SOURCE

4.6.1 THE CONSTRUCTION OF THE SOURCE AND ITS OPERATING PRINCIPLES

Figure 4.13 shows the main features of a PIG ion source, the most often used internal ion source for acceleration of light ions in cyclotrons. The gas to be ionized flows into the anode, which is at a positive potential with respect to the two cathodes. As the anode voltage is increased, free electrons in the regions between the cathodes and the anode are accelerated towards the anode in the electric field and ionize the gas atoms. The anode current suddenly increases to a value limited by the power supply, which normally is capable of both voltage and current stabilization and limitation. Positive ions formed near a cathode, or leaving the anode, are accelerated towards the cathode and collide with it, thereby heating it and causing generation of more electrons through thermionic emission.

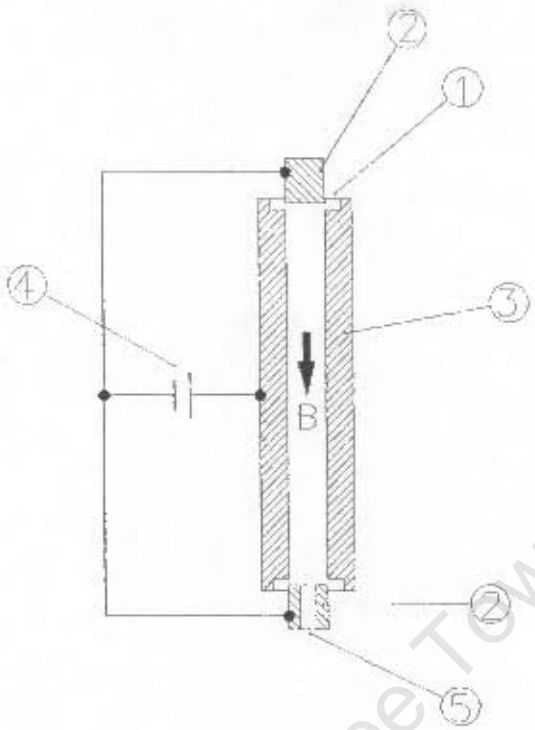

Figure 4.13: Schematic of a cold-cathode Penning (PIG) ion source showing: (1) the top cathode, (2) the cathode through which the beam is extracted, (3) the anode, (4) the anode power supply, (5) the opening through which the beam is extracted and the direction of the magnetic field B.

In some PIG sources one of the cathodes is heated with a Tungsten filament for better control of the discharge. Electrons emitted by the cathodes are accelerated in the electric field in the spaces between the cathodes and the anode, and move into the anode electrode. Similarly, electrons entering these regions from the anode are first retarded and then accelerated back into the anode to oscillate back and forth between the two cathodes, thereby forming a reflex discharge. Inside the anode particles are shielded from the electric field but not from the magnetic field that penetrates through the non-magnetic electrodes of the source. Electrons leave the cathode with horizontal, as well as vertical velocity components and therefore move down into the anode in spiral orbits. The plasma maintains itself at a positive potential with respect to the anode [Che74] to confine electrons electrostatically in addition to the magnetic confinement. The discharge mechanisms in a PIG source and the influence of the source parameters on the beam current have been described in several books [Bro89, Val77] and papers [Ben72, Sch76]. For dissociation of a Hydrogen molecule, an electron energy of at least 4.52 eV is required and for ionization of a Hydrogen atom 13.59 eV. The optimum energies for

dissociation and ionization are, respectively, 16.5 eV and 80 eV [Con92]. Figure 4.14 shows a cross-section of the Van de Graaff PIG source. The source has a diameter of 180mm and a length of 100mm. As in the previous figure the gas inlet is at the top and the beam is extracted axially at the lower cathode. The magnetic field is generated by the current sent through the coil windings and defined by the magnet steel configuration. The anode is made from stainless steel and is cooled by sending a coolant, with low electrical conductivity, through channels in an Aluminium block with which it is in good thermal contact.

4.6.2 EXPERIMENTAL RESULTS

4.6.2.1 OPTIMIZATION OF THE BEAM CURRENT BY VARYING THE EXTRACTION VOLTAGE

The solid lines in figure 4.15 show the measured beam current for different Hydrogen ion species as a function of the extraction voltage. The remaining ion source parameters were kept at the following constant values: arc current = 1 A, arc voltage = 800 V, pressure = 4×10^{-5} mbar and 50 V across the magnet coil. As before for the hot-catode duoplasmatron source it is expected that the beam current as a function of the extraction voltage should follow the Child-Langmuir law, i.e. the extracted ion beam current I should be proportional to the extraction voltage V to the power 3/2. The dotted lines in figure 4.15 are least-square fits of the equation $I = \text{constant} \times V^{3/2}$ to the measured data for the different ion species and show that the source behavior is to a large extent in agreement with the Child-Langmuir law which means that the beam current extracted from the source is limited by the space charge in the region between the anode and extraction electrode. It again also indicates that the beam losses in the beamline due to space-charge effects are small and only of importance for operation with low extraction voltages, as shown in figure 4.15. For high beam intensities the source should be operated at as high as possible an extraction voltage without excessive sparking.

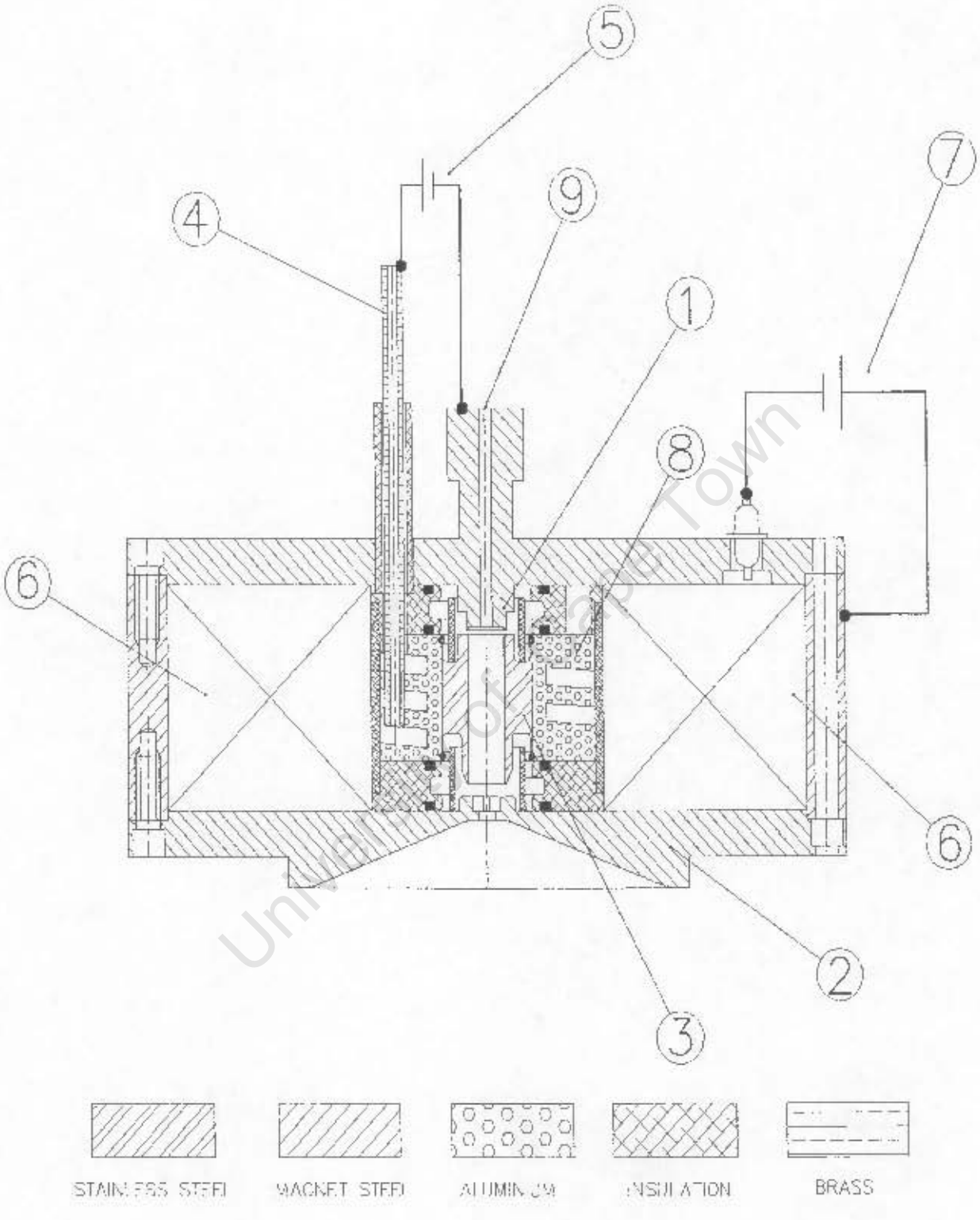

Figure 4.14: Cross-section of Van de Graaff Penning Ion Source showing: (1) the top cathode, (2) the cathode through which the beam is extracted, (3) the anode, (4) the coolant connection, (5) the anode power supply , (6) the magnet windings , (7 the magnet power

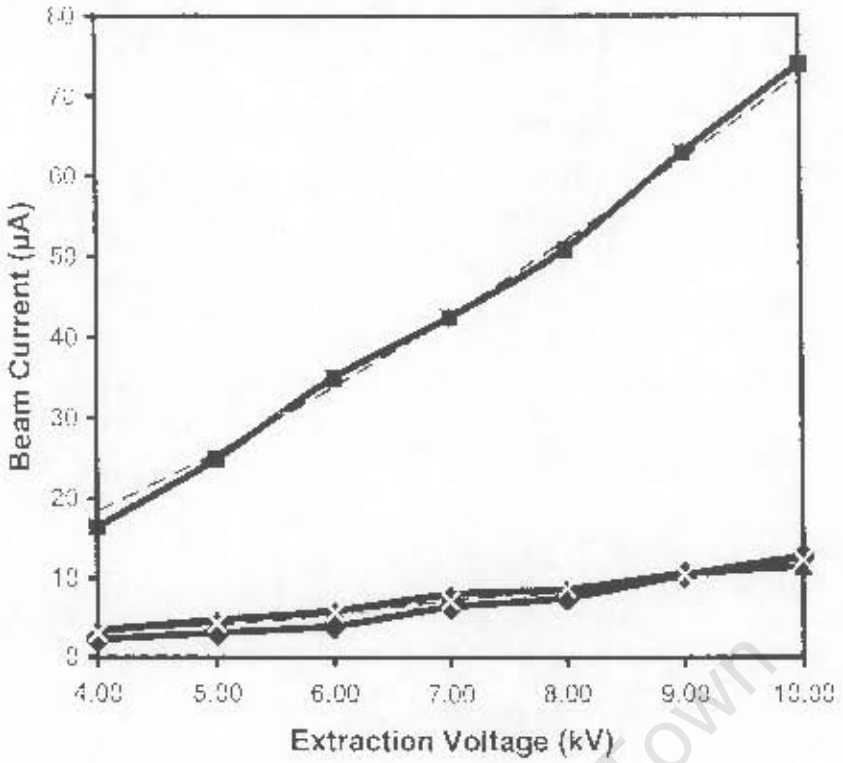

Figure 4.15: Measured beam current (solid lines) for different Hydrogen ion species as a function of the extraction voltage, for the Penning ion source and least- square fits (dotted lines) of the Child-Langmuir law. The measurements were made under the following conditions: arc current = 1A, arc voltage = 800 V, pressure = $4x10^{-5}$ mBar, magnet power supply = 50 V

4.6.2.2 OPTIMIZATION OF THE BEAM CURRENT BY VARYING THE ARC VOLTAGE AND THE PRESSURE

Figure 4.16 shows the beam current in μA as a function of arc voltage at a pressure of 10^{-5} mBar and an extraction of 8 kV for the Van de Graaff PIG ion source. The arc current also increases as the arc voltage is increased. As expected the beam current for all three Hydrogen ion species increases wit the arc voltage and arc power. This indicates that the source should be operated at an arc voltage just below the sparking limit. The life-time of the source is limited to only five to six days by sputtering, a process that is strongly enhanced by high arc currents and voltages, of the cathode and anit-cathode electrodes.

Figure 4.17 shows the beam current in μA as a function of the pressure in the beamline of the ion source test bench. At pressure values below 9×10^{-6} mbar the proton beam current increases sharply with decreasing pressure. This shows that to obtain intense proton beams the source should be operated at a pressure just above the value at which the source becomes unstable.

Emittance measurements, similar to those for the hot-cathode duoplasmatron ion source have been made for the PIG ion source. A value of 34π mm mrad for 96 % of the beam intensity has

been obtained.

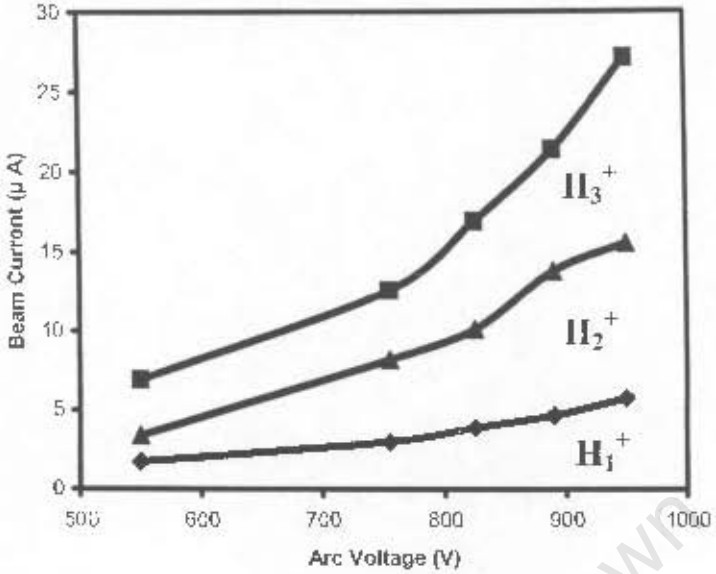

Figure 4.16: Measured beam current for different hydrogen ion species as a function of the arc voltage for the Penning ion source. The measurements were made under the following conditions: extraction voltage = 8 kV, pressure ~10^{-5} mBar, magnet power supply =50 V.

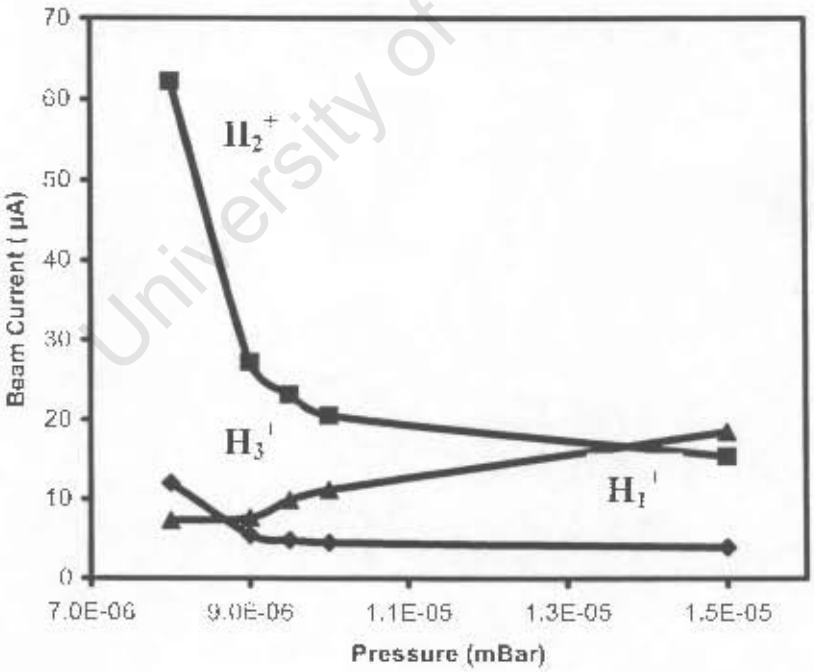

Figure 4.17: Measured beam current for different Hydrogen ion species as a function of the pressure for the Penning ion source. The measurements were made under the following conditions: extraction voltage = 8 kV, magnet power supply –50 V. The arc voltage varied between 800 and 900 volt. Current between 30 -45 mA

4.7 CONCLUSIONS

The operating principles of the two duoplasmatron ion sources and the PIG source available for the Van de Graaff accelerator have been determined qualitatively, mainly by studying the extensive literature on ion sources. No quantitative treatment of such sources by which their performance can be calculated in terms of their dimensions, the applied voltages and the gas flow could be obtained from the literature. The main characteristics of the three sources have therefore been determined experimentally on an ion source test bench. Important parameters of the sources such as the pressure and temperature in different regions of the sources could, because of space limitations, not be measured. However, in spite of these limitations in the quantitative understanding of the sources, sufficient information to continue with the study of the beam transport through the Van de Graaff accelerator and its beamlines could be obtained from these measurements. With regard to beam intensity, life-time and gas consumption the measurements showed that the hot-cathode duoplasmatron is at present by far the most suitable source for the van de Graaff accelerator. In future microwave ion sources could be considered for the Van de Graaff accelerator for higher beam intensities and better beam quality.

CHAPTER 5

UPGRADING OF THE VAN DE GRAAFF ACCELERATOR

5.1 INTRODUCTION

The Van de Graaff accelerator at iThemba LABS was manufactured by High Voltage Engineering Corporation, Burlington Massachusetts, U.S.A, and installed at Faure in 1962. During the past few years numerous breakdowns occurred, due to ageing of components. The time needed for servicing the accelerator and tuning of the beam increased by more than 600% from 1999 to 2004. The beam quality and intensity were seldom sufficient for the scheduled experiments to be performed. A major upgrade of the whole facility, with the aim of increasing the reliability of the accelerator and beamlines and improving the quality of the beam from the accelerator, started in 2002. It is estimated that the upgrade will extend the useful lifetime of the Van de Graaff by approximately a further 10 to 15 years.

An important aspect of the upgrade was a thorough study of the beam optics from the ion source to the exit of the accelerator, in order to understand the poor beam transmission at terminal voltages below 3 MV and also to find means of increasing the beam intensity delivered by the accelerator. During operation of the accelerator over a period of months it was found impossible to match the focusing condition of the beam at the exit of the accelerator to the admittance of the beam line with the ion source at extraction voltages of more than 5 kV, with the original design of the electrode configuration and power supplies. Limiting the extraction voltage to less than 5 kV has, however, a huge influence on the maximum beam current that can be obtained from the ion source and therefore on the beam intensity available from the accelerator. To understand this behavior and to find a solution to the problem the beam optics of the accelerator has to be fully understood. The software programs TRANSPORT, IGUN and TOSCA were used to calculate the beam characteristics. The detailed investigation of the beam optics as well as the modifications to improve the transmission through the accelerator and the beam intensity at the exit of the accelerator will be discussed in the rest of the chapter.

5.2 LAYOUT OF THE VAN DE GRAAFF ACCELERATOR

For the calculation of the electrostatic fields and paths of charged particles in the accelerator the dimensions of the accelerator electrodes and the distances between them have to be known accurately. Since no proper drawings of accelerator components were available at the beginning of this study all the components in the terminal section were dismantled and detailed drawings of every component were made. A photo of the high-voltage terminal section is shown in figure 5.1 with the dome removed, was also made and used to calculate the electric field and particle paths.

Figures 5.2 and 5.3 show the layout of the components in the terminal section. The ion source, at the top in figure 5.2, is at a positive voltage of several kilovolts with respect to the extractor electrode. A particle beam, extracted from the source, next passes through two flat plates, steerer 1 in figure 5.2, with a tapered gap opening downwards to accommodate the diverging beam, that are used to steer the beam transversely by adjusting the voltage of the DC power supply connected between them. One of these two plates is connected to the extractor electrode. Since the potential difference between the two plates is typically of the order of a few hundred volt the gain in energy as particles move from the extractor electrode to the gap between the plates is small in comparison with the particle energy at this point in the accelerator. While the particles move from the gap between the plates to the first of the three electrodes of einzel lens 1 the slight gain in energy in the steerer is lost again since this electrode is at the same electrostatic potential as the extractor electrode. The second electrode of the einzel lens 1 is at an adjustable negative potential, of typically several hundred volt, with respect to the ion source, which means that it is at a positive voltage of the order of kilovolts with respect to the first electrode of the lens. The third electrode is again at the same potential as the extractor electrode, i.e. at a negative potential of the order of kilovolts with respect to the second electrode of the lens. Particles in the beam therefore loose a large fraction of their energy in the first gap of the lens and gain the same amount of energy in the second gap while the beam is focused in both directions perpendicular to the axis of the accelerator in both gaps of the lens. In the first half of the first gap it is defocused and in the second half focused, but because the particles are strongly retarded in the gap they remain a longer time in the second half of the gap, where the force on them is directed towards the axis, than in the first half of the

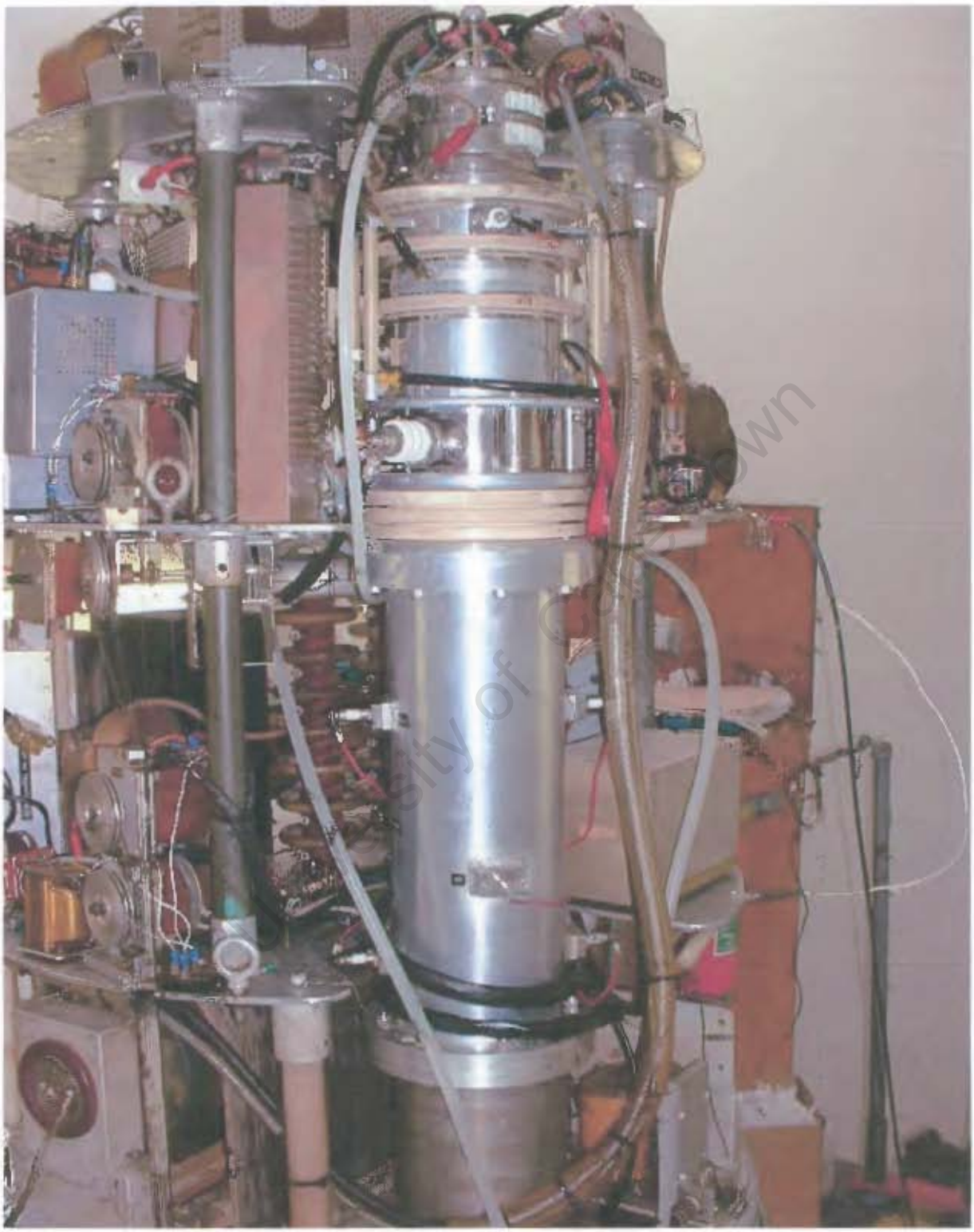

Figure 5.1: The high-voltage terminal of the accelerator with the dome removed.

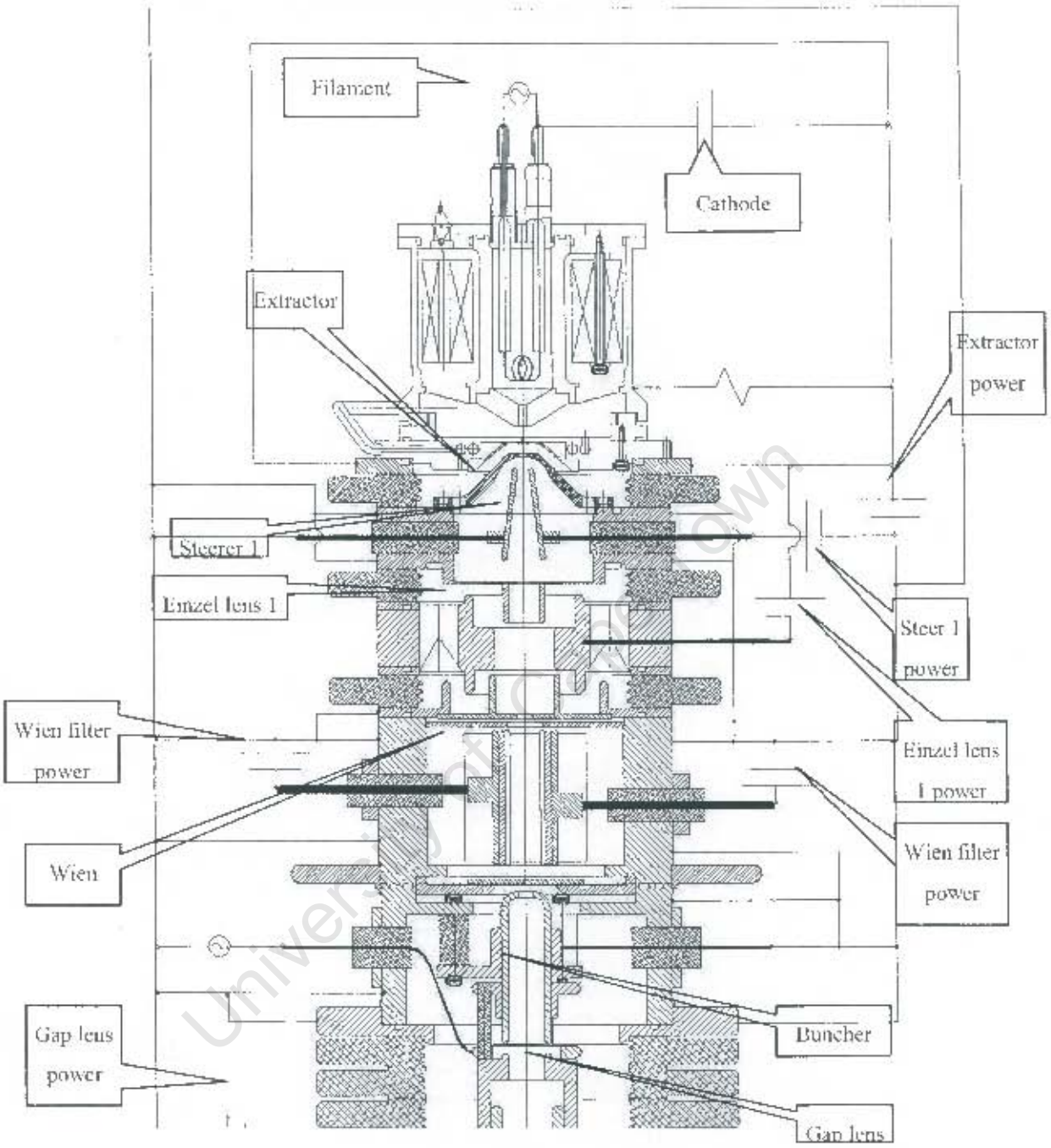

Figure 5.2: Layout of the ion source and the electrodes in the first section of the high-voltage terminal of the accelerator.

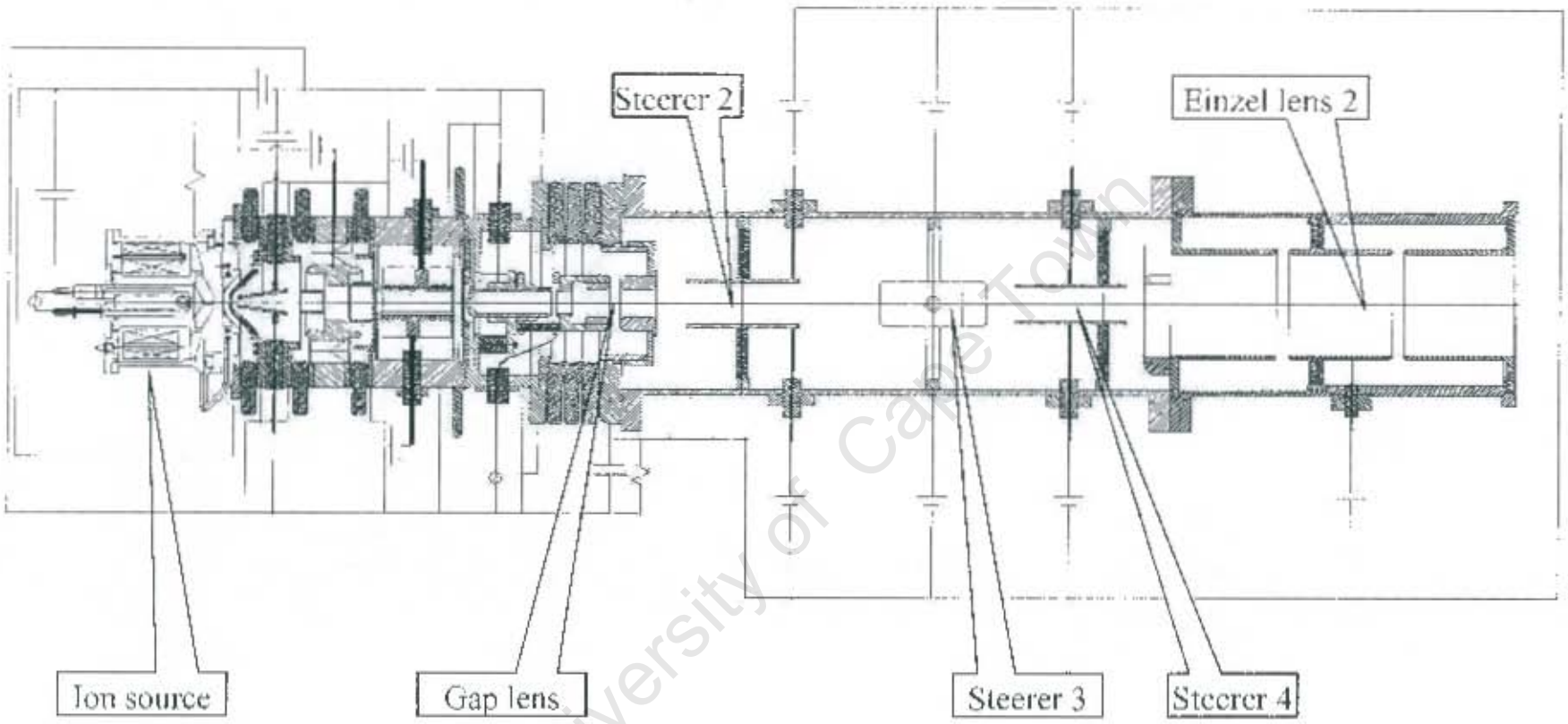

Figure 5.3: Layout of the ion source and the electrodes in the high-voltage terminal section of the Van de Graaff accelerator.

gap, where the force is directed away from the gap. The opposite happens in the second gap in which the particles gain energy and remain for a longer time in the first half of the gap, in which the force is directed towards the axis, than in the second half of the gap, in which the force is directed away from the axis. The voltage on the einzel lens 1 is adjusted to focus the beam on a collimator directly downstream from the next component in figure 5.2, the Wien filter. The Wien filter consists of two parallel plates, between which a DC voltage is applied, in the pole gap of a permanent magnet with the plates perpendicular to the poles, resulting in an electric field perpendicular to the magnetic field, and is used to select ions with a specific charge-to-mass ratio from the different ions species such as for example H_3^-, H_2^+ and H^+ and some heavy ions that are delivered by the duoplasmatron ion source. By adjusting the voltage the force on a particle with speed v, mass m, charge q due to the electric E van be made equal in magnitude but opposite in direction to the force due to the magnetic field B: $qE = qvB$. Only particles with a speed $v = E/B$ will therefore pass through the collimator behind the Wien filter. At an energy of a few keV the speed of the particles can be approximated by $v = (2qV/m)^{1/2}$, with V the potential difference through which the particles have been accelerated from rest. By selecting a particular value of v for particles with the same energy a particular charge-to-mass ratio is selected. In the case of the Wien filter two power supplies, one positive and one negative with their common electrodes connected to the third electrode of einzel lens 1, are used to create the electric field between the plates, with the result that for particles moving on the axis of the accelerator there is no change in energy along their paths through the Wien filter. Particles moving off the axis will gain and loose energy along their paths through the Wien filter, but will experience no net change in energy.

The collimator after the Wien filter is followed by the buncher electrodes, to one of which a high-frequency voltage is applied when pulsed beams are required, and a lens, called the gap lens, which focuses the beam, in the same way as an einzel lens, as well as accelerates the analyzed beam. Between the gap lens and the einzel lens 2, that focuses the beam at the entrance of the accelerator, there are three sets of steerer plates as shown in figure 5.3, all of them with positive and negative power supplies to leave the energy of particles on the axis unaltered along their paths, to align the beam with the axis of the accelerator. In the accelerator tube, in which there are in total 140 electrodes, all similar in size and shape, the beam is accelerated to ground potential. The final beam energy is determined by the potential of the high voltage terminal with respect to ground potential. The accelerator tube has a relatively small optical strength and introduces only small variations in the optical properties of the beam

formed in the terminal section of the accelerator.

5.3 COMPUTER PROGRAMS FOR THE CALCULATION OF BEAM CHARACTERISTICS

The computer programs TRANSPORT [Car72, 81], and TOSCA [Bor97] were available at iThemba LABS for the calculation of particle paths through the accelerator. In order to include space-charge effects in the calculations the program IGUN [Bec92, Bec93, Bec98] was acquired. The results obtained with the different codes are discussed and compared and also compared with experimentally obtained data. Finally, the applicability of the three computer codes for this specific task is reviewed.

5.3.1 THE COMPUTER PROGRAM IGUN

IGUN (an acronym for Ion Gun) is a two-dimensional ray tracing code that has been developed for simulation of the extraction of positive ions from plasmas. A pre-processor, GPED (an acronym for Graphic Polygon Editor) for IGUN, has also been developed to set up the boundary conditions, including the definition of internal electrodes, dielectric boundaries, and slanted Neumann boundaries (field lines as boundary elements). The boundary input is mesh independent and can use any coordinate system from a drawing, and the program accepts any offsets in coordinate values. The output of equipotentials, field lines and particle trajectories, which can be used in further runs of the program has the same offsets and use the same units, which greatly eases the organization of concatenated runs, e.g. with higher mesh resolution in the plasma region and lower mesh resolution further on downstream. Special post processor programs allow output to be sent to pen plotters, using the programs HPGL and XHPPLOT, to postscript printers with the program XPSPLOT, or converted to AUTOCAD files (AUTOCAD is the name of a company and CAD is an acronym for Computer Aided Design). Another computer program, DXFPLOT, is available for further processing of the data.

The program has found widespread application in the optimization of electrode design, which has resulted in well-acknowledged feedback for improvements from users. Results of calculations with IGUN have been compared with those obtained with more elaborate and expensive computer programs at CERN (European Organization for Nuclear Research) [Han01] as well as with known solutions and experimental data, for the same electrode geometry. Although the different programs agree within 2% with approximate analytical solutions for

as well as with known solutions and experimental data, for the same electrode geometry. Although the different programs agree within 2% with approximate analytical solutions for space-charge calculations and within one in a thousand of the maximum voltage for the calculation of potential distributions, the calculated emittance is 20% lower and the calculated transmitted current 30% higher than could experimentally be obtained. Figure 5.4 shows the results of typical calculation that was done with the program IGUN for the high-voltage terminal for the Van de Graaff accelerator. The current at the second collimator downstream from einzel lens 2, as well as the voltages on the electrodes were specified.

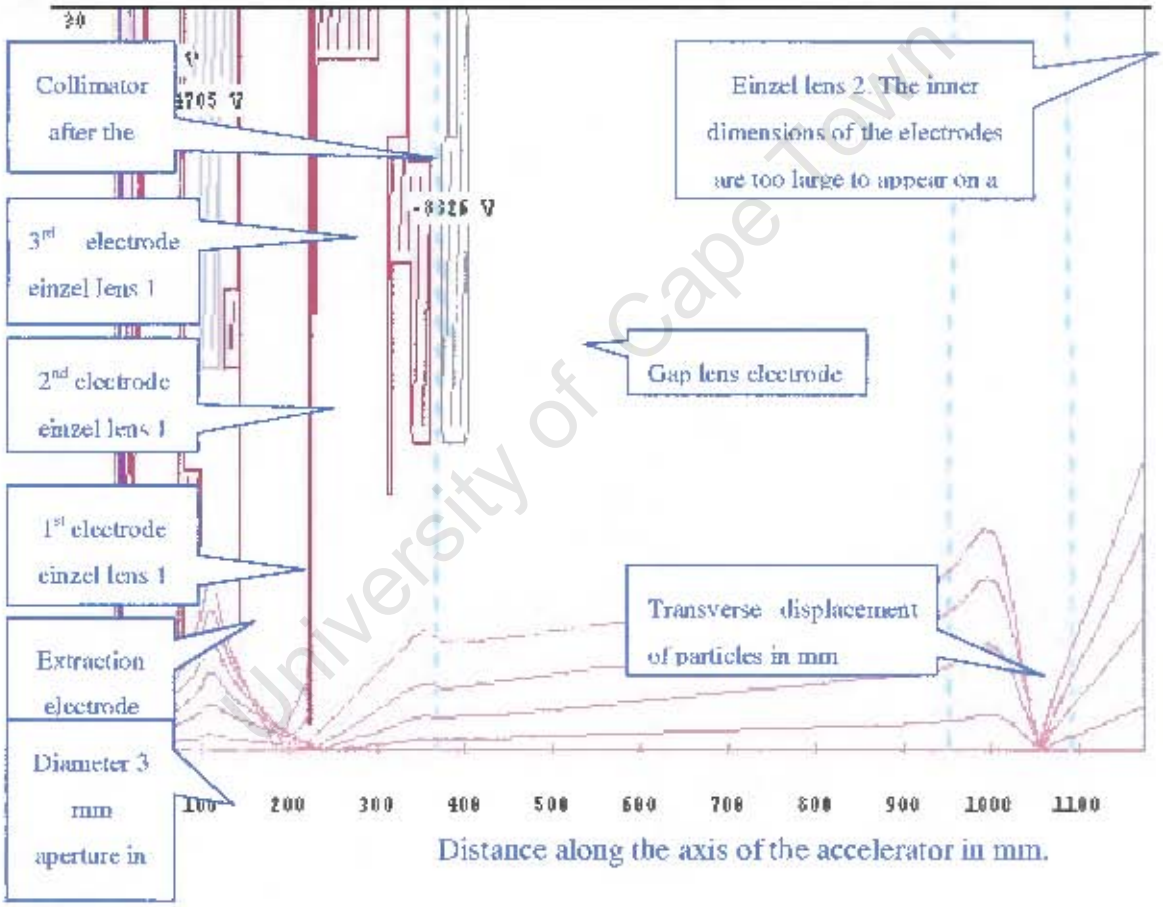

Figure 5.4 Transverse beam dimensions in mm, in the high-voltage terminal section of the Van de Graaff accelerator, calculated with the program IGUN for a round ion source aperture of 3 mm diameter. The potential differences between the electrodes in the figure are the same as in the accelerator, but the absolute values differ. The ion source, as well as the collimator after the Wien filter, is at zero potential. The potential of the extraction electrode is 5285 Volt. The second electrode of the first einzel lens is at 4705 Volt. The electrode of the gap lens is at a potential of –8325 Volt. The beam envelope up to and through the second einzel lens is shown. The collimators

The voltages on the electrodes, obtained by optimizing the beam through the Van de Graaff accelerator have been used to calculate the beam profile, shown in figure 5.4, with IGUN. The program adjusts the plasma density at the ion source aperture automatically and traces the paths of particles, taking space-charge forces into account, through the electrodes and collimators. In the calculated beam profile the focal points of the beam coincide with the positions of the two collimators, which is essential for good transmission through the machine. It can therefore be concluded that the beam profile in the accelerator can be calculated with the program IGUN with reasonable accuracy and that IGUN can be used for design of new electrode configurations.

5.3.2 THE COMPUTER PROGRAM TOSCA

The TOSCA analysis package, for the calculation of three dimensional magnetostatic and electrostatic fields, a module of the OPERA-3d integrated suite of finite element software for 3D electromagnetic design, analysis and simulation, is a commercial software product from Vector Fields in the U.K. [Vec04]. The TOSCA-module uses a discrete finite element model to solve partial differential equations governing the behavior of static electric and magnetic fields in three dimensions. The 3D POST-processor interfaces to the TOSCA database which contains the calculated electromagnetic field distribution and allows the user to display the results of the analysis in a number of ways, e.g. by tracking of particles through the calculated fields. A set of standard operating values for the extraction voltage and the different lenses between the ion source and the accelerator tube, obtained by optimizing the beam transmission through the accelerator experimentally, were used to calculate particle orbits through the Van de Graaff accelerator.

There is very good agreement between results obtained with the programs IGUN and TOSCA as can be seen by comparing the beam envelopes in figures 5.4 and 5.5. The calculated positions of the two focal points, at the collimator following the Wien filter and the collimator at the entrance of the accelerator, with TOSCA and IGUN agree within a few millimeters, although the OPERA package does not take space-charge forces into account. The results also correspond well with the measured beam transmission through the different apertures in the terminal.

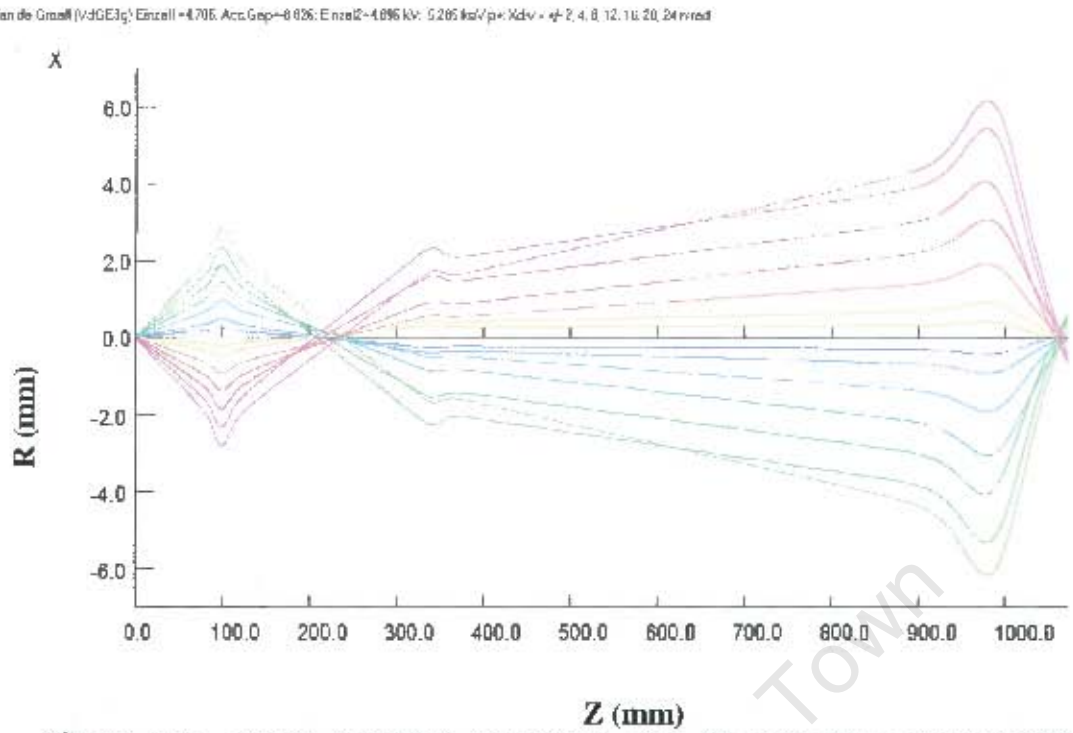

Figure 5.5: Beam envelopes calculated with the computer program TOSCA. The trajectories of a number of particles with the same starting position but different angular deviations are shown. The voltages on the electrodes are the same as those which have been used with the program IGUN in figure 5.4.

5.1.2 THE COMPUTER PROGRAM TRANSPORT

For the design of beam lines, it is convenient to consider the behavior of the beam in phase space in addition to the dimensions and position of the beam in laboratory space. For this purpose the computer program TRANSPORT is used in all major accelerator laboratories. The program calculates first-, second- and third-order effects by matrix multiplication. Matrices are used to describe the beam optical elements and the charged particle beam itself. By successive matrix multiplication the transmission of particles through a beam line can be calculated. The program can also vary the physical parameters of the line to fit the elements of matrices in order to obtain values and conditions, which are specified by the user. The program calculates the beam envelope and beam transfer matrices for the whole beam line, using values for the physical parameters specified by the user. Printout of the results is also available on request. Provision is made to vary some of the input parameters to achieve a desired final beam. The beam envelope obtained with the program TRANSPORT for experimentally obtained voltage values for the different lenses did not give a good agreement with the other two programs

TOSCA and IGUN and also not with the experimental measurements. The main reason for this discrepancy is the way that electrostatic lenses are simulated in the program. The einzel lenses are specified only by the voltage of the center electrode and the gap between the center electrode and two outer electrodes. There is no way to specify the radius of the different electrodes. From calculations with IGUN and TOSCA it could be shown that the radii of the different electrodes have a huge influence on the focusing properties of an einzel lens. The beam envelope calculated with the program TRANSPORT for the experimental values of voltages on the different lenses is shown in fig 5.6. This beam has a focal point about 40mm in front of the collimator following the Wien filter, but no focal point at the entrance of the accelerator.

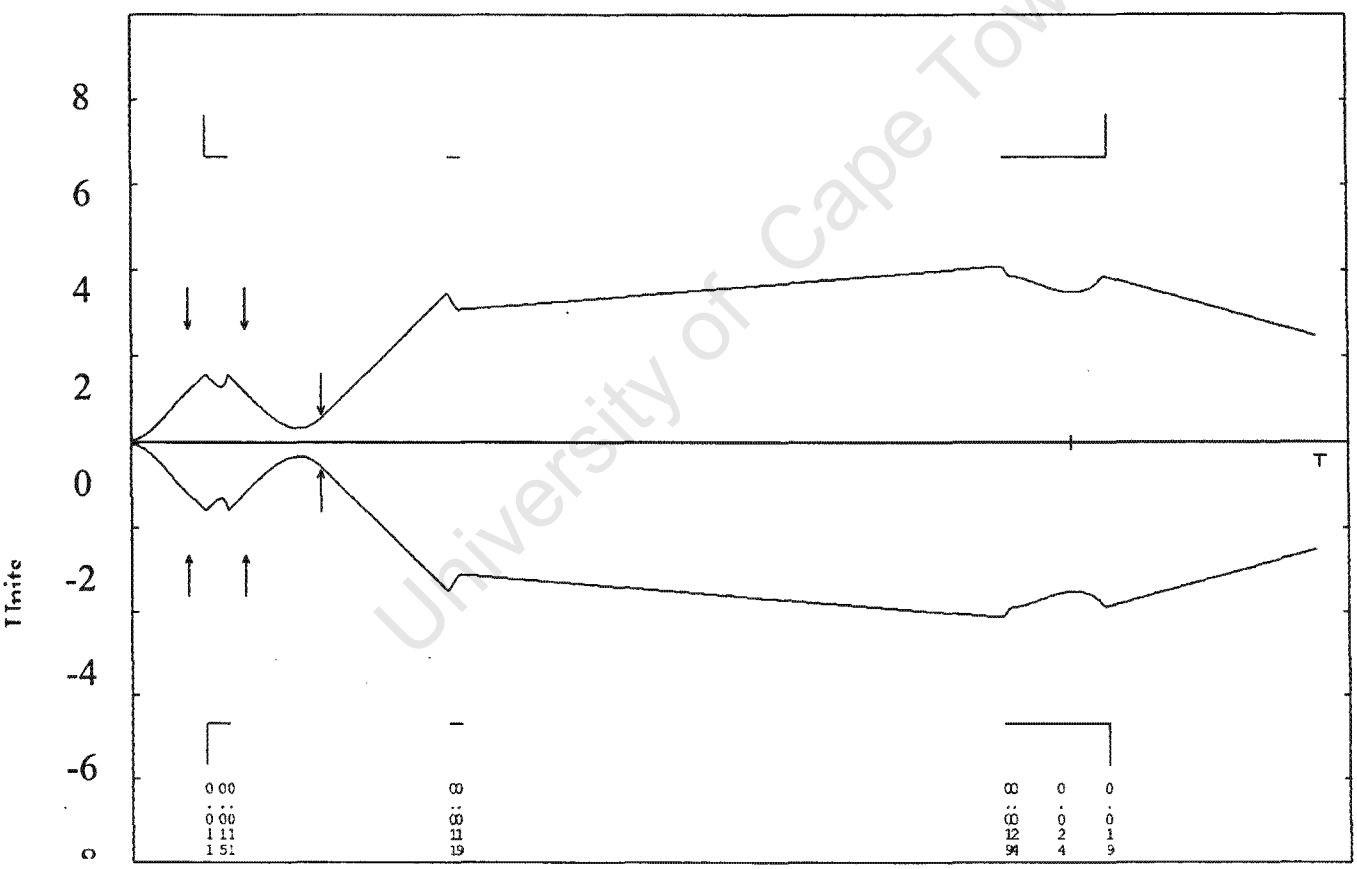

Figure 5.6: Beam envelope calculated with the program TRANSPORT(see Appendix B). The trajectories of two particles with the same starting position but different angular deviations are shown. The voltages on the electrodes are the same as that which have been used with the program IGUN in figure 5.4 and TRANSPORT in figure 5.5.

It is, however, possible to obtain with TRANSPORT the same beam envelopes as those calculated with the programs IGUN and TOSCA by artificial modification of the lengths of the center electrodes and the gap lengths of the different einzel lenses in the program TRANSPORT. The center electrodes and gap length were modified in such a way that the over-all length of the different einzel lenses remained the same. Figure 5.7 shows the beam envelope calculated with the modified gap and center electrodes lengths of the einzel lenses. Future calculations can now be done with TRANSPORT, which is much faster than the other two programs, using the modified apertures of the lenses. The results of calculations done in this way with TRANSPORT show satisfactory agreement with those calculations with TOSCA. The three computer programs can now with confidence be used to study various aspects of the optical characteristics of the Van de Graaff accelerator.

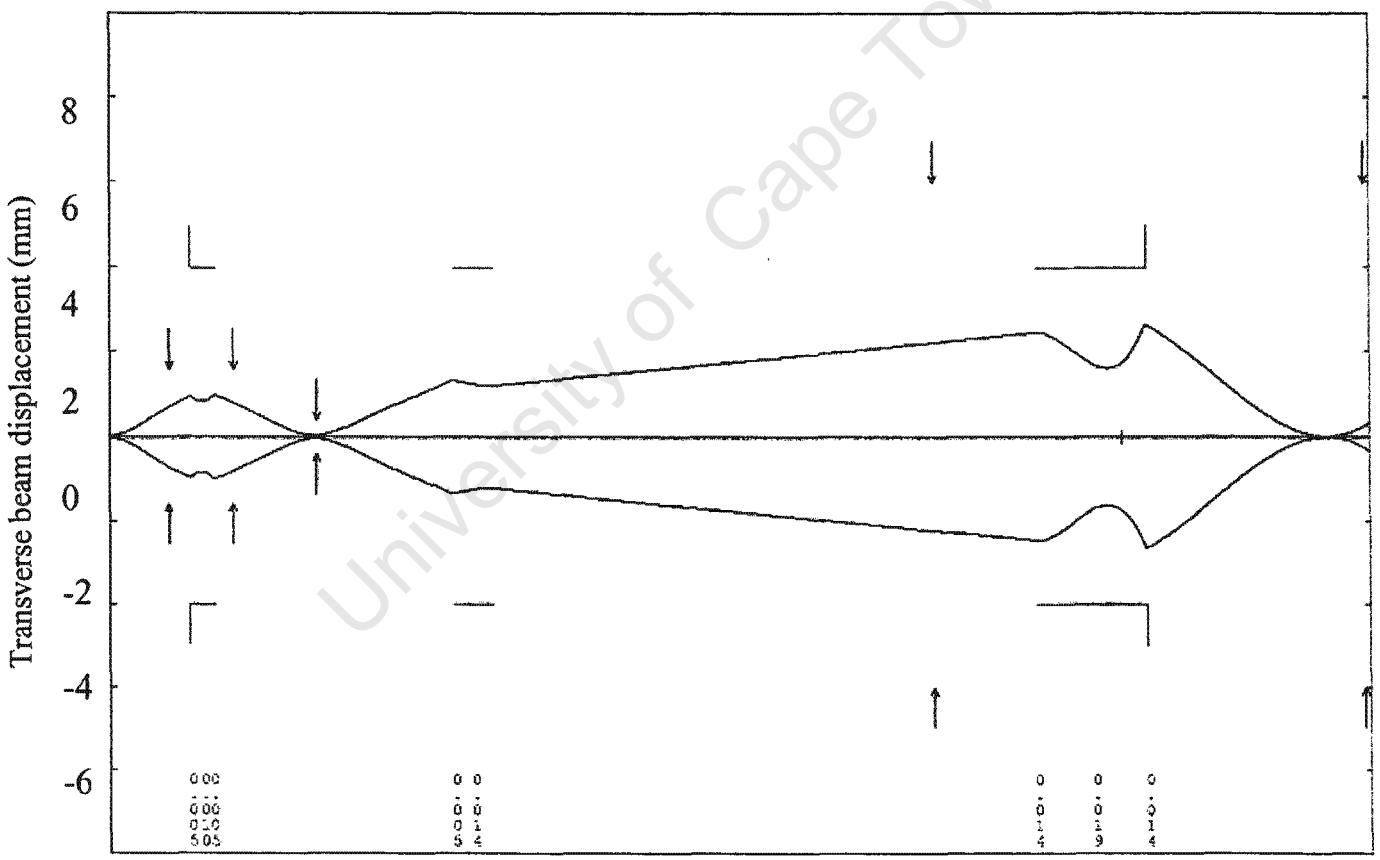

Figure 5.7: Beam envelope plots calculated with the program TRANSPORT(see Appendix B) through the Van de Graaff accelerator tube. The calculations done with TRANSPORT and TOSCA show satisfactory agreement.

5.4 CALCULATION OF THE OPTICAL CHARACTERISTICS OF THE VAN DE GRAAFF ACCELERATOR

For the calculation of the beam optics through the accelerator over its full length only the program TOSCA and TRANSPORT have been used, since the number of data points required to represent the accelerator tube exceeds the maximum number available in the program IGUN. The results from TOSCA can only be evaluated against the beam width measured at the exit of the accelerator. If the measured beam width at the exit of the accelerator agrees with the width calculated with TOSCA it could be accepted that the beam optical characteristics of the accelerator can be calculated reasonably well with the program TOSCA, especially since the TOSCA results for the terminal section agreed with those of IGUN. The possibility of adapting the accelerator electrodes for the program TRANSPORT to match the results obtained with TOSCA has also been investigated.

For calculation of the beam characteristics in the Van de Graaff accelerator the dimensions of the electrodes in the accelerator tube, which consists of two tubes, are required. The available drawings of the tubes are assembly drawings that show little detail. The dimensions were therefore determined by accurately measuring the electrodes in a set of spare tubes. The beam characteristics, as calculated above in section 5.3, at the end of the terminal section were used as the starting condition for the accelerator. The results of the terminal section and the accelerator were then combined to give an overall calculated beam envelope from the ion source to the exit of the accelerator.

The beam envelope calculated with TOSCA is shown in figure 5.8. The settings that were used for these calculations correspond to the experimentally determined optimal settings for the power supplies of the electrodes in the terminal and accelerator. The measured beam width at the exit of the accelerator agrees very well with the width calculated with TOSCA.

The dimensions of the gaps between the first few electrodes of the first accelerator tube were modified in the program TRANSPORT to obtain similar focusing conditions at the exit of the accelerator as with the program TOSCA. The beam envelope calculated with TRANSPORT, with the modification to the gap lengths, is shown in figure 5.9. The correlation with TOSCA is good and in the future the transport input file can be used to calculate beam envelopes in the Van de Graaff accelerator for different settings of the electrode potentials. It is much faster to do the calculation with TRANSPORT than with the program TOSCA.

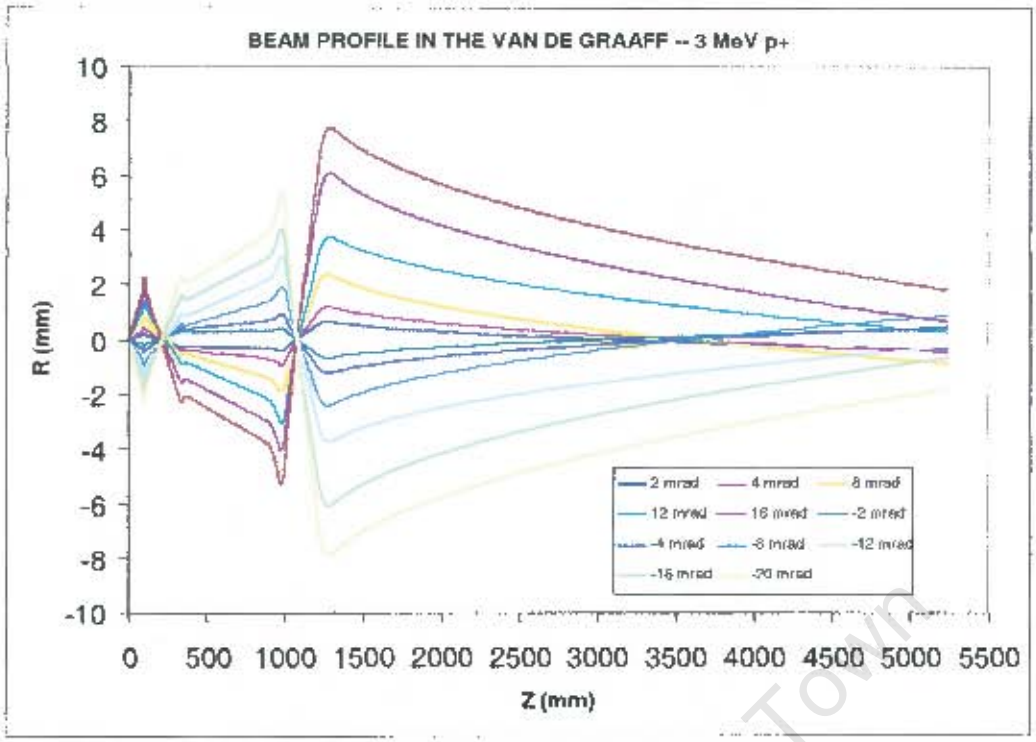

Figure 5.8: The beam profile from the ion source to the exit of the accelerator, calculated with the program TOSCA. The beam width and the focusing condition of the beam at the exit of the accelerator agree very well with the measured beam profile.

5.1 MODIFICATION OF THE VAN DE GRAAFF ACCELERATOR FOR HIGHER BEAM CURRENTS OVER A WIDER ENERGY RANGE

5.5.1 INTRODUCTION

With the beam behavior in the accelerator now fully understood, the poor beam transmission through the accelerator at terminal voltages below 3 MV and means of increasing the beam intensity available from the accelerator can be investigated. During operation of the accelerator over a period of years it was found impossible to match the beam emittance at the exit of the accelerator to the admittance of the beam line, at extraction voltages of more than 5 kV, with the present design of the lens electrode configuration and power supplies. Limiting the extraction voltage to less than 5 kV has a strong influence on the maximum beam current that can be obtained from the ion source and therefore on the beam intensity available from the accelerator. Modifications to the lenses in the terminal section of the accelerator to solve these

problems will be investigated, mainly by doing beam envelope calculations with the programs TOSCA.

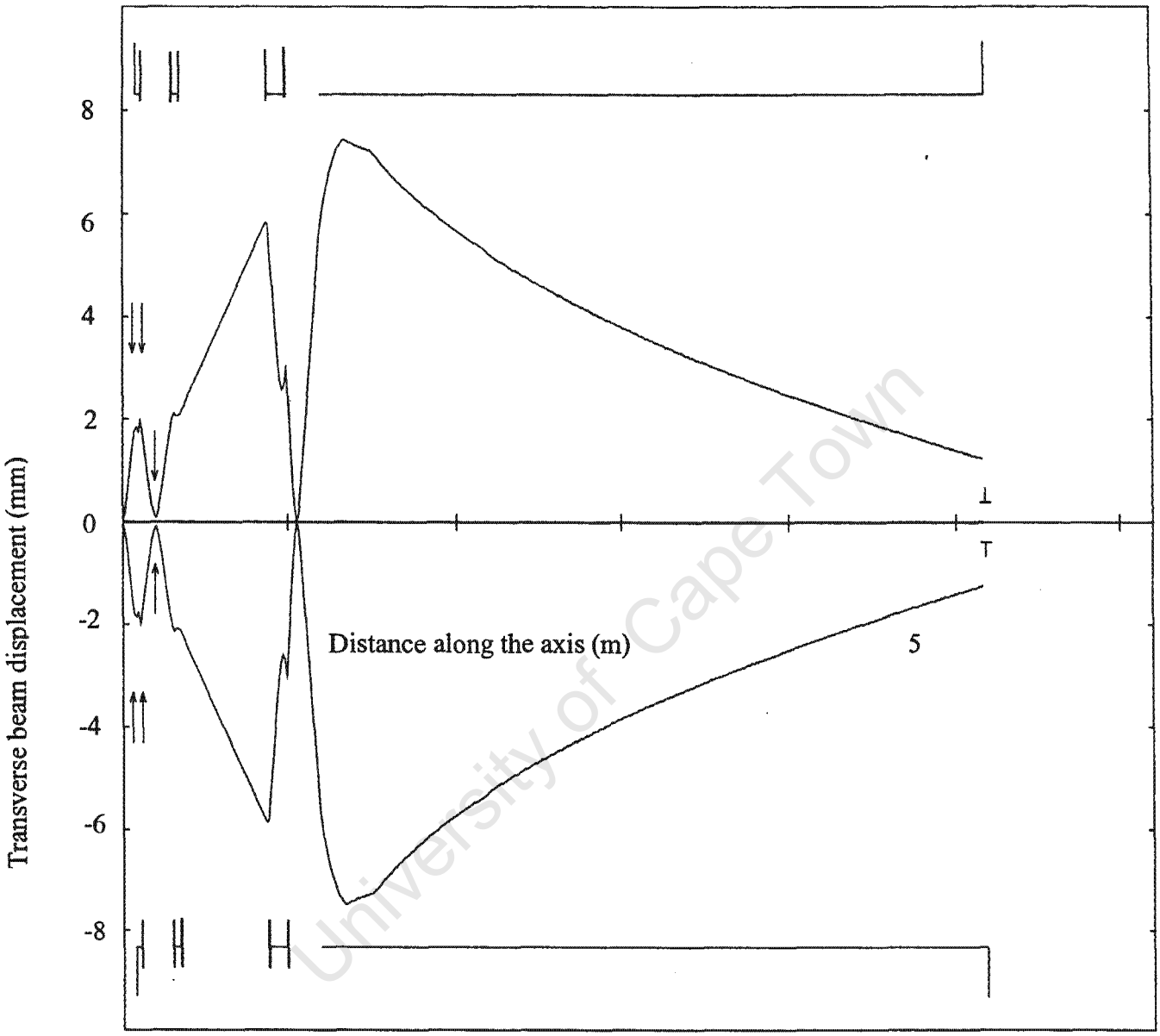

Figure 5.9: The beam profile calculated with the program TRANSPORT from the ion source to the exit of the Van de Graaff accelerator. The gaps of all the einzel lenses, as well as the first few acceleration gaps of the accelerator tube, were modified to yield the same beam profile as that calculated with the program TOSCA.

5.5.2 BEAM TRANSMISSION THROUGH THE ACCELERATOR AT TERMINAL VOLTAGES BELOW 3 MV

To investigate the poor transmission through the accelerator at terminal voltage below 3 MV the

beam profile from the ion source to the exit of the accelerator was calculated with the program TOSCA, using experimentally determined voltages for the different lenses as starting conditions. By linear scaling of the ion source extraction voltage and the voltages of the electrostatic lenses in the terminal section with the terminal voltage of the Van de Graaff accelerator the beam envelope in the accelerator remains constant as expected. It is therefore clear that there is nothing inherently wrong with beam focusing in accelerator. However, it follows from these calculations that the proper beam focus at the exit of the accelerator can only be obtained with the correct focusing condition at the entrance of the accelerator as well as the correct injection energy into the accelerator.

With the current layout it is possible to get the correct focusing condition at injection into the accelerator, but not the required beam energy. There are two parameters that influence the injection energy: the extraction voltage and the voltage on the gap lens. For lower terminal voltages the voltage on the gap lens has to be decreased linearly with the terminal voltage to keep the beam focus at injection constant, and can therefore not be used in addition to adjust the injection energy. The only other parameter with which the injection energy can be varied is the extraction voltage of the ion source. Lowering the extraction voltage below 5kV has, however, a detrimental effect on the beam intensity that can be extracted from the ion source. Therefore, to extract sufficient beam current from the source the extraction voltage has to remain above 5kV with the consequence that the injection energy into the accelerator is too high. Working with a higher extraction voltage than required for injection into the accelerator implies that the voltage on the gap lens has to be increased to give the correct beam focus at injection, but this would increase the injection energy even further. With much too high injection energy the beam is no longer properly focused in the accelerator. This is the reason for the poor beam transmission through the accelerator and also why the beam at the exit of the accelerator is also not properly matched to the beam line.

5.5.3 IMPROVEMENT OF BEAM TRANSMISSION THROUGH THE ACCELERATOR AT TERMINAL VOLTAGES BELOW 3 MV AND ENHANCEMENT OF THE BEAM CURRENT

To solve the problem of the injection energy into the accelerator a method is needed with which the injection energy can be adjusted, preferably without varying the beam focus in the terminal section. For this an additional focusing element is needed in the terminal section. By installing an additional focusing element close to the gap lens this additional lens can fulfill the focusing

properties of the gap lens and the gap lens together with the extraction voltage can then be used to adjust the injection energy of the beam at the entrance to the accelerator. Although the gap lens would still have some influence on the focusing this could easily be corrected by adjustment of the focal strength of the additional einzel lens.

With the present layout of the terminal section extensive changes have to be made to install an additional lens. To solve this problem with the minimum interruption to the normal operating schedule the possibility of using some of the buncher electrodes as an additional lens has been investigated. The buncher consists of three electrodes. The alternating voltage for acceleration of pulsed beams is applied to the central electrode. The first electrode is at ground potential. An additional einzel lens can be implemented by using the first electrode of the buncher as the central electrode of an einzel lens. The collimator that follows the Wien filter could be the first electrode of the einzel lens and the central electrode of the buncher the third electrode of the einzel lens. The position of the additional einzel length is shown in figure 5.2.

With this configuration of the additional einzel lens a large number of beam envelopes have been calculated. These calculations show that the injection energy as well as the focusing can be adjusted independently. Figures 5.10 and 5.11 show beam envelopes from the ion source to the exit of the accelerator for different extraction voltages of the ion source, as calculated with the program TOSCA, are numbered 1-6 correspond to initial divergence values ranging from 20 to 2mrad, respectively. A, B, C and D indicate einzel lens 1, the additional lens, the gap lens and einzel lens 2, respectively. The beam width and the focusing condition of the beam at the exit of the accelerator agree very well with the measured beam profile. The results are in agreement with those calculated with the program TRANSPORT. The beam profiles through the accelerator in the two cases are practically the same because the injection energy into the accelerator is scaled according to the energy of the accelerator and the focusing condition at injection into the accelerator is practically the same for both cases. The injection energy was matched by using the gap lens and the focusing at injection was matched by using the additional einzel lens. With this additional lens it is now possible to increase the extraction voltage to a value that extracts sufficient beam intensity from the ion source and while the injection energy and the focus of the beam remain matched to the accelerator.

5.5.4 RESULTS OF MEASUREMENTS

An additional high voltage power supply was installed in the high-voltage terminal, where space is severely limited, to implement the additional einzel lens. The first measurements

with the additional lens gave a huge increase in the beam current and also a well-matched beam at the exit of the accelerator. The first measurements with the additional lens yielded a factor two increase in the beam current as well as a well-matched beam at the exit of the accelerator. The beam brightness increased by a factor of more than three to a maximum value of 26 pA/($\mu m^2 mrad^2 MeV$) for a beam intensity of 700 pA and typical settings of the microprobe and spot size of 2-3 μm. This is a factor more than 3 to 4 increase in beam intensity. In the future it will be possible to increase the beam current at the exit of the accelerator even further by operating the accelerator with higher extraction voltages. At the moment it is, however, not possible because the output of the power supply of the additional einzel lens is limited to only 3 kV and it is running close to its maximum value. In the near future, middle of 2005, the power supply will be upgraded to 6 kV, at which operation with higher extraction voltages, and therefore higher beam intensities from the ion source, will be possible. The beam current delivered by the accelerator will also improve.

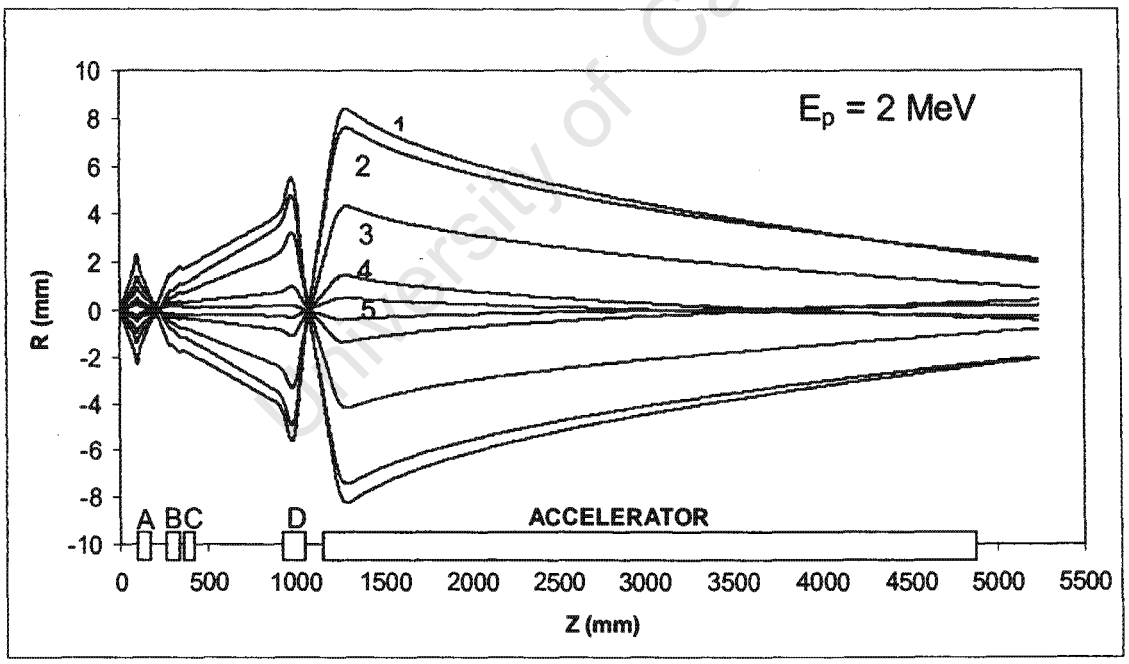

Figure 5.10: The beam envelopes from the ion source to the exit accelerator, as calculated with the program TOSCA, are numbered 1-5 correspond to initial divergence values ranging from 20 to 2mrad, respectively. A, B, C, and D indicate einzel lens 1, the additional lens, the gap lens and einzel lens 2, respectively. The effect of the additional lens B can clearly been seen. The beam width and the focusing condition of the beam at the exit of the accelerator agree very well with the measured beam profile. The beam energy is 2 MeV at the exit of the accelerator

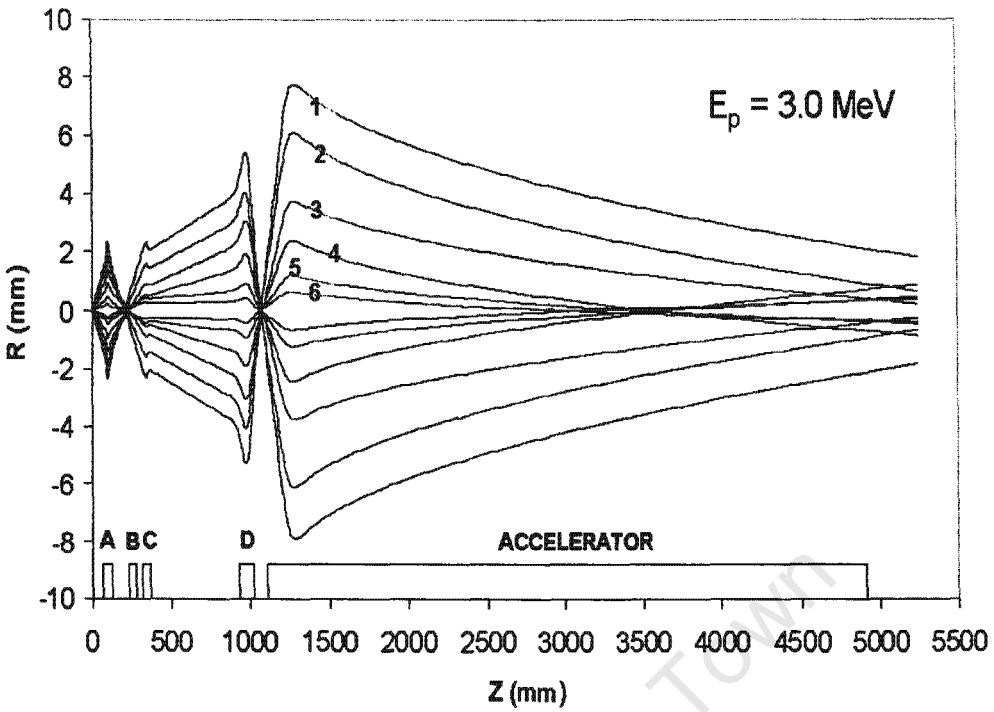

Figure 5.11: The beam envelopes from the ion source to the exit accelerator, as calculated with the program TOSCA, are numbered 1-6 correspond to initial divergence values ranging from 20 to 2mrad, respectively. A, B, C, and D indicate einzel lens 1, the additional lens, the gap lens and einzel lens 2, respectively. The additional lens B is not switched on. The effect of the additional lens B can clearly be seen. The beam width and the focusing condition of the beam at the exit of the accelerator agree very well with the measured beam profile. The beam energy at the end of the accelerator is 3 MeV

Beam tuning in the accelerator is now much less time-consuming, due to the fact that the focusing of the beam and the injection energy of the beam is decoupled. In the past when the gap lens was set for the focusing the injection energy change and thus all the elements in the terminal section that follow the gap lens have to be changed to compensate for the change in energy. With the present lens configuration the gap lens and the extraction voltage are adjusted for the required injection energy. Thereafter the additional einzel lens and einzel lens two are adjusted to match the beam to the accelerator. This is a much faster procedure than in the past. Since twice as much beam as in the past is now available it is no longer necessary to fine tune the machine for hours on end to obtain sufficient beam intensity. Even with the focusing and steering elements not properly set up the intensity gain is still more than 50% compared to what it used to be in the past. The setup time has therefore also been reduced since fine-tuning of the optical elements is no longer necessary to achieve the required beam intensity.

6. CONCLUSIONS

The dimensions of the electrodes and the distances between them were measured and documented for calculation of the beam optical characteristics of the accelerator. Different computer programs have been used for these calculations from the ion source through the terminal section, the accelerator and beam line up to the Nuclear Microprobe (NMP). The results obtained with the computer programs IGUN, which includes space-charge effects, and TOSCA yielded similar results for the beam optics in the terminal section and compared very well with the experimentally determined optimum voltages on the different lenses. The computer program TRANSPORT is, however, not suitable for accurate calculation of beam profiles through complex electrostatic lenses, because no provision is made in the program for different lens shapes. The only parameters that can be specified in TRANSPORT are the voltage and the gap widths between the different sections of a lens. However, if the beam envelope is known from calculations with the programs TOSCA or IGUN, the gap sizes of the different lenses can be adapted to yield the same beam envelope with TRANSPORT as obtained with TOSCA and IGUN. With these modified gap sizes known further calculations for different energies and lens settings can be done with TRANSPORT, which is easier and faster to use.

Once the beam characteristics from the ion source through the accelerator could be calculated accurately and were fully understood, the problems experienced in the past with poor beam transmission below terminal voltages of 3 MV and the limitation of the maximum extraction voltage to 5 kV could be explained. A simple and complete solution to these problems was found by using existing electrodes in the terminal section, and without modifying this very complex structure, as an additional einzel lens. Higher beam currents are now available, terminal voltages below 3 MV can be used without deterioration of the beam characteristics and the voltages on the electrodes are no longer critical.

Detailed and accurate knowledge of the beam characteristics in the accelerator from the source to the exit are now available and can, together with the measured ion source characteristics discussed in the previous chapter, be used for future development work.

Chapter 6

THEORETICAL BACKGROUND ON NUCLEAR MICROPROBE APPLIED TO BIO-MEDICAL MATERIALS

6.1 INTRODUCTION

The Nuclear Microprobe (NMP) is an accelerator based technique used for elemental microanalysis, with imaging capabilities and particularly suitable for the measurement of trace elements in bio-medical tissues [Wat87, Joh95,]. World-wide in the last two decades it has been applied extensively in areas such as materials science, geology and archaeometry, and has currently found a prominent role in the biomedical sciences where a relatively high resolution probe and adequate detection limits are required [Vis84, Lla98, Pro00].

It makes use of the numerous types of prompt-emitted radiations resulting from the interaction of MeV charged particles with matter. Particle Induced X-ray Emission (PIXE), Proton Backscattering Spectrometry (p-BS), Particle Induced Gamma-ray Emission (PIGE), Nuclear Reaction Analysis (NRA), are techniques which can be simultaneously carried out using a particle microbeam. The NMP competes with many other techniques available for high-resolution characterization of materials, and therefore it has become essential to equip this instrument with the latest technologies available to stay competitive. It has also become clear that the NMP has superior performance in particular areas of application such as in biology and medicine [Mor96, Prz99, Pro00].

A major goal for research in bio-medical science over the last few decades has been to quantify the concentration of elements, particularly trace elements (TE) in human tissues. Considerable amount of research has been carried out to elucidate the effect of accumulation of certain trace elements in human organs and tissues [Lla98, Mor96,

Vis84]. Both deficiencies and excesses of the concentration of these TE may induce a wide range of pathological disorders in the human body which will detrimentally affect the standard of health as a whole. On the other hand these toxic elements are known to be harmful even at extremely low concentrations [Vis84]. For these reasons trace element analysis by ion beam techniques has become important both in medical research and as a diagnostic tool [Nur 01, Lla98, Bar96].

The nuclear microprobe, with its high sensitivity, remarkable quantitative accuracy and useful structural imaging capabilities, is at present one of the most valuable instrumental methodologies to carry on or develop new interesting cross-disciplinary between nuclear microscopy and medical studies. Research problems such as the study of kidney concretions, teeth erosion in children or hair trace elements profiling are some of the many applications where NMP allows measurements with excellent scanning capabilities, particularly for elements heavier than magnesium [Bar 96].

The NMP unit at iThemba LABS has for many years focused its research programmes on studies of biological material, ranging from applications in medicine to agriculture and botany. Recent optimization work on the VDG accelerator optic systems has improved the quality of critical physical parameters such as the aberration components of the beam pulse and therefore facilitate the increase on beam resolution at target surface (see Chap. 4 and 5). Coupled with all the improved optimal properties, the NMP globally and at Ithemba LABS in particular has become in the last decade, an established tool for a variety of applications related to the characterization of hard and soft human tissue as well as the TE variability in relation to the respective medical problematic.

A number of analytical techniques has been implemented at the NMP, iThemba LABS where highly energetic ions (H^+, H_2^+, He^+ with energy per nucleon of ~1.5 –3 MeV) are used to irradiate and characterise sample materials. These ions penetrating the target interact with orbital electrons and nuclei of the elements present in the irradiated target volume. This leads to excitation of orbital electronic shells and sub-shells (figure 6.1), which rearrange after spontaneous emission of electromagnetic radiation (X-rays, Auger electrons and light). Furthermore the ions can be backscattered by the nuclei or even

excite nuclei, which results in the emission of γ rays, X-rays and secondary particles. Since the interaction processes depend on the encountered atoms, on the structure of the sample and on the sort and energy of ions, the detection of and energy quantification of these secondary products allows the determination of the elemental content and their distribution in a sample. [But97]. The most important techniques used at Ithemba LABS will be described in the next sections below.

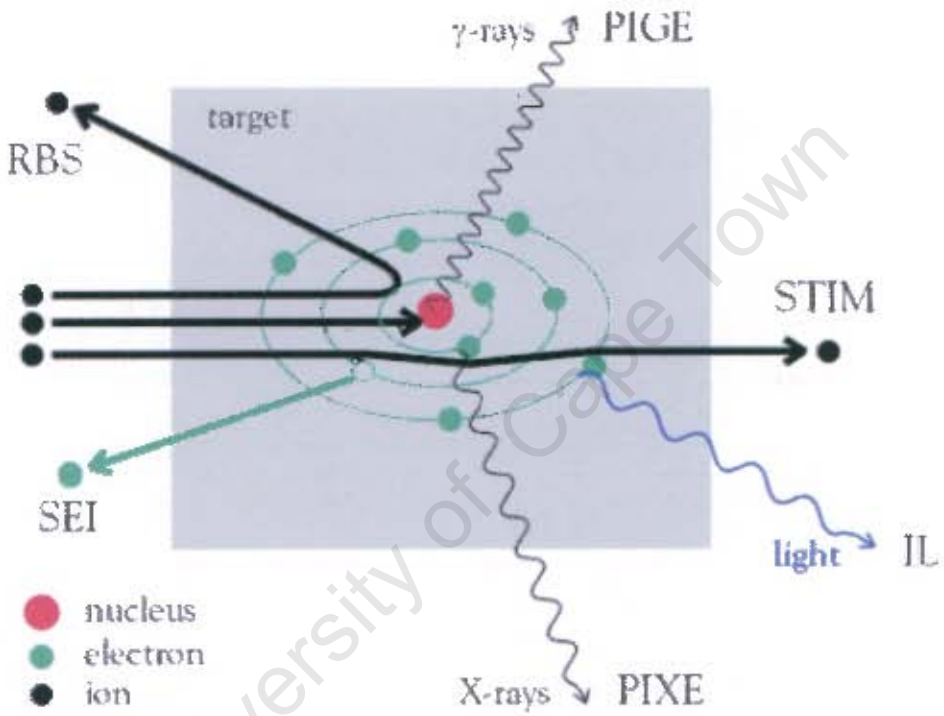

Figure (6.1) Schematic illustration of the origin of the **Ion Beam Analytical Methods**. Proton Induced Gamma-ray Emission (PIGE), Rutherforford Backscattering (RBS), Proton Induced X-ray Emission (PIXE), Scanning Transmission Ion Microscopy (STIM), Scanning Electron Imaging (SEI), and Ionoluminescence (IL) [But97]

6.2. PARTICLE-INDUCED X-RAY EMISSION (PIXE)

PIXE is an analytical method based on atomic physics principles. The specimen to be analyzed is irradiated by accelerated, charged particles (ie. protons). Characteristic X-rays are produced by the creation of vacancies in the inner electron shells, followed by

the subsequent filling of those vacancies by the less tightly bound electrons from outer shells. Since the energy of the X-rays is equal to the energy difference between binding energies of the electrons in the two shells, each element has a set of characteristic X-rays which are energetically unique. These can be analyzed with the aid of a suitable energy-dispersive spectrometer system [Joh95]. Electron vacancies in atoms can be generated with photons, X-ray Fluorescence (XRF), or with charged particles (PIXE). Several books about the theory and practice of the PIXE principles are available in the literature [Joh88, Joh95].

Protons emerging from the Van de Graaff accelerator are injected into the beamline through an analyzing magnet and then directed horizontally over a distance of several meters to the specimen chamber by simple magnetic or electrostatic dipole steering elements (refer to Chapter 1-5 for more detailed information). A very important aspect of PIXE is the sensitivity that can be achieved under normal routine operating conditions. The main limitation of its sensitivity is the amount of background (secondary electron and bremsstrahlung) interfering with the characteristic X-ray lines.

There are a number of significant sources of background, which contribute to the experimental background. The projectile bremsstrahlung arises from scattering with nuclei in the target and contributes a fairly uniform flat background over the whole energy range of the X-ray spectrum. Moreover the intensity of this background is lower than for an electron beam by about six orders of magnitude [Wat87]. The PIXE method has the advantage that it is multielemental and yields results for a wide range of elements in a single irradiation. The simplest case is that of a thin film, in which matrix effects are negligible.

6.2.1. THICK TARGET PIXE (TTPIXE)

The application of PIXE for the determination of elemental composition in thick target materials is often referred to as thick target PIXE (TTPIXE). As for thin films, most of the advantages are retained for thick targets. However, heat-sensitive specimens may be damaged during irradiation and the detection limits for some elements may be

detrimentally affected, due to the intense low energy background generated by fast secondary electrons. The methodology of TTPIXE used in the macro-mode can equally be applied in the micro-mode. However, even though the principles of the technique are applicable in both environments, some effects, often neglected in the macro-mode using unfocused ion beams, can determine the accuracy in the micro-mode [Pei87, Pin92, Cam90, Joh95], in particular the problem of pile-up and sum peaks.

Several ways to deal with this exist but the most popular is the use of electron suppression ring (applied voltage of -1500 V) with carbon coating of the surface specimen. With this in mind the quantitative evaluation of the elemental X-ray yields and concentrations in a thick-target requires a very good understanding and knowledge of the matrix composition under investigation. In order to better understand the quantification of elemental concentrations in TTPIXE the evaluation of the simpler thin-target case algorithm will be described followed by the full description of the thick target case.

A thin material is defined as one in which the energy loss of a bombarding proton beam is negligible. The X-ray yield, $Y_o(Z)$ (in counts per second), for an element with atomic number Z and atomic mass A_z, in a thin film of areal density $M_a(Z)$ (in $\mu g.cm^{-2}$), bombarded with proton beams of energy E_0 (in MeV) is given by

$$Y_0(Z) = N_p M_a(Z)\sigma_I(Z,E)\omega_z b_z \varepsilon_z N_A \Omega T / A_z \qquad (6.1)$$

Where,

N_p is the bombarding current (in protons per second),

$\sigma_I(Z,E)$ is the ionization cross section of element Z, at energy E,

ω_z is the fluorescence yield,

b_z is the branching ratio,

ε_z is the detection efficiency for the measured X-rays,

N_A is the Avogadro's number,

Ω is the solid angle subtended by the detector,

T is the transmission fraction with $T = e^{-\mu_T \cdot X}$; μ_T is the total mass attenuation coefficient and X is the depth within the target from which the X-ray line originate.

If we define the constant factor k(Z) which includes geometrical factors and yield constants, by:

$$k(Z) = \omega_z b_z \varepsilon_z N_A \Omega / A_z \qquad (6.2)$$

then

$$Y_0(Z) = N_p M_a(Z) k(Z) \sigma_I(Z,E) T \qquad (6.3)$$

T is the transmission factor and has the value of unity when there is no absorption of the measured X-ray within the target material. Table (6.1) shows the transmission fractions for the K_α line of elements with $20 \leq Z \leq 38$ through an Al (102 μm) and a Be (125 μm) absorbers, which are the most frequently used in this work. The K-shell ionization cross sections for 3.0 MeV protons are also shown to emphasise the excitation function of lighter elements which are absorbed by the two different absorbing materials. Similarly values for the mentioned parameters of the L-shell are presented for lead. The transmission factors even for proton energy loss of few hundredth of keV from lighter elements such as Ca to Cr, is still significant.

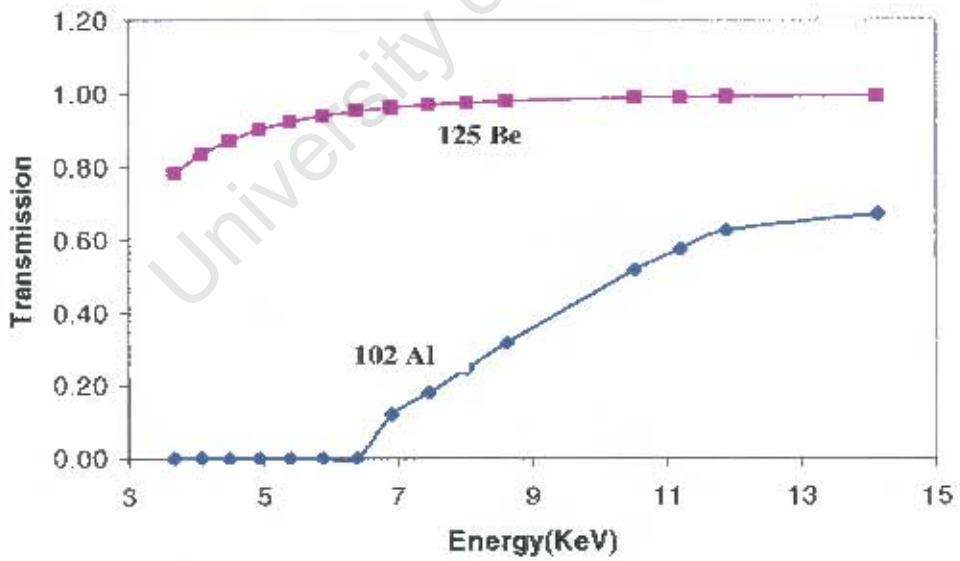

Figure(6.2) Relationship between the transmission fraction and the energy of K_α X-rays for elements with $20 \leq Z \leq 38$ going through Al (102 μm) and Be (125 μm) absorbers. Note that although the threshold for X-ray transmission occurs at ~6 keV elements with X-ray energies lower than this value may be detected at appropriate beam currents.

Figure (6.2) shows the relation between the excitation energy and the absorption due to 102 μm Al and 125 μm Be absorbers. Note that although the threshold for X-ray transmission occurs at ~6 keV, elements with X-ray energies lower than this value may be detected at appropriate beam current rates. For a finite thin target, in which the bombarding beam losses a small amount of energy, and the X-ray production cross section undergoes a variation of only a few percent, the final energy, E_f, is approximately the same as the initial energy E_0 (the bombarding energy).

Table (6.1): Transmission factors (in %) for the K_α line of elements with $20 \leq Z \leq 38$ through Al (102 μm) and a Be (125 μm) absorbers. The K-shell ionization cross sections for 3.0 MeV protons are shown as well to emphasise the excitation function of lighter elements which are absorbed by the two different absorbing materials. Similarly values for the mentioned parameters of the L-shell are presented for lead.

Z	A_Z	K_α (keV)	Transmission Fraction[a]		$\sigma_E(Z)$ (Barns)[b] (Ep=3.0 MeV) (at the surface)
			Al (102 μm)	Be (125 μm)	
Ca	20	3.69	4.621×10^{-6}	0.79	2.978×10^{3}
Sc	21	4.09	9.796×10^{-5}	0.84	2.178×10^{3}
Ti	22	4.51	8.862×10^{-4}	0.88	1.614×10^{3}
V	23	4.95	4.441×10^{-3}	0.90	1.197×10^{3}
Cr	24	5.41	1.464×10^{-2}	0.92	8.921×10^{2}
Mn	25	5.89	3.589×10^{-3}	0.94	6.672×10^{2}
Fe	26	6.39	7.091×10-2	0.95	5.022×10^{2}
Co	27	6.92	0.12	0.96	3.796×10^{2}
Ni	28	7.47	0.18	0.97	2.879×10^{2}
Cu	29	8.04	0.25	0.98	2.196×10^{2}
Zn	30	8.63	0.32	0.98	1.676×10^{2}
As	33	10.53	0.52	0.99	7.593×10^{1}
Se	34	11.20	0.57	0.99	5.878×10^{1}
Br	35	11.90	0.63	0.99	4.569×10^{1}
Sr	38	14.13	0.67	0.995	2.184×10^{1}
PbL_α	82	10.50[c]	0.52	0.993	1.377×10^{1}

a. Values were calculated with by the subroutine ABSCO, GeoPIXE [Rya90b].
b. Cross-sections values are taken from [Coh85].
c. Value for the L_α X-ray line of Pb.

In this case the areal density can be re-defined as $\rho(Z)dx$ where $\rho(Z)$ is the density of the element Z in the sample and dx can be considered as the thickness of an infinitesimal layer of the target material, i.e. $E_f \simeq E_0$ and $M_\alpha(Z) = \rho(Z)dx$

In the portion of its path from depth x_i to $x_i + dx_i$ the proton energy falls from E_i to $E_i - dE_i$ and the relationship between x_i and E_i is

$$x_i = \int_{E_0}^{E_i} \frac{dE}{\rho S(E)} \tag{6.4}$$

Where $S(E)$ is the matrix stopping power in eV per unit thickness and ρ_i is the total target density.

By definition $\frac{\rho(Z)}{\rho}$ is the trace element concentration C_z. Then the mass of the trace element per unit area in the slice $(x_i, x_i + dx)$ is,

$$\rho(Z)dx = C_z \frac{dE}{S(E)} \tag{6.5}$$

Now equation 6.3 can be written as:

$$Y_0(Z) = N_p k(Z)\, \sigma_I(E_0, Z)\, C_z \frac{dE}{S(E)} T \tag{6.6}$$

For any layer, i, of thickness ΔE_i, in a thick target, the yield of X-rays from element Z is given by

$$Y_i(Z) = N_p k(Z)\, \sigma_I(E_i, Z)\; T(E_i) C_z \frac{\Delta E}{S(E)} \tag{6.7}$$

where $T(E_i)$ is the absorption from a depth x_i of the matrix.

The thick target material may be considered as consisting of n layers, in each of which the bombarding beam loses an equal amount of energy, ΔE, and in which the mean energy, E_i is considered to be constant over the entire layer. Then the total X-ray yield for element Z resulting from the generation of X-rays from all the n layers is equal to

$$Y(Z) = N_p k(Z) C_z \frac{E_0}{n} \sum_{i=1}^{n} \sigma_I(E_i, Z) \frac{T(E_i)}{S(E)} \tag{6.8}$$

This summation can be converted to:

$$Y(Z) = N_p k(Z) C_z \int_{E_0}^{0} \sigma_I(E_i, Z) \frac{T(E_i)}{S(E)} dE \qquad (6.9)$$

Multiplying and dividing by the ionisation cross section at the surface $\sigma(E_0, Z)$ which is approximately constant then the X-ray yield can be expressed in terms of a unitless relative ionization cross section $\sigma_R(E, Z)$,

$$Y(Z) = N_p K(Z) C_z \int_{E_0}^{0} \frac{\sigma_R(E, Z) T(E)}{S(E)} dE \qquad (6.10)$$

Where $K(Z) = k(Z)\sigma(E_0, Z)$ is known as the geometrical factor or sensitivity factor which determine the level of sensitivity of the PIXE detection system. Its variation with X-ray energy and for different proton energy is shown in Fig. 6.3. The maxima at 1,2,3 and 4 MeV occur for X-ray energies which correspond to Ti, Cr, Mn and Fe respectively. Equation 6.10 can also be written as,

$$Y(Z) = N_p K(Z) C_z I(Z) \qquad (6.11)$$

Where $I(Z)$ is the integral dependent on the matrix type of the sample material and denotes a matrix correction factor (MCF) for the yield Y in *thick targets.* [Pin92].

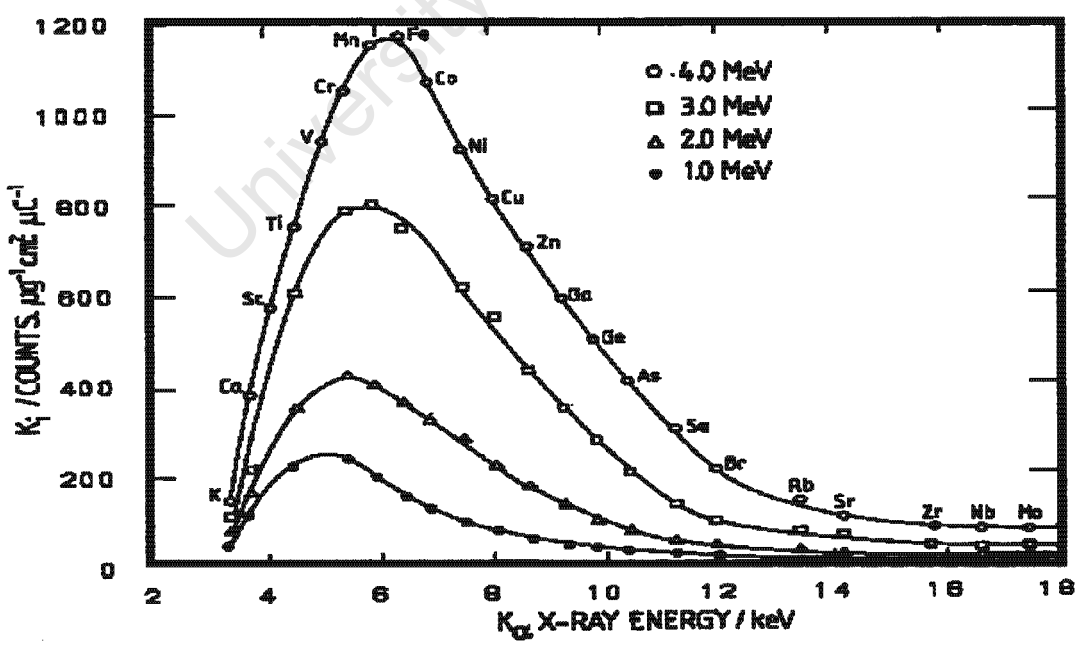

Figure 6.3 The variation with the energy of K_α X-rays of the sensitivity factors, K(Z) for proton bombarding energies of 1,2,3 and 4 MeV [Pin92].

Writing the inverse function of $I(Z)$ as $F(Z) = I(Z)^{-1}$, the plotted values of these inverse MCF as a function of X-ray energy for each element with $20 < Z < 56$ and for different proton bombarding energies are shown in Fig. 6.4. It should be noted that the corrections due to matrix effects increase rapidly for light elements (ex: Na, Mg, Al), making it more difficult to quantify such elements. This has to be taken into consideration for the estimation of concentration errors (see section 6.2.3) which is heavily dependent on theoretical databases.

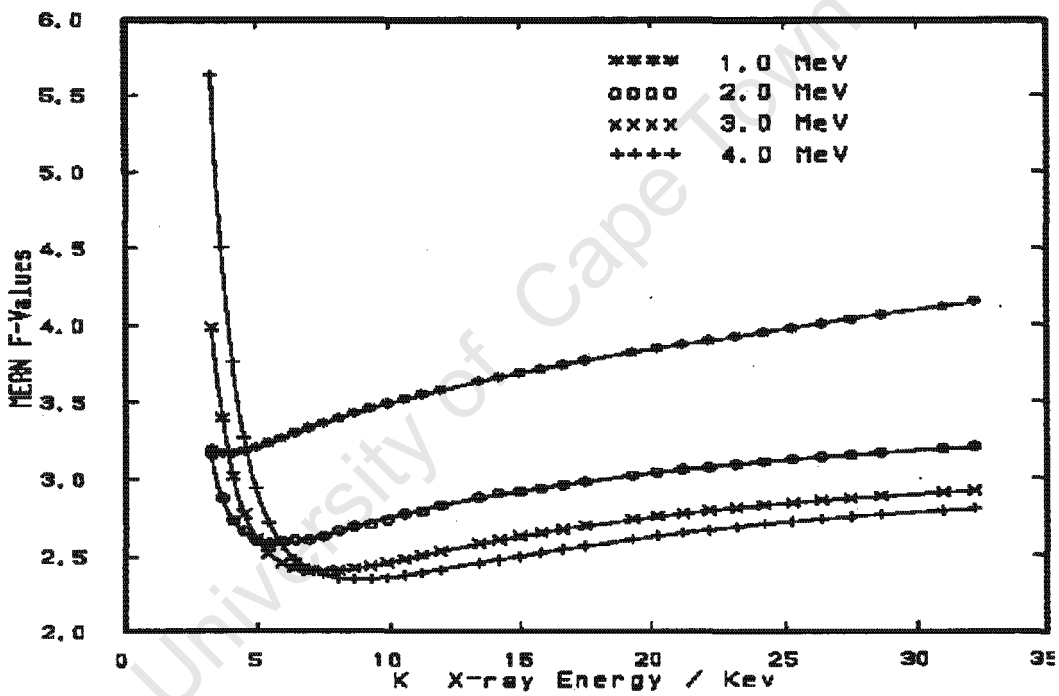

Figure 6.4 The variation of F(Z)-values with the K_α X-ray energy for the bombardment of carbon-rich materials with protons between 1 and 4 MeV [Pin92].

6.2.2 SOFTWARE FOR EVALUATION OF PIXE SPECTRA

There are several computer codes available world-wide for the evaluation of PIXE spectra from which GUPIX [Cam00] and GeoPIXE [Rya90b, Rya02a] are the two most commonly used at international laboratories. The first generation of the GeoPIXE algorithm was released on 1990 [Rya90b]. This version was implemented for use with the

VMS Digital MicroComputer platform at iThemba LABS [Chu93], with a windows-like GUI. The basic databases for physical parameters required for calculations were stored as polynomial as well as direct interpolation from data tables. The exclusive need for VMS platform was a limiting factor, although the software was applicable to online analysis as well as event by event mode. The GeoPIXE code has three main sub-programs (see Fig. 6.5): 1) FLASH, is an interactive spectrum display and manipulation program; 2) PIXE_FIT is a batch mode PIXE spectrum fitting program; 3) LAYER, perform the X-ray yield calculation by integrating X-ray production over the path of the proton beam.

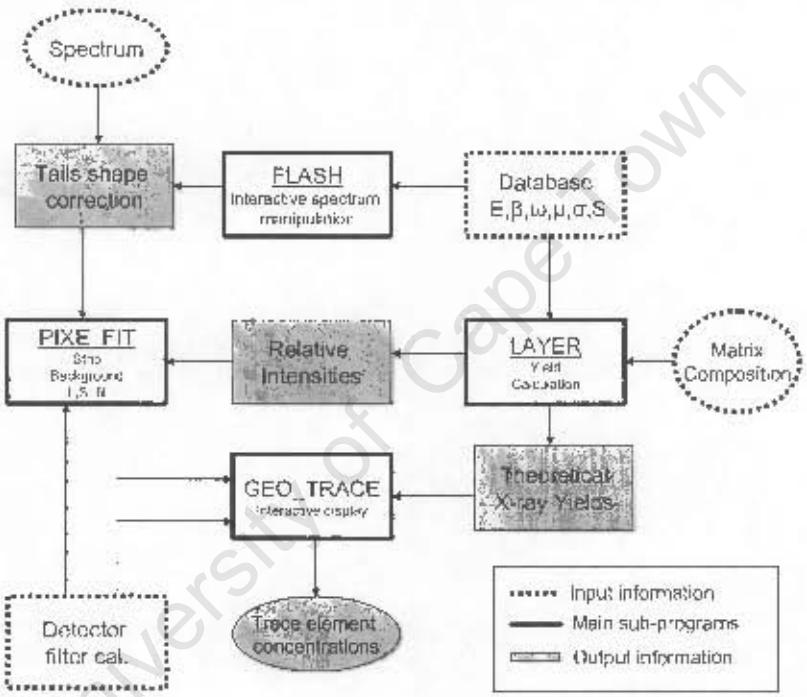

Figure 6.5: Flow of data manipulation through the GeoPIXE code. Basic input information: databases, initial matrix composition and spectrum data, are used by the main sub-programs, LAYER, PIXE-FIT and FLASH. Final report of elemental concentration is given by GEO_TRACE (diagram modified from original [Ray90b]).

Includes self-absorption and secondary fluorescence effects and can treat multilayered targets. A unique feature of GeoPIXE is that X-ray yields are precalculated for every X-ray line of K and L shells. Up to 16 L lines and 9 K lines are treated.

Since elemental concentrations evaluation in GeoPIXE depends heavily on theoretical and experimental values for physical parameters, databases quality-values for these

parameters have to be acceptable. GeoPIXE build-in database-sources for most relevant parameters are: 1) stopping power *S(E)* parametrisation by [And77]; mass attenuation coefficients μ_T by [Thi67]; X-ray production cross sections expressed in terms of the ECPSSR ionization cross sections by [Coh85]; fluorescence yields ω_z by [Kra79]; branching ratios b_z by [Sal74] for K lines and relative intensities [Coh86, Coh87] for the case of L lines. A detailed discussion on the accuracy of these parameters will be given in section 6.2.4.

An initial pass PIXE data analysis approach is used which usually incorporates the major element composition of the sample determined by Electron microprobe (EMP) prior to NMP analysis. This composition can be used as a first approximation for the matrix composition and later optimized by software iteration. Furthermore this optimized composition is used to calculate the correct X-ray yields and relative intensities of all the X-ray lines required for all pre-determined elements (see Fig. 6.5). In cases where self-absorption and secondary fluorescence are not severe, a representative composition is used to calculate yields for the analysis of sample materials of similar composition. The calculated relative intensities are used in the least square fit to deconvolute the spectrum. The most important feature of this deconvolution is the use of a fixed background evaluated from the same spectrum using the Statistical Non-linear Iterative Peak-clipping (SNIP) algorithm [Rya90a]. This background treatment takes particular care to treat statistical fluctuations to provide a reliable approximation of the continuum background under peaks, even in regions of the spectrum with low counts. [Rya90a].

A new generation of the software package; GeoPIXE II [Rya02b] has been released for quantitative PIXE image and analysis using the dynamic analysis (DA) method [Rya93]. This algorithm is written on the IDL language, with more flexibility for usage in different platforms. It provides sorting of list-mode (event-by-event) data, projection of quantitative images, extraction of concentration averages and line projections from arbitrary regions, correction for various spatial matrix effects, and export and reporting options for different users systems. Basically GeoPIXE II [Rya02b] is similar to the first version [Rya90a] as far as the flow structure of the algorithm. It calculates X-ray relative intensities in a similar way following the data flow shown in Fig. 6.5. The strength of GeoPIXE II depends on the user-friendly interface as well as a flexible environment for

PIXE spectra analyses, generation of elemental maps using the DA method and image display and output into various formats. An additional bonus is the ability to extract quantitative data from elemental maps interactively. More detail information about the operation of GeoPIXE II can be found in [Rya02b].

6.2.2.1 THE DYNAMIC ANALYSIS METHOD

Before 1993 traditional PIXE deconvolution software at iThemba LABS worked on analysis performed in single point and/or scanning mode without continuous feedback and evaluation of elemental maps based on energy gates on selected X-ray lines. Spectra were evaluated off-line usually relaying on SRM. The introduction of GeoPIXE solved the problem of continuity and Dynamic Analysis (DA) solved the problem of peak-to-peak interference due to the use of energy gating [Rya93]. The DA scheme performed spectrum decomposition in live time that provides a good approximation to a nonlinear least-squares fit (LSF) treatment as the data accumulate [Rya93]. Next section 6.2.2.2 below will describe the formalism of DA.

The GeoPIXE sub-routine PIXE-FIT generates a dynamic analysis transform matrix. This enables the projection of list-mode, or event-by-event data (EVT data files) directly onto quantitative elemental images. This process resolves element overlaps, strongly rejecting artifacts from overlapping elements and detector response effects (escape peaks, tails and pile up). The results are quantitative images in ppm. μC units. Furthermore, GeoPIXE II accumulates concentration variance images (at half resolution to minimize memory usage), so that error estimates and detection limits can be provided for all extracted concentration values and line profile projections [Rya02a].

6.2.2.2 DYNAMIC ANALYSIS FORMALISM

The quantitative analysis of a typical PIXE spectrum involves fitting the spectrum with an analytical function $f(i;a)$ that includes terms representing the line-shape contributions for each element, including detector artifacts, plus a background term . In general, this formulation is nonlinear in the adjustable parameters a_k in the vector $\boldsymbol{a}$, which are obtained iteratively by varying **a** until χ^2 is minimized. If the function is linear in its

parameters, or if the nonlinear parameters have converged in prior nonlinear iterations and can be fixed, then a linear least-squares treatment can be used.

The condition of χ^2 minimum in a linear-squares fit to a PIXE spectrum, viz. $\frac{\partial \chi^2}{\partial a_k}=0$ for all a_k, leads to values of the a_k at the minimum satisfying the equations

$$\sum\sum w_i(\partial f_i/\partial a_j)(\partial f_i/\partial a_k)a_k = \sum_i wi(\partial f_i/\partial a_j)S_i \qquad (6.12)$$

Here, $f = f(i;\ \boldsymbol{a})$, S_i is the channel count and w_i is the statistical weight at each channel i, where i spans the fitted channel range of the spectrum. The parameters a_k represent the peak-area of the major X-ray line for each element and the strength of the background term. This can be cast as the matrix equation

$$\boldsymbol{\alpha a} = \boldsymbol{\beta S} \qquad (6.13)$$

in terms of the spectrum vector $\boldsymbol{S}$ and the matrices α and β, with elements given by

$$\alpha_{jk} = \sum_i w_i^{-1}\beta_{ji}\beta_{ki} \qquad (6.14)$$

$$\beta_{ji} = w_i(\partial f_i/\partial a_j) \qquad (6.15)$$

Inverting $\boldsymbol{\alpha}$ yields the vector $\boldsymbol{a}$

$$\boldsymbol{a} = \boldsymbol{\alpha}^{-1}\boldsymbol{\beta S} \qquad (6.16)$$

The parameter a_k, representing the major-line peak-area for element k, is related to C_k, the concentration of element k, by the equation

$$a_k = Q\Omega\varepsilon_k T_k Y_k C_k \qquad (6.17)$$

Here, Q is the integrated beam charge, Ω and ε_k are the detector solid-angle and efficiency, T_k is the filter transmission, and Y_k is the PIXE yield per ppm of element k, per unit charge and detector solid-angle. Combining Equations. (6.16) and (6.17) yields a matrix equation for the vector $\boldsymbol{C}$,

$$\boldsymbol{C} = Q^{-1}\Gamma\boldsymbol{S} \qquad (6.18)$$

In terms of a matrix Γ. The elements of Γ are given by

$$\Gamma_{ki} = (\Omega\varepsilon_k T_k Y_k)^{-1}\sum_j \alpha^{-1}{}_{kj}\beta_{ji} \qquad (6.19)$$

Eq. (6.18) is a matrix equation which transforms directly from spectrum vector $\boldsymbol{S}$ to concentration vector $\boldsymbol{C}$ [Rya93].

The Γ matrix is calculated using the least-squares fit program PIXE_FIT (see Fig 6.5). The assumption is made that the matrix Γ, is precalculated using a representative *master spectrum* to set the statistical weights for each X-ray line, and can be used to interpret spectra with varying peak areas. These on-line calculation for each PIXE spectrum per pixel take about 2 seconds [Rya90b, Rya95].

6.2.2.3 OVERLAP-RESOLVED ELEMENTAL IMAGING

Events are processed as (*e*, x, y) triplets, where *e* is the channel number of the detected event in the X-ray detector pre-amplifier and (x,y) are the coordinates of event *e*. Equa. 6.18 therefore, permit the calculation of on-line elemental imaging data. For each pixel the instantaneous charge Q is collected and mapping data is normalized to this value. For every scanning pass the contribution of each element is stored and this increment is added to the total concentration at each pixel. In this way elemental distribution images can be generated which are: 1) inherently element overlap-resolved and background-substracted; 2) quantitative to within a small yield correction (see discussion in next section); 3) and images are formed directly as data accumulate [GeoPIXE, Rya95]. In other words each image is a close representation of the distribution of a single element, free of artifacts created by element overlaps, tails, escape peaks and background. With the modern version GeoPIXE II, the above imaging evaluation is less cumbersome since re-construction of imaging can be performed off-line on list mode files [Rya02a].

6.2.3. ACCURACY OF THE TTPIXE TECHNIQUE

The development of modern computer codes for the quasi-quantitative deconvolution of PIXE spectra generated much interest on standardless techniques in which the mathematical process of calculation of elemental concentrations depend heavily on the accurate knowledge of physical parameters involved in Equation 6.10 [Max89, Rya90b]. From all these parameters ($\sigma_i(E_i,Z)$, *S(E)*, μ_T, ω_z, b_z) the ionization cross section is the most critical. While theoretical X-ray relative intensities obtained (by PIXE_FIT) using

the known databases for those parameters (see section 6.2.3), for each element and every X-ray line, discrepancies may occur between the theoretical and experimental values. These variations from the experimental values may lead to errors of up to ~10^3 ppm for certain elements [Rya90b].

GeoPIXE' main task is to recalculate X-ray relative intensities to reflect a close approximation according to matrix effects due to the real specimen under investigation. There are however small residual systematic errors originating from uncertainties in all databases. As pointed out in section 6.2.1 the uncertainty in values of physical parameters may influence the final accuracy in the calculation of elemental concentrations by PIXE. On the other hand, additional experimental sources of possible error such as measurement of dead time, current integration and electronic background noise, could affect the final accuracy. An overview of the magnitude of error for all these parameters is shown in Table 6.2 with a reference to the respective databases from literature used in the code GeoPIXE [Rya90a, Rya02a].

It was pointed out that the accuracy of standardless PIXE analysis in mineral grains is of the order of 9% (STD) using a digital current integration [Rya90a]. However by using a chopper as current integration system the accuracy was reduced to 3% (STD) [Rya90a]. Current integration at the iThemba NMP facility uses a current digitizer CD1010 [EGG82] which according to our records has a accuracy ot 10^{-14} for pA levels.

Quantitative elemental imaging (on-line) is defined to indicate an image that is free from artifacts and accurate to within ~10% [Rya95]. However the new version GeoPIXE II has an additional sub-program to correct for spatial variability of matrix composition that has an influence in reducing the uncertainty due to wrong assumption of localized matrix composition [Rya02a].

The parameters for counting efficiency have to be measured or at least known from detectors manufactures for standard Si(Li) and/or HpInt(Ge) detectors. These values may be included in the software package available see Table 7.2 for more details. Of importance are specific details related to Si dead layers, Au contact and ice layer which may be develop during the course of several month depending on the type of application. In particular, work related to analysis where a cool environment in vacuum prevails,

Table 6.2: Overview of the estimated uncertainties for physical parameters, which influence the accuracy for different procedures involved in the calculation of elemental concentrations by the first version of GeoPIXE [Rya90b].

PROCEDURE	Type of Parameter	Symbol	Value (%)	Ref:
Type I: Systematic				
• Theoretical & Experimental relative intensities calculation: PIXE_FIT • Generic X-ray Yields • Tails shape & background corrections • LSF by PIXE_FIT • Calculation of final concentrations by GEO_TRACE	Ionization cross sections	σ_I	~10%	[Coh85]
	Fluorescence Yields	ω_z	1-2%	[Kra79]
	Branching ratios	b_z	<2%[a]	[Sal74]
	Mass Absorption coefficients	μ_z	2-5%	[Thi67]
	Stopping power	$S(E)$	~1%	[And77]
Type II: Experimental				
• Theoretical & Experimental detector definition • Calibration of absorber thickness • Integration of current at pA level • Electronic noise	Detector efficiency	ε_z	~3%[b]	[Rya02b]
	Detector solid state	Ω	~3%	
	Matrix composition	MS[c]	~5%	
	Total charge at each pixel	Q	~0.2%[d]	[EGG82]
	Dead time measurement	Δt	~1%[e]	

[a] Estimated value for K_α/K_β
[b] X-ray with energies above 3.5 keV
[c] For the initial calibration of master spectrum (MS) as determined by EMP or other technique
[d] pA range
[e] At count rates ~1 KHz

effort should be may to prevent the formation of ice layer on the surface of the Be window detector.

Besides the above parameters the correct solid angle should be determined from SRM data. This procedure combined with the knowledge of the X-ray absorber used for analysis should be characterized with absolute accuracy. See Table 7.2 for details of absorbers used at iThemba LABS NMP facility.

6.3 RUTHERFORD BACK SCATTERING (RBS) WITH PROTONS

When a target material is bombarded by protons of energy E_p, energy loss during collisions with nuclei may always occur. These collisions can be elastic (Rutherford) or inelastic (Non-Rutherford) depending on the proton energy as well as on the Coulomb threshold for each atom-nuclei. The magnitude of the proton energy loss is related to the particular atom-nuclei from which it was backscattered. In other words, energy is transferred from the moving proton to the stationary atom and the energy reduction of the scattered proton depends on the masses of both the proton and the target atoms [Leo86]. The basic analytical characteristics of proton RBS, the capability of mass, depth, and quantitative analysis, are based on the energy exchange, the slowing down of the proton in the target material, and on the scattering cross sections. The underlying fundamental principles of RBS have been discussed by several authors [Rau92] A comprehensive discussion on the RBS subject can be found in the book by [Chu78].

6.3.1 KINEMATICS OF THE ELASTIC COLLISION

Energy transfer or kinematics in elastic collisions can be solved fully by applying the principle of conservation of momentum and energy. For incident protons of energy E_0, mass M_p, velocity v_p on target atoms of mass M_a at rest, the conservation of energy and momentum parallel and perpendicular to the direction of incidence can be expressed as :

$$\tfrac{1}{2}M_p v^2 = \tfrac{1}{2}M_p v_p^2 + \tfrac{1}{2}M_a v_a^2 \qquad 6.20$$

$$M_p v = M_p v_p \cos\theta + M_a v_a \cos\phi \qquad 6.21$$

$$0 = M_p v_p \sin\theta - M_a v_a \sin\phi \qquad 6.22$$

Eliminating ϕ first and then v_a, the ratio of particle velocities is given by:

$$\frac{v}{v_p} = [\pm(M_a^2 - M_p^2 \sin^2\theta)^{1/2} + M_p \cos\theta]/(M_a + M_p) \qquad 6.23$$

The ratio of the incident proton before and after collision for $M_p < M_a$, where the plus sign applies, is

$$\frac{E_p}{E_0} = \left[\frac{(M_2^2 - M_1^2 \sin^2\theta)^{1/2} + M_1 \cos\theta}{M_1 + M_2}\right]^2 \qquad 6.24$$

this energy ratio, called the kinematic factor (KF) $K = \frac{E_p}{E_0}$, shows that the energy after scattering is determined only by the masses of proton and target atoms, and the scattering angle θ. This scattering angle at the iThemba LABS NMP geometry is currently 176^0 measured with reference to the beam path, in the backscattering direction (see figure 6.6). In such geometry, when protons of few MeV strike light elements such as C, N, P and Si, it is usually possible to resolve C from N or P from Si, even though these elements differ in mass by only about 1 amu.

However, as the mass of the atom being struck increases, a smaller portion of the projectile energy is transferred to the target during collision, and the energy of the backscattered atom asymptotically approaches the energy of the beam. It is not possible to resolve for example W from Ta, particularly when these elements are present at the same depths in the sample, even though these heavier elements also differ in mass by only about 1 amu. In general the kinematics of the collision and the scattering cross section are independent of chemical bonding, and hence backscattering measurements are insensitive to electronic configuration or chemical bonding within the target.

6.3.2 ENERGY LOSS

The energy loss of charged particles passing through matter depends on the direct energy transfer to target atom-nuclei (nuclear component), excitation or ionization of electronic

states (electronic component) and possible correlations between these two mechanisms [Rau92]. As the proton energy change inside the target material the probability for proton backscattering from an atom-nucleus as well as the magnitude of the energy exchange will decrease. Due to the slowing of charged particles, the energy loss fluctuates and the width of the proton beam energy distribution increases with penetration depth. This is called energy straggling, which affects the energy resolution of the technique. At target surface with proton velocity exciding the velocity of orbital electrons, the target-atom may be treated as a bare nucleus, stripped of all electrons. However at low proton energies, deep inside below the surface the proton is slowed down by electron capture. In the intermediate energy region no solid theoretical framework exists [Rau92]. Stopping powers cross sections and ranges for protons were compiled by [Zie85] but a more modern one, [Kon98] report values that may have a deviation for some energies and elements of the order of 7-10% [Gen05] with respect to that of [Zie85]. So care must be exercised when selecting an adequate list of stopping power data.

6.3.3 RUTHERFORD BACKSCATTERING CROSS SECTIONS

The probability (σ) to observe a proton by detector D (see Fig 6.6) after scattering, in a differential solid angle $d\Omega$ is given by

$$\frac{d\sigma}{d\Omega} = \left(\frac{Z_1 Z_2 e^2}{16\pi\varepsilon_0 E_0}\right)^2 \frac{4}{\sin^4\theta} \frac{\left[\sqrt{1-(\frac{M_1}{M_2})^2 \sin^2\theta} + \cos\theta\right]^2}{\sqrt{1-(\frac{M_1}{M_2})^2 \sin^2\theta}} \qquad (6.25)$$

where Z_1, M_1 and Z_2, M_2 are the atomic numbers and masses of the proton and atom-target respectively. E_0 is the incident proton energy. And θ is the scattering angle in the laboratory frame of reference. This Rutherford differential cross section describes the probability ratio of Coulomb interaction between the proton and the target. This interaction does not actually involve direct contact between the proton and target atom. Energy exchange occurs as a result of Coulomb repulsion forces between nuclei and incident proton.

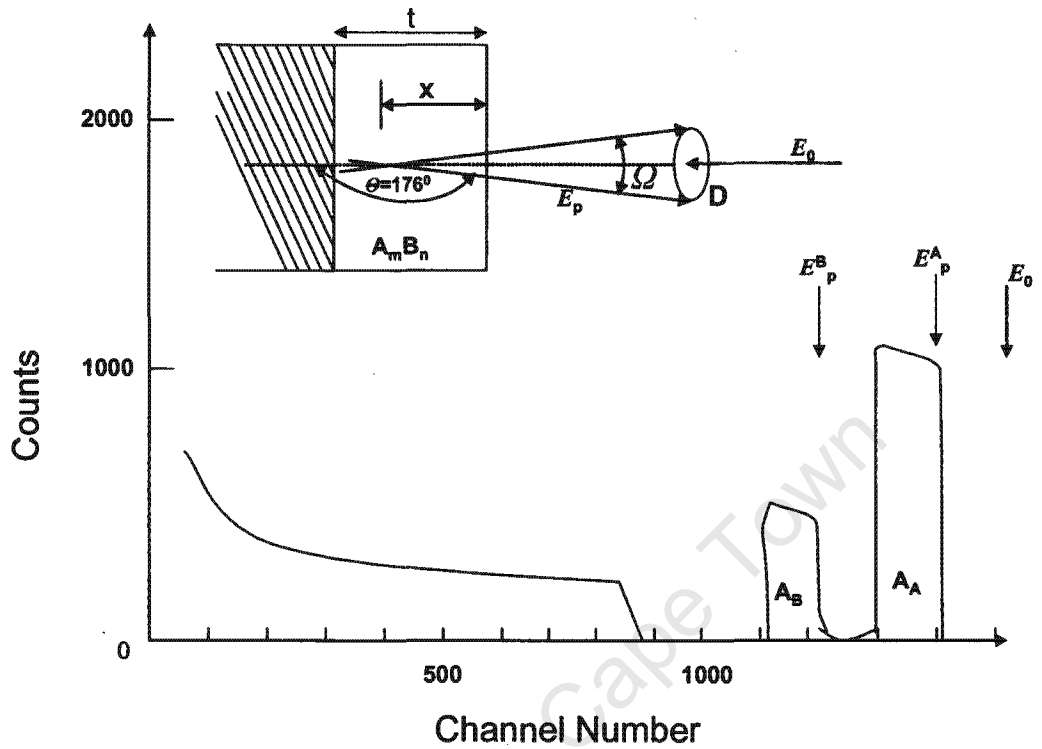

Figure 6.6: Typical experimental geometry for RBS and example of spectrum response from a target composed of two atom phases A and B with atomic fractions m and n. D = annular silicon surface barrier detector; Ω = solid angle (mSr); E_0 = incident proton energy at surface; E_p proton scattering energy; θ = scattering angle; t is the thickness of the thin compound deposited onto a thick substrate; X is a depth at which the detected proton is scattered.

6.3.4 NON-RUTHERFORD BACKSCATTERING CROSS SECTIONS

Backscattering analysis with protons is a very powerful analytical technique in micro-analysis of biological materials. Protons elastic scattering by light nuclei which result from nuclear potential scattering in addition to Coulomb interaction is dominated by resonances particularly when using proton energies of 1-3 MeV [Liu93, Ami93, Gur98]. The proton energy is such that it traverse the Coulomb barrier of the target atom. At this point the influence of the nuclear forces for the scattering become significant with a high probability of resonances to occur [Nur01].

Proton elastic backscattering (p-BS) has the advantage of greater penetrability, smaller straggling and better sensitivity for light element detection than other ions. However in

the usual energy region for quantitative p-BS analysis of light elements, scattering cross sections are non-Rutherford, and cannot accurately be calculated from theory. Hence, accurate measurements of cross sections for scattering of protons by light nuclei are necessary [Liu93, Ami93, Gur98].

6.3.5 ANALYTICAL CAPABILITIES

The numbers of backscattering events that occur from a given element in a sample depend upon two factors: the concentration of the element and the effective size of its nucleus hence the scattering cross section. The atomic ratios m,n of atoms A and B in Fig 6.6 can be quantitatively determined from the RBS spectrum by measuring the heights of the backscattering signals from the target material nuclei. The ration m/n is given by the expression:

$$\frac{m}{n} = \frac{H_{A,0}}{H_{B,0}} \frac{\sigma_B(E_0)}{\sigma_A(E_0)} \cdot \frac{[\varepsilon_0]_A^{AB}}{[\varepsilon_0]_B^{AB}} \qquad 6.26$$

where $\frac{H_{A,0}}{H_{B,0}}$ is the ratio of heights from individual signals (A and B) generated by protons detected with energy E_0 near the surface; $\frac{\sigma_B(E_0)}{\sigma_A(E_0)}$ is the inverse ratio of their cross section; and $\frac{[\varepsilon_0]_A^{AB}}{[\varepsilon_0]_B^{AB}}$ the ratio of their stopping cross sections which can be taken as unit in a zeroth-order approximation [Chu78]. Tabulations for the Rutherford cross section have been compiled from several authors [Chu78, Jos95].

Several computer programs have been developed to perform simulations of RBS spectra in ion beam analysis research [May98, Bar98, Mor95]. The most commonly used is the RUMP code by Doolittle [Doo85, Doo86]. This program computes spectra and plot graphs of normalized yield vs. energy. However you may need to have a qualitative understanding about the sample structure to be used as a first approximation for matrix composition. This is particularly useful in analysis of more complex spectra, where

RUMP can successfully calculate the atomic ratios of main atomic phases in a thick target material.

6.4 PARTICLE-INDUCED GAMMA-RAY EMISSION (PIGE)

In the interaction between energetic protons (with energies of 1-4 MeV) with matter, many prompt nuclear reactions are present, in which the transitions from excited states occur too rapidly (with half-lives less than nano-seconds). These rapid decays provide much information of analytical interest based on emission yield of gamma-rays as well as secondary products. The emission of gamma-rays is relatively easy to measure since the energy and amounts of nuclei present in the target-material is proportional to the energy and yields of these gamma-rays. Several studies on the theory and experimental procedures of proton induced gamma-ray emission has been published, [Eva55, Gih82, Deb88].

6.4.1 KINEMATICS OF NUCLEAR REACTIONS

A characteristic nuclear reaction yielding prompt-γ-rays may be written in the style of a chemical reaction as

$$A+p \rightarrow B+b+\gamma+Q \tag{6.27}$$

Where Q is the energy released during the reaction of a proton p, impinging on a target nucleus A to yield a product nucleus B with the emission of light products, b accompanying the γ-rays [Eva55]. Symbolically this written as:

$$A(p,b\gamma)B \tag{6.28}$$

In the non-relativistic case, and for those reactions where b is a single particle, the kinematics relationships between the reactants and products may be deduced from the laws of conservation of energy and momentum [Gih82]. For a reaction on a target nucleus at rest (in the laboratory system of co-ordinates) the conservation of total energy requires that

$$E_p+Q=E_b+E_B+E\gamma \tag{6.29}$$

where:

$$Q=(M_A+M_p-M_b-M_B)c^2 \tag{6.30}$$

c is the velocity of light in vacuum, Eγ is the energy of the γ-rays and E and M refer respectively to the kinetic energy and mass of the particles denoted by subscripts.
If Q is positive, the reaction is said to be exoergic and kinetic energy is gained in the reaction. If Q is negative, the reaction is said to be endogenic and there is a threshold energy E_{th}, for the incident particle, below which the reaction cannot occur [Gih82]. This threshold energy is always greater than |Q |and is given by the relationship:

$$E_{th} = -Q\frac{M_B + M_b}{M_B + M_b - M_a} \tag{6.31}$$

6.4.2 NUCLEAR REACTION CROSS SECTION

The probability dn of a nuclear reaction of type A(p,bγ) B occurring is proportional to the product of the number of incident protons per second ϕ_p and the number of target nuclei per unit volume

$$dn = \sigma(E_p)\phi_p N_A dx \tag{6.32}$$

with dx is the thickness of the target material and/or the proton range. The proportionality constant $\sigma(E_p)$ has dimension of area (barns) and is called the cross-section of the reaction for a proton bombarding energy E_p. The relationship between $\sigma(E_p)$ and the bombarding energy E_p is called the excitation function of the specific nuclear reaction. Since the energy of incident protons continually change as it penetrates the target, these $\sigma(E_p)$ will also change, sometimes appreciably with resonance variations. However analysts are more concerned with the variation of $\sigma(E_p)$ rather than with its absolute value. A common practice therefore is to measure the yield excitation curve experimentally, which is time-consuming but allow the determination of efficient resonance energies which will maximize the analytical γ-rays yield. Since protons are slowed down rapidly within the target the $\sigma(E_p)$, is expected to vary drastically with depth of analysis.

6.4.3 QUANTITATIVE ANALYSIS WITH GAMMA-RAYS EMISSION

If the yield, Y_s, for a nuclide W, in a target-material is given by the equation,

$$Y_s = \phi C_w \frac{1}{M_w} \int_{E_i}^{E_{th}} \sigma(E)\left(\frac{\rho dx}{dE(x)}\right)dE \tag{6.33}$$

where $\frac{dE(x)}{\rho dx}$, is the stopping power, E the kinetic energy of protons at depth x in the sample, ρ, is the sample density, C_w is the concentration of W in the sample and M_w its atomic mass. If we define the matrix correction factor U_s as

$$U_s = \int_{E_i}^{E_{th}} \sigma(E)\left(\frac{\rho dx}{dE(x)}\right)dE \tag{6.34}$$

the ratio between the measured yields induced in a sample, S, and in a standard, can be written as:

$$\frac{Y_s}{Y_0} = \frac{\phi_s}{\phi_0}\frac{(C_w)_s}{(C_w)_0}\frac{U_s}{U_0} \tag{6.35}$$

the superscript 0 refers to the standard and S, to the sample. If we assume that the matrix composition of the sample and standard are similar then the values of U *and* ϕ for both the standard and the sample are similar for an average cross-section and stopping powers. [Ish78a, Ish78b, Gih82]. Therefore, we could assume, with a fair approximation, that the ratio of γ-rays yields is proportional to the concentrations of nuclide W in the target-material.

CHAPTER 7

NUCLEAR MICROSCOPY EXPERIMENTAL TECHNIQUES

7.1 INTRODUCTION

Focused proton beams of several MeV are obtained by demagnification of a beam object by magnetic quadrupoles into a small cross-sectional area, which focal plane is at the analytical surface of the target material. The main goal of the focused proton beam for micro-analysis is to probe small areas with enough resolution as to obtain relevant information about the content and distribution of elements present in a specimen. This chapter will give a brief outline of the physical layout related to the iThemba LABS, NMP and peripheral instrumentation used for elemental mapping.

7.2 NUCLEAR MICROPROBE COMPONENTS

With the aim of improving the reliability and stability of the proton beam delivered to the NMP, as well as the characteristics of beam optics along the VDG beam, relevant modifications were implemented during the last several years affecting mainly: a) poor terminal voltage stability, b) power supply ripple, c) stray field distortions which give rise to poor energy beam distribution introducing severe chromatic aberrations, d) horizontal beam resolution and e) optimum current on target. The beam-optical set up from ion source to the analyzing magnet was optimized using different computer codes (refer to Chapter 5). The accelerator can provide the microprobe with a wide variety of beams and energies, including pulsed beams with a high timing resolution. The high voltage terminal can host two different ion sources: a duoplasmatron and a penning source [ref. Chapter1-5]. The first predominantly being used for the production of light ion beams [Tap93]. A description of the different optics components will follow

7.2.1 VAN DE GRAAF ACCELERATOR

The 6 MV Van De Graaff accelerator has been described in detail in chapters 1-5. For the purpose of illustrating the aspects of the accelerator which are more related to the operation

of the microprobe we are going to limit the discussion here on the instrumentation which applies mainly to the optics of the microprobe, by emphasizing the relevance and impact of modifications done in Chapters 4 and 5 on the quality and optimization of the NMP operation (refer to Figure 2.3).

7.2.2 OPTICS SET UP

The diagram in Figure 7.1 shows a schematic representation of the layout of the VDG accelerator and beam lines. The NMP is installed in the 0^0 line at the 6 MeV single-ended Van de Graff accelerator at iThemba LABS. The beam of ions produced by the ion source (I) is accelerated vertically downwards passing through sets of quadrupoles (Q_1) for focusing this beam, and slit objects (C_1) for collimating. Energy selection of the accelerated particles is made by a 90^0 analyzing magnet (M). After the analyzing magnet, the beam passes through energy stabilization slits (C_2), situated before the main beam stop (see Figure 7.1). The quadrupole doublet (Q_2) after the beam stop focuses the beam at the object slits. This is lead by three computer controlled Faraday cups situated along the line up to the target, which facilitate the current optimization.

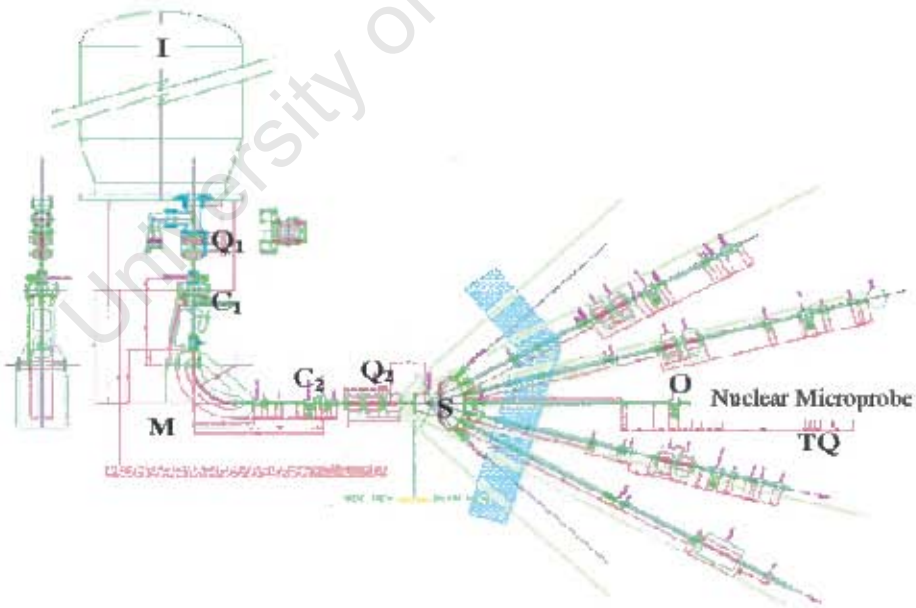

Figure (7.1) Sectional side view of the VDG accelerator showing a cross section of the vertical layout from ion source to switching magnet and a top view of the experimental lines, including the microprobe at 0^0; I: hot-cathode duoplasmatron ion source; Q_1: is the condenser; M: analysing magnet; Q_2: quadrupole set; C_1, C_2: set of collimators; S: switching magnet; O: object slits; TQ: set of triple quadruple lens.

Ion source

A hot-cathode magnetic ion source, duoplasmatron type is typically used for microprobe work (see Chapter 4). It is fitted with a tungsten filament, and coated with a film of Sr_2N_2 to maximize its yield of positive ions (see Appendix A). It is operated at an arc current of typically 100 A through it; gas flow outlet diameter is 0.5 mm; filament current of 25 A; extraction voltage of 5 kV; and an operating pressure of ~10^{-5} mBar.

Vertical line section up to analyzing magnet

Protons from the ion source are accelerated to the required proton energy in the tube. In order to match the beam emittance at the exit of the accelerator to the emittance of the beam line (at extraction voltages of more than 5kV) and additional Einzel lens was implemented in the terminal section of the original (High Voltage) VDG, near the gap lens which is used for beam focusing and acceleration (refer to Chapter 5). This additional lens can fulfill the focusing properties of the gap lens, and the gap lens together with the extraction voltage can then be used to adjust the injection energy of the beam at the entrance of the accelerator (for more details refer to optics discussion in Chapter 4-5). At the exit of the tube a new set of quadrupoles ensure the focusing of the beam into a set of object slits located before the bending magnet.

Analyzing magnet and condenser lens

A set of quadrupole doublet lenses condense the proton beam into the 90^0 analyzing magnet. This is complemented by a set of steerers before and after the magnet, to ensure that the beam is aligned to the correct on-axis direction and maximize the beam transmitted into the microprobe line. The microprobe beam line has been mounted at the 0^0 direction of the switching magnet, in order to avoid problems with energy dispersion of the beam [Tap93].

The object slit

The object slit is of a four independent jaws configuration, with manual micrometer aperture control to allow accurate object alignment. It is an OM-10 model manufactured by Oxford Microbeams [Oxf90]. This object slit works in tandem with the high-excitation quadrupole lens system. A computer controlled Faraday cup is located before the object slit to monitor the maximum current which is of the order of 30 nA. It is water cooled to prevent object size variations due to thermal expansion.

Steering coil

A long steering coil (80 cm long) manufactured at iThemba LABS is installed on the 6 m path between the object and the antiscatter slit. This will steer the beam on-axis direction to ensure maximum proton beam intensity at the quadrupoles.

Beam on demand: Deflection system

Beam ripple is one of the most important problems arising in the operation of accelerators in particular older ones. This is translated into a lower count rate than expected when the beam intensity is high. This results in high count rate for short periods and thus high pile-up. An on-demand beam deflection system ODDS (see Figures 7.2) is used to prevent event losses due to high X-ray count rates. It consists of two parallel plates 40 cm long (2) that operate at ground potential with applied voltages depending on the energy of the proton beam. The linear relationship between these voltages and proton energy is shown in Figure 7.3.

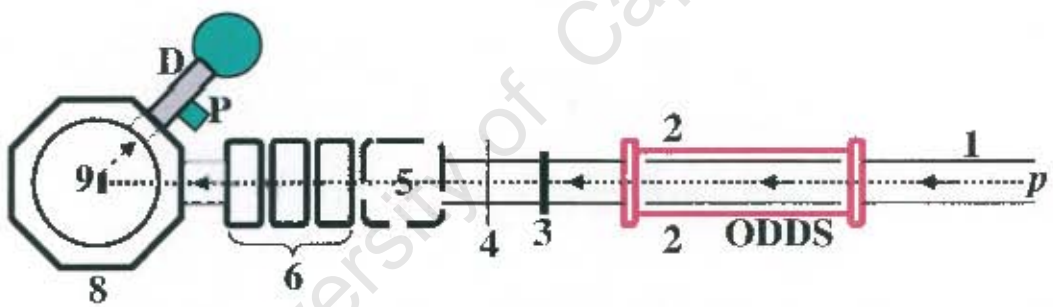

Figure 7.2 Illustration (not to scale) of the location of the beam on demand deflection system (ODDS) with respect to the target-material (9), situated at the center of the scattering chamber (8). Other conventions are: *p* is the incoming proton beam; (1) is the beam pipe through which the beam pass; (2) are the deflection plates; (3) is the beam-dump; (4) is the antiscatter slit; (5) the scanning coil used to scan the position of the beam over the target surface; (6) are quadrupole lenses for focusing the beam; (D) is the Si(Li) detector and (P) the detector preamplifier. The plates have a length of 40 cm and are situated 2 meters from the specimen.

In the framework of PIXE analysis, the principle of such on-demand beam deflection system can be equated to a deflection of the proton beam by an electric field between the two plates.

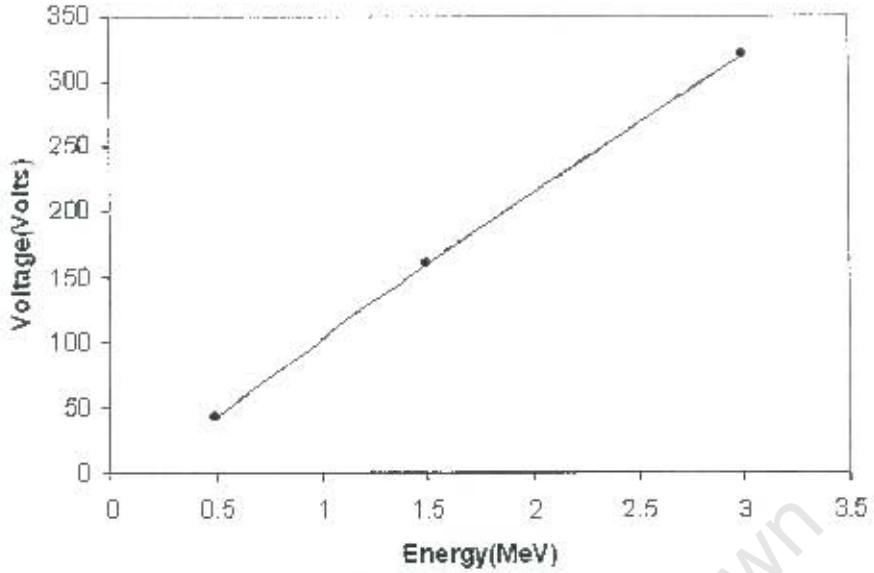

Figure (7.3) Linear relationship of the beam on-demand voltage-applied to the deflection plates v.s. proton energy.

each time that the fast discriminator in the amplifier senses a pulse from the X-ray detector preamplifier which is not accounted for. This deflection of the beam from the target happens for a fixed time interval. The minimum deflection necessary for optimal operation is defined by the vertical dimension of the beam at the acceptance slits.

A benefit from this deflection is the reduction of pulse pile-up which normally occurs at high count rates as well as the reduction in continuum background which results in a significant improvement of the analytical detection limits for microPIXE at the iThemba LABS facility. On the other hand, the enforced absence of the beam from the target surface, while each X-ray pulse undergoes processing by the electronic system, reduces damage to the specimen [Tee88, Pro 95].

The antiscatter slits

The ion trajectories with the largest divergence generally suffer the worst aberration when focused. The purpose of the antiscatter slit is to limit this divergence entering the lens system (see Figure 7.2). The slit is of the same type OM-10 [Oxf90] as the object slit.

X,Y scanning coil

A magnetic coil OM-25 [Oxf90] is located before the lenses. Although is not the optimal location for the coil due to the movement of the beam inside the lens [Wat87], this geometry is the original from manufactures, and dates back to the installation of the NMP at iThemba

LABS in 1992. The coil is computer controlled to allow beam scanning and beam positioning of the beam probe over the area for analysis

Quadrupole lenses system (include lens alignment and focusing procedures)

The high quality magnetic lens system was purchased from Oxford Microbeam in 1990. A triple-quadrupole lenses type OM-150 [Oxf90] was selected. Lens specifications are: 1) Yoke dimension: 100mm x 150 mm Ø; 2) Maximum current: 100 Amps. It operates in a CDC (converging, diverging, converging) configuration, forming a ±20 demagnified image of the object aperture at the focal point inside the scattering chamber, with low aberration for beam probe spot lateral diameters of the order of 1-3 μm and below with currents of ~100 pA. Periodically alignments of the lens magnetic axis are done to ensure optimal resolution for routine work.

Figure (7.4) Photograph showing the layout of the nuclear microprobe (NMP) system, H is the halo slits, S is the scanning coils used to position the beam probe on the specimen surface, LN is the container for cooling the Si(Li) detector used in the detection of X-rays, Q the set of quadrupole lenses, used in the focusing of the beam, M the optical microscope for viewing the specimens, C is the nuclear microprobe scattering chamber and SC is the sample change mechanism.

A picture with the main components of the OM-150 system is shown in Figure 7.4. The OM-150 system uses a OM-50c constant current power supply capable of producing 100 A at 4 V with better than 5ppm long term stability and settable optimized to better than 10ppm. [Oxf90].

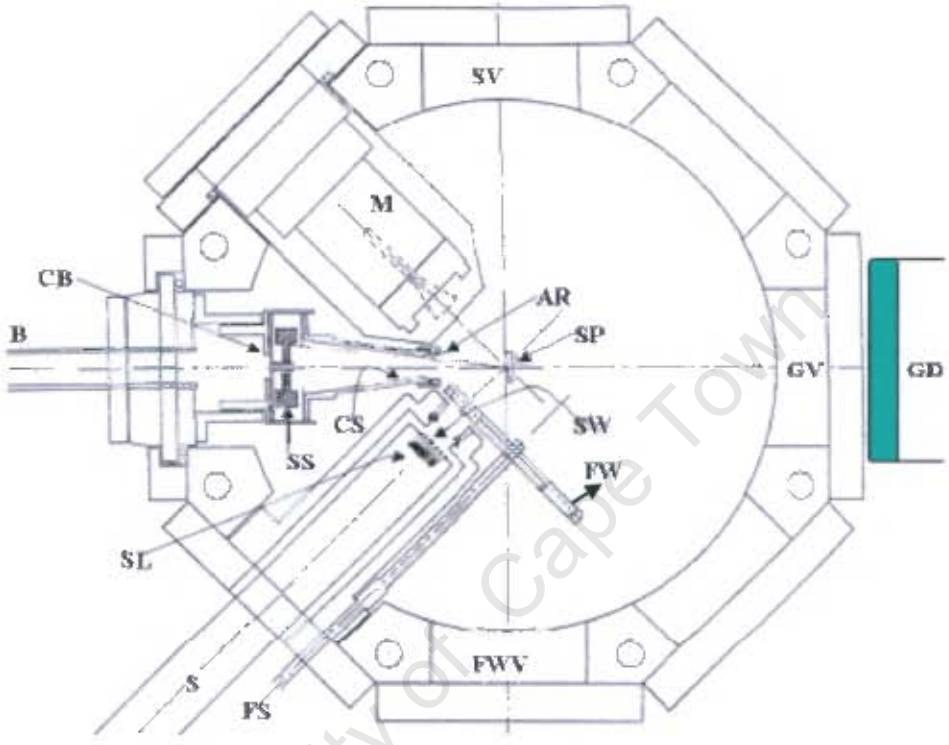

Figure (7.5) Top cross-section view of the NMP chamber. SV is the specimen view port, M the microscope, B the incoming beam, CB the collimator preventing the reflection of beam, AR the suppression ring, SP the specimen, SS the silicon surface barrier detector, CS the collimator preventing the beam from being reflected on the surface barrier detector, S the Si(Li) detector, SL the Si crystal, SW is the Si(Li) detector window, FW the filter wheel and FS the shaft for changing filters FWV the view port for the filter wheel GV a view port and GD is the γ-ray detector

7.2.3 SCATTERING CHAMBER

The microprobe bought back in 1990 included the original Oxford scattering chamber OM-70c (C in Figure 7.4) supplied by manufacturers [Oxf90, Tap93]. However modifications have been done during past years to accommodate additional needed instrumentation. This included the re-design of the sample positioning mechanism to allow for fast computer control of the target surface (SC in Figure 7.4). A schematic cross sectional diagram of the

OM-70e scattering chamber with latest modifications is given in figure (7.5). The chamber was designed for optimum efficiency and for the simultaneous use of several detectors such as: 1) Si(Li), (Link, PGT or HP-Int(Ge)) for PIXE; 2) SSB for proton Backscattering; and 3) Ge(Li) for γ-ray spectrometry.

Other features include:

a) A port (at 135° to the incoming ion beam direction) to fit an X-ray detector (S) dipstick, which Be window surface can be accurately positioned at various lengths from the target surface (typically 22-35 mm) by way of a manually controlled platform,

b) An annular Si surface barrier (SBD) detector (SS) situated at ~6cm in front of the analytical target surface, 176° from the direction of the ion beam;

c) A Cu electron suppression ring situated in front of the beam focal point at about ~2-3 mm; A voltage of -500 to -1500 V is usually used for analysis of biological tissue at room temperatures.

d) An optical microscope with a working distance of 35 mm and demagnification 20-110 with a 10x eyepiece, placed at 45° with respect to the normal to the sample surface,

e) Lighting in the target chamber is enabled through two separate light sources in front of (for reflected light) and behind the target.

f) Allows for stepper motor control of samples in X, Y and Z axes, with maximum movement obtainable with the new target sample changer mechanism (see SC in Figure 7.4) of 250 mm in the Y direction, 40 mm in the X and 30 mm in the Z (focusing) direction. This facilitates the accurate positioning of beam-probe and the selection of required micro-regions for analysis.

g) The stepper motor control and the large movement obtained in the Y direction allows the installation of a permanent set of standards obtained from ASTIMEX©. The set is composed of standard materials embedded in epoxy and polished to a very flat surface. This includes one for pure elements, with 44 elements available and another one of minerals. Pre-programmed settings allow the automatic movement by computer control of the sample holder to any one of the ASTIMEX© standards [Pro95].

h) A wheel with a set of 11 filters is positioned in front of the X-ray detector. The wheel can be fitted with eleven filters to allow for selective attenuation of X-rays and to reduce the bremsstrahlung intensity, depending on the requirements of the analysis (see Table 7.1). Analytical grade high purity metals (Be, Al) and polymers (Kapton) are used for the

absorbers: The thickness of these absorbers are shown in Table 7.1. For this investigation Be of 125μm and Al of 102 μm absorbers were typically used (see Table 7.1).

Table (7.1) List of the set of materials used as X-rays absorbers. All are of Analytical grade with low level of impurities.

Position	Filter material	Thickness [μm]	Thickness [mg/cm^2]
1	Hole(not filtered)	--	--
2	Al	408	110.1
3	Al	102	(28.1)27.5
4	Al	153	41.3
5	Al	203.5	54.9
6	Be	125	22.5
7	Al	253	68.3
8	Kapton $C_{22}H_{10}N_2O_4$ D=1.42	76.5	10.9
9	Kapton $C_{22}H_{10}N2O_4$ D=1.42	156	22.0
10	Be	25	4.51
11	Hole (collimated)	--	--

i) A Faraday cup is located at 90^0 to the back plane of the target to collect the numbers of ions per second. This signal is fed into a current integrator (EG & G-ESN model CD-1010) with digital output.

7.2.4 DETECTORS

For the following discussion about detectors refer to Table 7.2.

Si(Li)

During this investigation two different detectors for X-ray detection were used. A Link™ Pentafet Model C6648 one supplied by OXFORD Instruments, plc, Oxon, UK, and a PGT supplied by Princeton-Gamma-Tech, Inc., USA. The Link detector was used mostly for determinations with 3.0 MeV protons and the PGT was used with protons at 1.5 MeV and 3.0 MeV. Both detectors have a low noise Pulsed Optical Feedback (POF) pre-amplifier type which includes a field effect transistor (FET) cooled in the cryostat (see Table 7.2). This allows to increase the peak/background by about ten-fold to greater than 1000:1 for most of the useful X-ray energy ranges. Both Si(Li) detectors are build in with an horizontal dipstick of ~20 mm

diameter and 60 cm length and fitted onto a vertical cryostat, were positioned inside the scattering chamber through one of its ports (see Figure 7.5) at 135° to the incoming beam.

High purity Intrinsic Germanium Hp(Ge)

An Intrinsic high purity germanium detector Hp(Ge) supplied by EURISYS Measures Tanneries, France, was also used for both X-ray and γ-ray detection measurements simultaneously, particularly when looking at low energy gamma-rays from ^{19}F decay (110, 197 keV). This detector have an operating voltage of −1000 V with resolution of 154 eV measured at time constant 12μs; count rate 1000 cps/s; negative polarity (see Table 7.2).

Other detectors used

An annular silicon surface barrier (SSB) detector with an active area of ~100 mm^2 and a typical resolution of ~25 keV for the measurements of protons was used primarily for the evaluation of the composition of thick target-material such as hard human tissues. A lithium-drifted germanium detector (Ge(Li), was used simultaneously with the Si(Li) detector for the detection of prompt gamma-rays to obtain information on minor components (see Table 7.2 for specifications). Before discussing in detail the detection interface we may give a brief description of the two modes in which the probe can be used for analytical work.

7.2.5 SCANNING MODES

As explained in section 7.2.2 a magnetic coil OM-25 [Oxf90] is located before the quadrupole lens (see Figure 7.7) and is used to control beam-probe movement over the analytical area by using a scan amplifier OM-40e [Oxf90] to generate the required (x,y) coordinates voltages associated with the beam-probe position on the target. The computer selection of this coordinates by an external PC computer - using a locally developed LabVIEW code "CCSCAN-II" [Chu93]- allows for accurate positioning of the probe over the target surface. These coordinates are fed into both the data acquisition software and another external PC (MicroControl PC in Figure 7.7). " CCSCAN-II" is also used for the real time display of the map generated by the X-ray signal response. With typical beam spot resolutions of the order of 1-3 μm (~100 pA current) the proton-probe can be left static (single point analysis) or in scanning mode (mapping analysis). These two modes can be used to obtain particular elemental information from the target-material according to requirements.

Table 7.2 Specifications of detectors used in experiments

Detector	Active area	Crystal Thickness	Au dead layer	Be Window	Si dead layer	Voltage	Resolution	
	[mm^2]	[mm]	[μm]	[μm]	[μm]	[Volts]	Manufacturer [eV]	Experimental [eV]
Link	80	4.8	0.01	8.0	0.1	-500	138-170	~201[5]
PGT	30	3.0	0.02	8.5	0.018	-600	160	~192[6]
Hp(Ge)[1]	100	7.0	0	12.5	0.5[2]	-1000	154	~161[5]
Ge(Li)	~2800	~50	0	~500	500[3]	+4500	~1.86/keV [4]	~2.5/keV[4]
Si[7]	~100	--	--	--	~300	+50	~14/keV	~25/ keV

[1] It has an additional 0.3 μm Al absorber
[2] Ge dead layer
[3] Li contact thickness
[4] Measured at 1332 keV with a Na-22 source
[5] Measured at 5.9 keV on Hydroxyapatite
[6] Measured at 5.9 keV on Keratin
[7] Annular Surface Barrier

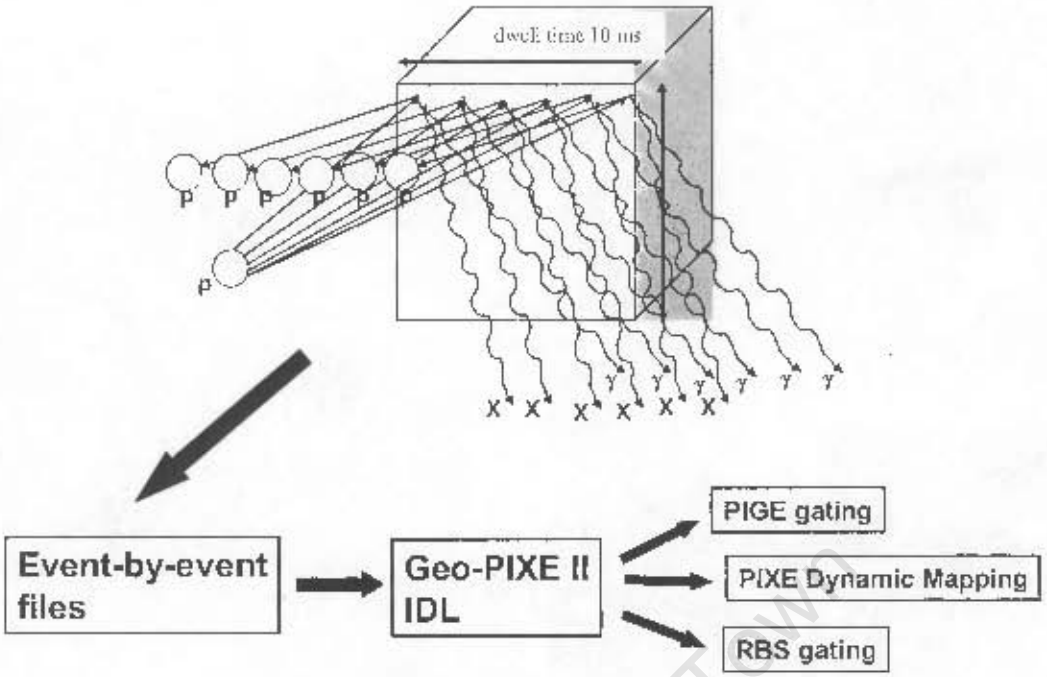

Figure 7.6 The scanning process: the beam probe moves along each X,Y directions from pixel to pixel with a dual time of 10 ms. At each pixel X-ray, scattered protons and gamma-ray signals are detected. Evaluation of each spectrum by GeoPIXE II is done using the DA method (for X-ray) and gating (BS and PIGE)

X-rays, scattered protons and gamma-rays signals are detected at each scanned pixel with a dwell time of 10 ms (see Figure 7.6). At each pixel an event e(E,x,y) is recorded and evaluation of each spectrum by GeoPIXE II is done using the DA method (for X-ray) and gating (BS and PIGE).

Single point analysers

Since beam current densities at microprobe level are usually high (~ 100 pA/μm^2), point analysis on sensitive targets such as biological tissues have to be performed at low current intensities. A fair compromise between the X-ray count rate, the type of material hardness and the available beam charge should be exercised to be able to perform point analysis by PIXE in such specimens. Furthermore, the resolution needed for a particular point should always be related to the temperature sensitivity of the material.

Elemental mapping

Most of the best advantages from the NMP are fully utilized when a focused ion beam is scanned in a particular micro-area to obtain 2-dimensional spatial information related to the distribution of major, minor and trace elements present in the target material This spatial

information has become especially relevant for micron and sub-micron level analysis in bio-medical sciences where relatively small detail is required. An image of the sample micro-region is obtained by scanning of the ion beam from left to right at a particular speed over the pre-selected area. The main objective is to construct elemental maps of the elements present in such area.

The optical resolution of the map *i.e.,* the depth of detail visualization depend on the number of steps that the ion beam moves over the line scan, in other words, the number of pixels defined for the re-construction of the maps. In addition to the experimental hardware set-up required for this elemental mapping to occur a critical aspect in modern PIXE work is devoted to the on/off line analysis of the PIXE spectra.

7.2.6 DETECTION AND DATA ACQUISITION SYSTEMS

The detection system at the NMP at iThemba LABS can be described depending on the type of secondary prompt signal detected. Since detection of the X-rays originating in the target-material is the main thrust of microprobe work it is logical to devote most of the discussion to this technique. However, since in most of the experimental work both PIXE and/or BS and PIGE are run simultaneously, a brief explanation of the detection-flow schematics for backscattered protons and gamma-ray signals will be presented.

System outline

Some of the components of the system for detection and data acquisition of pulses have already been discussed earlier. The main feature of this system is the dependence on a CAMAC-VME-VAX4000 configuration with facility for multiparameter data acquisition. The software package XSYS is used for data-acquisition and analysis. The system is used in a VAX configuration with MBD controller as the front-end interface to CAMAC. The iThemba version is based on the Indiana University Cyclotron Facility [Iuc84] with small differences.

This XSYS software has the possibility to collect simultaneous data areas for each analytical technique including allocation of mapping areas and scaler control for current integration, time and others parameters required. Data acquisition for elemental mapping is stored in list mode as event-by-event computer files. The set of energy, x and y coordinates e(E,x,y) are stored as an event for each detected and analysed pulse and elemental maps can therefore be reconstructed off-line using the program GeoPIXE II.

A dedicated control code written in LabVIEW is used as an intelligent scanner

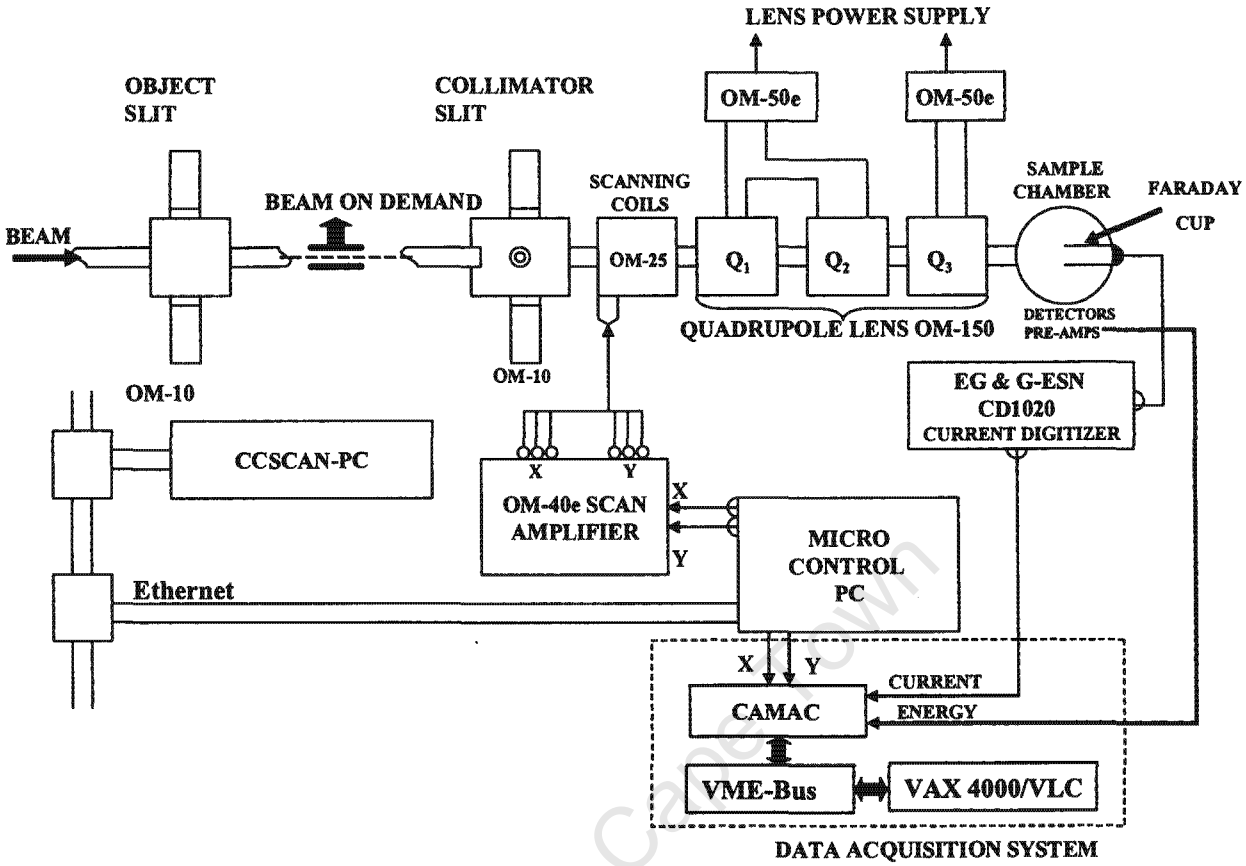

Figure 7.7 Schematic diagram of the nuclear microprobe highlighting the main components involved in the focussing, scanning and data acquisition processes.

(MICROCONTROL PC in Figure 7.7). For the purpose of simplicity we will direct all the further discussion in this section to the electronics schematic diagram details in Figure 7.8

Flow operation of electronic interface (refer to Figure 7.8)

1) When a start acquisition command (mapping or single point mode) is issued by the LabVIEW CCSCAN II program, the acquisition will only start if the Busy line is disabled by the acquisition program XSYS, A scan or single point test can be done on the CCSCAN II control PC with a Busy signal disable by XSYS.

2)The ADC enable signal from the CCSCAN II control PC is disabled when the beam is moved from one point to the next or when data acquisition is being stopped by XSYS. The period that the ADC enable signal is disabled varies during the raster scans (short when moving pixel, longer when moving line and longest when a new frame is started). This ADC enable-signal is used to enable ADCs for backscattering and gamma-ray signals.

3) The X-ray detector pre-amplifier analogue output is fed into a spectroscopy amplifier Canberra 2024 with a long shaping time constant (12μs) and also into another spectroscopy amplifier with a short time constant. The 2024 amplifier shaping-time constant is chosen so as to give the best resolution for a particular X-ray detector and its output is then fed into a Canberra 8077 ADC. The data is then read by the acquisition program XSYS via the VMEbus VAX-interface.

4) When the LG (Linear Gate) signal from the 8077 X-ray ADC is active during the processing of a pulse a reject (Rej) signal is passed on to the ADC so as to inhibit pileup. The inhibit signal from the X-ray detector pre-amp is fed on to the 2024 Amp to inhibit the amplifier from processing any pulses during the Pre-amp reset period. This inhibit signal is also used to inhibit any ICR pulses from being passed to the CAMAC.

5) The spectroscopy amplifier with a short time constant (mentioned above) is used as a filter/ amplifier and its bipolar output is fed to a timing SCA which then generates the ICR pulse on its LL output. As mentioned above the ICR pulses are inhibited by the pre-amp inhibit signal. This timing SCA is used as a discriminator and its Lower Level should be set just above the noise level. The timing SCA output is also fed to a pulse generator which is used to generate a stretched pulse with longer period than the total processing time of X-ray event. From here it is then fed to an OR gate and DT/busy (from X-ray Amp) signals so that the output from this OR gate will switch the beam off using two electrostatic plates in the beam line via the dynamic pile-up rejection unit (see beam on demand section 7.2.2).

7) Furthermore, the beam will be switched off when the pixel is moved (ADC enable) or during the processing of an X-ray event (pulse generator) or when the X-ray Amp is busy (DT/Busy). The total processing time of an X-ray event is approximately 60 μs (see Figure 7.9) and thus dynamic pile-up rejection is done to eliminate pile-up due to beam intensity fluctuations. The second output from the pulse generator is delayed and stretched so that the X-ray ADC is only gated on when the pixel is not moved. The ratio of ICR pulses and total events in the X-ray spectrum gives the dead time for the X-ray system. The total time for processing including the ADC time is 80 μs (see Figure 7.9).

8) The RBS events are read into XSYS via the CAMAC and its ADC is only gated off when the pixel is moved. The LG and Rej. hand-shaking is handled the same way as described above for the X-ray system.

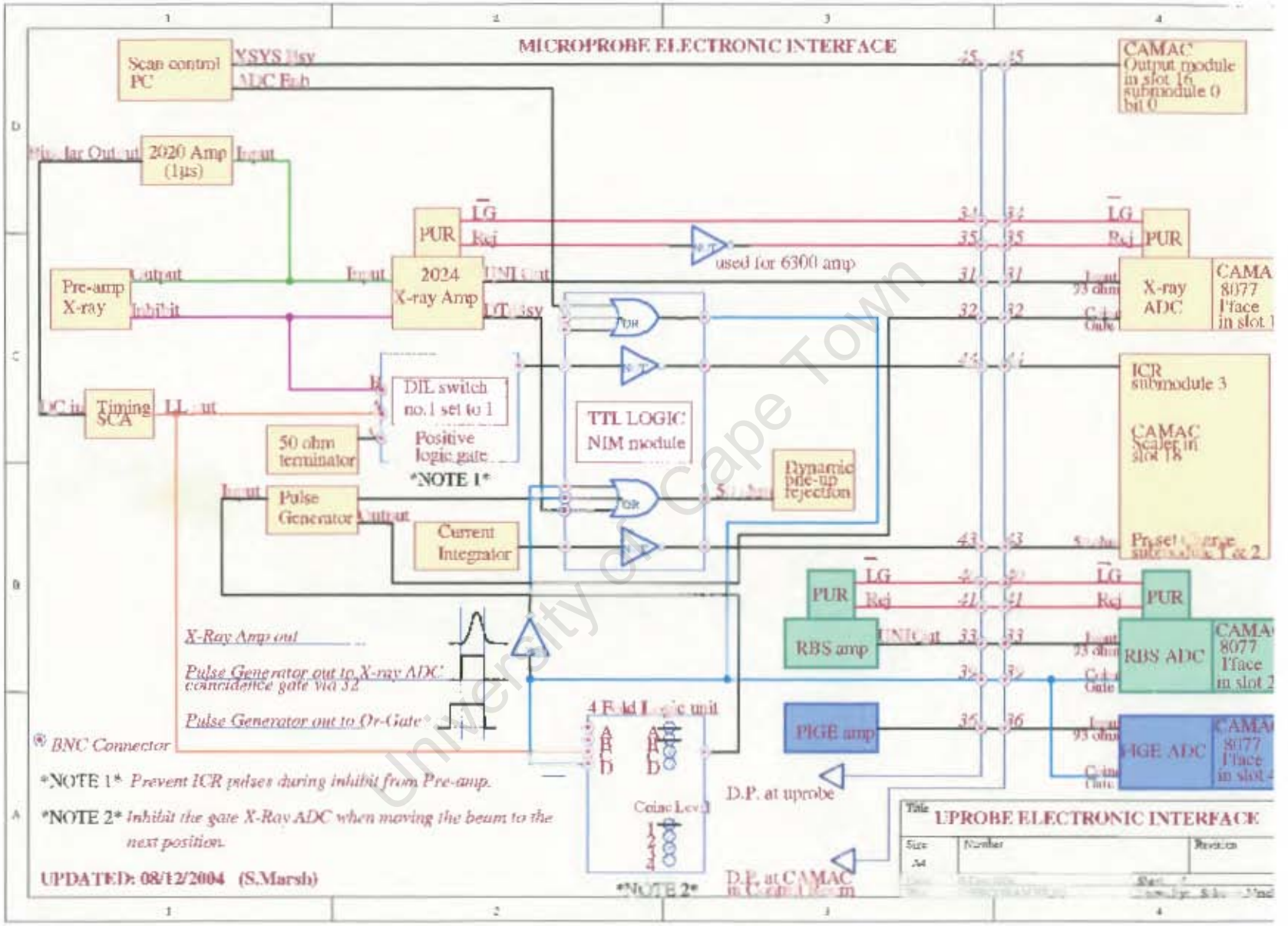

Figure 7.8: Schematic diagram of the electronic interface for theiThemba LABS nuclear microprobe. The main circuit is for the X-ray signal. The detection of the scattered protons and gamma-rays are indicated in green and blue respectively

9) The PIGE events are read into XSYS via the CAMAC and its ADC is only gated off when the beam probe is moving towards the next pixel.

10) The current integrator output frequency is fed into a CAMAC scaler with a value representing the desired charge. This process is followed by an interrupt when the scaler has been counted down to zero.

7.2.7. OFF-LINE DATA PROCESSING

PIXE spectra and mapping by GeOPIXE

The algorithm of the GeoPIXE II [Rya02b] software was introduced in section 6.2.3. Off-line Evaluation of PIXE data comprises the re-construction of elemental maps by sorting of events from list mode files. Procedures which not mentioned in 6.2.3 and more related to the deconvolution and manipulation of spectra include:

- Full display window of one or various spectra in the same window for qualitative comparison of elemental profile, visualization of pile-up and escape background spectra.; identification of X-ray lines for the K, L and M lines of most elements; recalibration of spectra and complete control over the definition of each detector parameters; display of fitted spectra and report on results which includes information about minimum detection limits, relative error, detector resolution and calculated nominal yields.
- Sorting of list mode files written by XSYS as event-by-event with control over the scan size (in pixels), the dynamic analysis projection file, detector definition and spectra energy calibration.
- An image analysis window for display of reconstructed elemental maps. This allow for the display of as many maps as required simultaneously in cloned windows. Display of maps in concentration values as well as the variance is available. If necessary PIXE, BS and/or PIGE spectra can be extracted from selected regions within the map by sorting of events in this selected areas. Different types of analyzing shapes are available including: box, circle and spline with 10 and 32 nodes. Operations such as filtering of mapping data as well as elemental mapping distribution correlations are also possible.

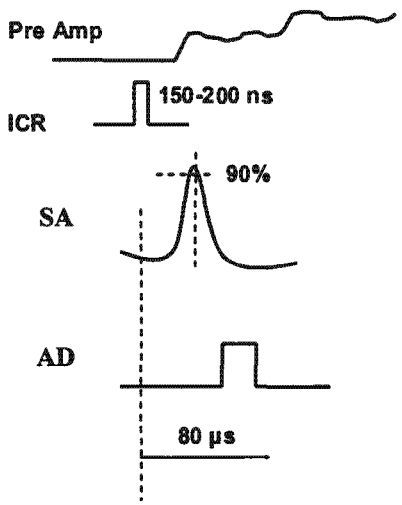

Figure (7.9) Illustration of the signals emitted during the specimen irradiation. Pre Amp represents the signal from the pre-amplifier, ICR the signal from the incoming counting rate unit, SA the signal from the spectroscopic amplifier and AD the analogue to digital converter signal. The signal for the ICR is the faster as it is processed in time duration of 150 to 200 nanoseconds. The spectroscopic amplifier transmits the signal only after 90% is processed and the time duration is about 60 µs. the AD processing times takes about 20 µs. The total time then is about 80 µs

- Outputs of quantitative maps and data can be saved and/or exported in files of specific standard formats such as cgm and png,

Backscattering spectra: RUMP

The RUMP version 2.0 is used at iThemba LABS [Gen05] for evaluation of BS spectra. This allow the simulation of spectra from thick target of human biological tissues which are predominately carbon and calcium rich.

Correspondence analysis

Correspondence analysis is a data analysis technique which simultaneously displays the rows and columns of a two-way contingency table in a low dimensional space. It belongs to the family of statistical techniques that have as their common feature the calculation of a singular value decomposition of a data matrix (principal components analysis, canonical

correlation analysis, discriminant analysis, factor analysis and biplot [Gra84]. In the context of multielemental trace analysis, the display in two dimensions may be interpreted as a map. Samples which are plotted close together are (in a certain sense) similar, and elements (independent variables) plotted close together are (using the term loosely) correlated. The simultaneous display of the rows (samples) and columns (elements) is justified by the 'transition formulae', enabling one to see not only which sample cluster, but also to understand why they are clustered. Correspondence analysis is thus related to, but an improvement on cluster analysis [Pin01].

CHAPTER 8

APPLICATIONS TO MICROANALYSIS OF HARD HUMAN TISSUES

8.1 INTRODUCTION

Prompt analysis of bio-medical tissues with protons has been given a substantial stride forward with the improvements of the microprobe mode and development of sophisticated software for on/off line deconvolution of X-ray spectra [Rya02C, Rya00]. Some of the fields in which the nuclear microprobe (NMP) has been most powerful is in bio-medical studies of soft tissue materials for which the low levels of detection limits combined with the availability of multi-techniques and multivariate capabilities has proven to be the instrument of choice in many applications[Lla98, Pin01, Pal93,Pal97].

An important step in the analysis by NMP of soft bio-medical specimens in general is their adequate preparation for analysis under high vacuum conditions. Typically this will involve strict protocols for sample preparation at low temperature. In addition, a "true" representation of elemental concentrations is critical and this depends to a large extent on the optimal protocol used [Prz99, Lla98, Hay00]. On the other hand, biological hard tissues do not require in general the use of cryogenics since the mobility of ions in such hard materials is minimal. This research was concentrated on the advantages of the NMP for the analysis of human hard tissues prepared at room temperature. The steps for preparation of each tissue type will be described briefly in the corresponding chapter-section.

As in any other instrumental analytical technique the optimization of three important experimental parameters in micro-PIXE to obtain the best minimum limits of detection (MDL) plays a major role in the determination of trace elements present in hard tissue.

Particularly since most of such tissues are rich in carbon, calcium, phosphorus and sulphur. For example in the analysis of trace elements such as Mg, Na, Al and Si present in a Ca-rich matrix type, an adequate (1) absorber must be chosen to minimize the high background due to secondary electrons as well as to reduce the high intensity X-ray signal from Ca. However this is not an easy task when considering (2) the energy of the protons used for X-ray excitation as well as the detector exposure to scattered protons through the absorber. On the other hand this high intensity background can also be generated due to a (3) high beam current on target. Therefore a compromise has to be reached between these three parameters in order to be able to minimize the MDLs.

The problem is less complicated when higher proton energies ($2.5 < E_p < 3.0$ MeV) are used for determination of heavier elements such as Ca, Ti, Mn, Fe, Ni, Cu, Zn and Br, since the insertion of a thicker absorber will control both the background and the high matrix signal. By experience we have found that for low energy protons ($1.0 < E_p < 1.5$ MeV) a Be absorber 25 μm thick works well; and for high energy protons bombardment ($2.5 < E_p < 3.0$ MeV) an Al absorber 102 μm thick is the most suitable.

The level beam intensity used for analysis of hard tissues, depends on the type of specimen material. As a general rule we irradiate the samples in such a way to prevent evaporation of elements to maintain the true composition of materials stable while under bombardment. Typically a current of between 50-300 pA is required depending on the type of hard tissue, the size of the micro-region irradiated and the number of pixels used in the scan. These current levels ensure that a true non-destructive analysis is performed in most sample materials. Total deposited charge depends as well on the concentration levels of trace elements of interest. PIXE has two critical parameters – solid angle subtended by the Si(Li) detector and thickness of absorber positioned between the specimen and the detector –which are routinely calibrated using standard reference materials of pure metals and minerals supplied by Astimex®. Selected micro-regions were scanned with proton beams focused to 1.5 – 4.5 μm^2 spot size. The scan size was typically of 64 x 64 or 128 x 128 pixels with a 10 ms dwell time.

As an application to demonstrate the capabilities of the NMP at iThemba LABS after recent optics optimization of the VDG accelerator, this work here will deal with a set of selected bio-medical applications, particularly in relation to spatial distribution of trace metals in hard human tissues such as kidney stone concretions, teeth enamel and hair.

8.2 ELEMENTAL MAPPING OF TEETH ENAMEL-DENTINE INTERFACE EXPOSED TO ACIDIC CONDITIONS

8.2.1 INTRODUCTION

Erosion in teeth is defined as a chemical dissolution of the dental hard tissues in a process which does not involve bacteria, when acidic solutions came into contact with teeth for prolonged periods of time. Previous investigations on teeth erosion with low energy protons [Pro00] revealed certain areas of depletion of major components Ca and P in and around the interface enamel-dentine (hydroxyapatite matrix). Figure 8.1 shows a diagrammatic representation of the main causes and steps leading to the process of early lesion formation (de-mineralization) in teeth. Since this dissolution may include the depletion of TE associated with morphological changes [Meu91, Mil95], an investigation into the role of TE in erosive processes in and around the enamel-dentine boundary was undertaken. This present study focused on the detection and quantification of mineral loss in early artificial erosion lesions.

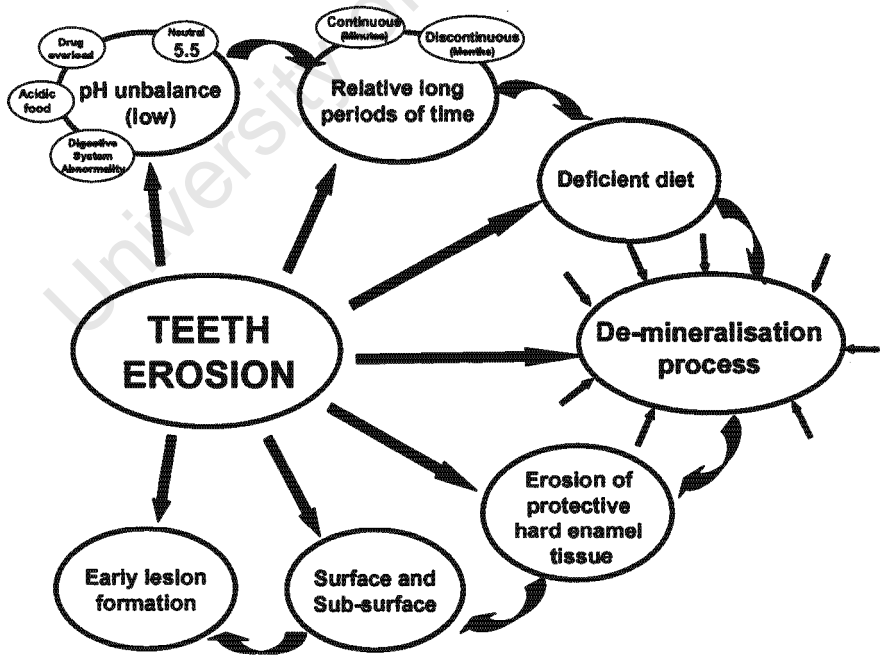

Figure 8.1: Basic model for the process of erosion in teeth, highlighting the main steps leading to the de-mineralization of the surface and sub-surface of the enamel.

Particular reference to variability on the spatial distribution of TE in human enamel and dentine was investigated and their correlation with de-mineralisation and re-mineralisation processes especially for Ca, P, Fe, Ni, Cu, Zn and Sr was investigated. The detection and quantification of mineral loss in early erosive lesions was achieved by using nuclear microprobe (NMP) techniques PIXE and proton-BS [Pin04].

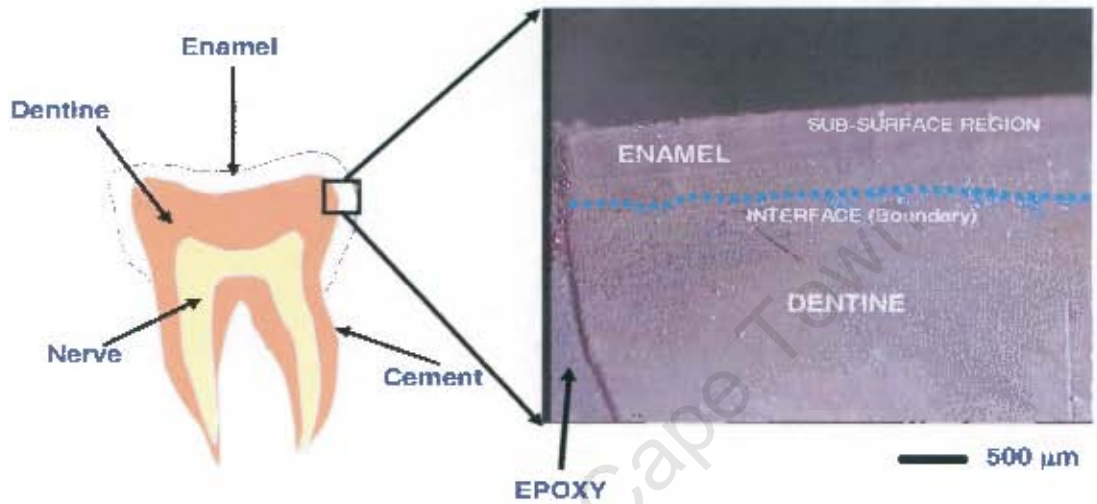

Figure 8.2: Diagram showing the way in which the teeth sections (size ~2 x 2 mm^2) were extracted as well as an optical photograph of the specimen surface prior to analysis.

8.2.2 IN VITRO EROSION SIMULATION AND MEASUREMENTS

An *in vitro* simulation of erosion processes in a set of healthy molar human teeth (tests) was performed in an acidic solution with pH 3.6 for 20 h. A control group was also exposed to a neutral solution (threshold pH 5.6) with pH value in the range 5.6 – 6.0, for the same period of time. For both tests and controls a sub-set of dentine and enamels were considered: 6 enamels and 2 dentine for tests; and 4 enamels and 2 dentine for controls. In average rectangular teeth sections of approximately 10 mm^3 in volume were cut from the molar teeth (Figure 8.2 shows a diagram of the way in which the sections were extracted: the sections included the enamel layer ~500 µm thick and a substantial portion of the dentine material).

Before exposure to acidic media each tooth section was divided into two blocks of ~2 x 2 mm^2 cross-sectional area. One block was used for treatment of the enamel and the other

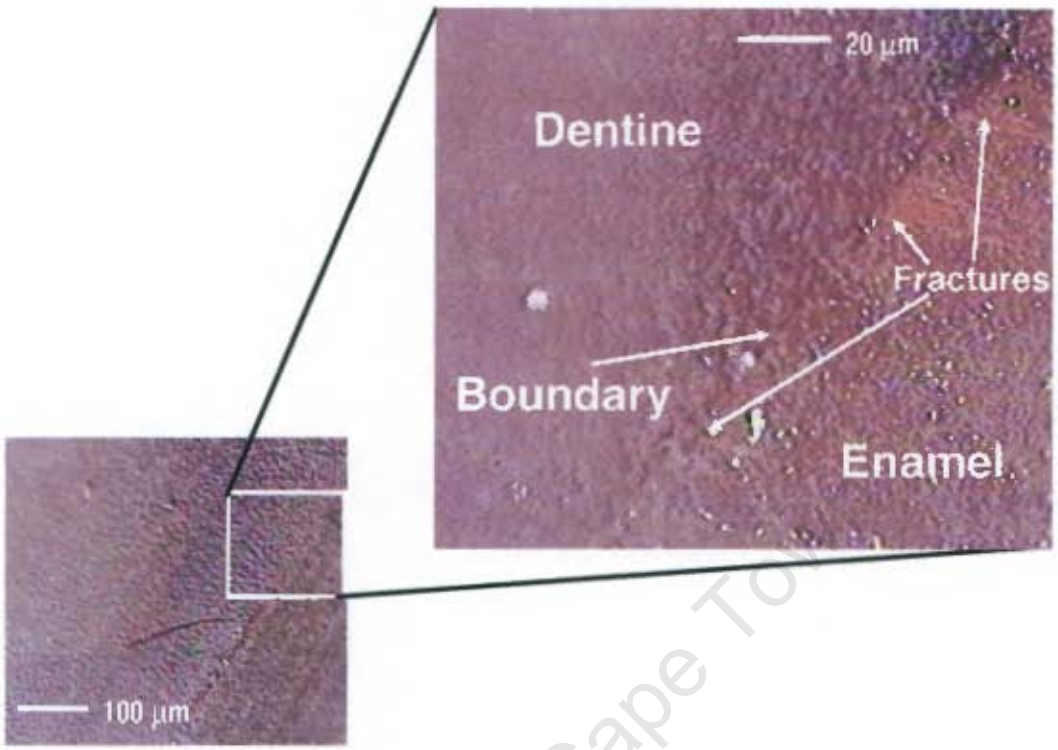

Figure 8.3: Optical micrograph of a tooth section though the interface enamel-dentine showing some fractures in a transversal direction to the plane of the interface

for treatment of the dentine surface. Either the enamel or the dentine was protected selectively from the acid solution exposure by the application of a varnish layer over the outer surface of the area not required for exposure to the acidic solution. Of particular interest was the interface enamel-dentine where a change in the gradient of major and trace elements could indicate changes of the elemental profile and distribution in relation to the boundary metal distribution and erosion in the sub-surface of the enamel. Furthermore, fractures in the enamel near the interface may be play a role in the elemental de-mineralization or re-mineralization in the erosion process [Chi04]. Figure 8.3 shows an optical micrograph of a tooth section though the interface enamel-dentine showing some fractures in a transversal direction to the plane of the interface.

Subsequent to the *in vitro* simulation, samples surfaces were embedded in epoxy and carbon coated prior to proton beam irradiation. Analyses were performed with a 3.0 MeV protons, focused to ~1.5 x 3 μm^2 and scanned over areas from ~10^6 μm^2 down to ~10^4 μm^2 on selected areas of the enamel or dentine. The beam current was maintained at

between 200-400 pA to ensure that the stability of metal distribution and content was not disturbed. Total average accumulated charge for all size areas was of ~0.5 μC. Information on major components such as C, O, P and Ca were performed by proton-BS and analysis of trace elements by micro-PIXE using a Hp(Ge) detector which a solid angle of 174 mSr. An aluminum absorber 102 μm thick was interposed between target and X-ray detector to reduce the high intensity Ca X-ray signals. Since the high content of Ca in the hydroxyapatite matrix is high (~40 %) which subsequent high X-ray count rates, care was taken to ensure the pile-up rejection was well controlled by the beam-on-demand system (refer to section 7.2.2). In average this pile-up was not bigger than 10 %. Evaluation of X-ray spectra for both groups (control and test) enamel and dentine was deconvoluted and true, overlap-resolved elemental maps were obtained using the method of Dynamic Analysis. All samples were thick for the 3.0 MeV protons with an average effective depth of analysis range of ~50 mg/cm^2 for most of elements.

8.2.3 CHARACTERIZATION OF THE HYDROXYAPATITE STOICHIOMETRY

The assumed composition of the teeth matrix was hydroxyapatite with major components being C, O, F and P. Analysis by p-BS confirmed this assumption. Also included in the p-BS analysis was the determination of the fluorine content as atomic fraction of the major components. Atomic ratios of major components O, Ca, P, and F were determined by simulation of BS spectra using the software package RUMP [Doo86]. Typical values of major components atomic fractions for a set of analysis in either the dentine and/or the enamels in the control group were similar ($O_5P_1Ca_3F_1$) as compared to the test group in which these fractions values were $O_6P_{0.5}Ca_3F_{0.5}$ for both enamel and dentine. Table 8.1 shows the reported values for each experimental series indicating the similarity of matrix composition for the dentine and the enamels independently of being a control or a test. A comparison of the p-BS spectra for a control and test enamel is shown in Figure 8.4. It is important to mention here that the determination of the F content by p-BS, contains a certain level of uncertainty since the data for non-Rutherford cross sections used were not exactly at the 176^0 angle required for measurement of backscattered protons ($1.0 < E_p < 3.0$ MeV) at our facility. In stead the database for non-Rutherford cross section at 165^0 from [Jes01] were used. The possible overestimation of the F atomic ratio non-complying

with the hydroxyapatite stoichiometric value may be explained by resonances present in the proton energy range under investigation. More precise measurement of the Non-

Table 8.1: Evaluation of the typical atomic fractions for the components of the hydroxyapatite enamels and dentines.

		O	P	F	Ca
CONTROL	Dentine	5.1	1.1	1.0	2.9
	Enamel	5.0	0.9	1.1	3.0
TESTS	Dentine	6.5	0.5	0.5	2.5
	Enamel	6.0	0.4	0.6	3.0

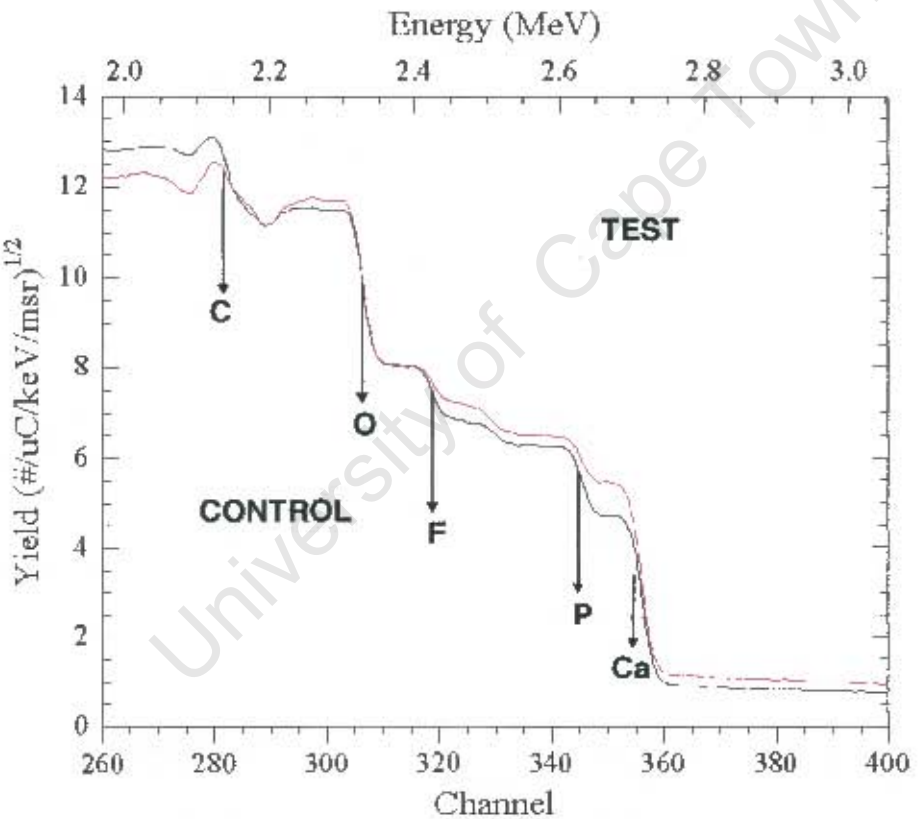

Figure 8.4: Comparison of backscattering spectra for an enamel control and test specimens showing the edge inflexion point for each element. E_p = 3.0 MeV. Accumulated charge was ~5 μC.

Rutherford cross section at our 176^0 geometry are needed in order to be able to have a "true" value for the cross sections. Data on these are in the process of being measured and evaluated. In spite of the above discussion we have confidence on the simulated

spectra by RUMP on the p-BS spectra of fluorine. Simulation of p-BS spectrum from an enamel control is shown in Figure 8.5 with the edges for C, O, F, P and Ca marked on the figure.

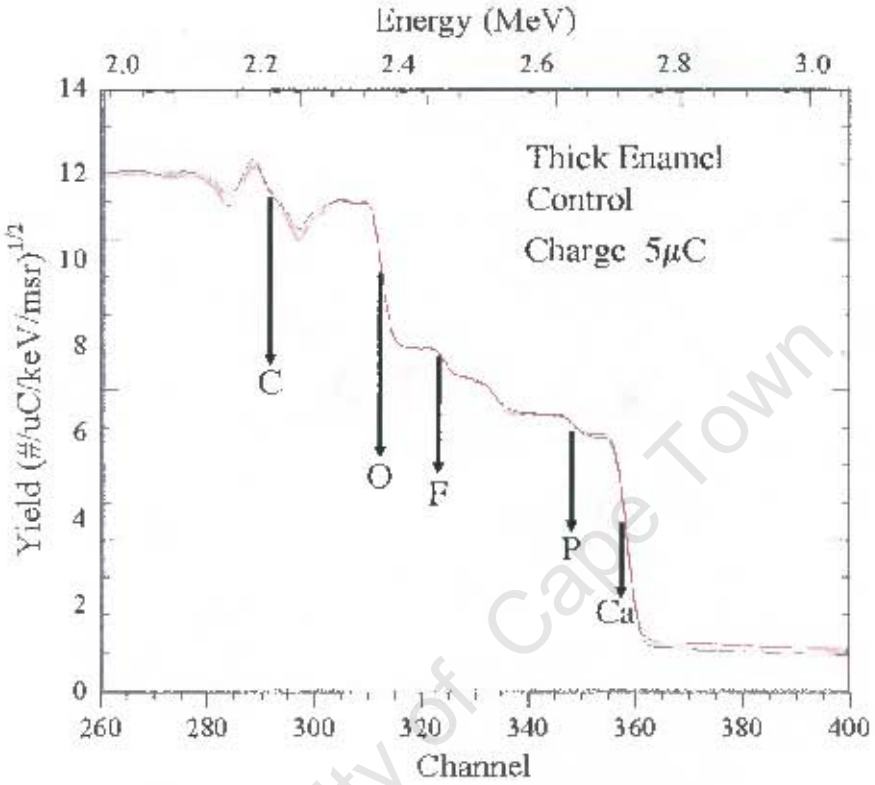

Figure 8.5: Simulation of backscattering spectrum for a thick enamel control specimen showing energy location for each element. $E_p = 3.0$ MeV. Accumulated charge was ~5 μC.

8.2.4 DISCUSSION ON TOTAL X-RAY ELEMENTAL ANALYSIS

Elemental analysis was restricted to the determination of trace elements with $Z > 19$. Main elements detected were Ca, Mn, Fe, Ni, Cu, Zn and Sr with traces of Pb, particularly after the 20 hours exposure to the acidic solution. This is probably a contamination product from the solution and/or the epoxy used for embedding. Spectra of specimens' material for enamel controls and tests are shown in Figure 8.6. A clear difference can be observed on the concentration value of Zn and Sr. A similar comparison is shown in Figure 8.7 for the case of the dentine controls and tests where differences were observed on Cu, Zn and Sr

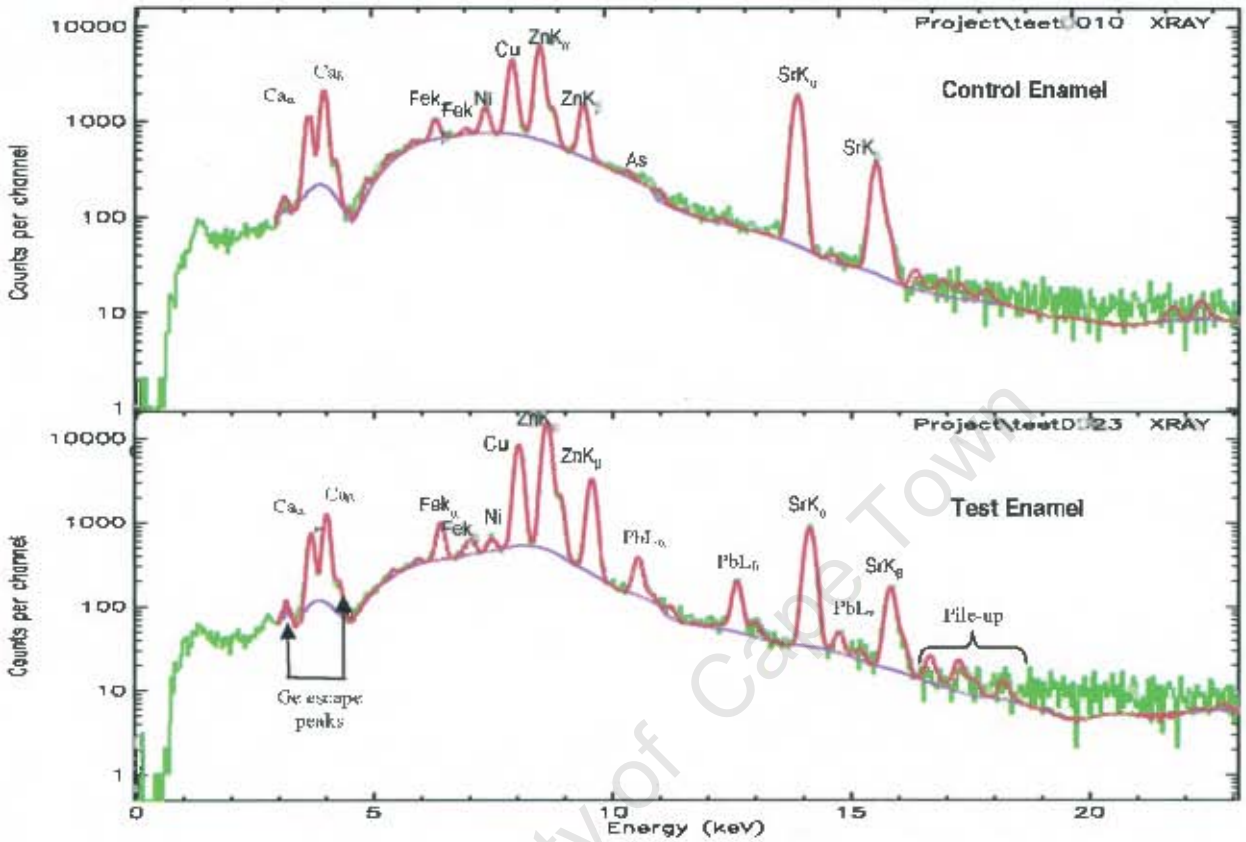

Figure 8.6: Extracted X-ray spectra by GeoPIXE II, showing the elements detected on a control and test enamel. Total deposited charge per unit area was ~ 0.025 nC.μm^{-2}.

Table 8.2 shows the concentration values (in μg.g^{-1}) as determined by micro-PIXE for such elements determined as total contribution from all pixels analyzed in each scanned area. Data are shown for the controls and tests samples on dentine and enamel. By inspecting the concentration levels for Sr in the controls (~140 μgg^{-1}) we notice that after treatment their average concentration was reduced to ~80 μgg^{-1}. This is a significant reduction, which occurred in all tests samples independent of being enamel or dentine. A similar situation appears to be occurring for Zn, although to a lesser extent, since there are two test enamels for which the Zn levels rather increase substantially (see Table 8.2). Since Zn and Sr are two biological important TE in relation to the structure of the teeth it is logical to think that the depletion of such elements after the exposure to the acidic solution treatment is related to an erosive process.

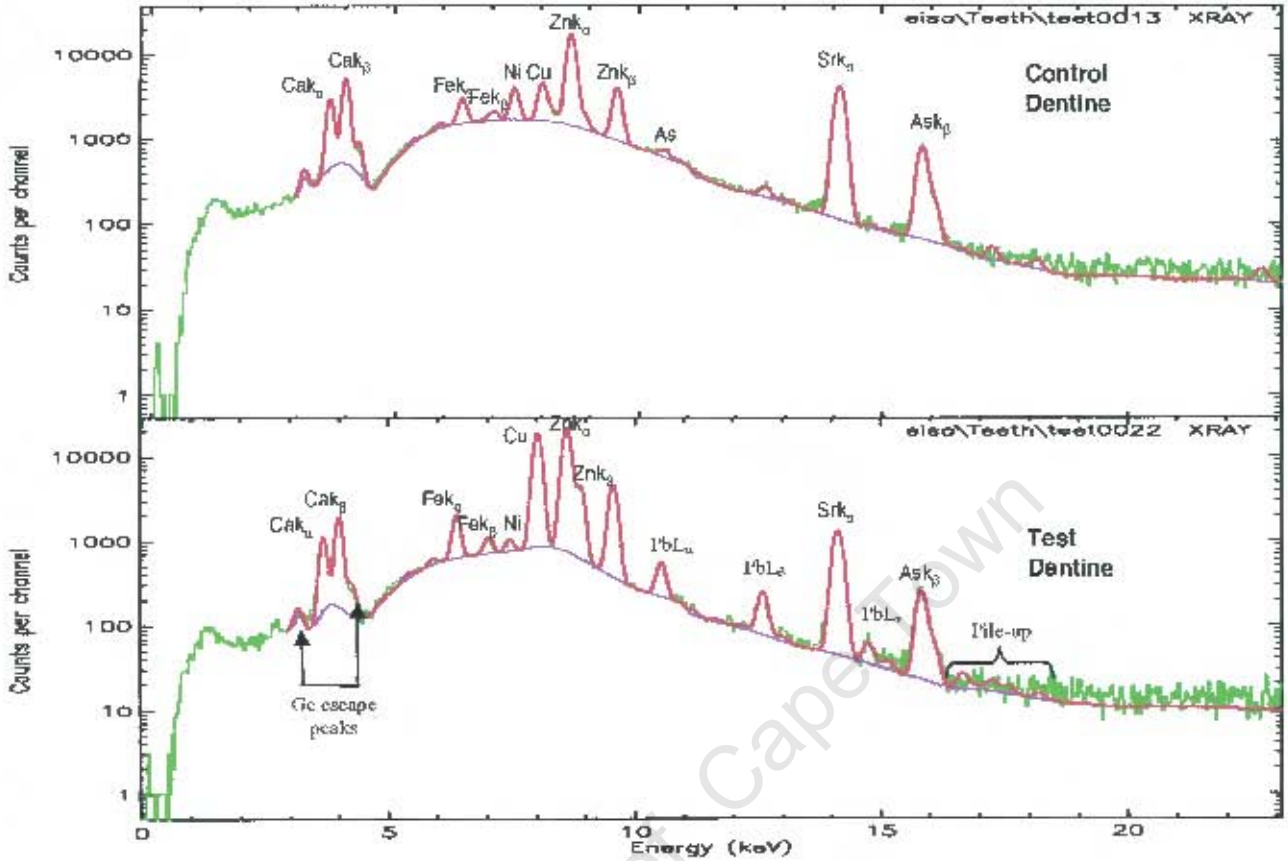

Figure 8.7: Same as Figure 8.6 but for the case of dentine.

Since an opposite situation does occur for Fe and Cu it is possible that a re-mineralisation mechanism may also occur. As a way to compare the concentration levels of Ca found by PIXE, these were compared to those found by p-BS expressed in weight % and assuming a density of similar value to that of hydroxyapatite (~3.19 g.cm^{-3}). The estimated error on the concentration found by p-BS is taken as an average over the whole scanned area. This value can be deduced from the expected chi-square from simulated and experimental data. Evaluated values from RUMP give a figure of ~10%. Concentration levels (in %) for the major components of some dentine and enamel specimens, including an interface measurement, as determined by p-BS with protons of 3.0 MeV are shown in Table 8.3. Ca in particular varies in the range 20-43% with the exception of one enamel for which value was 51.21%. If we compare these values to those found by PIXE (Table 8.2) we

with the hydroxyapatite stoichiometric value may be explained by resonances present in the proton energy range under investigation. More precise measurement of the Non-

Table 8.1: Evaluation of the typical atomic fractions for the components of the hydroxyapatite enamels and dentines.

		O	P	F	Ca
CONTROL	Dentine	5.1	1.1	1.0	2.9
	Enamel	5.0	0.9	1.1	3.0
TESTS	Dentine	6.5	0.5	0.5	2.5
	Enamel	6.0	0.4	0.6	3.0

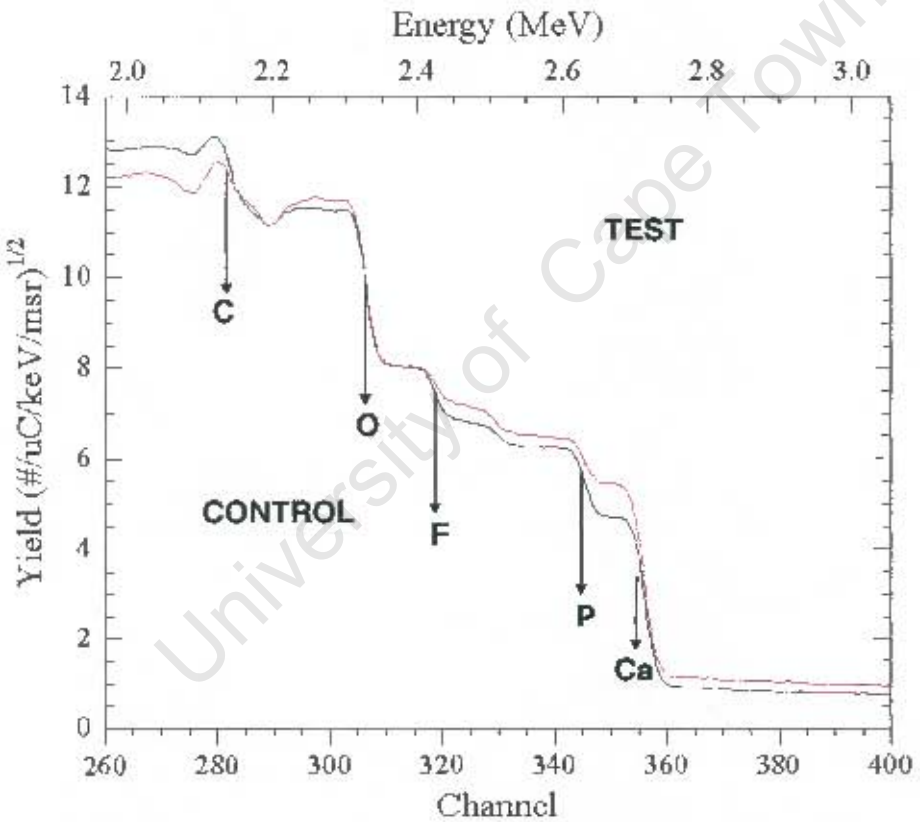

Figure 8.4: Comparison of backscattering spectra for an enamel control and test specimens showing the edge inflexion point for each element. E_p = 3.0 MeV. Accumulated charge was ~5 μC.

Rutherford cross section at our 176° geometry are needed in order to be able to have a "true" value for the cross sections. Data on these are in the process of being measured and evaluated. In spite of the above discussion we have confidence on the simulated

may observe that Ca oscillate between 26-36%. Considering that the variation of metal components in biological system is bound to relatively high standard deviations, it

Table 8.2: Trace element concentrations (in $\mu g.g^{-1}$) including Ca (in %) as determined by micro-PIXE in selected areas (enamel, dentine or the boundary between them) of specimens surfaces and sub-surfaces. Values in brackets represent the calculated MDLs. Some TE (Ni, Sr) appear to be depleted after erosive treatment. On the contrary Fe and Zn tend to increase in value with erosion.

	SURFACE TREATED	Irradiated on	Ca	Mn	Fe	Ni	Cu	Zn	Sr
CONTROLS	Dentine	Boundary	36.23±0.5 (0.39)	6±2 (2.5)	11±1 (1.4)	18.1±0.9 (1.1)	84±1 (0.9)	139±2 (0.8)	150±1 (0.7)
	Dentine	Dentine	31.37±0.6 (0.67)	5±2 (3.7)	27±1 (2.1)	16.6±0.7 (1.6)	169±3 (1.5)	324±3 (1.2)	123±2 (1)
	Dentine	Boundary	32.95±0.71 (0.47)	5±2 (3.1)	21±1 (1.8)	6.4±0.6 (1.3)	102±1 (1.2)	205±2 (0.9)	147±2 (0.9)
	Enamel	Enamel	36.10±0.42 (0.57)	5±2 (3)	15.7±0.9 (1.7)	18.6±0.8 (1.3)	80±1 (1.1)	188±2 (0.9)	146±2 (0.8)
	Enamel	Boundary	35.48±0.57 (0.65)	n.d.*	25±1 (1.9)	19.4±1 (1.5)	96±2 (1.3)	136±1 (1.1)	147±1 (1)
	Enamel	Boundary	32.22±0.57 (0.43)	n.d.*	34±1 (1.2)	25±1 (0.9)	29.6±0.5 (0.7)	149±2 (0.7)	132±1 (0.6)
TESTS	Dentine	Boundary	32.53±0.74 (0.65)	n.d.*	30±2 (2)	4.1±0.7 (1.6)	449±5 (1.4)	116±1 (1.2)	83±1 (1)
	Dentine	Boundary	31.13±0.55 (0.61)	n.d.*	46±1 (1.8)	2.1±0.7 (1.5)	502±6 (1.3)	131±1 (1.1)	85±1 (0.9)
	Dentine	Boundary	31.45±0.62 (0.58)	n.d.*	78±2 (1.7)	3.6±0.8 (1.4)	473±6 (1.2)	134±2 (1)	82±1 (0.9)
	Enamel	Boundary	28.61±0.54 (0.54)	n.d.*	77±2 (1.8)	7.4±0.8 (1.4)	441±5 (1.3)	469±4 (1.1)	95±2 (0.9)
	Enamel	Boundary	29.92±0.47 (0.72)	n.d.*	57±1 (2.2)	8±1 (1.8)	308±4 (1.7)	554±4 (1.4)	99±2 (1.3)
	Enamel	Boundary	26.95±0.82 (1.53)	n.d.*	56±3 (3.7)	7±1 (3.0)	561±7 (2.8)	709±5 (2.5)	120±3 (2.0)

*n.d: not detected

is logic to assume that the concentration of Ca found by p-BS is in some respect similar to that found by PIXE. Other major component such as O follow the same assumption. For the case of F its concentration is still dependent on the correction of the Non-Rutherford cross section database available at the present moment. However stoichiometric value of F on apatite (~1.24%) is quite similar to the found F mean value in Table 8.3 (~0.5%).

Table 8.3. Concentration levels (in %) for the major components of some dentine and enamel specimens, including an interface measurement, as determined by p-BS with protons of 3.0 MeV.

Specimen	Ca	P	F	O	C
Dentine	18.75	42.91	0.32	24.12	13.89
Enamel	28.43	26.10	0.041	32.28	13.16
Dentine	43.45	1.07	0.065	55.00	0.42
Interface	33.38	24.86	0.828	29.25	11.67
Dentine	28.62	30.18	0.048	32.33	8.83
Enamel	51.21	7.7	0.055	35.33	6.19
Dentine	23.69	30.49	0.386	32.39	13.03
Enamel	21.32	29.04	0.497	32.71	16.43

8.2.5 DYNAMIC MAPPING ANALYSIS

Elemental quantitative maps for Sr, and for Zn to a lesser extent, showed that their distribution levels over the area comprising the interface enamel-dentine were lower for the enamel. This applies particularly for specimens after erosion treatment. The depletion of Sr may act as a protectant against demineralization, contrary to the increase of concentration of certain elements such as Fe and Ni. Although it is not clear why there appears to be a re-mineralisation process for these two elements it is envisaged that their role in erosion is not well understood.

Figure 8.8 shows the Ca and Zn maps of a dentine control sample over an irradiated region covering its interface enamel-dentine. The mapping comparison between Ca and Zn maps (64 x 64 pixels; scan size ~1000 μm^2) in a two dimensional space (representing the level of correspondence between the two variables Ca and Zn) is shown on the left side of the figure. This clearly indicates two kinds of mapping distributions; each

associated with either the dentine or enamel area. The weakest mapping similarity corresponds to the enamel area. A similar type of rationale was found for the whole set of dentines.

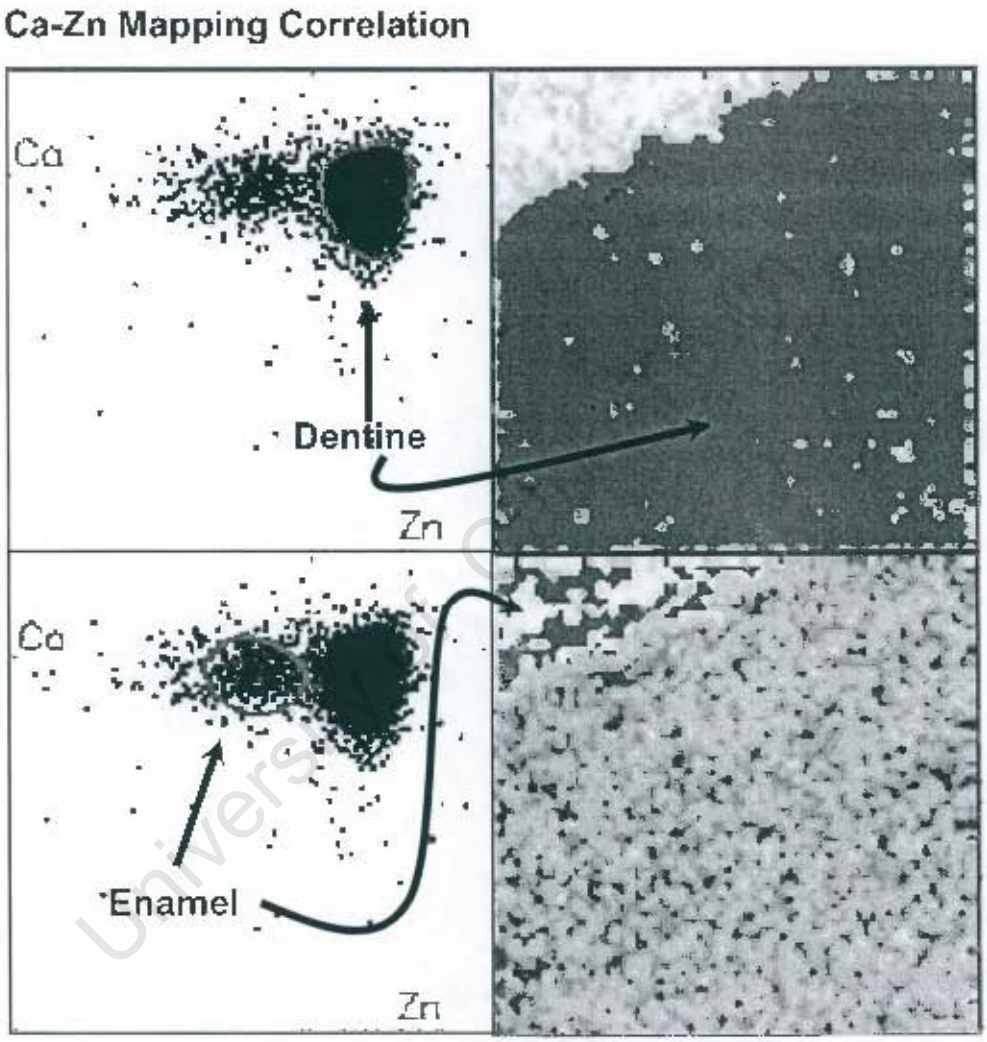

Figure 8.8: Ca and Zn mapping distribution in a dentine control sample irradiated over an area around the interface enamel-dentine. The similarity between the maps of both elements is shown on the left of the figure. This is expressed as two types of distributions, each associated with either the dentine or the enamel regions. These are indicated by different gray scales on the right side maps. The trend of the interface boundary is also visible. The weakest correlation corresponds to that of the enamel region.

The gradual variation of some elements such as Ni, Zn, Sr and to a lesser extent Cu and Fe over the interface enamel-dentine was investigated. The content of Zn and in particular Ni (not shown in the Figure 8.8) over the interface appeared as a wider band covering sections of the both the enamel and dentine regions with a gradual variation of the corresponding mapped element (see Figure 8.9). To assess these gradual linear variations, linear traverses were extracted from maps of selected elements. Figure 8.9

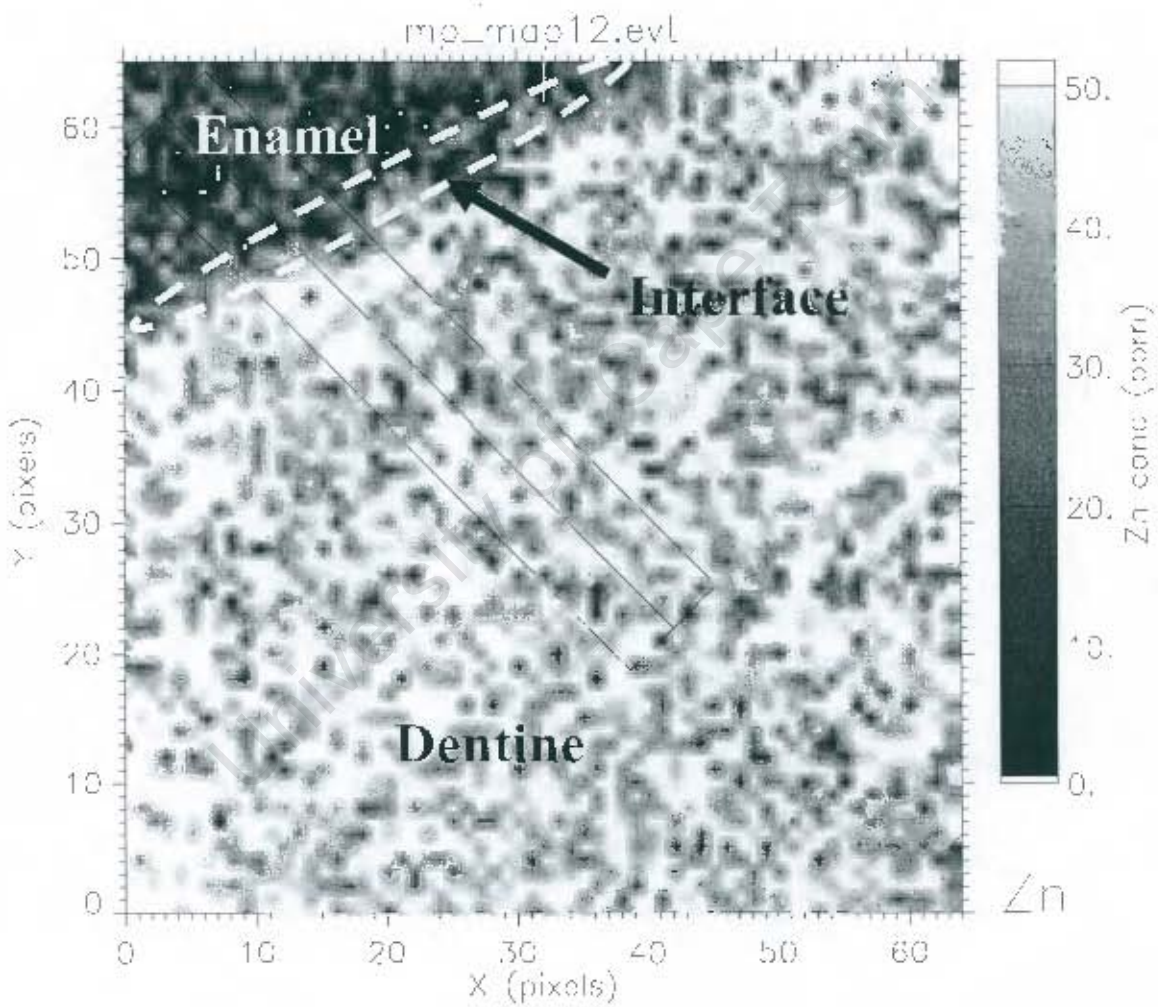

Figure 8.9: Quantitative maps of Zn for the same dentine control sample shown in Fig 8.8. The interface enamel-dentine is clearly visible. The rectangular shape highlighted over the map was used to extract the traverse profile by GeoPIXE II.

shows the map of Zn for the same dentine control sample (shown in Figure 8.8) where a transverse rectangular shape was used to extract the average elemental concentration over the linear direction of the rectangular shape. This information was plotted as a function of the distance (in μm) for Ca, Fe, Ni, Cu, Zn and Sr (see Figure 8.10).

It was found that most elements exhibit gradual variations of depletion or enrichment when considering the direction from the enamel to the dentine (see Figure 8.10). For example, Zn have a value of ~30 $\mu g.g^{-1}$ over the enamel region, its concentration level increased over the interface band to reach a value of ~70 $\mu g.g^{-1}$ in the direction to the dentine. Similar profile can be seeing for Ni. On the other hand Sr had an opposite behavior with lower values in the dentine area. Previous results on the concentration profiles of human teeth on the enamel-dentine interface showed similar trend for Sr [Pin04].

8.2.6 TEETH ENAMEL CHARACTERIZATION FROM A LOW INCOME POPULATION GROUP AT GUGULETHU, CAPE TOWN.

The problem of erosion in teeth has been addressed recently as one of the main causes of teeth decay, particularly in children from disadvantaged communities where the nutritional value of the daily diet is poor [Chi04]. At present there is relatively no data available on the concentration levels of major and trace elements in enamel in such population group. With a view to characterize the "true" elemental concentration levels of raw enamel, a set of about 30 intact teeth extracted from persons living in the Gugulethu region of Cape Town were obtained from the Department of Community Dentistry at the University of Stellenbosch, South Africa. Age distribution was for children (9-17 yrs) 17% and adults (8-68 yrs) 83%. Teeth samples from males (30%) and females (70%) were extracted under anesthesia. Most of the teeth consisted of molar and incisive specimens, some with the presence of decay at the top enamel surface. In order to gain information about the average elemental composition of enamel in such group and to establish a standard for enamel, PIXE using a Hp(Ge) detector was used at the nuclear microprobe at iThemba LABS. Since this detector efficiency covers a wider range of

energies including low energy gamma-rays such as the 110, 197 keV lines from the ^{19}F (p,pγ) ^{19}F reaction then simultaneous analysis of F was performed.

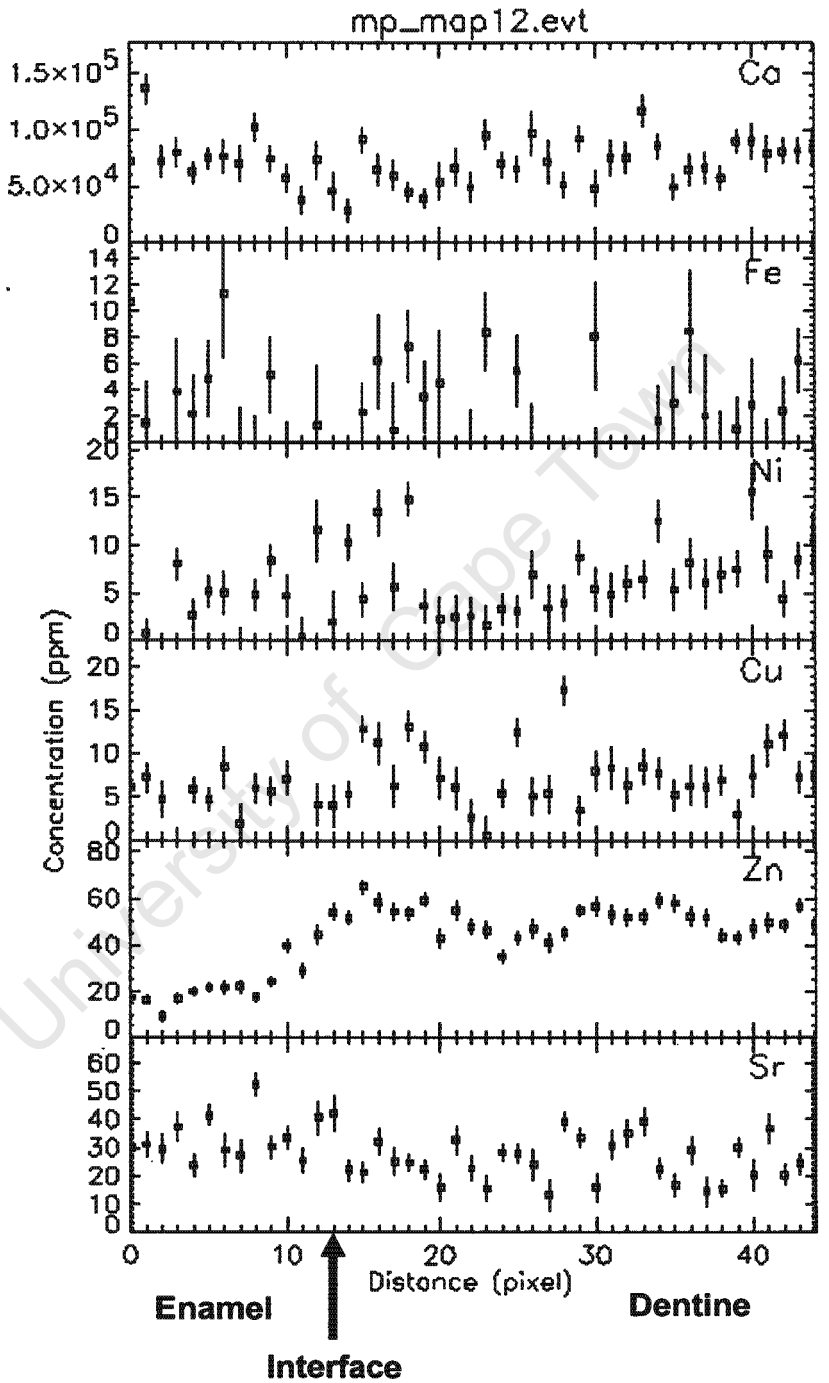

Figure 8.10: Linear traverses as indicated in Figure 4 extracted from maps of selected elements over the same area of Figure 8.9. Concentration levels (in $\mu g.g^{-1}$) are shown for the enamel and dentine region. The arrow indicates the position of their interface.

Samples were analysed intact without any prior chemical treatment. Only the area exposed to 3.0 MeV proton beam probe was cleaned with de-ionised water to remove possible organic material bounded to the teeth as particulates which may have influence the true content of trace elements. An aluminum absorber (102 μm thick) was selected. Irradiations were done on the outer surface (enamel) of all teeth. Since information at high resolution was not a requirement then the proton beam was focused to a size of ~3 x 4 μm^2. Scanned areas of ~200 μm^2 and beam current ranging between 200-300 pA (with a integrated total charge of about ~0.8 μC) were used. The dominant elements determined were Fe, Zn and Sr, using the X-ray Kα line and Fluorine using the 110 keV gamma-ray from the reaction ^{19}F (p,pγ) ^{19}F. This gamma-ray was detected simultaneously by the Hp(Ge) detector. For this purpose an energy calibration of 130 eV per channel was used to cover energies from 3 to 130 keV (see Table 8.4). The standard reference material Apatite supplied by Astimex Scientific Ltd. (Toronto) was used to convert gamma-ray yield into concentration (see section 6.4).

Mean concentration levels for all elements appeared similar when looking at the ratio of sex (Zn: 1.0, Sr: 1.4 and F: 1.1) and age (Zn: 0.8, Sr: 0.9 and F: 1.0), see Table 8.5. Although the standard deviations are high as expected from biological system variability, the mean values reflect some group homogeneity irrespective of sex and/or age. However this variability appear to be smaller for Zn and F in the children sub-group.

Table 8.4: Trace elemental concentrations (in $\mu g.g^{-1}$) by micro-PIXE on selected specimens of the Gugulethu teeth sample. The values for F are given in [%].

Sample Code	Age	Sex	Fe	Zn	Sr	F[%]*
Gug11	A[1]	F	n.d.	744±3	89±6	1.31
Gug12	A	M	18±7	999±8	43±3	0.67
Gug13	A	F	n.d.	379±3	84±4	0.39
Gug14	C[2]	M	12±4	693±9	65±5	2.15
Gug15	A	F	n.d.	972±7	52±4	0.69
Gug16	A	M	n.d.	783±6	68±5	0.13
Gug17	A	F	10±3	684±4	102±5	2.56
Gug18	n.a.	n.a.	n.d.	952±8	73±4	1.16
Gug19	A	F	46±6	45±2	161±7	0.41
Gug20	C	F	n.d.	751±5	55±4	0.67
Gug22	A	M	242±17	174±6	18±2	0.97
Gug23	A	F	n.d.	1144±11	66±4	4.72
Gug24	A	F	n.d.	638±4	92±4	1.42
Gug25	A	M	n.d.	716±4	102±6	4.20
Gug26	A	M	n.d.	494±4	94±6	1.00
Gug28	A	M	92±9	601±7	85±4	2.01
Gug29	n.a.	n.a.	16±4	733±4	105±5	5.71
Gug31	A	F	42±4	571±5	94±3	4.07
Gug32	C	F	n.d.	972±6	176±7	1.76
Gug33	A	F	47±4	631±5	44±3	2.92
Gug34	A	F	17±5	794±6	109±3.9	2.42
Gug45	C	M	57±11	692±4	82±6	1.77
Gug46	C	F	n.d.	973±4	n.d.	2.28
Gug47	A	F	22±3	592±6	105±2	2.86
Gug48	A	F	n.d.	121±4	n.d.	n.d.
Gug49	A	F	20±3	963±7	114±6	1.71
Gug50	A	F	17±3	955±7	110±5	1.94
Gug51	A	F	17±4	279±3	126±4	0.07
Gug52	A	F	n.d.	185±4	118±6	0.01
Gug53	A	F	n.d.	867±14	50±25	n.d.

* Relative error of determination estimated as 7%.

[1] A = Adult; [2] C = Child

n.d. = Not Detected

n.a. = Not availlable

Table 8.5: Descriptive statistics of the teeth sample concentration levels: mean, standard deviation (STD) and relative error. The ratio related to sex or age is also given.

BY SEX				
	Zn	Sr	F[%]*	Sex
Mean	663.0	97.1	1.8	F
STD	317.4	36.3	1.3	F
Rel. Err.	47.9	37.4	71.7	F
Ratio F/M	1.0	1.4	1.1	
Mean	644.0	69.6	1.6	M
STD	239.2	27.9	1.3	M
Rel. Err.	37.1	40.0	77.9	M
BY AGE				
	Zn	Sr	F[%]*	Age
Mean	623.1	87.5	1.7	A
STD	307.5	45.2	1.4	A
Rel. Err.	49.4	51.6	81.3	A
Ratio A/C	0.8	0.9	1.0	
Mean	816.2	94.5	1.7	C
STD	144.7	55.5	0.6	C
Rel. Err.	17.7	58.7	36.7	C

8.2.7. CONCLUSION AND DISCUSSION

The process of demineralization in teeth erosion due to exposure to acidic media was investigated in a group of test and control healthy human molar teeth. Information on the major components showed marked differences between controls and tests particularly for O, P and F. The atomic ratios of major constituents in the matrix were characteristic of test or controls with typical ratios: $O_5P_1Ca_3F_1$ for tests and $O_6P_{0.5}Ca_3F_{0.5}$ for controls. Analysis by micro-PIXE showed that the levels of trace elements (TE) were enriched and/or depleted according to the type of erosion treatment. Quantitative micro-PIXE results showed a significant depletion or increase in some TE, particularly Fe, Ni, Cu, Zn and Sr for tests samples (see Table 8.2). On the other hand the correlation between maps of Ca and Zn in and around the interface between dentine and enamel in control samples

showed two types of mapping similarities (for enamel and dentine). The strongest was related to the enamel area.

Mapping comparison showed that the spatial variability of TE within the enamel-dentine interface was distinguished for both enamel and dentine and might give vital information as to the role of TE in early erosion lesions. It appears that the structure of dentine and enamel is not uniform with respect to the spatial distribution of TE and this may determine the cause of teeth demineralization processes exposed to acidic media. On the other hand the weak or strong reaction of the teeth to overcome the depletion of minerals and their clinical implications should be studied in the future.

In relation to the study of teeth from a disadvantaged community in Gugulethu, Cape Town, the main conclusion to be made is that in spite of high variability of the trace elements concentration the mean value appear to be similar for all sub-groups (male, females, adult or children). A smaller standard deviation was found for the children sub-group, particularly for Zn and F. A novel methodology which has been explored recently [Sha04] was the determination of F from the 110 keV gamma-ray simultaneously with X-ray signal from Zn and Sr using the strength of the Hp(Ge) detector. With this information on hand, future investigations will allow us to correlate the content of F with possible de-mineralization in teeth and nutritional value.

8.3 ANALYSIS OF HUMAN KIDNEY STONES: COMPARISON BETEEWN TWO POPULATION GROUPS

8.3.1 Introduction

During the past two decades a great deal of scientific effort has been directed at the characterization and studying the formation of kidney stones [Bro81, Smi81, Sch85, Gal89, Pal90, Pin94, Pin96, and Ash01]. However the hope that such studies would reveal the cause of urinary calculus formation has not yet been realized, the main reason being the multiplicity of factors contributing to the process of formation of stones. Amongst these causal factors, pathological changes of the kidney and metabolic disorders [Pak76], in addition to geographical, environmental, ethnic and family related parameters have been shown to predispose certain people to stone formation [Vah79].

The analyses of calculi have shown that all stones formed within the urinary tract, irrespective of cause or composition, have, in addition to the crystalline inorganic substances a second basic component, namely an organic matrix mixed with the crystal aggregates [Boy59]. The most common matrix observed in kidney stones is calcium oxalate. The calcium oxalate appears typically in three forms: the monohydrate $CaC_2O_4.H_2O$ (COM), the dihydrate $CaC_2O_4.2H_2O$ (COD) and the trihydrate $CaC_2O_4.3H_2O$ (COT). Each one of these could also be present as different crystallographic sub-groups, such as two COM monoclinic varieties with different unit cell parameters sizes. However other crystallographic variations of these common three may also occur (see Figure 8.11). This knowledge, together with data obtained from crystallization experiments, has led to the development of the known theories of stones formation. There are three mechanisms which are of importance in kidney stone formation. These are nucleation, crystal growth and aggregation [Nan83]. Nucleation refers to the birth of sub-microscopic molecular species of critical size within the supersaturated solution [Ver68]. This initial event can be either homogeneous or heterogeneous, involving nucleation of more than one phase. As a consequence of recurrent supersaturation and other factors, aggregation of the formed crystal may occur, either by sintering or by interparticle bridging of polymeric

material [Fin77]. With the subsequent trapping of the resulting polycrystalline mass in the kidney, a stone is formed.

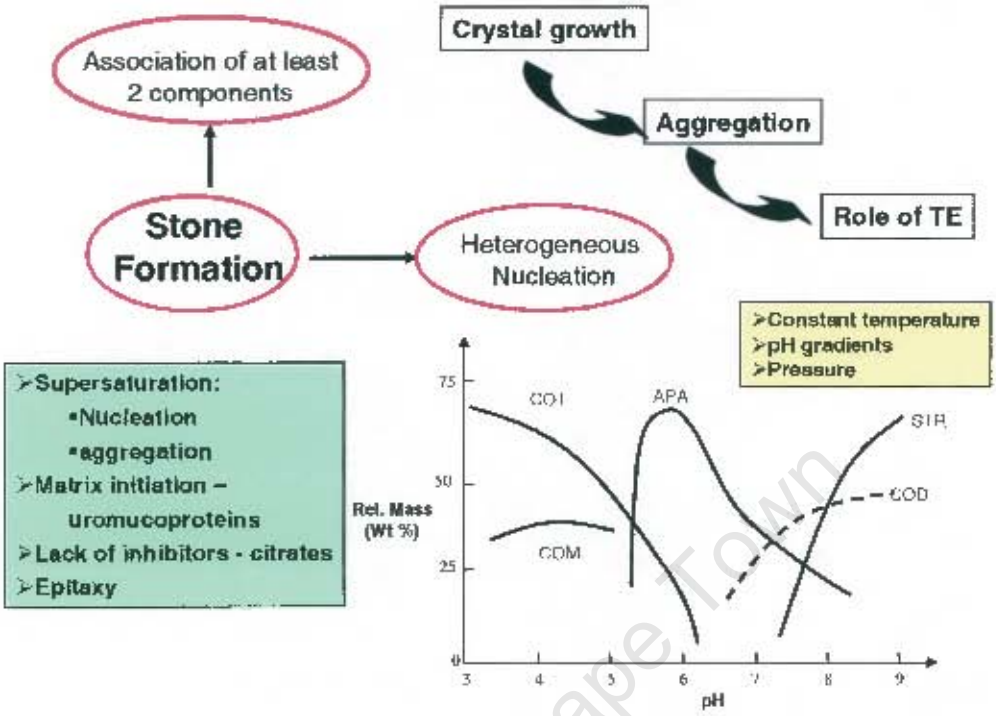

Figue 8.11: Calcium oxalate kidney stone formation model showing the rate of phase development with pH of supersaturated solution. (APA: Apatite; STR: Struvite). Temperature, pressure and lack of inhibitors such as citrates are also critical in the nucleation stage [Wan86].

Two clinical studies have addressed the important question of whether any correlation exists between the trace elements (TE) contents of calculi and that of urine and serum of the patient from whom the stones were obtained [Joo87, Hof89].

In the context of calcium oxalate stones particular interest is being paid to the effect of trace element aggregates as promoters or inhibitors in the three stages of stone formation.

The present study concentrates on the determination of trace elements (TE) in human kidney stones by nuclear microprobe (NMP). Interest was focused on determining levels of variability in elemental concentration of Ca and TE throughout selected micro-regions of two sets of kidney stones, from Sudan and from South Africa. The emphasis was on a statistical comparison of the two groups in terms of their elemental profile content by country and to establish if a general trend in terms of elemental

variability could be establish based on data obtained from microanalysis by PIXE and proton backscattering (BS). A statistical comparison of the two groups of stones is significant since this could highlight differences in terms of climatic conditions, geographical circumstances as well as diet.

8.3.2 Concretions description and measurements methodology

Eleven kidney concretions from the central regions of Sudan and eight from the Western regions of South Africa were considered for this investigation. Size of stones varied from small (~1-3 mm) to big (~1-3 cm) with masses of 5 mg to 5 g (see Figure 8.12). The topography was rough with accentuated sharp edges. Colour of stones varied from light brown to darkish grey. Clinically removed concretions were embedded in epoxy at room temperature. Cross sections through the core were cut with a diamond saw. The two resulting flat half surfaces were carbon coated prior to proton bombardment (see Figure 8.13). One half was used for micro-PIXE and the second one for X-ray diffraction (XRD) analysis.

Figure 8.12: A South African calcium oxalate calculi (left side) exhibiting the three phases COM, COD and COT. Sudanese were mostly oxalates with some showing an uricite structure at the core (right side)

Most analyses were focused into measurements in and around the core region of the stone. However irradiations were perform as well in the outercore, to study the elemental profile at particular growth localization outside the nucleation volume. The nucleation cell at the core of the concretions, in particular, some times could contain

crystals of mixed phases which could generate epitaxial growth of phases other than the currently present at the core of kidney stones [Mcy75, Man80]. This can be observed clearly in the South African stone in Figure 8.12 where both the COM and a mixture of COD/COT are present. Typically the nucleation zone occupies a small volume within the bulk of the calculi, which size depends on the type and mass of the whole concretion. For example the uricite stone in Figure 8.13a with a diameter of ~30 mm has a nucleation core of ~ 2-4 mm with layers of growth formed in the radial direction towards the outer core. For the South African kidney stones series on the other hand, where average mass was smaller (~2-6 mm in diameter), the core measured only tens of μm. In Figure 8.13b micrographs of some concretions for both South African and Sudanese groups show clearly these variations in size and structure of the flat concretions surface. In general South African calculi were smaller than the Sudanese however most of then were calcium oxalates.

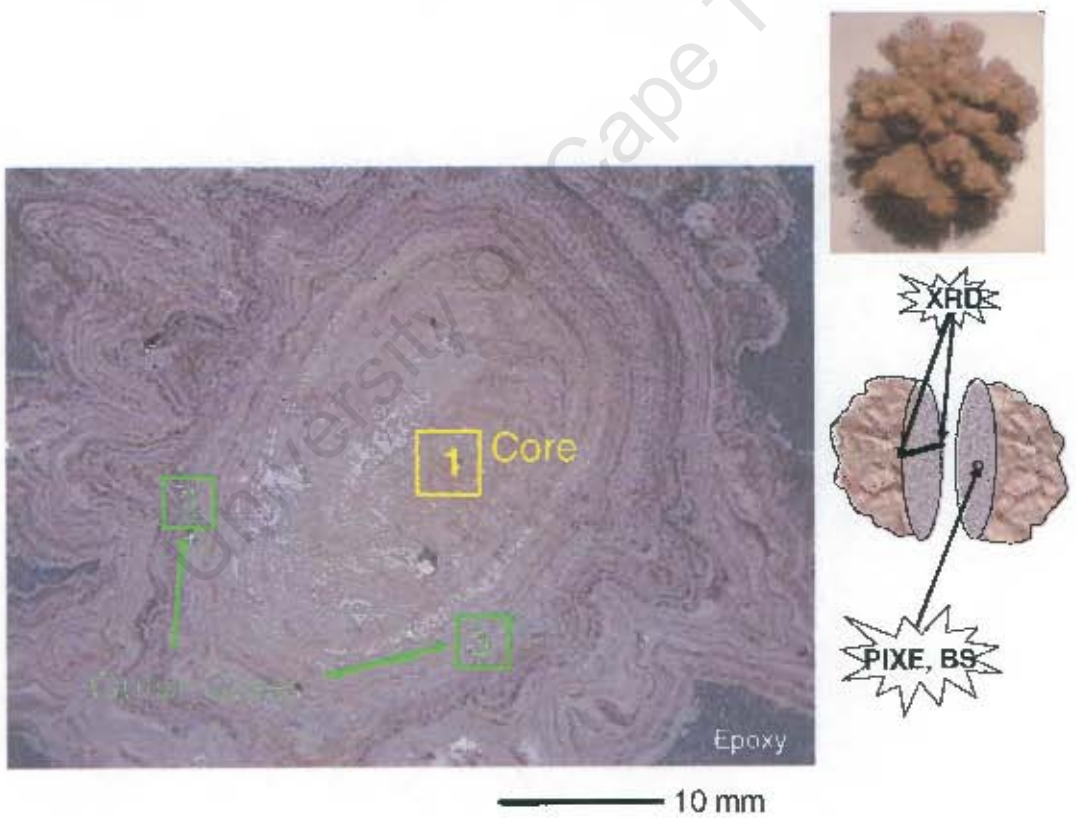

Figure 8.13a: A Sudanese calculi flat surface after cutting through the core with a diamond saw. Two halves were obtained: one used for PIXE and p-BS, and the other one for powder XRD spectrometry.(1) Core (2and3) Out of the Core

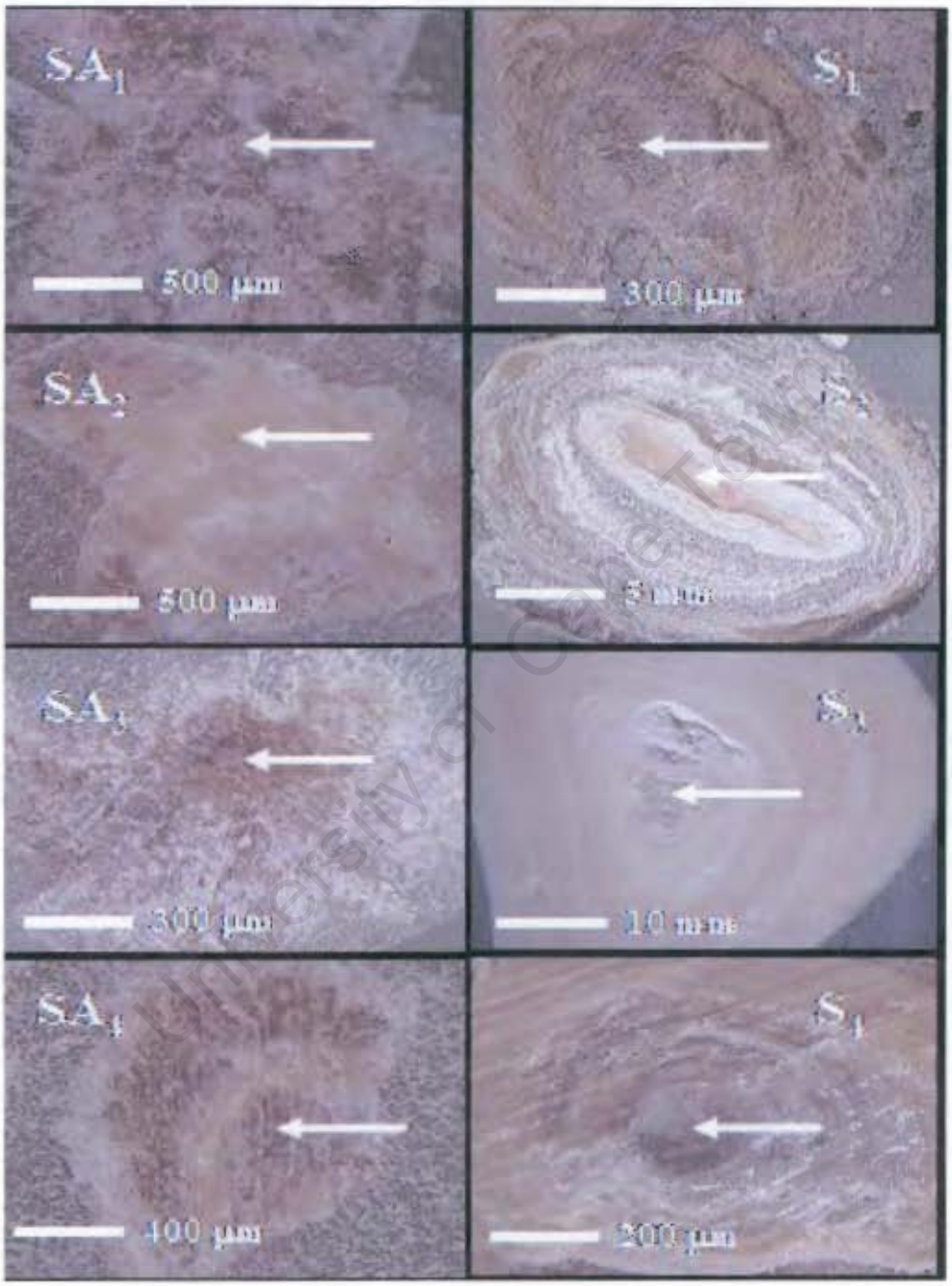

Figure 8.13b: Micrographs of some of representative calculi for the South African (SA) and Sudanese (S) groups. The size is indicated by the scale bar and the white arrow is pointing to the nucleation region, where analyses were normally performed.

A summary of the main steps of the analytical methodology is shown in Figure 8.14. Samples were irradiated with 3 MeV protons. Beam currents of ~200-400 pA were used to ensure that no loss of metal constituents occurred due to possible a rise in temperature generated at the probed sample volume (to a depth of ~30 mg/cm^2). Micro-regions (~100-1000 μm^2) of interest were scanned by the 2-4 μm beam probe, at dwell time of 10 ms, Scan size of 128 x 128 pixels were used to ensure a good resolution for mapping visualization. True, overlap-resolved elemental maps as well as total micro-PIXE data were obtained using the method of Dynamic Analysis (DA) [Rya02c]. Simultaneous proton-BS information was also recorded for on major/minor components.

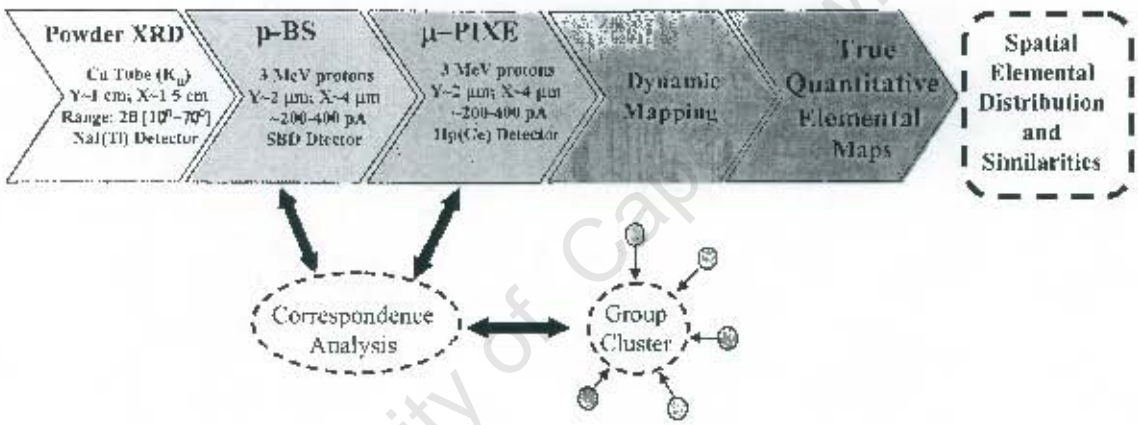

Figure 8.14: Main steps in the methodology for characterization of the kidney stone concretions. Correspondence Analysis (CA) provides a tool for cluster classification according to region.

8.3.3 p-BS and XRD spectrometry determinations

Major components C, O, N and Ca were determined by proton-BS. Table 8.6 shows the atomic ratios as determined by BS, as well as the phase identification on kidney stone samples as determined by X-Ray powder diffractometry (XRD). Phases determination were done using the 1998 ICDD release data [Pow98]. Of interest is the fact that some of the stone phase identification did not correspond to the BS ratio evaluation. Since the size of the micro-region irradiated in and around the stones core by micro-PIXE was of few hundred μm^2, the actual elemental results by PIXE are

focused exclusively to this micro-area. In contrast, the analytical area in XRD determinations was ~ 1 x 1.5 cm^2.

The rationale for the above discussion is substantiated well by the BS spectra of Figure 8.14a, where a South African sample (2240A, with COM/COD core structure) and a Sudanese (S5, with uricite core structure) are compared. It shows the presence of nitrogen in the Sudanese stone (S5) which is related to the core phase structure as determined by p-BS. Moreover analyses by XRD showed that the main structure in S5 was COM. The simulations of both spectra are also shown in the figure. The relative high chi-square value found for the simulation of the South African sample in particular, may be connected to the use of non-Rutherford scattering cross section for protons at a geometry angle (176^0) which is not the exact angle used at iThemba LABS.

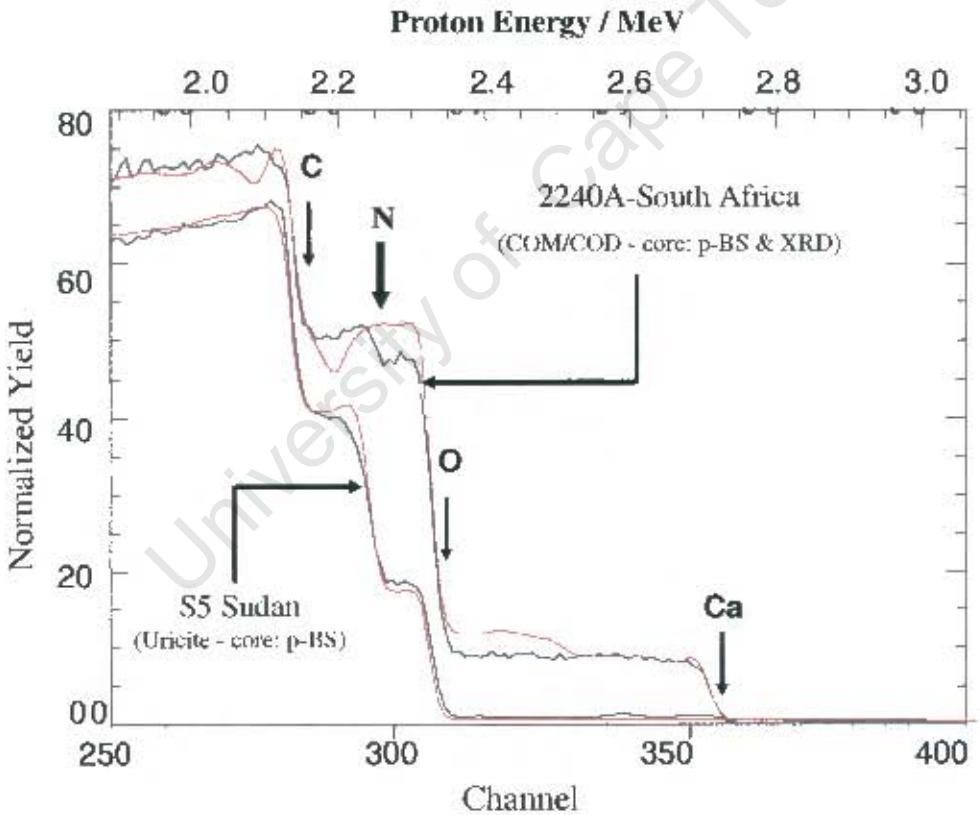

Figure 8.14a: Comparison of p-BS spectra for a calcium oxalate South African (2240A) and a uricite Sudanese (S5) calculi analysed at the core. Notice the presence of N in the Sudanese stone.

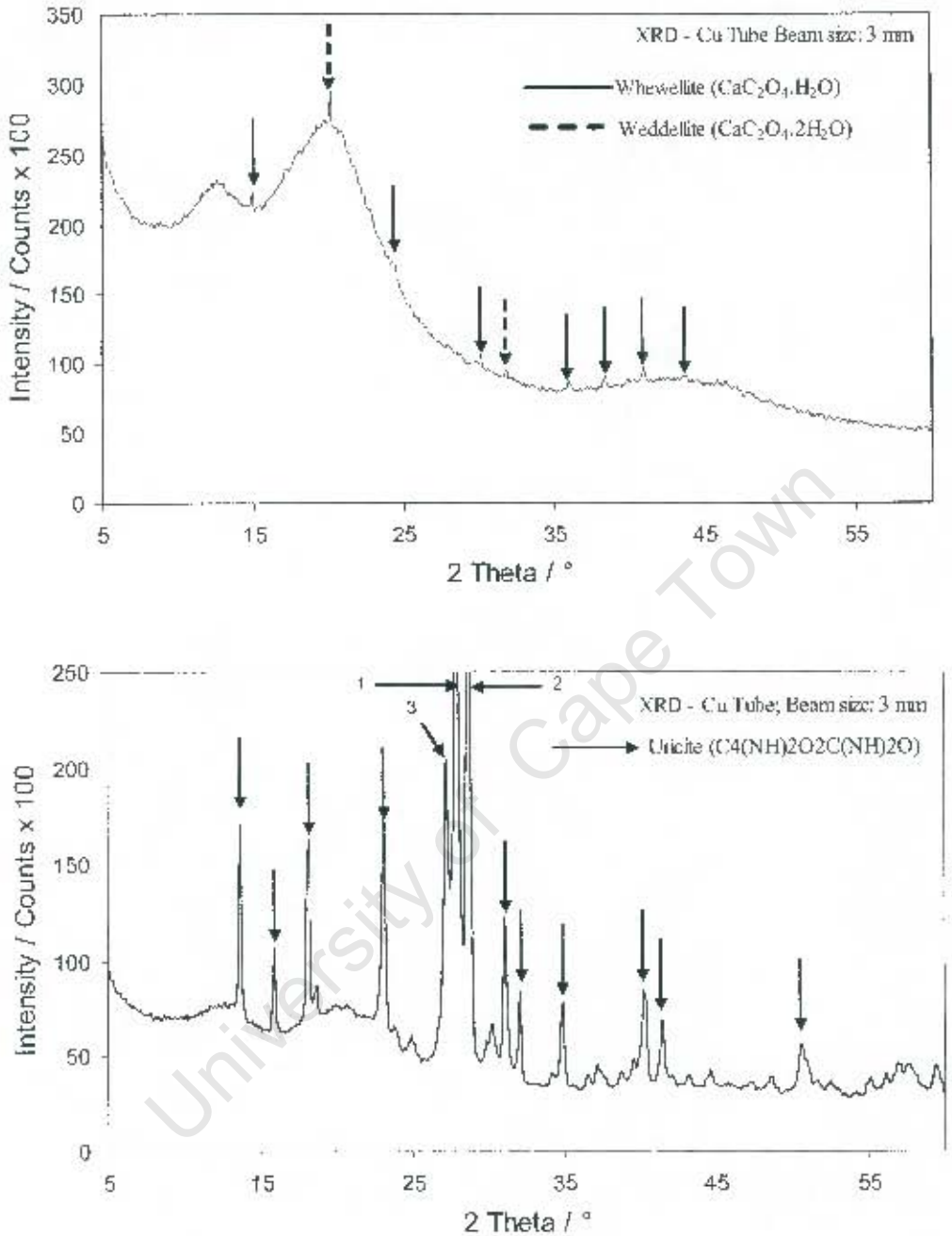

Figure 8.15: XRD spectrum of a Whewellite-Weddellite (COM-COD) type sample (2240 from South Africa; see Table 8.6) and an Uricite type (4 from Sudan; see Table 8.6).

Their matrix composition (as determined by proton-BS) was in general calcium oxalate monohydrate: Whewellite (COM) and/or dehydrate: Weddellite (COD) (see Figure 8.15). The Sudanese group had matrices, which exhibit a combination of both COD and COM, but in addition some of the stones areas were rich in other type of

phases such as uricite (see Table 8.6 and Figure 8.15). On the other hand some Sudanese samples exhibited two phases of COM monoclinic shown in Figure 8.16 for stone S5. The occurrence of the two COM monoclinic phases may suggest that a similar combination could also appear in the case of other crystallographic groups such uricite. However this hypothesis was not explored in this work.

Since the XRD analysis performed with the XRD powder machine at iThemba LABS use a Cu X-Ray beam with a lateral size of 1.5 cm as compared with that of the NMP beam (size of ~2-3 μm), the total area analysed in XRD covered the whole stone surface. From the above we can deduce (see Table 8.6) that uricite matrix in the core of the 2260 stone did precipitate the formation of COD matrix in the outer core of the stone. This was found from a second irradiation of the stone in the outer core. A reverse process occurred in the case of the S3 stone from Sudan as shown in Table 8.6. The above discussion is illustrated in a better way in Figure 8.17, where the atomic ratios of the matrix composition (at the core) found by p-BS for stone S6 don't correlate with the COM phase found by XRD.

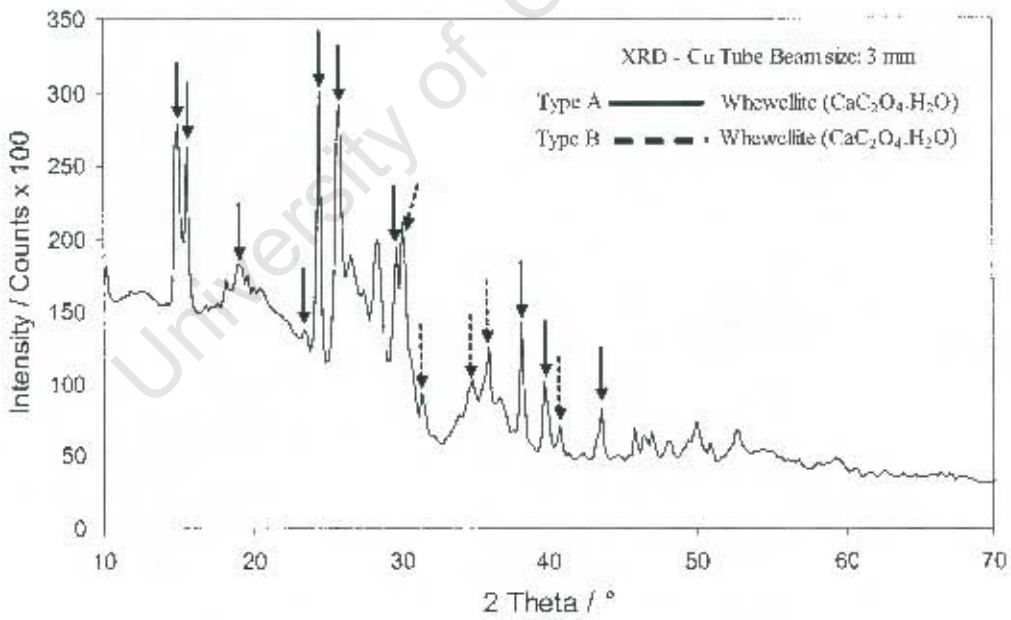

Figure 8.16: XRD spectrum of a Whewellite type sample (S5 from Sudan; see Table 8.6) showing the presence of two different monoclinic phases: Type A and B in the figure. Diffraction lines in the region around 50 degrees are also type A.

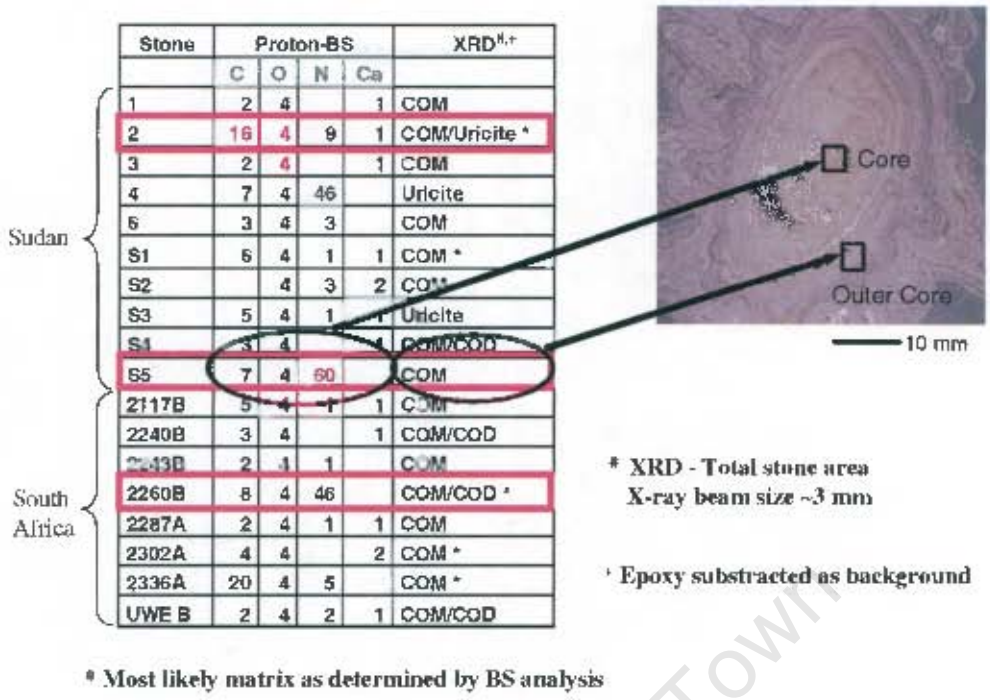

Figure 8.17: The atomic ratios for stone S5 (Sudan) found by p-BS (at the core) point out to a N-rich type matrix. For comparison the COM phase found by the XRD analysis at the outer core is shown. The opposite occurred for the stone S3.

8.3.4 μ-PIXE determinations: results from total content

The elements Fe, Cu, Zn, Sr, Br and Sr were determined by μPIXE. Their concentration levels are shown in Table 8.6. The analyses were directed primarily to the core of the concretions. Therefore the concentrations given in Table 8.6 are related to the particular phase found within the core of each kidney stone. In general, the spatial distribution of Ca (as major component) in most stones was non-uniform, with concentration values in the range 15-40%. Our focus were on micro-PIXE data showing the spatial distribution of TE, particularly Fe, Cu, Zn and Sr for both groups of kidney concretions. Two typical PIXE spectra of the total X-ray counts over a whole particular area are shown in Figure 8.18. In addition to the main elements cited previously small traces of Mn, Ni and Pb were also detected, however these were not included in the analysis of results. Due to the presence of pile-up in and around the region of Pb L_α lines (~10.5 keV) this element was not included in the final results. On the other hand Mn and Ni were below the detection limits in most of samples.

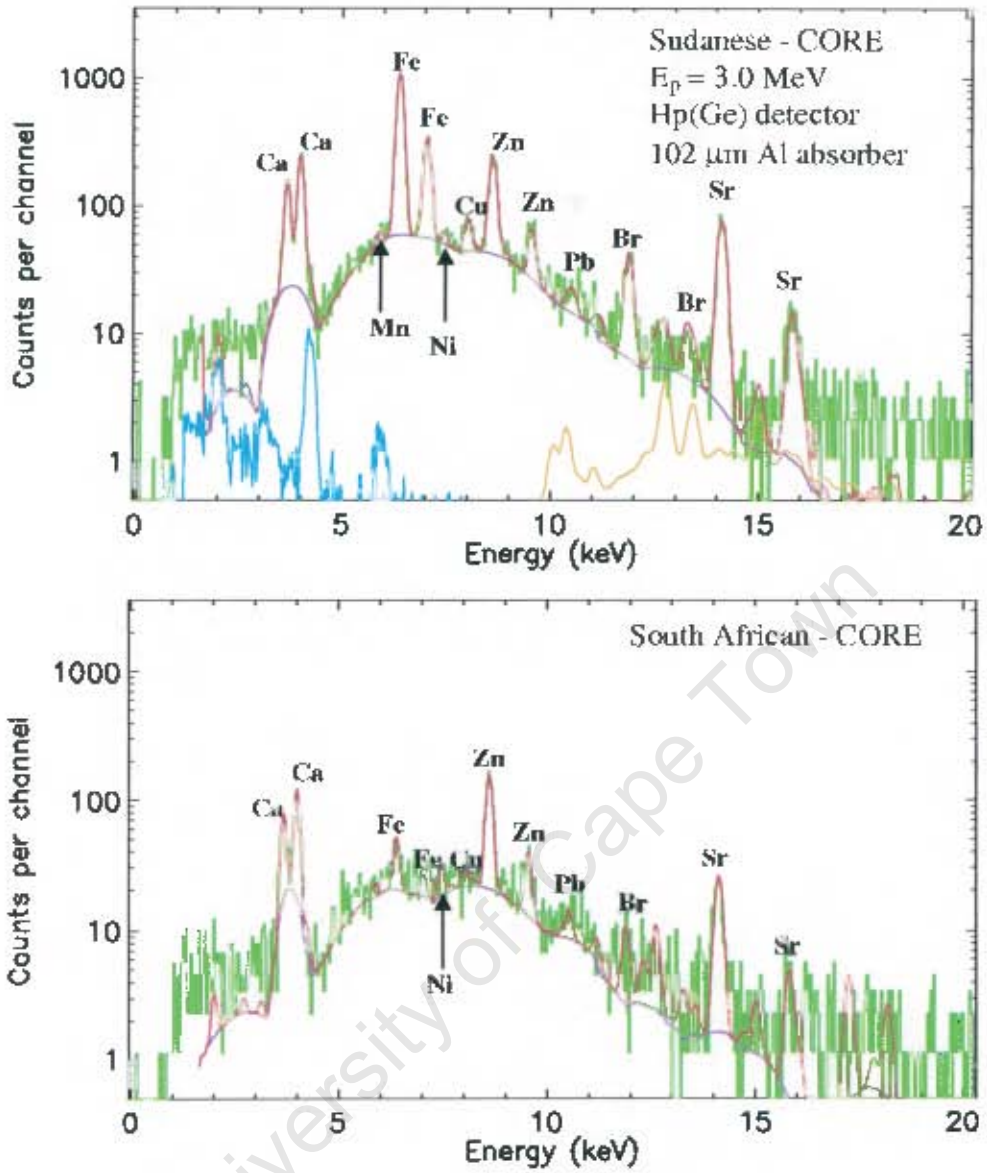

Figure 8.18: PIXE spectra obtained with 3 MeV protons and a Hp(Ge) detector (see details in section 7.3) on South African and a Sudanese stones. A 102 µm Al absorber was used to reduce the high intensity signal for the Ca K-lines. The pile-up and Ge escape peak profiles are also shown in the figure.

The histogram of the elemental concentrations ($\mu g g^{-1}$) at the core for the two kidney stones series is shown in Figure 8.19. Of importance are the high levels of Fe and Zn for some Sudanese concretions (S1, S3) and South Africans (2302A, 2240B). The Sample 4 (an Uricite matrix) showed elevated levels of Sr which correlate with the fact that analysis by XRD gave an overall COM type. matrix for the outer core.

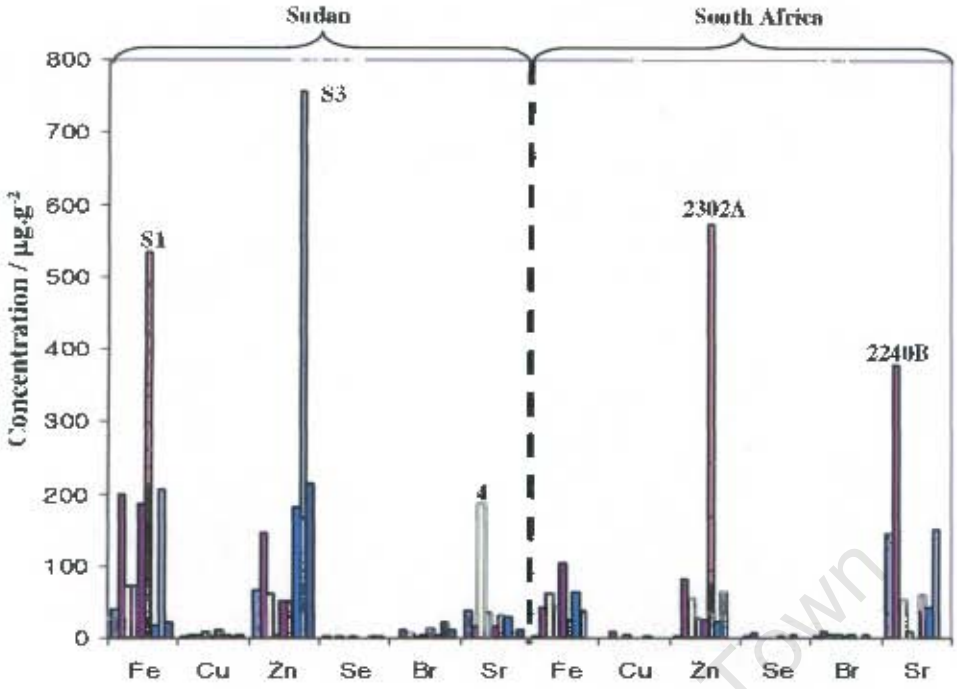

Figure 8.19: Histogram of the elemental concentrations ($\mu g g^{-1}$) at the core for the two kidney stones series. Notice the high levels of Fe and Zn for some Sudanese concretions (S1, S3) and South African (2302A, 2240B). Sample 4 (an Uricite matrix) showed elevated levels of Sr.

Mean values of the concentration levels for each TE in each population group were plotted to determine the level of correlation between the mean trace elemental profiles of each group. This relationship (shown in Figure 8.20) highlights a type of linear correlation between mean profiles. In particular it can be clearly noted two kind of distribution governed in one hand by Zn, Fe and Sr, and Se, Cu and Br on the other hand. This point to a possible separation between group of stones which can be visualized by other kind of statistical analysis such as correspondence analysis (CA). Elemental concentrations of all stones as determined by µPIXE were submitted to correspondence analysis (CA) [Gre90]. Figure 8.21 shows the plot of the CA for the first two axes, which contains approximately 80% of all the statistical information. The South African stones were tight grouped near the origin of the CA plot and are mostly defined by Cu, Br and Sr, with a high correlation between Cu and Br.

Table 8.6: Trace elemental concentrations as determined by micro-PIXE in $mg.g^{-1}$ for the two South African and Sudanese groups. A set of sub-groups from Sudan (A and B) collected from population leaving in different regions of the Khartoum area are indicated in the left side of the table. Major components levels are given as atomic ratios determined by proton-BS. Qualitative identification of the kidney stones matrix phases were determined by powder XRD.

		Sample	Micro-PIXE						Proton-BS				XRD
			Fe	Cu	Zn	Se	Br	Sr	C	O	N	Ca	
Sudan	A	1	39±3.2	3.0±1.8	67±1.5	1.6±1.0	n.d.	151±1.6	2	4		1	COM
		2	200±2.7	5.5±1.0	145±1.3	1.1±0.9	10.3±1.1	43±1.4	16	4	9	1	COM/Uricite *
		3	73±5.4	4.0±2.4	61±2.5	3.0±2.5	6.0±2.0	59±2.5	2	4		1	COM
		4	73±1.3	8.7±0.51	4.2±0.37	0.9±0.3	1.8±0.4	0.6±0.4	7	4	46		Uricite
		6	185±2.6	3.3±1.2	50±0.95	1.4±0.7	4.8±0.73	9.1±0.9	3	4	3		COM
	B	S1	532±6.2	10.0±3.3	51±2.7	n.d.	13.0±2.6	52±2.6	6	4	1	1	COM *
		S2	17±4.3	4.0±2.6	182±2.2	n.d.	4.0±2.1	377±2.7		4	3	2	COM
		S3	205±2.6	2.6±1.6	755±1.4	3.1±1.1	22.8±1.4	143±1.9	5	4	1	1	Uricite
		S4	23±4.2	4.0±2.7	214±2.4	2.2±2.1	11.0±2.4	108±3.1	3	4		1	COM/COD
		S5	312±0.96	2.6±0.4	73.5±0.33	0.7±0.3	7.0±5.6	10.2±0.5	7	4	60		COM
South Africa		2117B	n.d.	n.d.	1.6±1.0	1.5±1.3	2.8±1.6	7±2.0	5	4	1	1	COM *
		2240B	41±6	8.0±4.6	81±4.2	7.0±5.6	9.0±5.6	29±6.0	3	4		1	COM/COD
		2243B	61±4.5	n.d.	55±2.9	n.d.	5.0±4.2	32±5.5	2	4	1		COM
		2260B	45±4.3	4.0±2.4	27±2.4	n.d.	3.8±1.8	16±2.0	8	4	46		COM/COD *
		2287A	103±4.5	n.d.	24±2.2	n.d.	3.2±2.0	36±2.1	2	4	1	1	COM
		2302A	25±2.3	n.d.	572±1.3	1.3±1.1	4.5±1.1	185±1.4	4	4		2	COM *
		2336A	63±1.4	1.4±0.9	21±0.6	n.d.	0.8±0.6	15.2±0.6	20	4	5		COM *
		UWE B	38±6.5	n.d.	63±4.2	4.0±3.3	5.0±2.7	37±3.3	2	4	2	1	COM/COD

* Most likely matrix as determined by RBS analysis

n.d. = value is below the minimum detection limit.

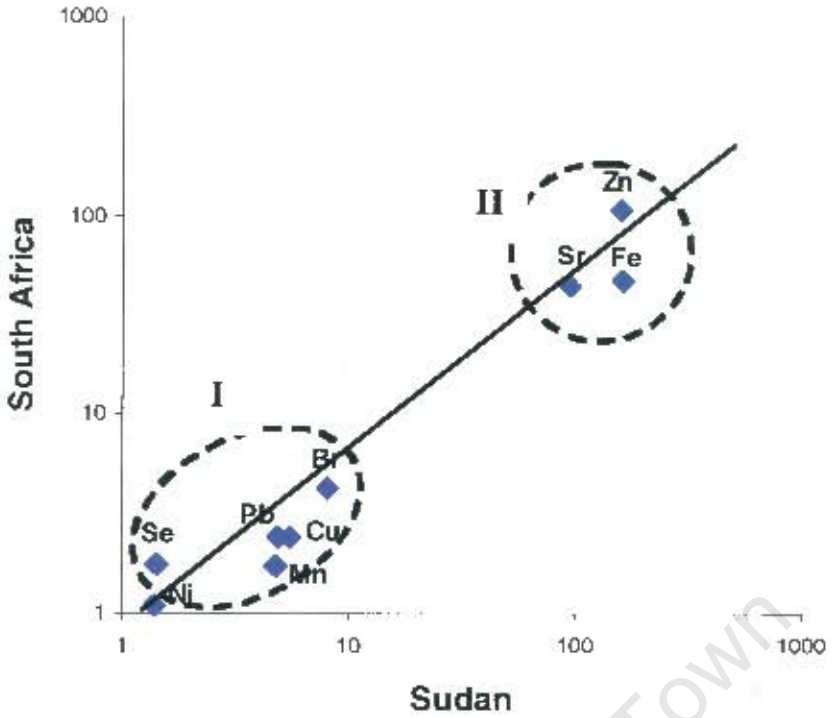

Figure 8.20: Plot of the mean value trace elemental profile for both the South African and Sudanese concretion groups. A type of linear relationship governs the relationship with two types of distributions: I and II. The position of Mn, Ni and Pb do not play a major role in the definition of the two.

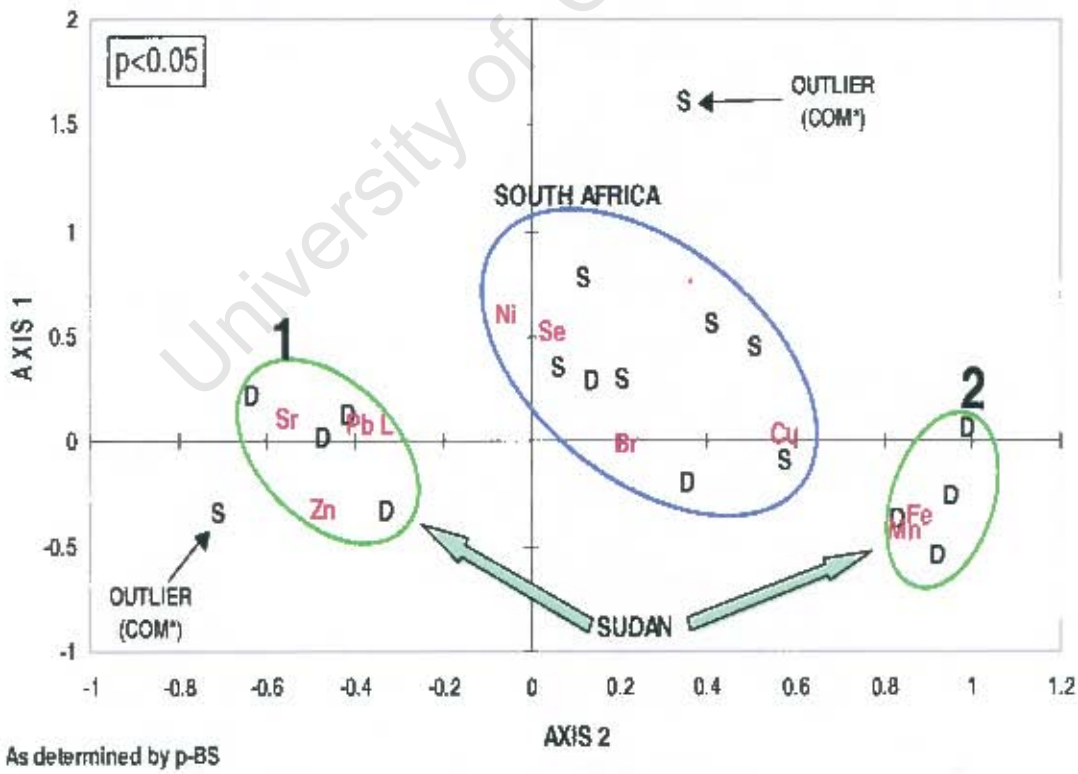

* As determined by p-BS

Figure 8.21: Correspondence Analysis of the first two axes for the two groups of kidney stones from Sudan (D) and South Africa (S). Stones from South Africa are clearly clustered into one group. One outlier (S) has elemental profile that resembles mostly the sub-group 1 from Sudan.

Two stones 2117 and 2302 were found to be outliers with 2302 mostly correlated with the Sudanese series.

The Sudanese series was clustered into two subgroups in the CA plot, characterized by high levels of Sr (sub-group 1) and Fe (sub-group 2). Two stones from Sudan 3A and 2B were found to be correlated with the South African group. Although the two subgroups of stones from Sudan (A and B) shown in Table 8.6, originated from two different regions within the Khartoum area in Sudan, the grouping found by CA analysis, does not appear to be associated with these two sub-groups (A and B) and therefore they are not associated with different geographical conditions prevalent in Sudan. On the contrary, Sudanese stones were grouped in the CA plot according to sub-groups 1 and 2 (see Figure 8.21). These two sub-groups contain Sudanese stones from both locations.

8.3.5 Elemental spatial distribution

As explained in Chapter 6 the calculation of elemental maps by the method of Dynamic Analysis take into consideration the calculation of a matrix transformation that convert counts into concentrations for a localised micro-region. Since in mapping mode the proton beam is moving pixel by pixel, it is expected, as discussed in section 8.3.3, that in average the matrix composition within a localised micro-region may change.

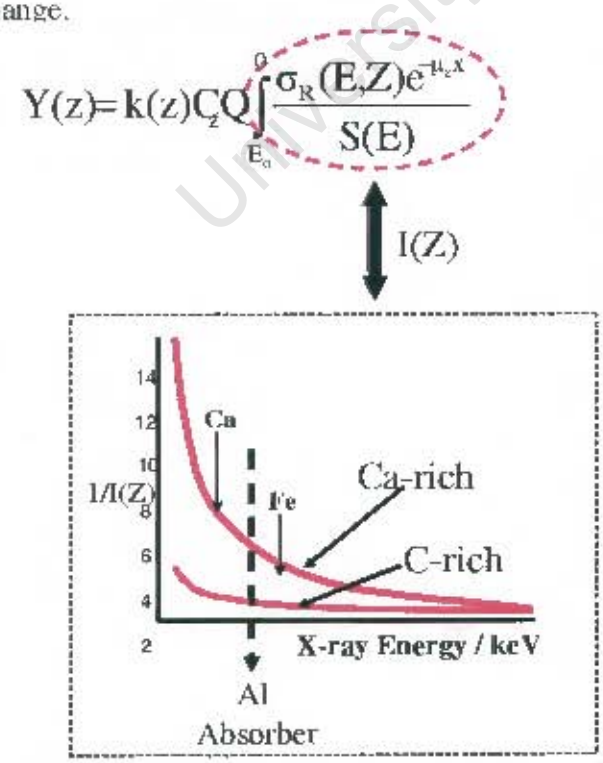

Figure 8.22: Variation of the matrix correction factor I(Z) with the X-ray energy in PIXE analysis. The X-ray yield Y(Z) involved in the calculation of the matrix transform during the method of Dynamic Mapping is heavily dependent on the localised matrix composition. This dependence is greatly influenced as well by the quality of database available.

This is particularly the case for Ca-rich biological materials in which the variation of the matrix correction factor I(Z) (see Figure 8.22) is heavily dependent on the localised matrix composition. This dependence is furthermore influenced by the quality of physical parameters database (see Chapter 6). Caution must therefore be exercised when dealing with this kind of systems, especially when using low energy protons ($1.0 < E_p < 2.0$ MeV) and thin absorbers. Since in this investigation we used a thick Al absorber to stop the 3.0 MeV protons as well as the high signals from Ca K-lines X-rays, we could confidently be sure that the uncertainty due to the evaluation of I(Z) for elements with $Z > 19$ is small.

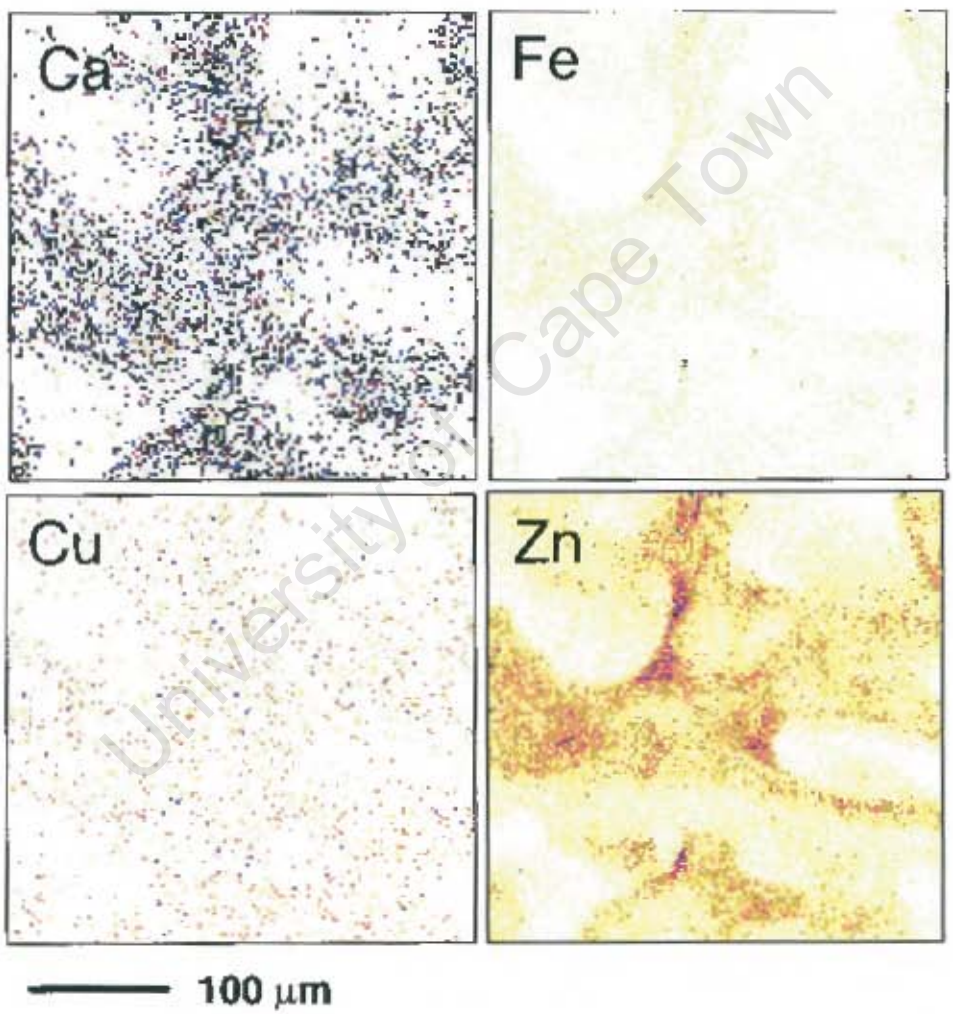

Figure 8.23: Elemental maps for Ca, Fe, Cu and Zn obtained by the method of Dynamic Analysis (DA) for sample S3 - Sudanese kidney stone at the core (Matrix composition Uricite as determined by XRD). Areas scanned were 128 x 128 pixels. Lateral beam resolution was ~2 μm. Total accumulated charge was 0.5 μC.

Mapping similarities on the series of kidney concretions showed that the spatial variability of TE within the areas analysed supply relevant information as to the role of TE in early kidney stone formation for particular elemental phases such as Zn and Sr. This phase normally correlate well with Ca in most of the South African and Sudanese calcium oxalate stones, with the exception of few [Pin85]. Figure 8.23 shows the elemental maps for Ca, Fe, Cu and Zn obtained for sample S3, Sudanese kidney stone at the core. Although the matrix composition as determined by XRD was Uricite, analysis by PIXE also detected Ca. This is well explained by the results obtained from the atomic ratios analysis by p-BS (see Table 8.6). Trace elements Fe and Zn (and Cu to a lesser extent) appear to correlate well with Ca.

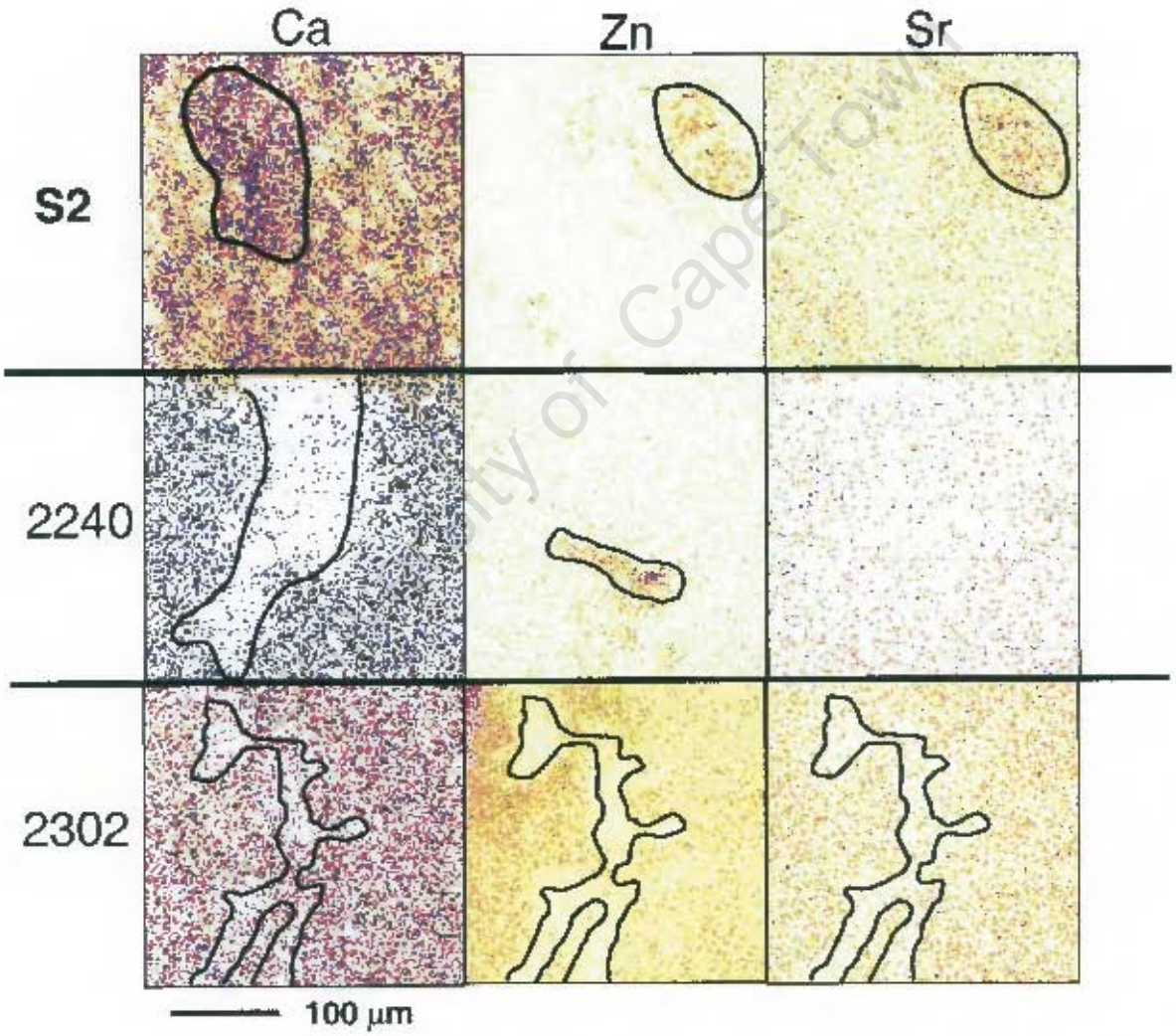

Figure 8.24: Elemental maps of Ca, Zn and Sr for samples S2 (Sudan), 2240 and 2302 (South Africa). Note the similarity in spatial distribution for the S2 and the 2302 sample. Experimental conditions were as in Figure 8.23

When maps of Ca, Zn and Sr are compared for sample 2302 (South Africa) a fair similarity in spatial distribution was found (see Figure 8.24). However for South African sample 2240 and Sudanese S2 such similarity did not occur. This could be explained from the correspondence analysis in Figure 8.21 where the South African sample appears as outlier in the statistical plot. The lack of similarity in maps of Ca, Zn and Sr for the sample S2 may be due to the presence of more than one phase class within the matrix core.

Linear traverses extracted from selected micro-regions of the stone-core supplied information as to the linear variability of concentration levels of certain elements such as Fe, Cu, Zn and Sr (see Figure 8.25). There was a tendency for Zn (and Fe to a lesser extent) to increase at the particular location, marked $\mathbf{m_1}$ in the figure, within the linear traverse. This location is thought to be related to the centre of the core region. Linear traverses for Sr however, did not show a similar trend for the two stones samples, with Sr having maxima at different locations.

8.3.6 Summary

Two groups of human kidney concretions from South Africa and Sudan are compared in terms of their matrix-phases as determined by XRD and proton-BS. The concentration values of the trace elements (TE) analysed by μPIXE (Fe, Cu, Zn, Se, Br and Sr) showed a linear trend when their mean was plotted for both groups of stones. Statistical analysis of μPIXE evaluated by Correspondence Analysis showed that the 2-dimensional plot of axis 1 and 2 (holding up to 85% of the data information) could explain the formation of two clusters, corresponding to each the South African and the Sudanese stone groups ($p<0.05$). Moreover the Sudanese group was clustered as two separated sub-groups which were not related to geographical conditions. The core of most stones was COM, COD or mixtures. Simulations of p-BS spectra for thick kidney stone targets help as a guide for quantitative phase identification of Ca oxalate phases. Differences in the ratio of certain elements such as Fe, Zn and Sr can be used to characterise possible role of TE in the development and growth of stones. The combination of XRD, proton-BS and μPIXE provided a powerful set of techniques to characterise the composition of kidney stones in the core region.

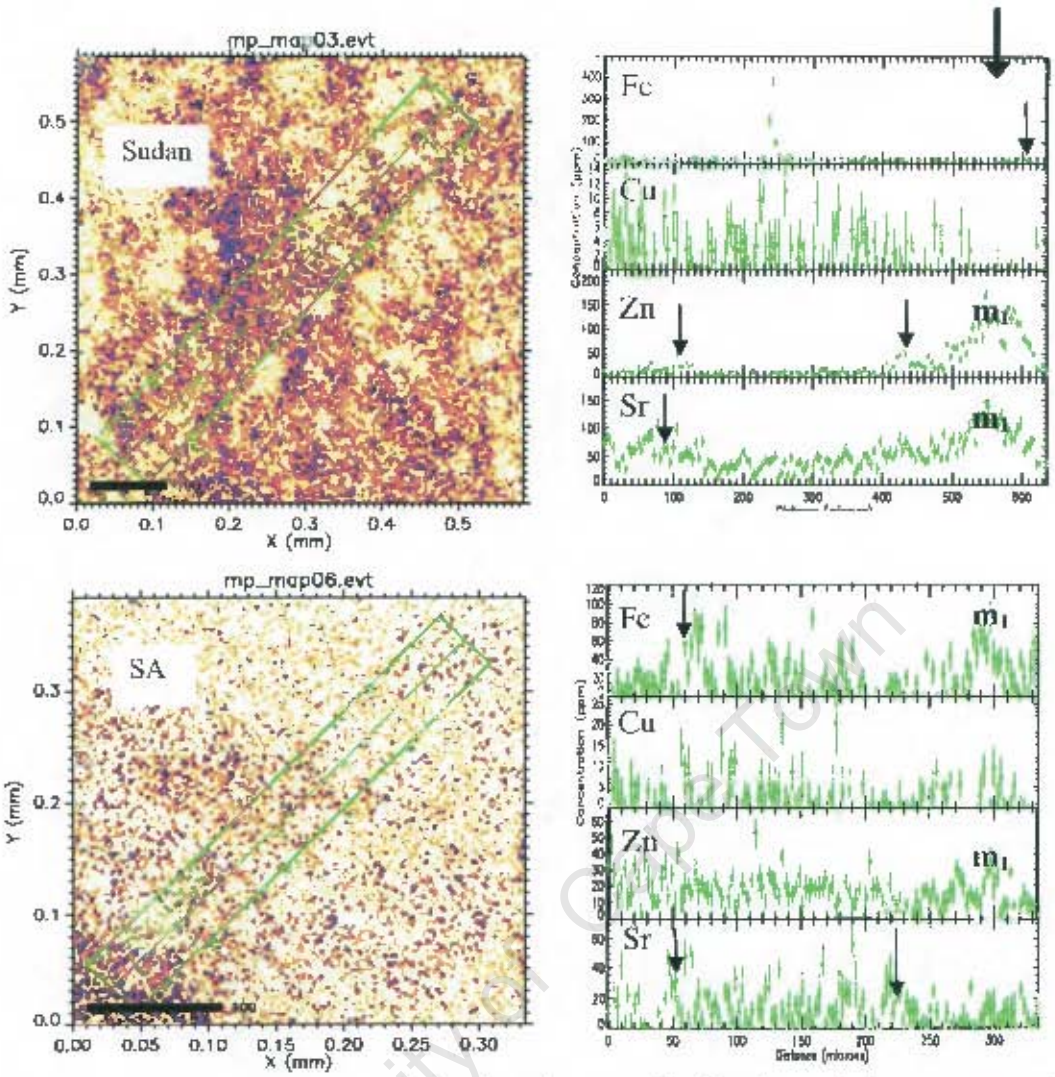

Figure 8.25 Linear traverses (right) for elements Fe, Cu, Zn and Sr as extracted from maps of selected micro-regions at the core (left) for two stones samples. Concentration levels are in $\mu g.g^{-1}$. The Sudanese stone (up) appear to have a Zn and Sr max at about 550 µm while the South African stone (down) have max for Fe and Zn to a lesser extent. Small arrows show the location of other possible maxima.

8.4 ANALYSIS OF HUMAN HAIR CROSS SECTIONS FROM TWO DIFFERENT POPULATION GROUPS

8.4.1. INTRODUCTION

As we move into the 21st century modern technologies which depend to a great extent on others such as nanotechnology, will have an impact on the way human bio-systems re-engineer themselves to adapt to new types of materials and chemicals which will bring implicitly new mechanisms and levels of toxicity not known at present. Currently, in modern society increasing amounts of anthropogenic and ubiquitous ultra-fine particles such as in exhaust emission aerosols, pigments, titanium and silicon oxides and many more (with sizes of ~20-200 nm diameter) are being manufactured for inclusion on product development to supply the cosmetics, surfactants, aerosols industries. It is well documented, that the threshold barrier at which the body controls absorption (through the lungs) of toxic fine particles is of the order of ~2.5 μm [Vil93]. On the other, hand the stratum corneum of skin serves as an important barrier function by keeping molecules and/or ultra-fine particles from passing into the body. This skin threshold barrier towards the environment or the mechanism to stop penetration of possible toxic substances is not well understood [For95]. Furthermore, it has been documented extensively that certain toxic elements are accumulated with time in the hair shaft as the hair grows [Hai01]. If toxic elements and/or compounds that are or will be manufactured in the future enter the body over short and/or long periods of time, they may create body dysfunctions and health problems (see Figure 8.26). Analytical techniques capable of determining the internal hair distribution of such toxic materials on cross sections of human hair shaft, such as PIXE will help to perform quality controls in parallel with other techniques which do not have the mapping capability [Pil78].

Earlier research on elemental analysis of hair cross sections by PIXE [Ilon85] showed a convenient way for quantitative determinations of metals radial distributions in hair. However, this approach was restricted to proton beams sizes of 8 x 25 μm^2. Furthermore bulk elemental analysis of human hair by other techniques such as Ion Inductive Coupled

Plasma Mass Spectrometry (ICP-MS), Atomic Absorption (AA), has been established as an important screening technique to assess body-nutrient levels associated with poor health conditions and/or toxicity due to environmental pollutants particular for long periods of time [Val96, Cag95, Jas96, and Cla85]. In spite of the great number of research analysis reported on this material by a wide variety of instrumental analytical techniques [Aud04, Cav03, and Hal04] relatively little is being done with IBA techniques, particularly with micro-PIXE [Val96]. The reasons for this may be the sensitivity of hair to structural changes during proton bombardment and/or sample preparation.

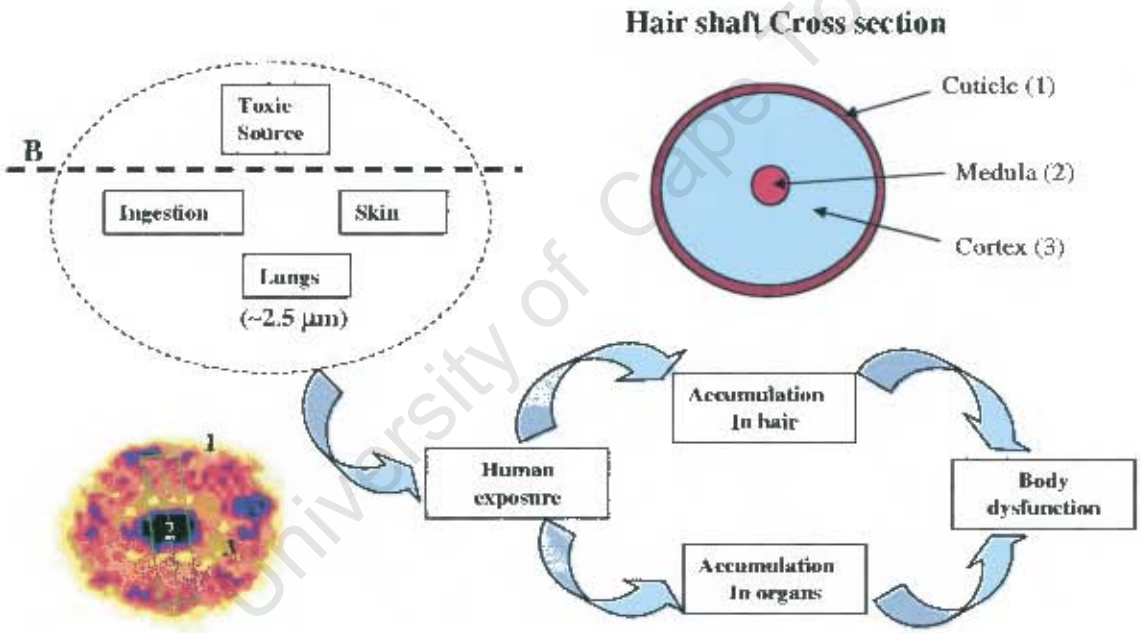

Figure 8.26: Elements pathway for absorption by the human body and accumulation in hair shaft. A threshold barrier B for every channel of absorption is defined: Ingestion; Skin [Fir95]; Lungs [Vil93]. Accumulation in the cuticle, cortex and medulla can be visualised well by micro analysis of hair cross-sections by DA methodology (see lower left side).

Reports of bulk analysis from one or several population groups have been reported [Pil81, Zha89, Ser02]. However, research of elemental mapping distribution and content

In the framework of human physiology, the concentration levels of elements in body tissues appear to be correlated with local nutritional and/or toxic conditions for a particular population group [Mur02, Zak98, Vas02]. Applying this same rationale to the case of human hair and considering that blood flow through the follicle brings in metals within the hair shaft growing process, a concise investigation into the metal content and distribution in hair cross sections from two different human populations groups was undertaken.

The main objective was to compare the internal elemental spatial distribution of hair shaft in these two groups to obtain information as to the level of correlation between live style and other environmental conditions of the two groups. This investigation dealt with the evaluation of elemental content differences in hair-shaft cross-sections from healthy individuals from Sudan and South Africa. Results on the elemental two-dimensional distribution and statistical significance of elemental profiles were also addressed.

8.4.2 Samples description and nuclear microscopy measurements

Hair sample material from healthy male South African (average age 36 years) and Sudanese (average age 35 years) living in urban areas within the areas of Cape Town and Khartoum was collected for analysis. Hair shaft of about 2 cm long was removed with a tungsten knife from the occipital scalp region of each subject. Samples were washed with de-ionised water, rinsed in ethanol and allow drying at room temperature. Thereafter hair samples were embedded in resin. Thin cross sections of ~ 5 μm were cut in a microtome. Block sections infinitely thick for the ion beam were also prepared. Prior to micro-PIXE analysis samples were carbon-coated to prevent charging during irradiation. Samples were stored in a desiccator until irradiation with 1.5 and 3.0 MeV protons. Beam current of ~50 pA was used to prevent evaporation of volatile elements exposed to a possible temporary temperature rise while under irradiation. Selected micro-regions were scanned with a proton beam focused to about 2 x 3 μm^2 spot size. The combination of low current intensity and a relatively small beam spot ensured the stability of the hair material at all times. Areas covering the whole cross section were scanned in a map-array of 128 x 128 pixels with 10 ms dwell time. PIXE and proton backscattering techniques were used simultaneously. Off-line analyses of experimental data recorded in event-by-event mode

were performed with GeoPIXE-II. Elemental concentrations based on PIXE spectra extracted from selected regions within the cross sections were obtained using Dynamic Analysis (DA) method. Concentrations of light elements not detected with PIXE (C, O and N) were obtained from p-BS spectra extracted from the same regions.

8.4.3. Discussion on total content of metals found by both techniques

Elemental matrix composition for major components found by RUMP (see Table 8.7) showed a similar trend in both population groups. With average composition $C_7O_{0.6}N_2S_{0.1}$ and $C_8O_{0.7}N_2S_{0.1}$ for the South African and Sudanese groups respectively. Figure (8.27) shows the typical p-BS spectra of the two population group. Observed concentration levels of major components are in the range values from hair standard reference materials.

Average concentration levels of S, K, Ca, Ti, Fe, Ni, Cu, Zn and Sr, obtained by irradiation over the whole cross-sections areas, with 3.0 MeV protons is given in Table 8.8. A South African sample (SA4) in particular had very low concentrations of S, Ca and Zn as compared with the other South African and Sudanese hair samples. The Sudanese group on the other hand appear to be more homogeneous as far as trace and major components is concerned.

Table 8.7: p-BS atomic ratios of major components in hair samples found by RUMP

	Sample	C	O	N	S
SUDAN	S1	5.2	0.1	1.4	0.1
	S2	6.2	0.3	1.6	0.1
	S3	6.8	0.9	2.1	0.1
	S4	8.0	1.3	2.8	0.1
	S5	10.0	1.3	3.0	0.1
SOUTH AFRICA	SA1	7.0	0.1	1.8	0.1
	SA2	8.7	0.8	2.4	0.1
	SA3	10.0	0.4	2.8	0.1
	SA4	8.5	1.6	1.8	0.2
	SA5	5.2	0.8	1.5	0.1

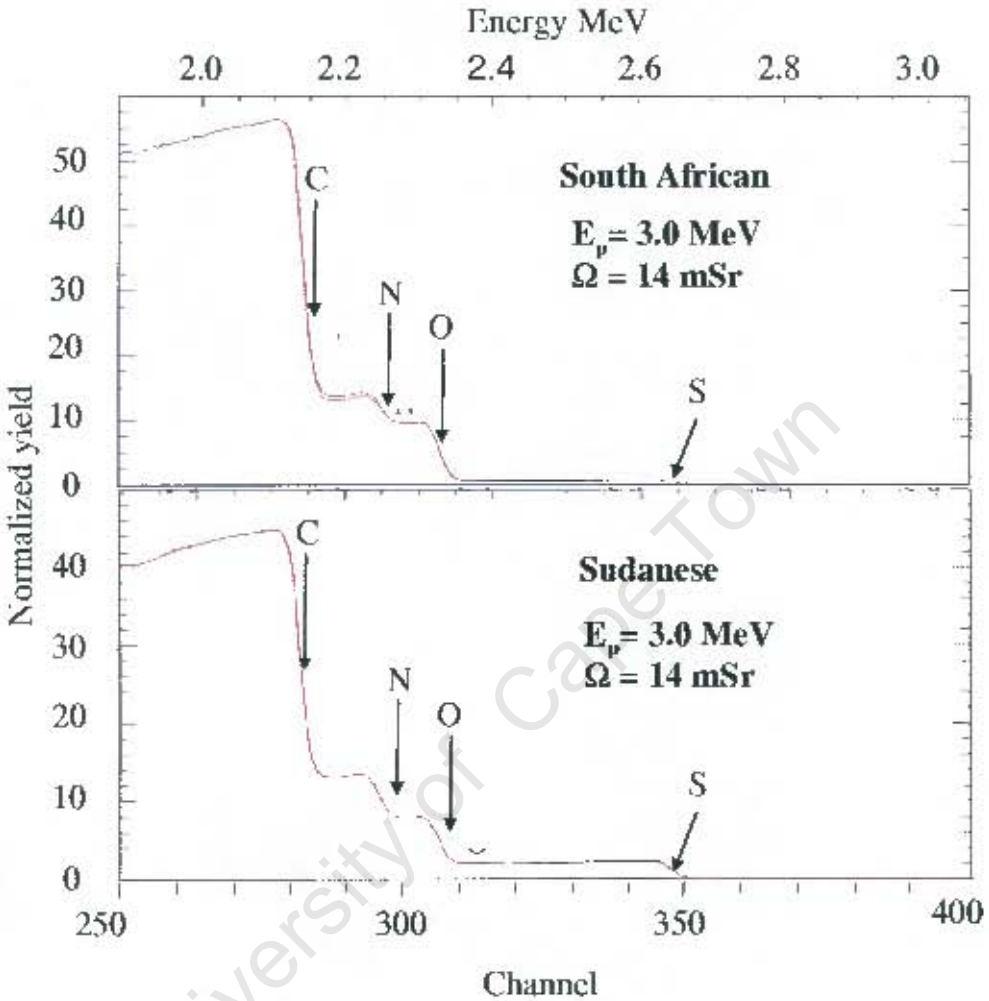

Figure 8.27: Typical p-BS spectra from a South African (up) and a Sudanese (down) hair cross-section. The total spectra show a similar trend in both groups with atomic ratios $C_7O_{0.6}N_2S_{0.1}$ and $C_8O_{0.7}N_2S_{0.1}$ for the South African and Sudanese samples respectively.

Of importance is the presence of Ti in both groups, although more pronounced in the group from Sudan, with highest value being ~450 $\mu g.g^{-1}$ for sample S1. Only sample S4 had a Ti concentration value similar to that of the South African group. Overall profiles for S (mainly in the cortex), Ti, Zn and Sr are also shown in Figures 8.28 and 8.29 where we could see in general that the concentrations of these elements are depleted in the

Table8.8: Elemental concentrations of human hair shaft cross-sections found by PIXE [in $\mu g g^{-1}$].

Element	Sudanese specimens				
	S1	S2	S3	S4	S5
S	26120±1300	29520±2300	18660±1150	16120±900	15720±800
K	353±14	323±11	232±13	82±9	192±9
Ca	415±13	262±10	558±12	159±4	237±5
Ti	446±11	228±8	300±6	10±10	161±8
Fe	141±2	65±1	107±2	18±1	140±3
Ni	7±0.8	21±1	n.d.	n.d.	1±0.4
Cu	11.±0.7	4.3±0.6	13±0.6	5±0.4	18±0.7
Zn	231±3	105±3	158±2	145±2	105±2
Sr	18±2	8±1	11±1	11±1	6±0.7

Element	South African specimens				
	SA1	SA2	SA3	SA4	SA5
S	11070±650	8500±330	8010±420	1360±156	14250±890
K	253±12	659±19	422±16	145±5	79±6
Ca	417±9	297±8	306±5	22±5	222±2
Ti	42±4	31±3	13±2	n.d.	32±2
Fe	20±0.6	73±2	9±0.4	5.2±0.5	18±0.4
Ni	n.d.	3±0.3	n.d.	n.d.	n.d.
Cu	6±0.4	7±0.4	6±0.3	1.1±0.2	5±0.3
Zn	52±1	68±2	47±0.7	2±0.5	62±3
Sr	2±0.6	n.d.	2.3±1	n.d.	1±0.2

n.d. == below detection limit

Elemental maps obtained by the method of dynamic analysis of shaft hair cross-sections obtained with proton beam of 1.5 MeV showed primarily the distribution of S, Ca, Ti and Zn. Their range values in all three areas (cuticle, cortex and medulla) are indicated in the Figures 8.30 and 8.31. Regions of enrichment and depletion were observed in the cuticle, cortex and medulla areas of the hair cross-sections. Figure 8.30 in particular shows the maps of S and Ca for typical a Sudanese and a South African samples. Ca had a level of ~0.4% in the medulla of the Sudanese hair while its value was 50 $\mu g.g^{-1}$ in the South African one. S on the other hand had a similar cortex distribution for both samples with

mean value content of ~3.5% (Sudan) and ~4.0% (South African). However the sulphur content in the central region is grater for the South African one.

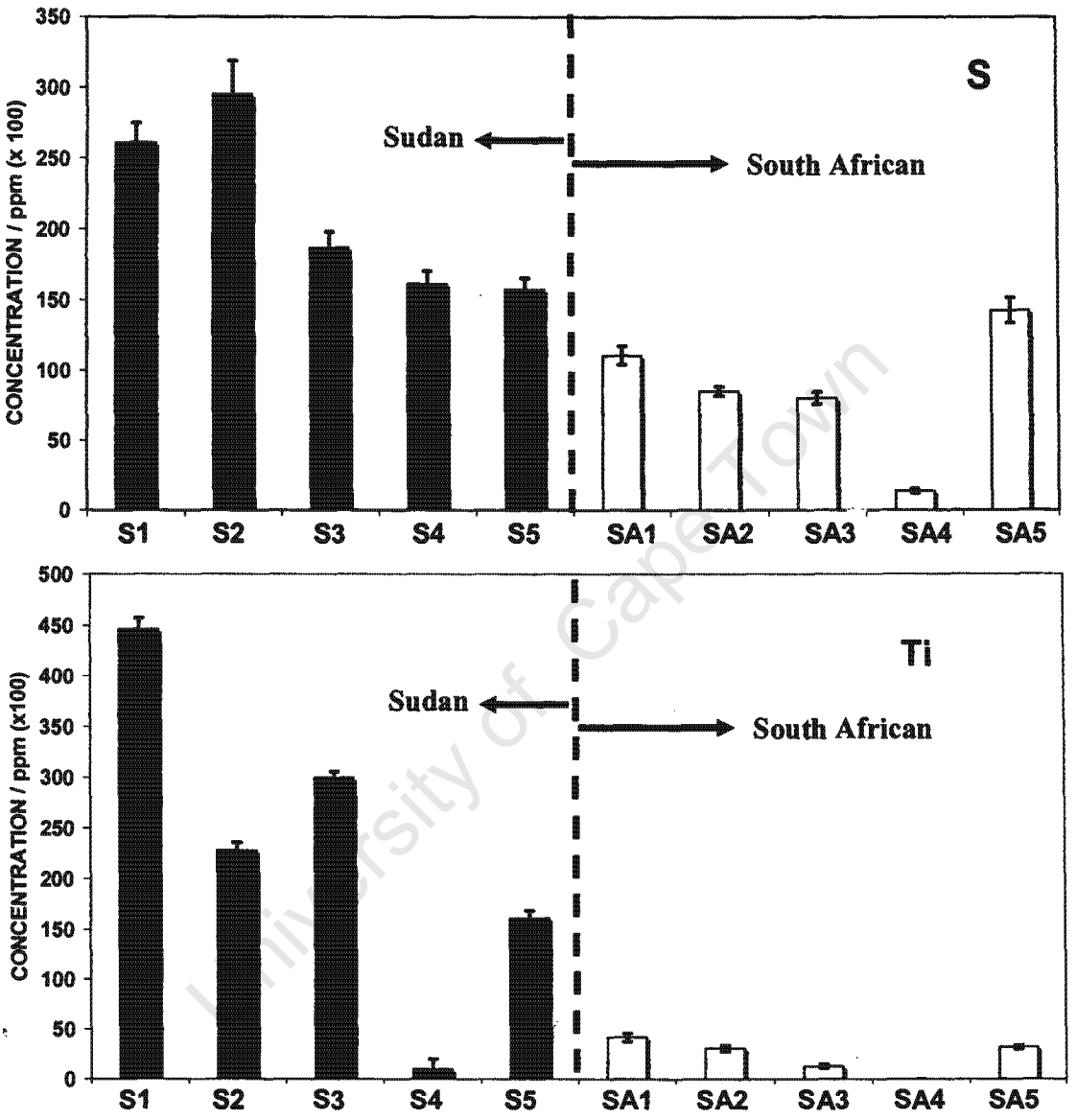

Figure 8.28: Elemental profile for S and Ti for both series of hair samples. The mean S ratio S(S)/S(SA) = 1.8 while that for Ti is 14. Sample S4 appear to have a similar Ti concentration as the South African group

Of significance is the positive correlation of the distribution for sulphur and calcium in both the medulla and the cortex regions for the Sudanese hair section. For example in the medulla region of the Sudanese hair cross-section the sulphur content is ~1.8% while that for calcium is ~0.4%. On the other hand a similar profile occurs for the cortex where the

mean values of sulphur and calcium are ~3.5% and ~0.1% respectively. A similar situation occurs for the South African sample on the right of Figure 8.30 medulla and cortex sulphur and calcium. However the values for Ca are much lower than for the case of the Sudanese hair section with medulla-calcium is ~50 $\mu g.g^{-1}$ and cortex-calcium is ~400 $\mu g.g^{-1}$. Normally the concentrations of both S and Ca were relatively smaller in the cuticle external region of the hair shaft when compared with the concentration levels in the cortex.

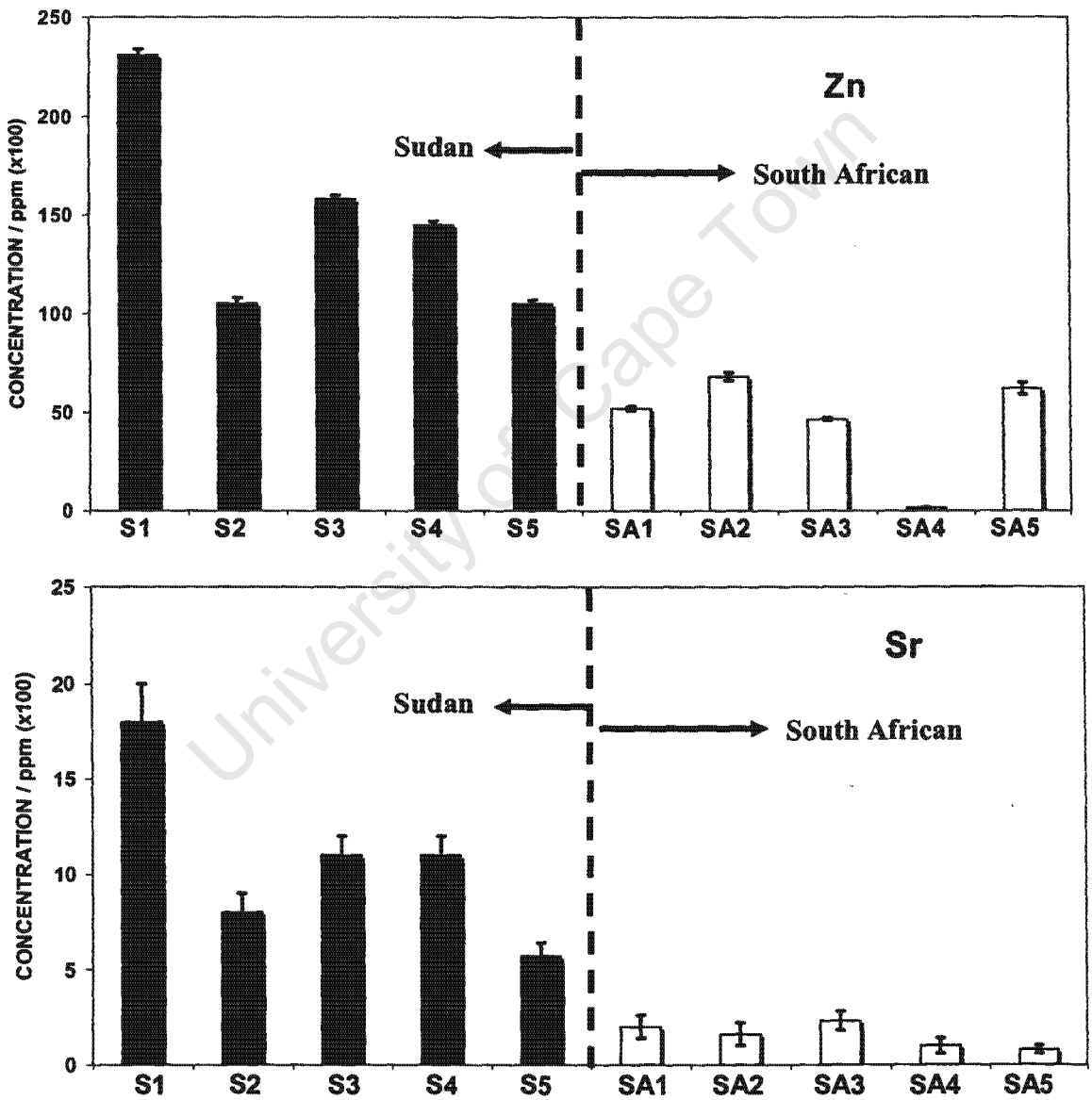

Figure 8.29: : Elemental profile for Zn and Sr for both series of hair samples. The mean Zn ratio Zn(S)/Zn(SA) = 2.1 while that for Sr is 5.

Furthermore the maps of Ti and Zn showed in Figure 8.31 gave a different picture. Although, Ti is present in all three sub-regions (cuticle, cortex and medulla) it has a higher concentration level in the cortex region with values of ~0.1% and ~300 $\mu g.g^{-1}$ for Sudanese and South African samples respectively. For the medulla region these values were ~250 $\mu g.g^{-1}$and ~300 $\mu g.g^{-1}$. The concentration levels of Zn follows an inverse pattern in the cortex area with values of 10-200 $\mu g.g^{-1}$ for the Sudanese and 100-250 $\mu g.g^{-1}$ for the South African.

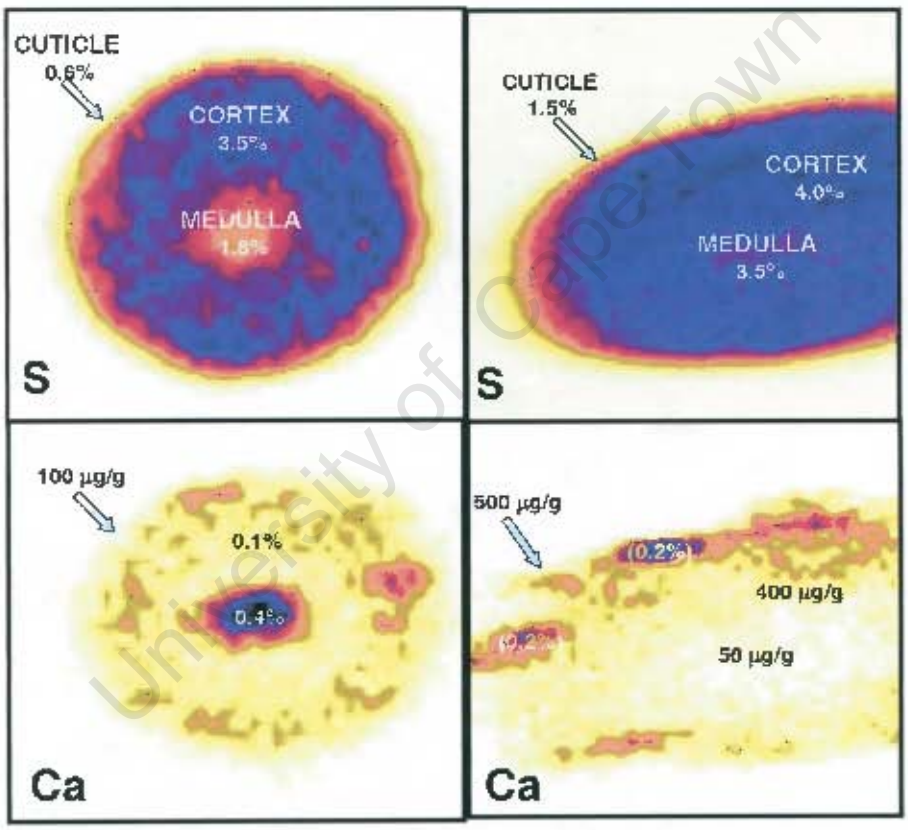

Figure 8.30: Maps of sulphur and calcium for a typical Sudanese (left) and South African (right) hair cross-sections. The range values in all three areas (cuticle, cortex and medulla) are indicated in the figure. Note the inverse correlation of these two elements in the medulla region. Sulphur appears to be distributed similarly in both samples.

Elemental data for PIXE and p-BS was submitted for evaluation to correspondence analysis. Figure 8.32 shows a plot of the first two dimensions taking all variables and samples into consideration. No supplementary points were defined since the total inertia

between both dimensions 1 and 2 amounted to more than 90% of the whole information. The Sudanese group appear to form a tight cluster while the South African group was scattered forming an elongated group. This elongation was determined primarily by the sample SA4 which have a low content of S, Ca and Zn. The Sudanese group on the other hand appear to be more homogeneous as far as trace and major components is concerned.

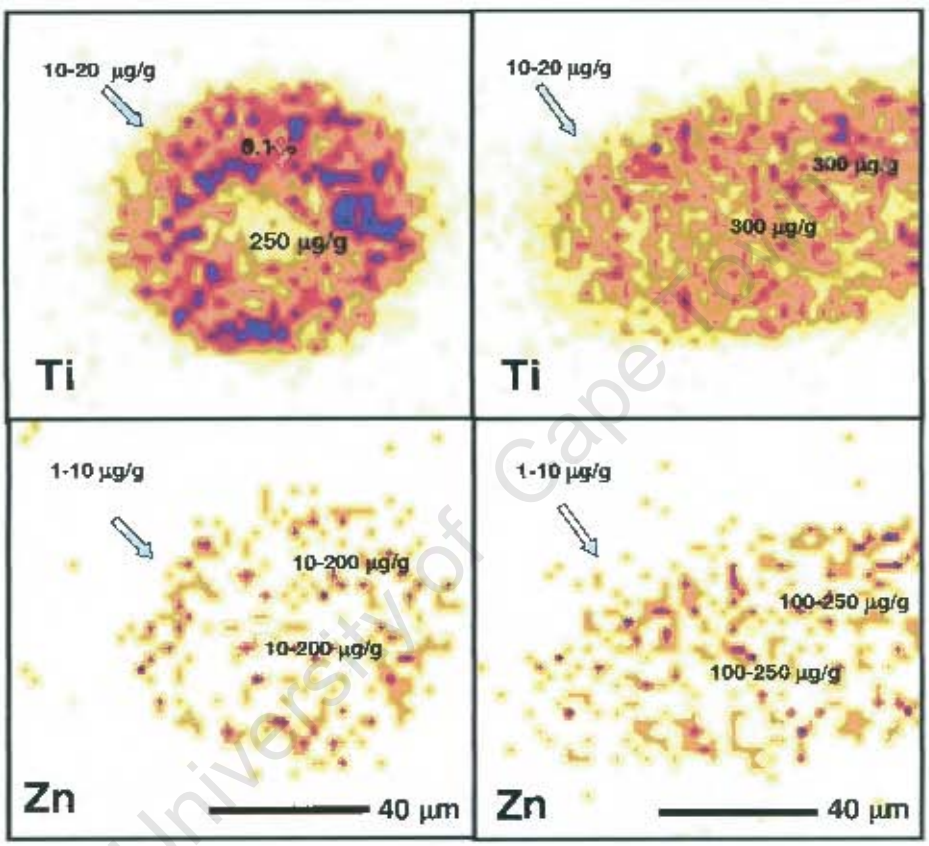

Figure 8.31: Same as Figure 8.30 but for zinc and strontium .The range values in all three areas (cuticle, cortex and medulla) are indicated in the figure. Ti is present in all three sub-regions with a higher level (0.1%) in the medulla.

8.4.4. DISCUSSION AND CONCLUSIONS

Both groups of hair samples originated from urban areas from healthy and medium class standard of living within Sudan (Khartoum region) and South Africa (Cape Town region). The similarity of mean matrix composition in the two groups as determined by backscattering analysis is significant since these are two completely different population groups miles a part and with different geographical conditions. However the South

African group presented a different pattern when considering the trace element analysis alone with depleted levels of Ni, Cu and Zn for most of them in addition to a relative variation in their content, as compared to the Sudanese data. The low contents for S, Ca and Zn in sample (S4) may be indicative of nutritional deficiency and/or toxicity conditions. However concentration levels of such elements in scalp hair from previous reported work is known to vary substantially (S: 1.5-4.5 %; Ca: 200-3000 $\mu g.g^{-1}$; Zn: 75-250 $\mu g.g^{-1}$ [Har82, Eng89] according to race, nutritional value and clima. The presence of Titanium in both groups particularly in the cortex may point to a possible intake of this element by the body. It is unlikely that Ti occurring from external environmental sources may have infiltrated through the cuticle into the cortex. Particularly since the values are rather high (1000 $\mu g.g^{-1}$).

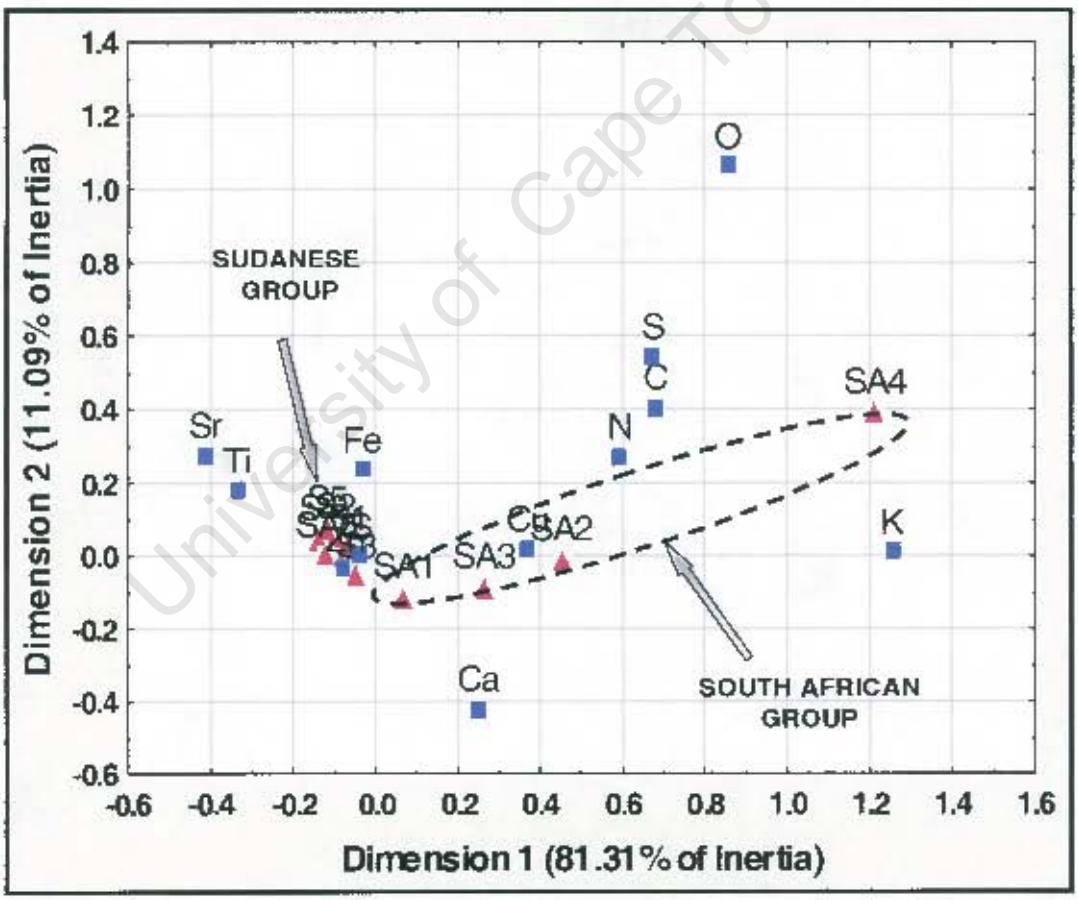

Figure 8.32: Correspondence Analysis plot of elemental concentrations data obtained for Sudanese and South African groups for dimensions 1 and 2. Notice the tight clustering of the Sudanese group.

This particular finding should be investigated further in the future in a bigger sample population to be able to draw final conclusions as to the more acceptable theory for the "true" source of Ti and its possible role in pathogenic conditions not known at present.
The data on trace elements exhibited in Table 8.8 has shown that the Sudanese group has a more homogeneous pattern although with a higher concentration of Ti than the South African group. In particular sample SA4, with very low levels for sulphur, calcium, and in general all trace elements is a special case that needs further investigation to be able to find the correlation of its metal content profile and a possible toxicity condition in the body. Statistical analysis of data by correspondence analysis generated a clear separation between the two population groups with the Sudanese group presenting a very tight cluster.

SUMMARY

Trace element analysis of hair was used to assess the content of metals in two population groups and to screen hair shaft of subjects for body-nutrient and/or toxicity levels due to environmental pollutants. The main objective was to compare element content and spatial distribution within scalp hair-shaft cross sections of these two distinct human population groups, and to assess possible similarities and/or differences. Proton backscattering and Micro-PIXE were used to determine the matrix composition and content of light and middle transition elements, with beam energies of 1.5 and 3.0 MeV. Mapping analysis showed a relatively similar content distribution for K and Ca within each group. However significant differences, particularly for heavier metals, such as Ti and Zn were also found. Correspondence Analysis of the data showed a clear separation between the two groups when the total content over the hair cross section was considered.

Appendix A

Input file for the IGUN Program for the Ion source simulation

IGUN has built in boundary processing of PLYGON, which gives a CAD- like user interface to set up the boundary, including definition of internal electrodes, dielectric boundaries, and slanted Neumann boundaries (field lines as boundary elements). The input now is mesh independent and can use any coordinates from a drawing, accepting any offset. The output of the equipotentials, field line and trajectories (to be used in a further run) has the same offset and units, which greatly eases the organization of concatenated runs, e.g. high mesh resolution in the plasma region, lower mesh resolution downstream

Ext_106c.in (90/65mA, Positive EE, EE by Dan)
&INPUT1 RLIM=45,ZLIM=5285,POTN=4,POT=0,4705,0,-8326, &END
3, 0, 0 (electrode No 3, and R, Z are polar coordinates)
3, 44, 0
2, 44, 5
2, 1, 5
2, 1, 6
2, 2.5, 7
2, 3.5, 7
2, 3.5, 9
2, 7.83309, 9
1002, 7.833095, 10.8
-1.8
2, 8.16406, 9.03069
2, 25, 22
2, 44, 22
1, 44, 34
1, 30, 34
1, 8, 13
1, 8, 19
1, 15, 26
1, 29, 39
1, 44, 39
1, 44, 75
1, 4, 75
1, 4, 76
1, 8, 76
1, 8, 95
1, 11, 95

```
1, 11, 76
1, 44, 76
1, 44, 100
4, 44, 101.5
4, 34, 101.5
4, 34, 85
4, 31, 85
4, 31, 80
4, 26, 80
4, 26, 97
4, 9.300003, 97
4, 9.300003, 118
4, 26, 118
4, 26, 130
4, 31, 130
4, 31, 119
4, 34, 119
4, 34, 103.5
4, 44, 103.5
1, 44, 105
1, 44, 138
1, 43, 138
1, 43, 124
1, 38, 124
1, 38, 140
1, 12.3, 140
1, 12.3, 121
1, 9.300003, 121
1, 9.300003, 140
1, 4, 140
1, 4, 142
1, 44, 142
1, 44, 216
1, 1, 216
1, 1, 219
1, 44, 219
1, 44, 224
1, 0, 224
3, 0, 0
 &INPUT5
MAXRAY=30,STEP=0.05,TE=4,UI=0,MASS=1,RP=2,ZP=1,NS=15,HOLD=15,
PDENS=5.7E11,AMPSO=0.00050,NSCAN=2,SY=8,DSCAN=5,ZSCAN=0,LASER=T,
WRTEQU=-5000 &END
 &BUNDLE RB2=4 &END
```

APPENDIX B

Input file for the TRANSPORT program from ion source to the end of the accelerator tube

```
/Ion Source+ Lens+ Accelerator tube. /
        0                                   (Indicator card means the following describes a
                                             new problem
15. 11.0 /MEV/ 0.001;                       (Input-output units)
15. 1.0 /MM/ 0.1;
1. 1  7  1  7 0. 0. 4.3323/BEAM/ ;          (Guess of initial beam parameters)
16. 4.0 100.0 ;                             (Special input parameters)
16. 3 1837.7 /MASS/;                        (Mass of the particles comprising the beam, in units
                                             of electron mass)
3. .061 /D/ ;                               (Drift Space)
6. 1.0 4 3.0 4;                             (Transformation matrix update)
3. .02/D/;
11. 0.0 .0029;
11. 0.002 1;                                (Electrostatic acceleration section)
11. .02 1;
11. 0.002 0.0;
3. .019/D/;
6. 1.0 4 3.0 4;
3. .081;
6. 1 1 3 1;
3. .002/D/;
3. .075/D/;
11. 0.0 .0028;
11. 0.005 1;
11. .05 1;
11. .014 0.0;
3. .461/D/;
6. 1 15 3 15;
11. 0.0 0.0064,
11. .01 1;
11. .09 1;
11. .01 0;
3. .118/D/;
6. 1 15 3 15;
3. .012/D/;
11. .0  5.988 ;
11. .027 .0051;
11. .027 .0103  ;
11. .027 .0153;
11. .027 .0205 ;
11. .027 .0256 ;
```

11. .027 .0307 ;
11. .027 .0359 ;
11. .027 .0410 ;
11. .027 .0462 ;
11. .027 .0538 ;
11. .027 .0615 ;
11. .027 .0692 ;
11. .027 .0769 ;
11. .027 .0846 ;
11. .027 .0923 ;
11. .027 .1076 ;
11. .027 .1153 ;
11. .027 .1231 ;
11. .027 .1307 ;
11. .027 .1385 ;
11. .027 .1461 ;
11. .027 .1583 ;
11. .027 .1615 ;
11. .027 .1692 ;
11. .027 .1796 ;
11. .027 .1846 ;
11. .027 .1923 ;
11. .027 .2000 ;
11. .027 .2076 ;
11. .027 .2153 ;
11. .027 .2230 ;
11. .027 .2307 ;
11. .027 .2384 ;
11. .027 .2461 ;
11. .027 .2538 ;
11. .027 .2615 ;
11. .027 .2692 ;
11. .027 .2769 ;
11. .027 .2846 ;
11. .027 .2923 ;
11. .027 .3000 ;
11. .027 .3076 ;
11. .027 .3153 ;
11. .027 .3231 ;
11. .027 .3307 ;
11. .027 .3384 ;
11. .027 .3514 ;
11. .027 .3538 ;
11. .027 .3615 ;
11. .027 .3693 ;
11. .027 .3784 ;

11. .027 .3846 ;
11. .027 .3923 ;
11. .027 .4000 ;
11. .027 .4076 ;
11. .027 .4153 ;
11. .027 .4231 ;
11. .027 .4307 ;
11. .027 .4380 ;
11. .027 .4462 ;
11. .027 .4538 ;
11. .027 .4615 ;
11. .027 .4692 ;
11. .027 .4769 ;
11. .027 .4846 ;
11. .027 .4923 ;
11. .027 .5000 ;
11. .027 .5076 ;
11. .027 .5154 ;
11. .027 .5231 ;
11. .027 .5307 ;
11 .027 .5384 ;
11. .027 .5462 ;
11. .027 .5538 ;
11. .027 .5615 ;
11. .027 .5692 ;
11. .027 .5769 ;
11. .027 .5846 ;
11. .027 .5920 ;
11. .027 .6000 ;
11. .027 .6076 ;
11. .027 .6154 ;
11. .027 .6230 ;
11. .027 .6300 ;
11. .027 .6380 ;
11. .027 .6462 ;
11. .027 .6538 ;
11. .027 .6615 ;
11. .027 .6692 ;
11. .027 .6769 ;
11. .027 .6846 ;
11. .027 .6923 ;
11. .027 .7000;
11. .027 .7076 ;
11. .027 .7153 ;
11. .027 .7230 ;
11. .027 .7307 ;

```
11. .027  .7385 ;
11. .027  .7462 ;
11. .027  .7538 ;
11. .027  .7615 ;
11. .027  .7692 ;
11. .027  .7764 ;
11. .027  .7840 ;
11. .027  .7923 ;
11. .027  .8000 ;
11. .027  .8076 ;
11. .027  .8154 ;
11. .027  .8230 ;
11. .027  .8307 ;
11. .027  .8384 ;
11. .027  .8462 ;
11. .027  .8538 ;
11. .027  .8615 ;
11. .027  .8692 ;
11. .027  .8769 ;
11. .027  .8846 ;
11. .027  .8923 ;
11. .027  .9000 ;
11. .027  .9076 ;
11. .027  .9153 ;
11. .027  .9230 ;
11. .027  .9307 ;
11. .027  .9385 ;
11. .027  .9462 ;
11. .027  .9538 ;
11. .027  .9616 ;
11. .027  .9692 ;
11. .027  .9769 ;
11. .027  .9846 ;
11. .027  .9923 ;
11. .027  1.000 ;
3. 1.0 /D/ ;
13. 48 ;                              (Bending magnet input specification)
16. 7.0 .7 ;
16. 7.0 .45 ;
16. 8.0 2.8 ;
13. 1.0 ;
13. 3.0 ;
3. .109 /L1/ ;
5.01 .110 -1.5 22.5/QUAD1/ ;     (First electrostatic quadrupole lens)
3. .085 /L2/ ;
13. 1.0 ;
```

5.01 .110 1.5 22.5 /QUAD2/ ;	(Second electrostatic quadrupole lens)
3. .440 /L3/ ;	
10. 1.0 1.0 .5 0.1 /FIT1/ ;	(Fitting beam size to y_{max}=0.5 mm)
10. 3.0 3.0 .5 0.1 /FIT2/ ;	(Fitting beam size to y_{max}=0.5 mm)
SENTINEL	(Plotting the TRANSPORT run to view the fitted bean envelope)
/*PLOT*/	
1	
SENTINEL	(First one signifies the problem is terminated)
SENTINEL	(The second one signifies the end of the TRANSPORT run)

Note that:

- Each element is given by a sequence of items, mostly numbers that are separated by spaces and terminated by a semicolon, which is a requirement to run TRANSPORT. The items, in order, are a type code number, a vary field, the physical parameter, and an optional label
- This TRANSPORRT run is a simultaneous multi envelope fit in which several sets of measured profile data are fitted. In this case six TRANSPORT run were fitted.
- The commands given I the appendix are merely stated to explain the meaning of the different elements in the beam card, and are not required when running the program

APPENDIX C

In chapter four the measured potential distribution in a hot-cathode duoplasmatron ion source was shown. The distribution has been explained in terms of four layers of charge between the cathode and anode of the source and by applying Gauss' law and Poisson's equation. To simulate the potential distribution in the ion source the potential distribution of four layers of charge between two parallel conducting plates, connected to a DC voltage source, has been calculated. For the calculation it is assumed that the transverse dimensions of the two plates and the layers of charge are large compared to the distance between the plates. Under these conditions the potential distribution in the region between the center points of the two plates is described approximately by the one-dimensional Poisson's equation. The calculation is further done for homogeneous charge distributions in each of the four layers. Poisson's equation is solved piece-wise for the nine regions between the two plates. The integration constants are determined from the distance between the two plates, the applied voltage, the position and width of the layers of charge as well as their densities, and the requirement that the potential and field strength should be continuous at the boundaries between layers of charge and charge-free regions.

The gap between the two plates, which extend in zy-planes, are divided in spaces numbered one to nine and are defined by the x-coordinates 0, x_1, x_2, x_3, x_4, x_5, x_6, x_7, x_8, x_9. The two conducting plates positioned at coordinates 0 and x_9, are at potentials 0 and V_a, respectively. The four layers of charge are located in the regions between coordinates x_1 and x_2, x_3 and x_4, x_5 and x_6, x_7 and x_8, respectively. The regions between coordinates x_2 and x_3, x_4 and x_5, x_6 and x_7, and x_8 and x_9, are free of charge.

Since the field between the plates do not vary with time and is independent of the z- and y-coordinates near the centre of the plates, the potential distribution in each of the nine regions can be calculated from:

$$\frac{\partial^2 V}{\partial x^2} = -\rho / \epsilon$$

where ρ is the charge density and ε the permittivity.

To simplify the equations below Poisson's equation is written in the following form, where n is the number of the region to which it is applied:

$$\frac{\partial^2 V}{\partial x^2} = k_{n2}$$

For each of the nine regions k_{n2} is a constant given by:

$k_{n2} = - \rho_n / \varepsilon$

The general solution of Poisson's equation is written in the following form for region number n:

$V = k_{n2} x^2 + k_{n1} x + k_{n0}$

The first derivative of the potential is given by:

$2 k_{n2} x + k_{n1} = - E_n$

with E_n the electrical field strength.

In region 1

$$\frac{\partial^2 V}{\partial x^2} = 0, \quad \text{since } k_{12} = 0$$

$$V = k_{11} x + k_{10}$$

for $x = 0$ $V = 0$, therefore $k_{10} = 0$

$$V = k_{11} x$$

In region 2

$$V = k_{22} x^2 + k_{21} x + k_{20}$$

At $x = x_1$:

$$k_{11} x_1 = k_{22} x_1^2 + k_{21} x_1 + k_{20}, \qquad (1)$$

since the potential should be continuous at the boundary.

In region 3

$$V = k_{31}x + k_{30}$$

At $x = x_2$:

$$k_{31}x_2 + k_{30} = k_{22}x_2^2 + k_{21}x_2 + k_{20} \quad (2)$$

In region 4

$$V = k_{42}x^2 + k_{41}x + k_{40}$$

At $x = x_3$:

$$k_{31}x_3 + k_{30} = k_{42}x_3^2 + k_{41}x_3 + k_{40} \quad (3)$$

In region 5

$$V = k_{51}x + k_{50}$$

At $x = x_4$:

$$k_{51}x_4 + k_{50} = k_{42}x_4^2 + k_{41}x_4 + k_{40} \quad (4)$$

In region 6

$$V = k_{62}x_2^{\ 2} + k_{61}x + k_{60}$$

At $x = x_5$:

$$k_{51}x_5 + k_{50} = k_{62}x_5^2 + k_{61}x_5 + k_{60} \quad (5)$$

In region 7

$$V = k_{71}x + k_{20}$$

At $x = x_6$:

$$k_{71}x_6 + k_{70} = k_{62}x_6^2 + k_{61}x_6 + k_{60} \quad (6)$$

In region 8

$$V = k_{82}x_2 + k_{81}x + k_{80}$$

At $x = x_7$:

$$k_{11}x_7 + k_{70} = k_{82}x_7^2 + k_{81}x_7 + k_{80} \quad (8)$$

In region 9

$$V = k_{91}x + k_{90}$$

At $x = x_8$:

$$k_{91}x_8 + k_{90} = k_{82}x_8^2 + k_{81}x_8 + k_{80} \quad (8)$$

At $x = x_9$:

$$k_{91}x_9 + k_{90} = V_a \quad (9)$$

At the boundaries between layers of charge and charge-free regions the first derivative of the potential in adjacent regions should be equal. The following equations arise from this requirement:

At $x = x_1$:

$$k_{11} = 2k_{22}x_1 + k_{21} \quad (10)$$

At $x = x_2$:

$$k_{31} = 2k_{22}x_2 + k_{21} \quad (11)$$

At $x = x_3$:

$$k_{31} = 2k_{42}x_3 + k_{41} \quad (12)$$

At $x = x_4$:

$$k_{51} = 2k_{42}x_3 + k_{41} \quad (13)$$

At $x = x5$:

$$k_{51} = 2k_{62}x_5 + k_{61} \quad (14)$$

At $x = x_6$:

$$k_{71} = 2k_{62}x_6 + k_{61} \quad (15)$$

At $x = x_7$:

$$k_{91} = 2k_{82}x_8 + k_{81} \quad (16)$$

At $x = x_8$:

$$k_{91} = 2k_{82}x_8 + k_{81} \quad (17)$$

The solutions for the k_{n1}- and k_{n0}-values in the above equations as follows:

$$k_{11} = -1/x_9(-V_a + k_{22}x_1^2 - k_{22}x_2^2 + k_{42}x_3^2 - k_{42}x_4^2 + k_{62}x_5^2 - K_{62}x_{66}^2 + k_{82}x_7^2 - k_{82}x_8^2 - 2k_{22}x_1x_9 + 2k_{22}x_2x_9 - 2k_{42}x_3x_9 + 2k_{42}x_4x_9 - 2k_{62}x_5x_9 + 2k_{62}x_6x_9 - 2k_{82}x_7x_9 + 2k_{82}x_8x_9$$

$$k_{21} = -1/x_9(-V_a + k_{22}x_1^2 - k_{22}x_2^2 + k_{42}x_3^2 - k_{42}x_4^2 + k_{62}x_5^2 - k_{62}x_6^2 + k_{82}x_7^2 - k_{82}x_8^2 + 2k_{22}x_2x_9 - 2k_{42}x_3x_9 + 2k_{42}x_4x_9 - 2k_{62}x_5x_9 + 2k_{62}x_6x_9 - 2k_{82}x_7x_9 + 2k_{82}x_8x_9)$$

$$k_{20} = k_{22}x_1^2$$

$$k_{31} = -1/x_9(-V_a + k_{22}x_1^2 - k_{22}x_2^2 + k_{42}x_3^2 - k_{42}x_4^2 + k_{62}x_5^2 - k_{62}x_6^2 + k_{82}x_7^2 - k_{82}x_8^2 - 2k_{42}x_3x_9 + 2k_{42}x_4x_9 - 2k_{62}x_5x_9 + 2k_{62}x_6x_9 - 2k_{82}x_7x_9 + 2k_{82}x_8x_9)$$

$$k_{30} = k_{22}x_1^2 - k_{22}x_2^2$$

$$k_{41} = -1/x_9(-V_a + k_{22}x_1^2 - k_{22}x_2^2 + k_{42}x_3^2 - k_{42}x_4^2 + k_{62}x_5^2 - k_{62}x_6^2 + k_{82}x_7^2 - k_{82}x_8^2 + 2k_{42}x_4x_9 - 2k_{62}x_5x_9 + 2k_{62}x_6x_9 - 2k_{82}x_7x_9 + 2k_{82}x_8x_9)$$

$$k_{40} = k_{22}x_1^2 - k_{22}x_2^2 + k_{42}x_3^2$$

$$k_{51}=-1/x_9(-V_a+k_{22}x_1^2-k_{22}x_2^2+k_{42}x_3^2-k_{42}x_4^2+k_{62}x_5^2-k_{62}x_6^2+k_{82}x_7^2-k_{82}x_8^2-2k_{62}x_5x_9+2k_{62}x_6x_9-2k_{82}x_7x_9+2k_{82}x_8x_9)$$

$$k_{50}=k_{22}x_1^2-k_{22}x_2^2+k_{42}x_3^2-k_{42}x_4^2$$

$$k_{61}=-1/x_9(-V_a+k_{22}x_1^2-k_{22}x_2^2+k_{42}x_3^2-k_{42}x_4^2+k_{62}x_5^2-k_{62}x_6^2+k_{82}x_7^2-k_{82}x_8^2+2k_{62}x_6x_9-2k_{82}x_7x_9+2k_{82}x_8x_9)$$

$$k_{60}=k_{22}x_1^2-k_{22}x_2^2+k_{42}x_3^2-k_{42}x_4^2+k_{62}x_5^2$$

$$k_{71}=-1/x_9(-V_a+k_{22}x_1^2-k_{22}x_2^2+k_{42}x_3^2-k_{42}x_4^2+k_{62}x_5^2-k_{62}x_6^2+k_{82}x_7^2-k_{82}x_8^2-2k_{82}x_7x_9+2k_{82}x_8x_9)$$

$$k_{70}=k_{22}x_1^2-k_{22}x_2^2+k_{42}x_3^2-k_{42}x_4^2+k_{62}x_5^2-k_{62}x_6^2$$

$$k_{81}=-1/x_9(-V_a+k_{22}x_1^2-k_{22}x_2^2+k_{42}x_3^2-k_{42}x_4^2+k_{62}x_5^2-k_{62}x_6^2+k_{82}x_7^2-k_{82}x_8^2+2k_{82}x_8x_9)$$

$$k_{80}=k_{22}x_1^2-k_{22}x_2^2+k_{42}x_3^2-k_{42}x_4^2+k_{62}x_5^2-k_{62}x_6^2+k_{82}x_7^2$$

$$k_{91}=-1/x_9(-V_a+k_{22}x_1^2-k_{22}x_2^2+k_{42}x_3^2-k_{42}x_4^2+k_{62}x_5^2-k_{62}x_6^2+k_{82}x_7^2-k_{82}x_8^2)$$

$$k_{90}=k_{22}x_1^2-k_{22}x_2^2+k_{42}x_3^2-k_{42}x_4^2+k_{62}x_5^2-k_{62}x_6^2+k_{82}x_7^2-k_{82}x_8^2$$

The potential distribution in figure A.1 has been obtained for the following values of k_{n2}:

$x_1 = 0.21$ to $x_2 = 0.60$: $k_{n2} = -700$ (positive charge)

$x_3 = 3.00$ to $x_4 = 3.30$: $k_{n4} = 800$ (negative charge)

$x_5 = 3.30$ to $x_6 = 3.60$: $k_{n6} = -700$ (positive charge)

$x_7 = 8.00$ to $x_8 = 9.90$: $k_{n8} = -100$ (positive charge)

The calculated potential distribution in the figure shows a strong resemblance to the distribution in figure 4.4 of chapter 4. It seems therefore reasonable that the distribution in figure 4.4 should be explained in terms of the four layers of charge.

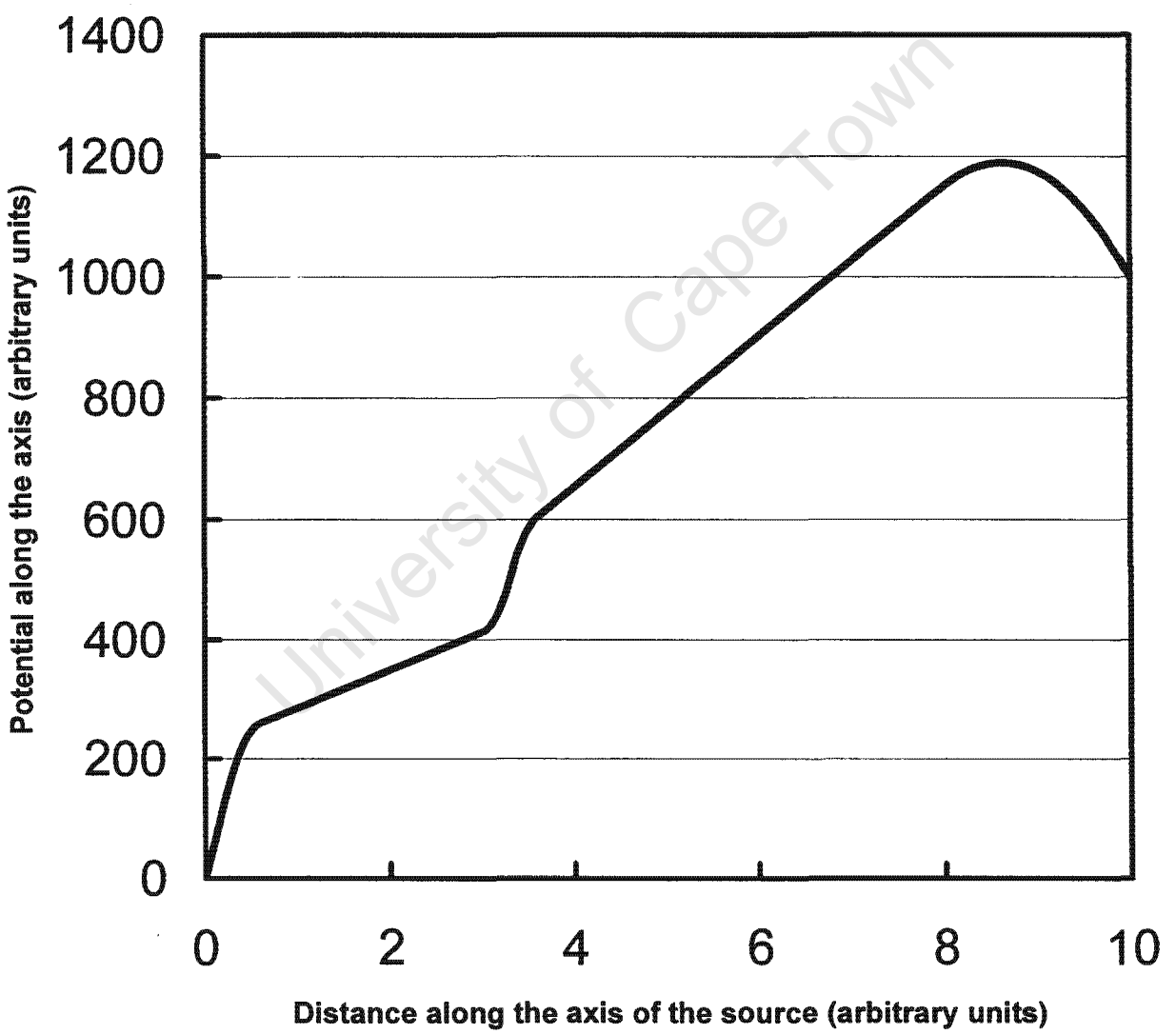

Figure A.1 Calculated potential distribution of four layers of charge between two parallel conducting plates, obtained by piece-wise solution of Possoin's equation.

REFERENCES

[Abi75] Abridged Report on the Requirements for and the choice of a National Accelerator Facility (1975) for the Republic of South Africa and the placing thereof board of control of the feasibility study unpublished.

[Ach 94] van Achterbergh, E.T. (1994) The development of the national accelerator centre proton microprobe as an analytical tool in geochemistry, M.Sc Thesis, Cape Town University.

[Alt87] .Alton, G.D, McConnell, J.W, Tajima, S.and.Nelson G.J. (1987)Emittance studies of high intensity negative ion sources equipped with continuous surface cylindrical and spherical geometry tungsten ionizers. *Nucl. Instrum. MethodsB.*, vol. 24/25 pp. 826-833.

[Ami93] Amirikas, R., Jameson, D.N. and Dooley, S.P. (1993) Measurement of (p, p) elastic cross sections for C, O and Si in the energy range 1.0–3.5 MeV. *Nucl. Instrum. Methods B.*,vol.77., pp. 110-116.

[And77] Anderson, H.H., Ziegler, J.F(1977)Hydrogen Stopping Powers and Ranges, New York, Pergamon Press.

[Ang94] Angert, N. (1994) Ion Sources, Fifth General Accelerator Physics Course, Proc. 1992 CERN Accelerator School, Ed. Turner, S., CERN 94-01 619.

[Ard56] von Ardenne, M.(1956) Atomkernenergie, vol1, 121.

[Art01] Nurmela, A.. (2001). Non-Rutherford elastic scattering cross sections for materials analysis , Ph.D Thesis, University of Helsinki, Finland.

[Ash01] Ashok M., Narayana S., Vijayan V. Magudapathy P. and Nair K.G.M. (2001) Investigation of the elemental concentration of kidney stones by PIXE analysis, *Inter. Journal of PIXE*, vol. 11 Nos 1&2,pp. 21-25.

[Ash01] Ashok, M., Narayana, S., Vijayan, V. Magudapath, P. and Nair, K.G.M. (2001) Investigation of the elemental concentration of kidney stones by PIXE analysis, *Inter. Journal of PIXE*, Vol. 11 Nos 1&2., pp. 21-25.

[Aud04] Audinot, J.-N., Schneider, S., Yegles, M., Hallegot, P., Wenning, R. and Migeon, H.-N. (2004) *Applied Surface Sci.*, vol.231/232 pp. 490-496.

[Ban66] Bandford, A. (1966) The transport of charged particle, London and Colchester, E&F.N. Spon Ltd.

[Bar89] Barton, G. (1989) *Elements of Green's Functions and Propagation, Potentials, Diffusion and Waves*, Clarendon Press, Oxford, Oxford University Press.

[Bar96] Bara, M.., Gueit-Bara, A. and Moretto, Ph.(1996) *Nuclear microprobes in biology and medicine Cell. and Mol. Bio, Special Issue:*, 42(1), Ed: Wegmann R., ISSN, France., pp. 0145-5680,.

[Bar98] Barradas, N.P., Marriott, P. K., Jeynes, C. and Webb, R. P. (1998) The RBS data furnace: Simulated annealin., *Nucl. Instrm. Meth*ods *B136-138*, pp.1157-1162.

[Bec92] Becker, R. and Herrmannsfeldt ,W.B. (1992) IGUN, A program for the simulation of positive ion extraction including magnetic fields, *Rev. Sci. Instrum.*, 63 (4), pp.2756-2761.

[Bec93] Becker, R. (1993) INTMAG: A Program for the Calculation of Magnetic Fields by Integration. *Nucl. Instrum. and Metods B42.*, pp. 303-306.

[Bec98] Becker, R. (1998) New features in the Simulation of Ion Extraction with IGUN, *Proceedings of the 6th European Particle Accelerator(EPAC) Stockholm*, Sweden. pp. 1165.

[Ben72] Bennet J.R.J. (1972) A Review of PIG Sources for Multiply Charged Heavy Ions, *IEEE Transactions on Nuclear Science,* vol. NS-19, No.2 pp. 48-68.

[Bor97] Borburgh, J.(1997)"2 Dimensional Finite Element Calculations on Septum Magnet with "Opera2D", CERN Note PS/CA/Note 97, pp. 27.

[Bot70] Botha, A.H. (1970) Theoretical and Experimental Study of the C.S.I.R.Cyclotron D.Sc. Thesis, University of Pretoria, unpublished

[Bot75] Botha, A.H. and Kritzinger, J.J.(1975) Design of an rf system for an open-sector cyclotron, *Proceedings of Seventh International Conference on*

Cyclotrons and their applications., Birkhäuser, Zürich, Basel, Switzerland, pp.156-159.

[Bot87a] Botha, A.H., Jungwirth, H. N., Kritzinger, J.J, Reinmann, D and Schneiclers, S, (1987) Cmmissioning of the NAC separated- sector cyclotron. In: *Proc. Eleventh Intern. Conf. On Cyclotrons and their Applications,* 1986, Tokyo, Japan pp Ionics,. 9-16.

[Bot87b] Botha, A.H., Burger, S.J. (1987) An injector cyclotron for acceleration of polarized and heavy ions at the NAC. *Proceedings Eleventh International Conference on Cyclotrons and their Applications* Tokyo, Japan, 1986, Ionics pp.515-518.

[Boy59] Boyce, W.H. and King, J.S. (1959) Crystal-matrix interrelations in calculi.*J. Urol.,* vol. 81, pp.351-363..

[Bro74] Brown, K.L. and Iselin, Ch. (1974). A computer Program for simulating charged particle beam transport systems. Internal Report CERN 74-2

[Bro81] Brockis, J.G. and Finlayson, B. (1981) Eds. Proceedings Int. Urinary Stone Conf. Perth, Australia, 1979 . Littleton, Mass., USA,: PSG Publishing Corp.

[Bro82] Brown, K.L. (1982) First-and Second-Order Matrix Theory for the Design of Beam Transport Systems and Charged Particle Spectrometers, SLAC-75, Revision 4, Stanford.

[Bro85] Brown, K.L and Servranckx R.V. (1985) first-and Second-Order Charged Particle Optics, Physics of High Energy Particle Accelerators, New York, American Institute of Physics.

[Bro89] Brown I.G.(1989) *The Physics and Technology of Ion Sources*, New York, John Wiley & Sons.

[Bur58] Burgerjon, J.J., Du Toit, S.J and Kritzinger, C.A.J. (1958) The Pretoria Cyclotron, *Nucl. Instrum. Methods.*, vol. 3,pp. 323-335.

[Bur60] Burgerjon, J.J and Weidemann, W. (1960) The Pretoria Cyclotron. *Nucl. Instrum. Methods.*, vol 8, pp.261-271.

[But97] Butz T. (1997) Nukleare Festkorperphyzik. [Internet] Available from http://www.uni-leipzig.de/~nfp/met_fr/htm [Accessed 2003].

[Cag95] Cargnello, J.A., Powell J.J., Thompson, R.P.H., Crocke,r P.R. and Watt F. (1995)Elemental Hair using Nuclear Microscopy and X-ray Energy Dispersive Spectroscopy., *Analyst*, 120, pp.783-.787

[Cam00] Campbell, J.L., Hopman, T.L., Maxwell, J.A. and Nejedly Z. (2000) The Guelph PIXE software package III: Alternative proton database. *Nucl. Intrum. Methods B.*, vol. 170, pp. 193- 204

[Cam90] Cmapbell, J.L., Maxwel,l J.A., Teesdale, W.J and Wang, J.-X. (1990) Micro-PIXE as a complement to electron probe microanalysis in mineralogy. *Nucl.r Intrum. Methods B*, vol. 44, pp. 347-356.

[Car 72] Carey, D.C. (1972) Computer Simulation of charged particle Beams, *Nucl. Nucl. Instrum. Methods.*, vol. 104 pp. 173-178.

[Car72] Carey, D.C. (1972) Computer simulation of charged particle beams. *Nucl. Instum. Methods.*, vol.104, pp. 173-178.

[Car72] Carey, D.C. (1972) Computer Simulation of Charged Particle Beams. *Nucl. Instrum. Methods.*, vol. 104 pp.173-178.

[Car81] Carey, D.C. (1981) High Energy charged particle Optics Computer Programs, *Nucl. Instrum. Methods.*, vol. 187 pp.97-102.

[Car81] Carey, D.C. (1981) High Energy Charged Particle Optics Computer Programs *Nucl. Instrum. Methods.*, vol. 187 pp.97-102.

[Car81] Carey, D.C. (1987) *The Optics of Charged Particle Beams*, New York, Harwood Academic Publishers.

[Car87] Carey, D.C (1987) *The Optics of Charged Particle Beams*, New York, Harwood Academic Publishers.

[Cav03] Carvalho, M.L., Marques, A.F and. Brito, J.(2003) Proceedings 19th International Conference on X-ray and Inner-Shell Processes, Edi(s) Bianconi A., Marcelli A. and Saini L., AIP, pp.522-528.

[Che74] Chen F.F(1974) *Introduction to Plasma Physics*, New York, Plenum Press.

[Chi04] Chikte, U.M.E. (2004) Private communication. Faculty of Sciences, School of Community Dentistry, University of Stellenboch, Bellville, South Africa.

[Chu78] Chu, W-K., Mayer, J.W. and Nicolet, J.A. (1978.) *Backscattering spectrometry*, New York, Academic Press.

[Chu93] Churms, C.L., Pilcher, J.V., Sprighorn, K.A. and Tapper U.A.S. (1993) A VAX and PC-based data acquisition system for MCA, scanning and list-mode analysis. *Nucl. Instrum. Methods B.,* vol.77, pp. 56-61

[Cla85] Clayton, E. and Wooller, K.K. (1985) *Anal. Chem.*, 57(6) pp. 1075-.1097

[Coh85] Cohen, D.C. and Harrigan, M. (1985) *At. Data and Nucl Data Tables.,* vol., 33 pp. 255-243.

[Coh86] Cohen, D.D. and Harrigan, M. (1986) Calculated *L*-Shell X-ray line intensities fro proton and helium ion impact. *At. Data Nucl. Data Table.s,* 34 pp. 393-414.

[Coh87] Cohen, D.D.(1987) Average L shell fluorescence yields, *Nucl. Instrum. Methods B.,* vol. 22, pp. 55-58

[Con04] Conradie, J.L., Eisa, M.E.M., Celliers, P.J., Delsink, J.L.G., Fourie, D.T., de Villiers, J.G., Maine, P.M., Springhorn, K.A. and Pineda-Vargas, C.A. (2004) *Proceedings of 9th Inter. Conf. on Nuclear Microprobe Tech. and Appl.*, Cavtat (ICNMTA04), Dubrovnik, Croatia, 13-17 September.

[Con92] Conradie, J.L(1992) Improved Proton Beam Quality and Intensity from a 200 MeV Cyclotron System Ph.D. Thesis, University of Stellenbosch.

[Deb88] Debertin, K., and Helmer, R.G. (1988.) Gamma-and X-ray Spectrometry with Semiconductor Detectors. New York, North Holland.

[Dew90] De Wolf, D.A. (1990) *Basics of Electron Optics*, New York, John Wiley & Sons, Inc.

[Dew90] De Wolf, D.A. (1990) *Basics of Electron Optics*, New York, John Wiley & Sons Inc.

[Doo85] Doolittle, L.R. (1986) Algorithms for the rapid simulation of Rutherford backscattering spectra.. *Nucl. Instrum. Methods B.,*vol.9, pp.344-351.

[Doo86] Doolittle, L.R.(1986) A semiautomatic algorithm for Rutherford backscattering analysis. *Nucl. Instrum. Methods B.,* vol. 15, pp. 227-231.

[Dut 87] Du Toit, Z.B., Celliers, O.J., Roels, M M, Conara, E P, Kritzinger J.J and Burger S. J.(1987)., Operating experience with the light-ion injector of the NAC, *Proc. Eleventh Intern. Conf. On Cyclotrons and their Applications* (Tokyo 1986), Ionics, Tokyo, ,pp109-112.

[Dut95] Du Toit Z.B., Celliers P.J(1975).,Commissioning of the injector cyclotron for polarized and heavy ions at NAC, *Proc. Fourteen Intern. Conf. on Cyclotrons and their Applications* (Cape Town 1995), World Scientific, Singapore., pp.28-31.

[EGG82] Instructions Manual(1982) München, Germany

[Eng89] Engström, P., Larsson, S., Rindby A.and Stocklassa B. (1989) A 200 μm X-ray microbeam spectrometer. *Nucl. Instrum. Methods B.,* vol.36, pp.222-226.

[Eva55] Evans, R.D. (1955) The atomic nucleus., New york., McGraw-Hill

[Fin77] B. Finlayson, (1977) In: Calcium metabolism in renal failure and nephrolithiasis, David D.S. Ed., New York : J. Wiley & Sons.

[For95] Forslind, Bo. (1995) The skin: upholder of physiological homeostasis. A physiological and (bio)physical study program. *Thrombosis Research,* vol. 80, No 1 , pp. 1-22.

[Gal 67] Galejs, A. and Rose, P.H. (1967) *Optics of Electrostatic Accelerator Tubes: Focusing of Charged Particles.,* vol. 2, New York, Academic Press Inc.

[Gal89] Galassini, S., Liu, N.Q., Moschini, G., Tasca, A., Villi, G. and Valkovic, V. (1989) Trace element variability in kidney stones. *Nucl. Instrum. Methods B.,* vol. 43, pp. 556-559.

[Gen05] GENPLOT, Stopping power calculations. (2005) [Internet] Available from: http://www.genplot.com/RUMP/new_stop.htm [Accessed: 10 January, 2005].

[Gih82] .Gihwala, D. (1982) Analytical application of proton-induced prompt photon spectrometry, Ph.D Thesis, University of Cape Town.

[Gol80] Goldstein, H. (1980) *Classical mechanics*. Second Edition, London, Addison-Wiley.

[Gor95] Gilmore G. and Hemingway J(1995) Practical Gamma-Ray Spectrometry. new York, Wiley, John & Sons.

[Gra84] Greenacre M.J.(1984) Theory and applications of correspondence analysis, London, Academic Press..

[Gre84] Greiner, W. (1984) *Theoretische Physik, Mechanik 1, Band 1,* Verlag Harri Deutsch, Reading, Massuacuseths, Thun und Frankfurt am Main.

[Gre90] Greenacre, M.J. Sim, C.A. (1990) Correspondence Analysis, User's Manual.

[Gro83] Grosser, J.(1983) *Einführung in die Teilchenoptik*, Germany, Teubner Studienbücher Stuttgart.

[Gur98] Gurbich A. H., Evaluation of non-Rutherford Proton elastic scattering cross section for carbon, *Nucl. Instrm. MethodsB.*, vol.136-138 (1998) 60-65.

[Han01] Hanke, K. Heising, S., Probert, G., Scrivens, R. (2001) Comparison of Simulation Codes for the Beam Dynamics of Low-energy Ions. Geneva, CERN/PS-pp. 061.

[Hai01] Hair analysis panel discussion: Exploring the state of the science, Summary Report (2001) Eastern Research Group, Lexington, MA.

[Hal04] Hallégot, P., Peteranderl, R. and Lechene, C., J.(2004) *Invest. Derma.*, vol.122, pp. 381-386.

[Har82] Harry, R.G.(1982) Harry's Cosmeticology, 7th Edition, New York., Chemical Publisher Co.

[Hed91] Heddle, D.W.O. (1991) *Electrostatic Lens Systems*, Philadelphia, Bristol.,IOP Publishing Ltd

[Hof89] Hofbauer, J. and Steffan, I. (1989) In: Urolithiasis. Walker, V.R., Sutton, R.A., Cameron, E.C.,. Pak, C.Y. and Robertson, W.G., Eds. New York, Plenum.

[Hon85] Hong-Kou, L.I. and Malmqvist, K.G. (1985) A simple method for determining the elemental distribution over the transverse cross section of a hair. *Nucl. Instrum. Methods B.*, vol.12, pp. 257-264.

[Huc01] Huck H., DiGregorio D.E., Fernández Niello J.O., Halac E.B., Igarzábal M., Orecchia J.and Reinoso M. E. (2001) New compact design for an ion source. *Nucl. Instrum. Methods B.*, vol. 175-177, pp.772-776.

[Hay00] Hayat, M.A.(2000) Princilples and techniques of electron microscopy: Biological aplplications , 4th Edition, Cambridge University Press, UK.

[Ill72] Illgen, J.J., Kirchner, R., Schulte and den Bäumen, J. (1972), Duoplasmatron Ion Sources, *IEEE Transactions on Nuclear Science,* vol. NS-19, No.2, pp.35-47.

[Ion69] General Ionex Corporation Manual(1969) Ionex, New York

[Ish78a] Ishii, K., Valladon, M. and Debrun, J.L. (1978) The average stopping power method for accuarate charged particle activation analysis. *Nucl. Instrm. Meth*ods., vol. 150, pp.213-219.

[Ish78b] Ishii, K., Sastri, C.S., Valladon, M., Borderie, B. and Debrun, J.L. (1978) Two reactions method for accuarate analysis by irradiation with charged particle. *Nucl. Instrm. Methods.*, vol.153, pp.507-509.

[Iuc84] Indiana University Cyclotron Facility (1984) Scientific and Technical Report. 165.

[Jas96] Jakšić, M., Bogdanović, I., Hopewel, l J.W., Wilkinson, J.H. and Valković V. (1996) *Cell. and Mol. Biol.*, vol. 42(1) pp. 127-131.

[Jes01] Jesus, A.P., Braizinha, B., Cruz, J., and Ribeiro, J.P., (2001) Influence of target thickness on resonant elastic scattering of proton by ^{19}F. *Nucl. Instrm. Methods B.*, vol.174, pp. 229-234.

[Joh88] Johansson, S.A.E. and Campbell, J.L.(1988) PIXE: A novel technique for elemental analysis, New York, Wiley, John & Sons.

[Joh95] Johansson, S.A.E., Campbell, J.L. and Malmqvist, K.G.(1995) Particle-Induced X-ray Emission Spectrometry (PIXE), Wiley, New York, John & Sons.

[Joo87] Joost, J. and Tessadri, R. (1987) Trace element investigations in kidney stones patients. *Eur. Urol.*, vol 13 pp. 264-270.

[Jos95]Tes Tesmer, J.R. and Nastasi, M., Eds.(1995) Hand Book of Modern Ion Beam Materials Analysis, , USA,. MRS, Pittsburgh.

[Jun75] Jungwirth, H.N., Bruins, L.D(1975)Design of magnets for an open-sector cyclotron, *Proc .Seventh Intern. Conf. On Cycltrons and their applications (*Zürich 1975), Birkhäuser, Basel., pp.193.

[Kis65] Kistemaker, J., Rol, P.K. and Politiek J. (1965) Some Plasma-Physical Aspects of Mono- and Duo-Plasmatron Ion Sources. *Nucl. Instrum. Methods.*, vol. 38, pp.1-11.

[Kon98] Konac, G., Kalbitzer, S., Klatt, Ch., Niemann, D. and Stoll, R., (1998) Energy loss and straggling of H and He ions of keV energies in Si and C. *Nucl. Instrm. Meth*ods, **B136-138**, 159-165.

[Kra79] Krause, M.O. (1979) Phys. Chem. Ref. Data 8, P.307.

[Lej74a] Lejeune, C. (1974) Theoretical and Experimental Study of the Duoplasmatron Ion Source, Part 1: Model of the Duoplasmatron Discharge. *Nucl. Instrum. Methods.,* vol.116, pp. 417-428.

[Lej74b] Lejeune C. (1974) Theoretical and Experimental Study of the Duoplasmatron Ion Source, Part 2: Emissive Properties of the Source. *Nucl. Instrum. Methods.,* vol. 116, pp.429-443.

[Leo86] Feldman, L.C. and Mayer, J.W.(1986) Fundamentals of Surface and Thin Films Analysis, Amsterdam, North Holland.

[Lic69] Lichtenberg, A.J.(1969) *Phase-space dynamics of particles*, New York, John Wiley & Sons, Inc.

[Liu93] Liu, Z, Duan, Z., and He, H. (1993) Cross section measurements for 170 backscattering of protons from carbon in the energy range 0.3-3.0 MeV., *Nucl. Instrm. Methods..*, vol.74, pp. 439-442.

[Lla98] Llabador, Y. and Moretto, Ph. (1998) Applications of nuclear microprobes in the life sciences, Singapore, World Scientific,

[Lov93] Lövestam N.E.G. (1993) Currently used control and data acquisition systems for nuclear microprobes, *Nucl. Instrum. Methods B.,*, vol. 77, pp.71-78.

[Mai02] Maine, P.M. and Conradie, J.L. (2002)., Design and Optimization of New Beamlines for *i*Themba Laboratory for Accelerator Based Sciences (*i*Themba LABS), M.Sc. (Applied Radiation Science and Technology) Thesis, University of North West, South Africa,

[Mal76] Mallory, M.L. and Crandall D.H. (1976) A Penning Multiply Charged Heavy Ion Source Test Facility. *IEEE Transactions on Nuclear Science,* vol. NS-23, No.2, pp. 1069-1072.

[Man80] Mandel, N.S., Mandel, G.S (1980) Epitaxis between stone-forming crystals at atomic level. In Nephrolithiasis, Eds L'or F., Brenner, P., Stein, J., Hill, Ch., Livingstone, New York, pp.37-58.

[Mat65] Mathews, J. and Walker, W A. Benjamin, R.L(1965) *Mathematical Methods Physics*, New York., Wiley & Sons, Inc.

[Max89] Maxwell, J. A., Campbell, J. L., and Teesdale W. J(1989) vol43The Guelph PIXE software package. *Nucl. Instrum. Methods.,* vol.43.,pp. 218-230.

[May98] Mayer, M., (1998) SIMNRA, A program for simulation of nuclear reaction análisis spectra. Juelich: Max-Planck-Institut.

[Mer80] Merry, C.M. and Cornel, l J.C.(1980) Charged Particle Beam Transport for Cyclotron Facility, Internal Report NAC/BT/80-01, National Accelerator Centre, NAC.

[Meu91] Meurman, J.H. and Frank, R.M. (1991) Scanning electron microscopic study of the effect of salivary pellicle on enamel erosion. *Caries Res.,*vol. 25, pp.1-6.

[Mey75] Meyer, J.L., Bergert, J.H., Smith, L.H., (1975) Epitaxial relationships in urolithiasis: the calcium oxalate monohydrate-hydroxyapatite system. *Sci. Mol. Medicine*, vol. 49, pp.369-374.

[Mil95] Millward, A., Shaw. L, Smith, A.J. (1995) In vitro techniques for erosive lesion formation and examination in dental enamel. *Journal of Oral Rehabilitation*, vol. 22, pp. 37-42.

[Mok02] Mokoduwe, P.S. (2002) Development of a Duoplasmatron Ion Source at *i*Themba Laboratory for Accelerated Based Sciences (*i*Themba LABS), M.Sc. (Applied Radiation Science and Technology) Thesis, unpublished

[Mor96] Moretto, Ph. (1996) Nuclear microprobe: a microanalytical technique in biology. *Cellular and Molecular Biology,* vol. 42(1) pp.1-16.

[Mor95] Moretto, Ph. and Razafindrabe, L. (1995) Simulation of RBS spectra for quantitative mapping of inhomogeneous biological tissue. *Nucl. Instrm. Meth*ods B104, 171-175.

[Mur02] Murao, S., Daisa E., Sera, K., Maglambayan, V.B., and Futatsugawa, S. (2002) PIXE measurement of human hairs from a small-scale mining site of the Philippines. *Nucl. Instrum. Methods B.,* vol.189, pp. 168-173.

[Nan83] Nancollas, G.H. (1983) The mechanism of formation of renal stone crystals. *Proc. Eur. Dial. Transplant. Assoc.*, vol. 20, pp. 386-397.

[Nur01] Nurmela, A. (2001). *Non-Rutherford elastic scattering cross for materials analysis,* Unpublished Doctoral Dissertation Report HU-P-D89, Helsinki,: University of Helsinki..

[Oln58] Olness, J.W., Vorona, J., and Lewis, H.W(1958) Elastic and inelastic scattering of protons by N^{14}., *Phys. Rev.*, vol 112, No2 , pp. 475-480.

[Oxf90] Oxford Microbeams(1990) Oxford, Oxford Microbeam System.

[Pak76] Pak, C.Y.C., (1976) In: The Kidney Vol II, Brenner, B.M. and. Rector, F.C., Jr. Eds., Philadelphia, Pa USA: Saunders.

[Pal90] Paluszkiewicz, C., Kwaitek, W.M. and Galka, M. (1990) Trace elements relations to renal stone phases. *Nucl. Instrum. Method B.,* vol. 49, pp. 234-237.

[Pal93] Pallon, J., Knox, J., Forslind, B., Verner,Y. and Pinheiro, T(1993)Application in medicine using the new Lund microprobe. *Nucl. Instrum. Methods B.*, vol. 77, pp. 287-293.

[Pal97] Pallon, J., Knox, J., Forslind, B., Verner,Y. and Pinheiro, T(1997)Applications of nuclear microprobe analysis to dermatological research. *Nucl. Instrum. Methods* B, vol. 219-220, pp. 454-459.

[Pei78] Peisach, M. J. (1987) *Radioanal. Nucl. Chem.*, Vol 110 No 2 , pp. 461-475.

[Pih99] Pinheiro, T., Carvalho M.L., Casaca, C., Barreiros, M.A., Cunha, A.S., Chevallier, P., (1999) Microprobe analysis of teeth by synchrotron radiation: environmental contamination. *Nucl. Instrum. Methods B.,* vol. 158, pp. 393-398.

[Pil78] Pillay, A.E. (1978) Determination of trace elements in human hair by nuclear methods, M.Sc. Thesis, University of Durban-Westville, Durban, South Africa.

[Pil81] Pillay, A.E. and Peisach, M. (1981) *J. Radioanal. Chem.*, 63(1) pp.85-95.

[Pin01] Pineda-Vargas, C.A., Prozesky, V.M. and Przybylowicz, W.J. (2001) Correspondence analysis evaluation of linear nutrient distribution in root tips of the tropical forage. *Brachiaria Brizantha, Nucl. Instrum. Methods B.,* vol. 181, pp. 493-498.

[Pin04] Pineda-Vargas, C.A., Eisa, M.E., Chikte, U.M.E. and Conradie, J.L. (2004) High-resolution nuclear microprobe elemental mapping of teeth enamel-

dentine interface exposed to acidic conditions. *Rad. Phy. And Chem.*, vol. 71, pp. 937-942.

[Pin92] Pineda, C.A.(1992) Thick Target PIXE Analysis, Ph.D Thesis, University of Cape Town.

[Pin94] Pineda, C.A., Peisach, M. (1994) Micro-analysis of kidney stones sequentially excreted from a single patient. *Nucl. Instrum. Methods B.*, vol. 85, pp.896-900.

[Pin95] Pineda, C.A., Rodgers, A.L., Przybylowicz, W.J. and Prozesky, V.M. (1995) Elemental mapping analysis of recurrent calcium oxalate human kidney stones. *Nucl. Instrum. Methods B.*, vol. 104, pp. 351-355.

[Pin96] Pineda, C.A., Rodgers, A.L., Prozesky, V.M. and Przybylowicz, W.J. (1996) Microanalysis of calcium-rich kidney stones at the NAC nuclear microprobe. *Cel.r and Mol.r Biology*, vol 42(1), pp. 119-126.

[Pin97] Pineda, C.A., Rodgers, A.L., Prozesky, V.M., Prybylowicz, W.J. (1997) ,in: Proc 14th Int. Conf. Appli. Accel. Res. and Ind., Eds J.L. Duggan and I.L. Morgan, AIP Press, New York, pp 571-574.

[Pow98] Powder Diffraction File (1998) International Centre for Diffraction Data,, Date Sets 1-48 Plus 70-85, Pennsylvania, USA.

[Pro00] Prozesky, V.M., Pineda, C.A., Mesjasz-Przybylowicz, J., Przybylowicz, W.J., Churms, C.L., Springhorn, K.A., Moretto, Ph., Michelet, C., Chikte, U. and Wenzel, P. (2000) The biological research programme of the nuclear microprobe at the National Accelerator Centre, Faure._*Nucl. Instrum. Methods B.*, vol. 161-163, pp.852-859.

[Pro95] Prozesky, V.M., Przybylowicz, W.J., van Achterbergh, E.,, Churms, C.L., Pineda, C.A., Springhon, K.A., Pilcher, J.V., Kritzinger, J., Scmitt, H. and Swart, T. (1995) The NAC nuclear microprobe facility._*Nucl. Instrum. Methods B.*, vol. 104, pp. 36-42.

[Prz01] Przybylowicz, W.J., Mesjasz-Przybylowicz, J., Pineda, C.A., Churms, C.L., Ryan, C.G., Prozesky, V.M., Frei, R., Slabbert, J.P., Padayachee J. and Reimold, W.U., (2001) Elemental mapping using proton-induced x-rays. *X-ray Spectrometry.*, vol 30 pp. 156-163.

[Prz99] Przybylowicz, W.J. ,Mesjasz-Przybylowicz, J, Pineda, C.A, Churms, C.L..Springhon, K.A and. Prozesky, V.M. (1999) Biological Application of the NAC Nuclear Microprobe, *X-ray spectrometry.*, vol. 28, pp.237-243

[Qay94] Qayyum, A. and Ahmad, S. (1994) Magnetically Confined Hollow-cathode Duoplasmatron for the PINSTECH Ion Implanter. *Nucl. Instrum. Methods B.*, vol. 94, pp. 597-600.

[Rau75] Rautenbatch, W.L.and Botha, A.H. *(*1975) Proposal for a South African National Accelerator Facility for physics and medicine, *Proceedings of Seventh International Conference on Cyclotrons and their applications*, Brikhäuser Zürich, Basel , Switzerland., pp. 117-122.

[Rau85] Rauhala, E. (1985) Proton elastic scattering cross sections of carbon, nitrogen and silicon for backscattering analysis in the energy range 0.7—2.5 MeV *Nucl. Instrum. Methods B.*, vol. 12, pp.447-452.

[Rau92] Rauhala, E. (1992). Ion backscattering spectrometry. In: *Elemental Analysis by Particle Accelerators.* Eds: Alfassi, Z.B. & Peisach, London, CRC Press, pp.179-241.

[Rei02] Reinert, T., Sakellariou, A., Schwertner, M., Voget, J and Butz, T. (2002) Scanning transmission ion microscopy tomography at the Leipzig nanoprobe LIPSION. *Nucl. Instrum. Methods B.*, vol.190, pp. 266-270.

[Roh01] Rohrer U, edited by Septier, A L.(2001), *Compendium of Transport Enhancements,* Ch-5232 Villigen, Switzeland, unpublished.

[Ron85] Ronald, D. Vis(1985.) The proton Microprobe Applications in the Biomedical Field, Boca Raton, Florida, CRC Press Inc

[Ros 64] Rose, P.H., Galejs, A. and Peck, L. (1964) Particle Trajectories in Accelerator Tubes, *Nucl. Instrum. Methods.*, vol. 31, pp. 262-268.

[Rya00] Ryan, C.G. (2000) Quantitative trace element imaging using PIXE and the Nuclear Microprobe. *Int. J. Imaging Sys. Tech.* (Special Issue on Quantitative Imaging) vol. 11, pp.219-230.

[Rya02a] Ryan, C.G., van Achterbergh, E., Yeats, C.J., Win, Tin. Tin and Gripps, G. (2002) Quantitative PIXE trace element imaging of minerals using the new CSIRO-GEMOC. *Nucl. Instrum. Methods.*, B189, pp. 400-407.

[Rya02b] Ryan, C.G, and Cousens, D.R. (2002) Geo-PIXE II Quantitative PIXE trace element imaging and analysis, CSIRO Exploration and Mining, North Ryde, NSW, Australia.

[Rya02c] Ryan, C.G., van Achterbergh, E., Yeats, C.J., Drieberg, S.L., Mark, G., McInnes, B.M., Win, TinTin., Cripps, G.,and Suter, G.F. (2002) Quantitative, high sensitivity, high resolution, nuclear microprobe imaging of fluids, melts and minerals. *Nucl. Instrum. Methods.*, B188, pp. 18-27.

[Rya04] Ryan, C.G (October 2004) personal communication.

[Rya90a] Ryan, C.G., Cousens, D.R., Sie, S.H. and Griffin, W.L. (1990) Quantitative analysis of PIXE spectra in geoscience applications. *Nucl. Instrum. Methods B.*, vol.. 49, pp.271-276.

[Rya90b] Ryan, C.G., Cousens, D.R., Sie S.H. and Griffin W.L., Suter G.F. and Clayton E. (1990) Quantitative PIXE microanalysis of geological material using the CSIRO proton microprobe *Nucl. Instrum. Methods B.*, vol. 47 pp. 55-71.

[Rya93] Ryan, C.G. and Jamieson, D.N. (1993) Dynamic analysis: on-line quantitative PIXE microanalysis and its use in overlap-resolved elemental mapping. *Nucl. Instrum. Method B.*, vol.77, pp. 203-214.

[Rya95] Ryan, C.G., Jamieson, D.N., Churms, C.L., Pilcher, J.V. (1995) A new method for on-line true-elemental imaging using PIXE and the proton microprobe. *Nucl. Instrum. Methods B.*, vol. 104, pp.157-165.

[Sal74] Salem, S.I., Panossian, S.L., and Krause, R.A(1974).Atomic Data and Nuclear Data Tables vol.14.pp.91-109.

[Sar95] Sarstedt,' M., Becke,r R.,. Klein, H.,. Maaser, A.,. Müller, J.,. Thomae, R. and Weber, M. *(1995)* Beam diagnostics using an emittance measurement device. *Nucl. Instrum. Methods B.*, vol. 99, pp. 721-724.

[Sch76] Schulte, M. and Wolf, B.H. (1976) Ion and Electron Flow in Hot-cathode PIG Sources for Multiply Charged Heavy Ions. *IEEE Transactions on Nucl. Science,* Vol. NS-23, No.2, pp.1053-1060.

[Sch85] Schwille, P.O., Smith L.H., Robertson, W.G.and Vahlensiek, W., Eds, (1985) Urolithiasis and related clinical research, New York, Plenum Press.

[Sch98] Schmidt, C. W. (1998) Duoplasmatron source modification for $^{3}He^{+}$ operation, *Rev. Sci. Instr.*, vol. 69, No. 2, pp. 1020-1023.

[Sei95] Ogata, Seiji. Hisamune, Takeshi and Seki, Seiji. (1995) Emittance measurement of mass-separated high-current ion beams *Nucl. Instrum. Methods A.*, vol. 363, pp. 468-472.

[Ser02] Sera, K., Futatsugawa, S., and Murao, S. (2002) Quantitative analysis of untreated hair samples for monitoring human exposure to heavy metals. *Nucl. Instrum. Methods B.*, vol.189, pp. 174-179.

[Sha04] Shariff, A., Kristiansson, P., Auzelyte, V.., Elfman, M., Malmqvist, K.G., Nilsso, Ch., Pallon, J. and Wegdén, M.(2004) Characterization of a new large area HPGE X-ray detector dor low beam current application.. *Nucl. Instrum. Methods B.*, vol. 219-220, pp. 485-489.

[Sim72] Simonyi ,K.(1972) *Physikalische Elecktronik*, Budapest, Académia Kiadó.

[Sjö96] Sjöland, K.A.and Kristiansson, P. (1996) Off-axis STIM nuclear microprobe analysis. *Nucl. Instrum. Methods B.*, vol. 118, pp. 451-455.

[Smi81] Smith, L.H., Robertson, W.G. and Finlayson, B. (1981) (Eds), Urolithiasis, Clinical and basic research, Proceedings 4th Int. Sym. Urolithiasis Res., Williamsburg, Virginia, U.S.A.,1980. New York, Plenum Press.

[Sta03] StaSoft, Inc. STATISTICA (Data analysis software system), Version 6.1 (2003). [Internet address]: www.statsoft.com.[accessed July 2003].

[Sto01] Stone, G. and Manjoo, Y (2001) National Accelerator Centre Annual Report.

[Stu55] Sturrock P.A. (1955) *Static and Dynamic Electron Optics*, Cambridge, Cambridge University Press.

[Stu55] Sturrock, P.A. (1955) *Static and Dynamic Electron Optics*, Cambridge, England, University Press.

[Szi88] Szilagyi, M. (1988) *Electron and Ion optics*, New York, Plenum Press.

[Tap 93] Tapper, U.A.S, McMurray, W.R., Ackermann, G.F., Churms, C.L., de Villiers, G., Fourie, D., Groenewald, P.J., Kritzinger, J., Pineda, C.A., Pilcher, J.V., Schmitt, H., Springhorn, K. and Swart, T. (1993) High-

brightness proton beams at the NAC nuclear microprobe by acceleration of H_2 ions. *Nucl. Instrum. Methods B.*, vol. 77, pp. 17-24.

[Tec76] National Accelerator Project (1976) Technical Report of the Accelerator Task Group.

[Tee 90] Teesdale, W.J. and Campbell, J.L. (1990) An on-demand beam deflection system for microbeam PIXE analysis *Nucl. Instrum. Methods B.*, vol.52, pp. 93-97.

[Tee88] Teesdale, W.J., Maxwell, J.A., Perujo, A., Campbell, J.L., van Der Zwan, L. and Jackman, T.E. (1988) Limits of detection and quantitation in PIXE analysis of thick targets. *Nucl. Instrum. Methods B.*, vol. B35, pp.57-66.

[Thi67] Thiesen, R.,Vollath,D., Tables of X-ray Mass Attenuation Coefficients(Verlag Stahleissen, M.B.H., Duseldorf, 1967)

[Vah79] Vahlensieck, W., Ed.(1979) Urolithiasis 1. Berlin: Springer.

[Vál77] Vályi, L. (1977) *Atom and Ion Sources.* London and Akadémiai Kiadó, Budapest, John Wiley & Sons.

[Val96] Valcović V., Jakšić M., Watt F., Grime G.M., Wells J. and Hopewell J.W. (1996) Effect of ionizing radiation on the trace element composition of hair. *Nucl. Instrum. Methods B.*, vol. 75, 173-176.

[Vas02] Vasconcellos M.B.A., Catharino M.G.M., Paletti G., Saiki M., Bode P., Fávaro D.I.T., Baruzzi R. and Rodrigues D.A.J. (2002) *Trace & Microprobe Tech.*, 20(4) pp. 527.

[Vec04] Vector Fields Ltd, 24 Bankside, Kidlington, Oxford OX5 1JE, England, Email: info@vectorfields.co.uk, www.vector-fields.com.

[Ver68] Vermeulen, C.W., Lyon, E.S. (1968) Mechanisms of genesis iand growth of calculi. *Am. J. Med.*, vol. 45, pp. 684-692.

[Vil93] De Villiers, M.G. (1993) The Cape Town brown haze pilot study. Final Report No CON 060, Energy Research Institute, University of Cape Town.

[Vis84] Vis, R. D., Van der Stap, C. C. A. H. and Bos, A. J. J. (1984) Macro- and micro-PIXE analyses of biological and medical samples. *Nucl. Instrum. Methods.*, vol 3, pp .319-325.

[Wan86] Wandt, M.A.E. (1986) Scientific aspects of urolithiasis: quantitative stone analyses and crystallization experiments. Doctoral Dissertation, Unpublished, University of Cape Town, Cape Town.

[Wat87] Watt, F. and Grime, G.W. (1987) Principle and Applications of High- Energy Ion Microbeams. Bristol, England Adam Hilger.

[Wei78] Chu Chu, Wei-Han, Mayer, J. W., Nicolet, M.-A. (1978) Backscattering Spectrometry. New York, London, Academic Press.

[Wie93] Wiedemann, H. (1993) *Particle Accelerator Physics, Basic Principles and Linear Beam Dynamics*, New York, Springer-Verlag.

[Wie95] Wiedemann, H. (1995) *Particle Accelerator Physics II, Nonlinear and Higher- Order Beam Dynamics*, New York, Springer-Verlag,.

[www03] http://www.unileipzig.de/%7Enfp/Research/Methods/[Accessed June 2004]. Ion_Beam_Analysis/ion_beam_analysis.html. [Accessed 15 Feb.2005].

[www05] http://www.eaglabs.com/cai/rbstheo/cairtheo.htm 1995-2005 [Accessed 15 Feb. 2005].

[Zak98] Zakrgynska-Fontaine, V., Dore, J.C., Ojasoo,T., Poirier-Duchene, F.and Viel, C. (1998)Study of the Age and Sex Dependence of Trace Elements in Hair by Correspondence Analysis., *Biol. Trace Elem. Res.*, vol. 61(7) pp. 151-186.

[Zha89] Zhang, D., Wang, N., Chen, S. and Chen, J. (1989)PIXE Analysis of trace elements in hair and their correlation with cerebrovascular. *Vacuum.*, vol. 39, pp. 139-141.

[Zie85] Ziegler, F., Biersack, J.P. and Littmark, U. (1985) The Stopping and Range of Ions in Solids. New York: Pergamon Press.